MODELLING VARIABLE RADIO EMISSION FROM YOUNG STELLAR FLARES

A THESIS SUBMITTED TO THE UNIVERSITY OF MANCHESTER
FOR THE DEGREE OF DOCTOR OF PHILOSOPHY
IN THE FACULTY OF SCIENCE AND ENGINEERING

2020

Charlotte O. G. Waterfall

Department of Physics and Astronomy in the School of Natural Sciences

Contents

3 Solar and T-Tauri flares 56

4 Gyrosynchrotron emission 95

Word Count: 36412

List of Tables

List of Figures

Abstract

MODELLING VARIABLE RADIO
EMISSION FROM YOUNG STELLAR FLARES
Charlotte O. G. Waterfall
A thesis submitted to the University of Manchester
for the degree of Doctor of Philosophy, 2020

Variable X-ray and radio emission is frequently observed from flares on the Sun as well as low mass, young stellar objects known as T-Tauri stars. These T-Tauri flares are several times more luminous than their solar analogues; a result of their more active magnetospheres. The temporal relationship between the thermal X-ray and non-thermal radio emission seen in flares is described by the Neupert effect, where the thermal X-rays are produced following the plasma heating by the non-thermal particles. The Güdel-Benz relation also correlates the peak of the thermal X-ray and non-thermal radio emission from flares. This relation has long been applied to solar flares as well as extended to flares on other main sequence stars. However, combining observations of T-Tauri flares from multiple sources suggests that the radio emission produced in the magnetospheres of T-Tauri stars is far greater than expected. Modelling of T-Tauri flares is carried out, using fast gyrosynchrotron codes to calculate the gyrosynchrotron emission produced from flux tubes that connect the star with its accretion disk. Initially, the effect of varying peak flaring parameters on the radio and X-ray emission is investigated. The resulting peak X-ray and radio luminosities of $\log L_X$ [erg s^{-1}] = 30.5, $\log L_R$ [erg s^{-1} Hz $^{-1}$] = 16.3 agree well with observations and also fall below the Güdel-Benz relation. A secondary model, that incorporates time dependent effects of the radio emission using 3D MHD data, also produces large radio luminosities that agree with observations. This model also provides the first multi-frequency ($1-1000$ GHz) intensity and circular polarisation predictions for a flaring T-Tauri star over time. In both models, the peak flux occurs around 30 GHz. The peak flux at each increasing time step is also found to decrease and move to lower frequencies. These models provide important constraints on the physical properties of the flaring star-disk

environment, as well as predictions for the observable fluxes from different viewing angles.

Declaration

No portion of the work referred to in this thesis has been submitted in support of an application for another degree or qualification of this or any other university or other institute of learning.

Copyright

i. The author of this thesis (including any appendices and/or schedules to this thesis) owns certain copyright or related rights in it (the “Copyright”) and s/he has given The University of Manchester certain rights to use such Copyright, including for administrative purposes.

ii. Copies of this thesis, either in full or in extracts and whether in hard or electronic copy, may be made **only** in accordance with the Copyright, Designs and Patents Act 1988 (as amended) and regulations issued under it or, where appropriate, in accordance with licensing agreements which the University has from time to time. This page must form part of any such copies made.

iii. The ownership of certain Copyright, patents, designs, trade marks and other intellectual property (the “Intellectual Property”) and any reproductions of copyright works in the thesis, for example graphs and tables (“Reproductions”), which may be described in this thesis, may not be owned by the author and may be owned by third parties. Such Intellectual Property and Reproductions cannot and must not be made available for use without the prior written permission of the owner(s) of the relevant Intellectual Property and/or Reproductions.

iv. Further information on the conditions under which disclosure, publication and commercialisation of this thesis, the Copyright and any Intellectual Property

Acknowledgments

I would like to thank STFC for studentship support as well as my supervisors, Professor Philippa Browning and Professor Gary Fuller, for their advice and guidance throughout my PhD. I would also like to thank my family, specifically my parents, for their continuous support and encouragement. Finally, I would like to thank my oldest friends, Poppy and Ziggy, and dedicate this thesis to them.

Chapter 1

Introduction

T-Tauri stars are low mass, young stars that exhibit variability over a range of wavelengths. The short term variability of these emissions is often attributed to flaring events within the star's magnetosphere. These flaring events are thought to be the result of ongoing accretion onto the forming star. For the T-Tauri stars that possess dense circumstellar disks, this accretion has been suggested to be driven by interactions between the star and disk. The flaring emission has also been attributed to accretion shocks near the surface and reconnection events within the magnetosphere. In the case of star-disk interactions, reconnection of the stellar and disk field lines drive the flare, producing large amounts of non-thermal radio and thermal X-ray emission. Similar emission signatures are seen on solar flares, where the peak radio and X-ray emission are correlated in what is known as the Güdel-Benz (GB) relation [Güdel and Benz, 1993]. This relation holds for solar flares and main sequence stellar flares over several orders of magnitude. Whether or not T-Tauri flares fit with this relation is explored in this thesis. There are numerous observations of the variable radio and X-ray emission from young stellar flares however there is a distinct lack of flare models that address both these emissions from star-disk interactions. This thesis will present the results from models that address this, examining the results from both a range of peak flaring scenarios as well as the variable radio flux and circular polarisation over time.

Chapter 2 presents an introduction to these T-Tauri stars, including an overview of observations and models of them. Characteristic parameters of T-Tauri flares, such as the density and temperature, are explored. These parameters will be used to define variables used in the models of flaring T-Tauri stars later in this thesis. Chapter 3 gives an overview of what a flare is and the processes and relevant emission mechanisms that occur. Scaling relations for emission measures, temperatures, X-ray luminosities and radio luminosities are also explored in this chapter. The observational results of T-Tauri stars from literature will be collated and compared to results from flares on the Sun as well as main sequence stars through the GB relation. Comparisons between solar and T-Tauri flare timescales will also be made here. Chapter 4 explores the radio emission processes from a flare in detail. The codes and simulators that will be used to model the gyrosynchrotron emission from a T-Tauri flare are also discussed in detail here. Chapter 5 presents and discusses the results from these simulators for the gyrosynchrotron emission from a flaring flux tube on a T-Tauri star. The gyrosynchrotron emission is calculated for two different flux tube configurations and for a range of peak flaring values. The calculated X-ray emission is combined with the simulated radio emission to compare the results with the GB relation and T-Tauri flare observations. Chapter 6 explores the time dependency of the variable radio emission from a T-Tauri flare interacting with its disk, combining 3D MHD data with an adapted version of the simulator used in Chapter 5. This model incorporates a flux tube populated with a distribution of non-thermal electrons. Properties of this flux tube, e.g. the loss rate of the electrons, are varied and the results discussed. The multi-frequency circular polarisation from this system is also discussed. Chapter 7 summarises the key findings of this thesis and indicates necessary future areas of research. There are two publications associated with this thesis: Waterfall et al. [2019] covers the material in Section 3.3.3 and Chapter 5, Waterfall et al. [2020] covers the material in Chapter 6.

Chapter 2

An introduction to T-Tauri stars

2.1 Young stars

The evolution of a young star from its birth to the zero-age main sequence is a rich area of research. From stellar birth in cold molecular clouds to planet formation in dissipating disks, there exist many different key phases in their evolution. The term young stellar object (YSO) is used to describe these young, normally low mass, stars that have not yet reached the main sequence. They are powered predominately through the accretion of surrounding material and gravitational contraction [Feigelson and Montmerle, 1999]. Once the star has evolved to the zero-age main sequence (ZAMS) it will be powered via nuclear processes.

2.1.1 Pre-main sequence evolutionary stages

YSO's are divided into four different evolutionary classes: 0, I, II and III. Class 0 and I define the protostar stage. Class II and III are used to describe the more evolved T-Tauri stage. Class 0 protostars are the youngest of stellar objects. They are comprised of a central accreting core, born out of the collapse of a dense molecular cloud. The

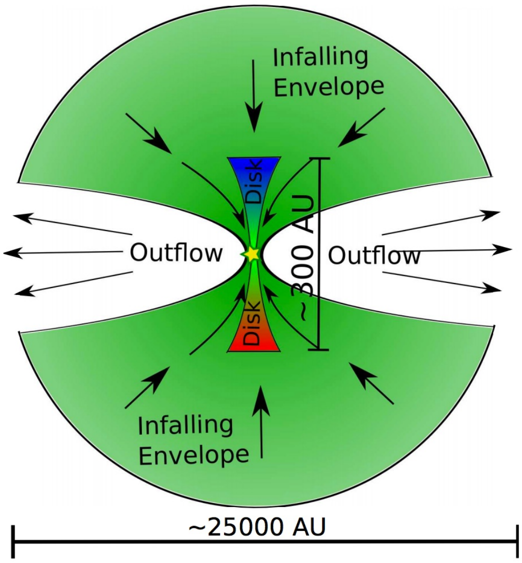

Figure 2.1: Diagram of a protostar in the class 0 phase. The central protostar is small (approximately 0.2 $M_\odot$), accreting mass from its large and dense surrounding envelope and circumstellar disk. Bipolar outflows are also present. The blue to red colour symbolises the velocity gradient present from the Keplerian rotation. Figure from Tobin et al. [2012].

envelope (where typically $M_* < M_{envelope}$) of remaining material surrounding this protostar is constantly being accreted onto it [Barsony, 1994]. Class 0 objects are therefore characterised by their large infalling envelopes, within which a circumstellar disk and outflows form. A schematic of one of these typical class 0 protostars is shown in Figure 2.1. They are very large in size (thousands of AU in diameter) compared to the more evolved YSOs (hundreds of AU in diameter) due to their envelope. This stage lasts approximately 10^4 years and can be observed primarily through thermal radio emission.

Once most of the protostellar envelope has accreted onto the protostar or surrounding disk, the star enters the class I stage. The star is still classed as a protostar at this point however the central object is less obscured by the envelope and has grown in size. The disk and outflows are still present and this stage lasts for several more thousand years. Now the envelope has cleared, X-ray emission is now observable from the accreting protostar. The final two stages, class II and III, are also referred to as the T-Tauri star (TTS) stage. These two classes are distinguished between by the presence or lack of a detectable disk. Class II and III objects are also referred to as classical and weak-lined T-Tauri stars respectively. The weak-lined T-Tauri's (WTT's) are so called for their weak emission lines associated with the dissipation or lack of a circumstellar (accretion) disk.

Class II stars, or classical T-Tauri star's (CTTS's) no longer have a surrounding envelope. They do still possess a distinct circumstellar disk from which they accrete, a key signature of these stars. They are $10^6 - 10^7$ years old. The age of a T-Tauri star is not indicative of its evolutionary stage however. Many WTTS's can be as young as their less evolved CTT counterparts [Hartmann et al., 2016]. The progression into the class III phase is defined by the steady disappearance of the disk. This disk is eroded over millions of years via stellar accretion from the inner region, as well as the forming of planetesimals within the outer regions. Figure 2.2 shows the comparative differences between CTT and WTTS's. The inner magnetosphere of CTTS's is truncated by the presence of the dense disk. This magnetosphere extends further in the WTT case, as the disk dissipates and becomes thinner.

There is sometimes a final subgroup associated with WTT's: the naked T-Tauri stars (NTTS). These stars have completely cleared their disks and are at the final stage of their evolution before nuclear processes start and the star joins the main sequence [Walter, 1987].

2.1.2 Infrared classification

The classification of young stars can be done in numerous ways. The most popular of these is done by examining the spectral energy distribution (SED). The spectral index, α, is calculated from the slope of the star's SED as:

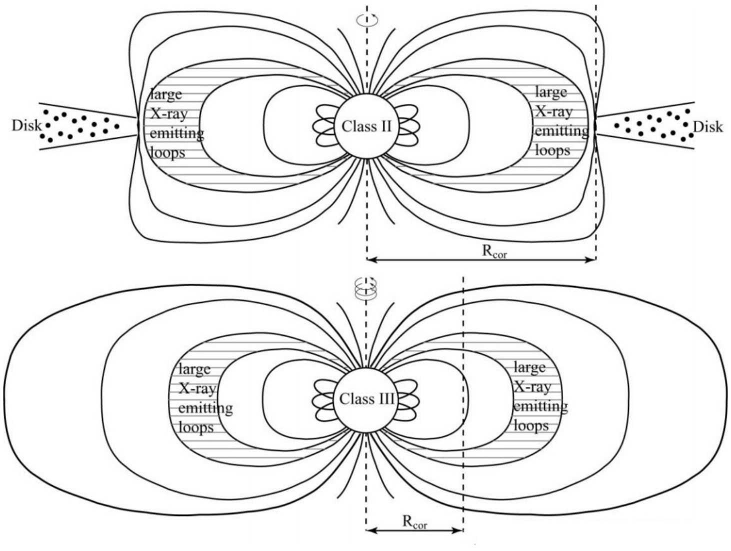

Figure 2.2: Illustration of a class II and III star from Getman et al. [2008]. The main difference is the dissipation of the disk between the two stages and the subsequent expansion of the magnetosphere.

$$\alpha = \frac{d\log(\lambda F_\lambda)}{d\log(\lambda)} \tag{2.1}$$

where F_λ is the flux density and λ is the wavelength. This α value is a measure of the object's flux density dependence on frequency and is typically measured in the near-infrared to far-infrared wavelength range ($2\,\mu$m to $20\,\mu$m) where these objects are detectable [Lada, 1987]. The spectral index value obtained from observations determines the stellar class as follows:

Class I (evolved protostar): $\alpha > 0.3$

Class II (CTT): $-0.3 > \alpha > -1.6$

Class III (WTT): $\alpha < -1.6$

Class 0 YSOs are undetectable at infrared wavelengths but have been observed via their dust continuum emission at sub-millimeter wavelengths [Andre et al., 1993]. Examining the slope of a star's SED informs us about the evolutionary stage. This is illustrated in Figure 2.3. A blackbody spectrum is shown in light blue with the SED

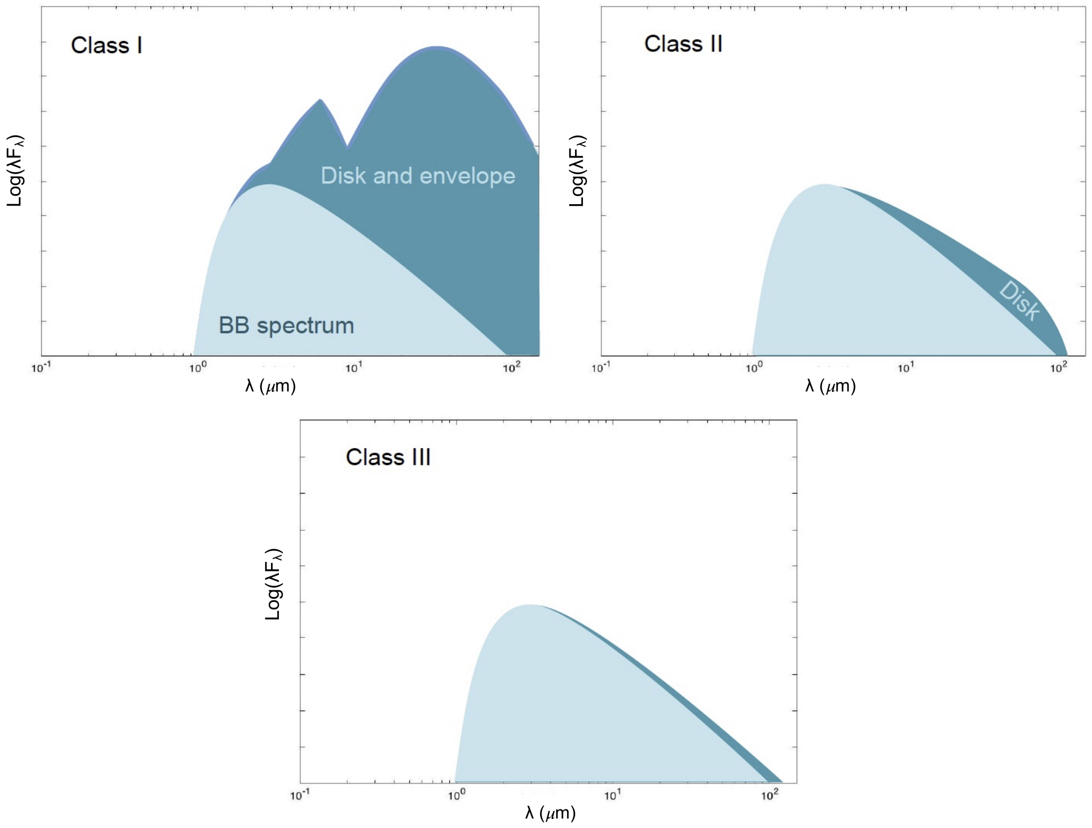

Figure 2.3: Spectral energy distribution of class I, II and III YSO's (dark blue) compared to that of a blackbody (light blue). The more evolved the YSO, the closer its spectrum resembles that of a blackbody.

of the YSO overlaid in dark blue (where $\alpha \geq -2$ for a blackbody). Class I YSOs have distinct features associated with their large envelopes and developing accretion disks. As this envelope dissipates and only the disk remains, the SED becomes more similar to that of a blackbody. The slope of the SED generally indicates whether it is a class II or III object being observed, with a slope more similar to that of a blackbody symbolising a more evolved (i.e. class III) object.

As the protostars lose their envelopes they become visible at other wavelengths and many observations of T-Tauri stars and their circumstellar disks have been performed. In particular, T-Tauri stars are frequently observed at both radio (thermal and non-thermal) and X-ray wavelengths. Their high levels of activity associated with ongoing accretion and evolution make them interesting astronomical objects and are the focus of this research. More discussion of observations of YSOs at different wavelengths is given in Section 2.3. Firstly however, a more in-depth discussion about T-Tauri stars and their properties is given.

2.2 T-Tauri stars

YSOs are generally very active due to their ongoing growth and evolution. The variable emission observed from T-Tauri stars is of particular interest here. Flaring signatures in emission can be directly observed from these objects. More focus is given in this section to specific examples of T-Tauri stars as well as their general features and attributes.

2.2.1 Features

T-Tauri stars were first defined by Joy [1945]. They are characterised by their low mass, $< 2\,M_\odot$, high activity and circumstellar disk. They are similar in size to the Sun, often being referred to as 'young Suns'. A typical radius for a T-Tauri star is $\approx 2\,R_\odot$.

They are notoriously highly magnetically active. This activity leads to the accretion of matter onto the central object from the inner regions of the disk, see Figure 2.4. These disks have radii of approximately 100AU. Non-steady state, violent accretion is thought to occur through funnelling directly onto the stellar surface, creating accretion shocks that are frequently modelled (e.g. Costa et al. [2017]). The reconnection of stellar field lines is also thought to be associated with accretion (e.g. Romanova et al. [2004]), with flaring emission being a common observable feature from these objects. They are also sometimes found in binary systems, with some flaring events being attributed to the interaction and reconnection of the stars' field lines [Tofflemire et al., 2017]. Radio emission (thermal and non-thermal), X-ray and Hα are all observable

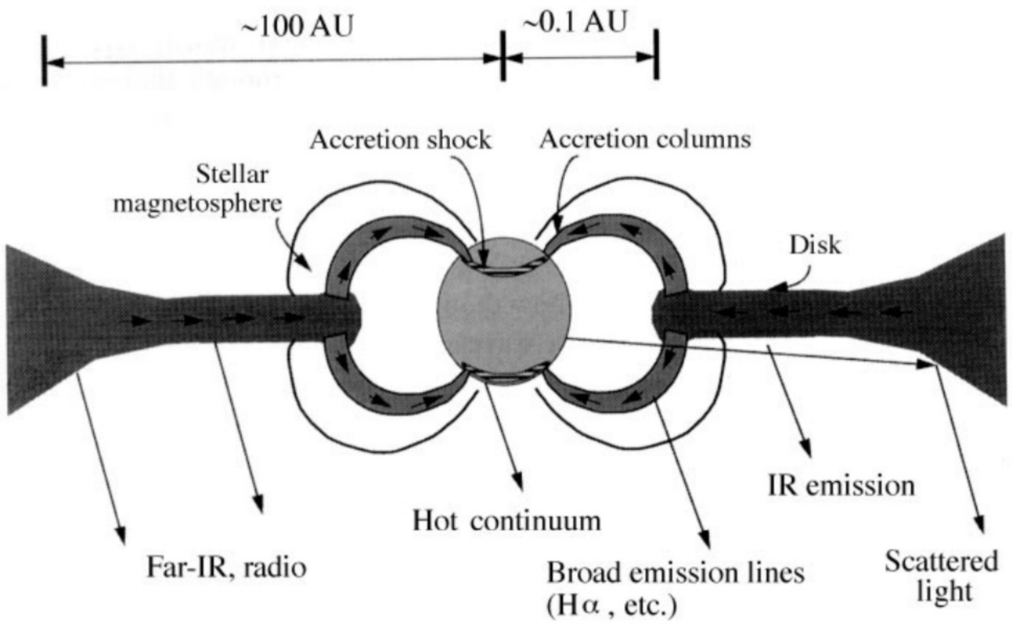

Figure 2.4: Figure from Hartmann [1999] of a classical T-Tauri star. Accretion funnels form between the inner edge of the circumstellar disk and the star, funnelling material onto the star causing accretion shocks that are visible across a range of wavelengths.

from these accreting T-Tauri systems. Winds and outflows are also frequently seen from these objects. They are frequently observed in the Taurus, ρ Ophiuchi, Serpens and Orion star forming regions amongst others.

2.2.2 Magnetic field strength

The properties of the large scale magnetic field geometries on T-Tauri stars can be investigated using the Zeeman-Doppler Imaging (ZDI) technique. The ZDI technique produces magnetic maps of T-Tauri stars from time-resolved spectropolarimetric observations. In the presence of a magnetic field, the spectral lines are split (Zeeman effect) and measurement of the broadening of these lines is used to calculate the magnetic field strength. These observations are taken over the course of several rotations of each T-Tauri star to fully investigate field configurations [Johnstone et al., 2013].

The magnetic maps for a range of classical T-Tauri stars were produced for the Magnetic Protostars and Planets project (MaPP) by Donati et al. [2010]. The surface field strengths reported are rarely more than a few kilo Gauss. The mean field strength of T-Tauri stars calculated by Johns-Krull [2007] from measurements of the broadening of spectral lines in unpolarised light (due to the Zeeman effect) ranged from 1.12 to 2.9 kG. These observed mean field strengths were larger than expected. T-Tauri stars are often approximated to have simple dipolar magnetic field configurations [Gregory et al., 2016].

The surface field strengths has been seen to increase to around 6 kG in locations where accretion is taking place [Gregory et al., 2016]. In general the surface field strengths in these accretion spots are much higher than the mean surface field strength. Other observations report equatorial field strengths in the range $0.6 - 2$ kG (where the equatorial field strength is half the polar field strength for a dipolar field) [Gregory et al., 2010]. While a dipolar configuration is an acceptable approximation for many models of T-Tauri stars, a multipolar field is more physically realistic. AA Tau, whose magnetic field is closest to a dipole [Gregory et al., 2010], has a non-negligible octupole component associated with it. Many other T-Tauri stars have also been reported to have an octupole component. This octupole component is sometimes larger than the dipole component. For example, V2247 Oph has a multipolar field with a dipole and octupole component of 110 G and 230 G respectively. In general however, the dipole component is usually observed to be larger. For example, AA Tau's octupole component is approximately 0.5 kG [Johnstone et al., 2013], and its mean surface field strength has been documented as 1.22 kG by Johnstone et al. [2013] and 2.78 kG by Johns-Krull [2007]. Models of quadrupole field configurations have been investigated, e.g. by Long et al. [2007], however in many T-Tauri stars it is an octupole component that is significant in the field configuration and is generally simpler to model than a quadrupole plus dipole field [Long et al., 2012]. For the models used in this thesis both a purely dipolar and a multipolar (dipole plus octupole) field configurations are used (see Chapter 5). For both models, a dipole surface field strength of between $1-2\,\mathrm{kG}$ is adopted but other values are also explored. When the multipole model is used the additional octupole component is set at $0.5\,\mathrm{kG}$.

2.2.3 Densities

The densities associated with T-Tauri stellar atmospheres can vary greatly. The densities of the accreting or flaring regions can be several orders of magnitude higher than the quiescent or pre-flare coronal densities [Benz and Güdel, 2010]. There is also the distinction between thermal and non-thermal densities. While non-thermal emission is frequently reported from flaring events, it is generally the thermal emission that is calculated from soft X-ray observations. The densities derived from accretion onto the surface range between $10^{11}-10^{13}\,\mathrm{cm}^{-3}$ (Johnstone et al. [2013], Hartmann et al. [2016]). Similarly, densities from flaring regions in general (e.g. from coronal regions) range from $10^{11}-10^{12.5}\,\mathrm{cm}^{-3}$ (Favata et al. [2001], Huenemoerder et al. [2007]). In contrast, the preflare coronal densities lie between $10^{9}-10^{10}\,\mathrm{cm}^{-3}$ (Johnstone et al. [2013], Hartmann et al. [2016], Namekata et al. [2017]). These high densities suggest that radiative losses are important during the cooling stages of young stellar flares and will dominate over conduction led cooling [Bian et al., 2016]. This is discussed more in Chapter 3. The focus of this research is the variable, non-thermal emission produced in these flaring events. As such, the non-thermal electron density of these regions is of particular interest. The models will set a background thermal density, as well as having a flaring thermal and non-thermal density. The non-thermal density will be set as some fraction of the flaring thermal density.

2.2.4 Temperatures

Similar to the density of these regions, the temperature varies greatly between the pre and post flare phases. The temperatures are obtained from the X-ray spectra, as for the densities. Two-temperature fits are commonly used to determine these values. The quiescent background coronal temperature of these stars has been reported between 1 and 50 MK (Güdel et al. [2001], Telleschi et al. [2007]). In contrast, flaring temperature have been reported around 100 MK in extreme flares [Benz and Güdel, 2010]. An average T-Tauri flare has a quiescent coronal plasma temperature around 10^6 K, rising to 10^7 K in general. For example, a flare from the CTT LkHα92 [Favata et al., 2001] had a peak temperature of 43 MK (and density $1.5 \times 10^{11}\,\mathrm{cm}^{-3}$). These properties are determined through observations as well as modelling of magnetospheric accretion and flares. Discussion about the different wavelength observations performed is given next, followed by details of existing models.

2.3 Observations of young stars

Once the envelope around YSOs has been cleared, the T-Tauri star is observable across a wide range of wavelengths. For examining the variable activity on these stars, two common wavelengths used are radio and X-ray. X-ray and radio emission is also used in studying solar flares, as discussed in Chapter 3. Examples of these wavelength observations and notable results are now discussed. Other supplementary information from observations in visible, UV, infrared (IR) is also provided.

2.3.1 Radio

Radio observations of T-Tauri stars date back several decades (e.g. Spencer and Schwartz [1974], Felli et al. [1982]). The physical processes associated with radio emission mechanisms are discussed in more detail in Chapter 4. Some early observations attributed the radio emission to thermal mechanisms (e.g. free-free emission), but future observations began detecting variability from these TTSs [O'Neal et al., 1990]. This variable emission was suggested to be caused by the production of gyrosynchrotron emission [O'Neal et al., 1990]. The further detection of circular polarisation from a weak-lined T-Tauri star by White et al. [1992] confirmed these stars to possess strong and varying magnetic fields. Observations by Carkner et al. [1997] further supported the idea of the radio emission being driven by gyrosynchrotron radiation mechanisms (see Chapter 4).

While X-ray observations of T-Tauri flares are more common, there have been several notable radio flares observed in the 21st century. For example, Furuya et al. [2003] monitored an extreme WTT flare which exhibited flux variations on the timescale of minutes over a 13 day period. While thermal radio emission is still observed from these stars, it is the non-thermal radio emission (that does not depend on temperature and is instead produced from particles gyrating around magnetic field lines) associated with these variable flaring events that is of most importance. The theory behind gyrosynchrotron emission, as well an in-depth look at the differences between thermal and non-thermal radio emission, are discussed in Chapter 4.

Non-thermal emission is observable from both classical and weak-lined T-Tauri stars. Accretion shocks from mass accretion could explain this variable emission. However, this can only be true for the T-Tauri stars which possess strong circumstellar disks. Weak-lined T-Tauri stars, with their sparse or non-existent disks should have less non-thermal emission if accretion was the main cause. It has been suggested that WTT stars are in fact more radio bright, producing more non-thermal emission [Gagné et al., 2004]. A natural explanation therefore is that the bulk of the non-thermal emission comes from flaring activity, similar to that on the Sun, occurring within the magnetosphere's of these active stars. Thermal (free-free) emission is commonly seen from

CTTS's outflows and jets. An overview of flares and their emission signatures is given in Chapter 3.

Several signatures of non-thermal emission exist. These include the detection of: circular polarisation, a non-zero spectral index (Equation 2.1), high brightness temperatures and relatively short timescale variability (minutes to hours). However, care has to be taken when attributing some of these properties alone to non-thermal emission. For example, dust or blackbody emission may be thermal in nature but also have a negative spectral index. Hubble 4, a WTT star in the Taurus star forming region was detected at three different wavelengths (3.6, 6 and 20 cm) by Skinner [1993]. This star was notably seen to have a flat spectral energy distribution but a high circular polarisation detection of 19% and the emission was determined to be non-thermal. One of the first T-Tauri stellar systems to be detected, so called 'T-Tauri', has been observed numerous times. Its binary components have shown significant ($> 20\,\%$) circular polarisation (at 2 cm) and a spectral index of 0.6 has also been detected Johnston et al. [2003]. The high brightness temperatures indicative of non-thermal emission are no higher than 10^{12} K, limited by inverse Compton scattering. Brightness temperatures of thermal emission do not reach above 10^{4} K due to the lower energy of the emitting particles when compared with non-thermal electrons (see Section 4.2). Observations of flaring weak-lined T-Tauri's by Phillips et al. [1991] detected high brightness temperatures between $10^{8} - 10^{9}$ K from non-thermal sources. Brightness temperatures from observations of T-Tauri non-thermal flares by Osten et al. [2004] were also reported to be as high as 10^{10} K. More recently, radio surveys of star forming regions have detected numerous young stars, e.g. Dzib et al. [2013], Ortiz-León et al. [2015] and Pech et al. [2016]. Many of these sources have also shown significant circular polarisation as well as negative spectral indices. The results from these surveys, specifically their flaring non-thermal radio luminosities, are discussed more in Chapter 3.

An important feature of the radio emission from YSOs is how the flux varies in time. This variability supports the notion of non-thermal gyrosynchrotron emission produced in a flaring-like event. Radio light curves exhibiting this variability have been seen in several instances. Light curves at two radio wavelengths from Osten and Wolk [2009] are shown in Figure 2.5. These sources, observed in the LkHα 101 region, were all detected simultaneously at X-ray and radio frequencies using Chandra and the VLA respectively. These simultaneous multi-wavelength observations are rarely performed for young stellar flares. However, as will be discussed in Chapter 3, radio and X-ray emission are important detectable emissions from flares and detecting sources at both wavelengths is therefore incredibly beneficial to understanding the nature of these flares. All four radio light curves in Figure 2.5 are from YSO sources which show variability on some timescale. BW88-1 shows variability on a 2 day timescale at 6 cm. BW88-3 shows 20 year (long term) as well as 2 day variability at both 3.6 and 6 cm. BW88-5 only shows long term variability.

This long term variability is seen in class I stars as well as T-Tauri's. For example, Choi et al. [2008] observed circular polarisation from class I stars as well as variability but on a timescale of years. The light curves are shown in Figure 2.6. The star reaches its peak flux over a period of two months, in contrast to the peak fluxes from Figure 2.5 that were reached over a period of hours to days. Similarly, Forbrich et al. [2006] monitored several class I sources and reported variability in their flux over a period of weeks along with circular polarisation. These light curves are shown in Figure 2.7. The fluxes from all these sources have similar values; in the mJy range. It is the detection of short period variability within this range that helps identify when flaring (i.e. non-thermal) emission is produced.

VLA surveys such as Ortiz-León et al. [2015] measured large degrees of variability in several T-Tauri sources at both 4.5 and 7.5 GHz. The percentage variability was calculated using the highest and lowest fluxes recorded in an epoch, i.e. $(S_{\nu,max} - S_{\nu,min})/S_{\nu,max}$, and was often above 50%. Variability of young stars in the Taurus star forming region

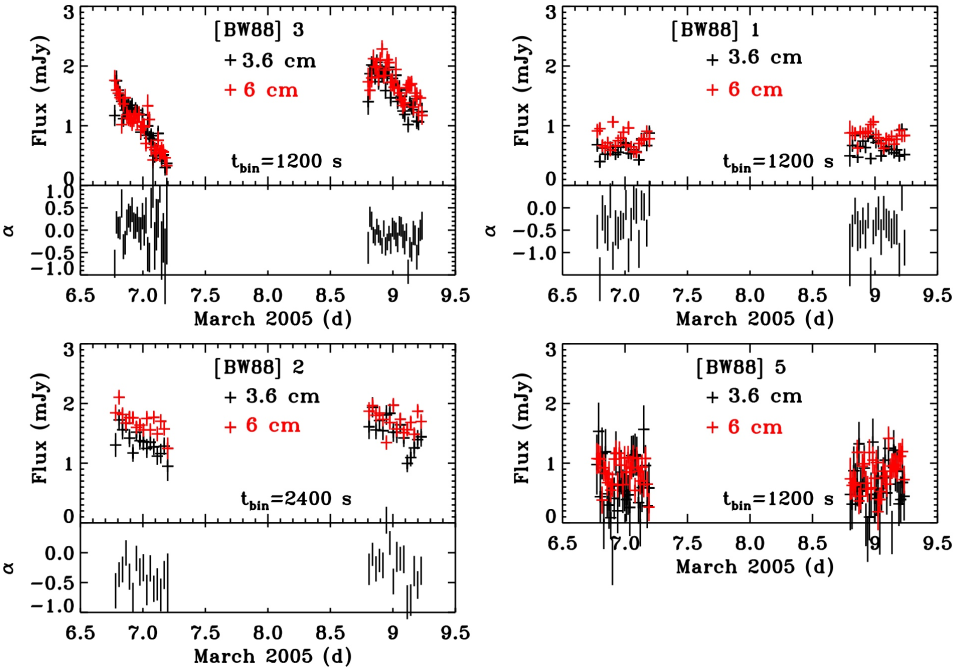

Figure 2.5: Figure from Osten and Wolk [2009] showing the multi-wavelength radio variability of four YSO sources in the Lkhα101 region. For each source, the 3.6 cm (black) and 6 cm (red) flux variability over a period of days is shown in the top panel, with the variation in α (the spectral index from Equation 2.1) shown in the bottom panel where available.

(calculated in this way) is given in Table 2.1 [Dzib et al., 2015]. The confirmed class of the star is given to highlight that high variability exists independent of evolutionary stage. All stars show high levels of variability at both frequencies, indicating the presence of non-thermal radio emission.

2.3.2 X-ray

While X-ray emission from deeply embedded class 0 objects is not observable, X-ray emission from class II and III stars is frequently observed [Feigelson and Montmerle, 1999]. This emission is linked to the flaring activity from these stars, a product of the rapid heating of plasma to around 100 MK within the magnetosphere. The soft and hard X-rays produced in this way are key signatures of flaring and/or accretion

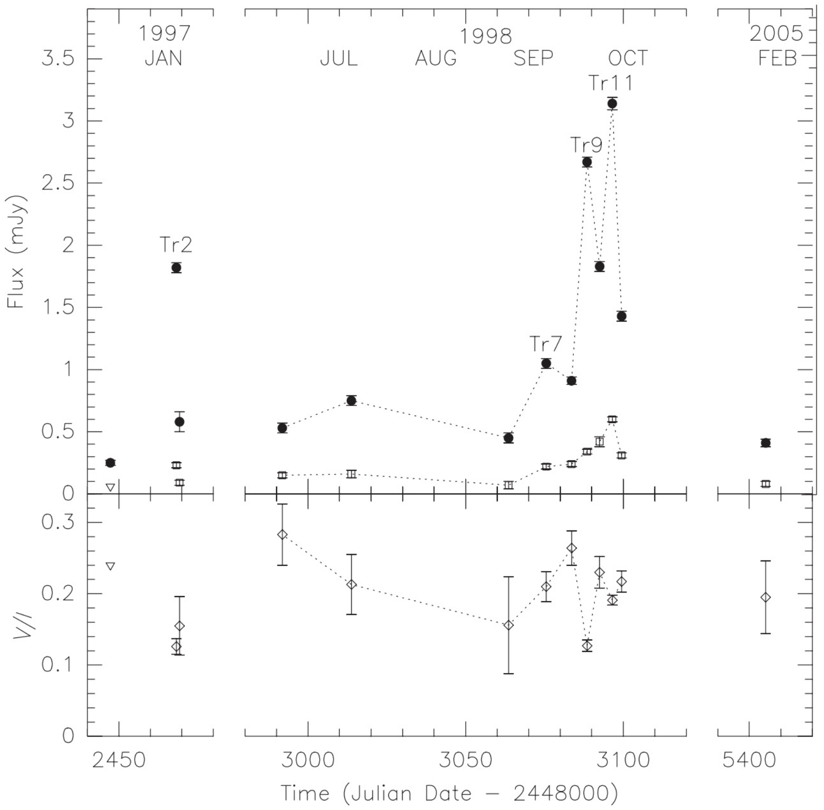

Figure 2.6: 3.5 cm radio light curves from class I sources detected by Choi et al. [2008]. The flux (top panel) is measured in mJy. The degree of circular polarisation is shown in the bottom panel.

occurring.

Observations of T-Tauri stars exhibiting flaring emission include the detection of a 100 MK X-ray flare by Tsuboi et al. [1998]. This WTT flare was observed over the 0.7 – 10 keV energy band over a period of approximately 24 hours. The light curves obtained, including the pre-flare phase, are shown in Figure 2.8. This preflare phase, as well as details about processes occurring in flares and their relevant emissions are given in Chapter 3. Each panel displays the different bands covered in the 0.7 – 10 keV range. The bottom panel, 1.7 – 10 keV, shows the light curve results for the hard band (crosses) with the best fit exponential model overlaid (solid line). Important to note

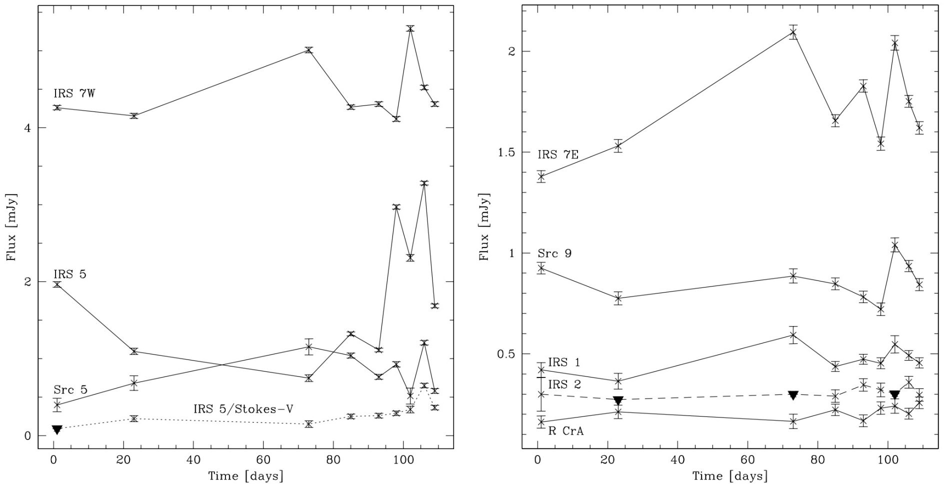

Figure 2.7: Figure from Forbrich et al. [2006] showing the 3.5 cm radio flux (in mJy) of several Class I sources varying over several weeks.

from this observation is once the flare had decayed to a constant count rate this post-flare count rate was still higher than that pre-flare and it is unclear why. Also, the peak luminosity observed (10^{33} erg s^{-1}) is expected to be lower than the true value, as the star went into Earth occultation during the peak of the flare.

Another large X-ray flare was detected from a WTT star by Uzawa et al. [2011]. A lower limit for the peak luminosity here is reported as 3×10^{32} erg s^{-1} in the $2 - 20$ keV band. Both of these powerful flares were observed from weak-lined T-Tauri stars possessing no circumstellar disk. They both showed a rapid increase in emission followed by an exponential decay during the post flare phase. These flaring events, when seen from WTT stars, are therefore often attributed to the reconnection of field lines within the magnetosphere and suffer no diminishing effects in their emission from the lack of a dense disk.

X-ray flares on CTTSs are also observed frequently, for example by Favata et al. [2005], Grosso et al. [2007], and Getman et al. [2008]. However there is ongoing disagreement about the nature of what causes these observed flares. As classical T-Tauri's possess a circumstellar disk from which they accrete, it is frequently suggested that the

Table 2.1: Percentage variability (at 4.5 or 7.5 GHz) of T-Tauri stars in the Taurus star forming region from Dzib et al. [2015]. A source is defined as being highly variable if its variability is greater than 50%. Sources are only included that are confirmed as either class II or III sources by Dzib et al. [2015].

Name	4.5 GHz (%)	7.5 GHz (%)	Class
MHO 2	49.1	>57.3	II
Elias 1	69.5	51.5	II
T Tau N(+S ab)	81.7	66.8	II
FS Tau A-B	>51.6	>52.8	II
XZ Tau	70.1	55.0	II
V807 Tau	22.4	51.0	II
CoKu Tau 3	>63.6	>90.3	II
V1095 Tau	>60.4	49.7	III
V1096 Tau	76.3	75.5	III
Hubble 4	88.3	91.0	III
V819 Tau	>87.7	>81.0	III
V1098 Tau	73.5	80.1	III
V1068 Tau	92.7	90.8	III
CoKu HP Tau G3	>86.4	>84.7	III
V999 Tau	43.8	62.4	III
HD 282630	92.3	89.4	III
V830 Tau	>89.7	>92.5	III
V1110 Tau	>63.4	>76.9	III
FF Tau A+B	>72.4	>64.6	III
HD 283641	>35.5	53.7	III
[HJS91] 4872	43.2	>55.8	III
DI Tau	>79.6	>82.0	III
V1320 Tau	>91.7	>94.9	III
V827 Tau	>95.9	>96.9	III

flaring emission observed is a result of these accretion-led star-disk interactions. Favata et al. [2005] deduced that the channels that connect the star and disk were also the ones funnelling material onto the star during an observed flare. The flares produced in this way are thought to be due to the post accretion shock as the matter infalls onto the star at free-fall velocities (Grosso et al. [2007], Hartmann et al. [2016]). However any interaction between the stellar and disk field lines could lead to reconnection and subsequent heating and X-ray production at this boundary. There have been models that

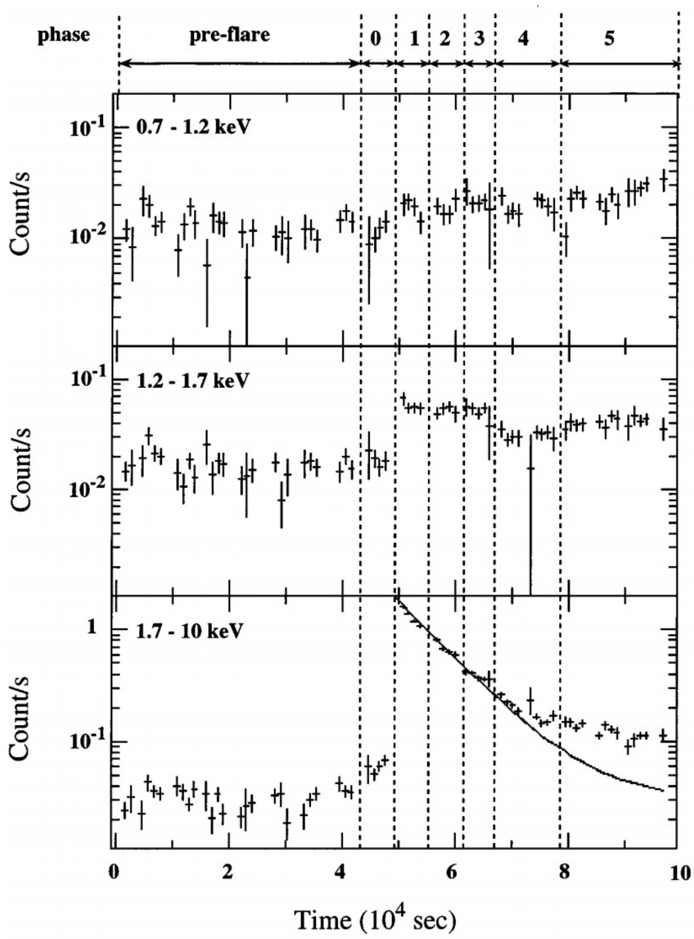

Figure 2.8: X-ray light curves from observations of a 100 MK flare on a WTT star. Figure from Tsuboi et al. [1998]. The crosses dictate the observed count rates and the solid line in the lower panel is the best fit model for these results after the flare has peaked.

simulate these large magnetic loops and these are discussed in Section 2.4. However others argue that there is no evidence for these flares being the result of such large magnetic configurations. Getman et al. [2008] argued that there was no evidence from their observations of the flares occurring in these star-disk loops. The explanation for these flares lies solely in powerful magnetic reconnection events. Getman et al. [2008] also found that classical T-Tauri stars exhibit shorter and hotter flares than their weak-lined counter parts.

2.3.2.1 Determining flare parameters

While the exact nature of X-ray flares remain an open question, there are several determinable factors from these observations which can guide subsequent models. The temperatures, densities and emission measures from a flaring event are all obtainable. While methods such as spectral line ratios are preferable in solar flares (see Chapter 3), spectral fitting is ubiquitously used in X-ray observations of young stellar flares. Instruments such as The European Photon Imaging Camera (EPIC) on-board XMM-Newton and the Advanced CCD Imaging Spectrometer (ACIS) on-board Chandra have been most frequently used for these observations in recent years. For example, EPIC consists of two MOS (metal oxide semi-conductor) CCD arrays and a PN CCD, and operates in the $0.2 - 10\,\text{keV}$ energy band covering soft and hard X-ray emission. Background subtracted X-ray light curves are attained with these instruments. Examples of T-Tauri X-ray observations from XMM-Newton are: Ozawa et al. [2005] and Giardino et al. [2006] . Examples of X-ray observations taken with Chandra are: Imanishi et al. [2001] and Grosso et al. [2004].

Flare parameters are obtained via spectral fitting using XSPEC (or similar). The observed, background-subtracted, X-ray spectra are compared to parameterised model spectra. These models typically consist of an emission (e.g. MEKAL, VAPEC, etc) plus absorption (e.g. WABS) model. The best fit parameters are then obtained, e.g. the temperature. In many cases, the spectra are fit with either a one or two temperature model, allowing for a ‘quiescent’ and ‘flaring’ temperature to be determined in the latter case. An example of some of these two temperature results from Güdel et al. [2007] are shown in Table 2.2. All the lower temperature values (T1) are around the $4 - 10\,\text{MK}$ range, whereas the ‘flaring’ values (the higher temperature component, T2) are all between approximately $20 - 40\,\text{MK}$. The lowest quiescent value from this sample is from FV Tau AB (a binary system) at $3.94\,\text{MK}$. This system’s T2 value is an order of magnitude higher at 39.65 MK. The highest flaring value is from CI Tau in this sample, at 43.71 MK. Its corresponding quiescent temperature is 7.88 MK.

Table 2.2: Results from a 2-temperature fit of X-ray observations of T-Tauri flares. T1 and T2 are the lower and higher temperature components respectively, measured in K. Data from Güdel et al. [2007].

Name	T1 / 10^6 K	T2 / 10^6 K
FM Tau	7.19	29.45
MHO 3	11.01	35.94
BP Tau	4.75	22.26
RY Tau	5.91	37.57
FV Tau AB	3.94	39.65
DH Tau AB	8.58	23.54
DK Tau AB	4.17	18.67
XZ Tau AB	8.70	26.43
FY Tau	9.28	27.94
JH 112	4.06	30.26
GI Tau	4.87	32.58
GK Tau AB	8.81	28.87
IS Tau AB	4.41	17.86
CI Tau	7.88	43.71
IT Tau AB	11.71	37.33
DN Tau	8.81	23.42
GO Tau	6.26	36.29
SU Aur	5.22	23.30

An example of light curves from the flare observed by Grosso et al. [2007] on AA Tau (a CTT) are shown in Figure 2.9. The observations were taken with XMM-Newton (third panel down) and the best fit spectra obtained for the emission measure, temperature and column density are shown respectively in the lower three panels. The plasma emission measure and temperature both peak on day 16, declining and then rising again towards the end of the observation period. The link between the emission measure and temperature during a flare is discussed in Chapter 3.

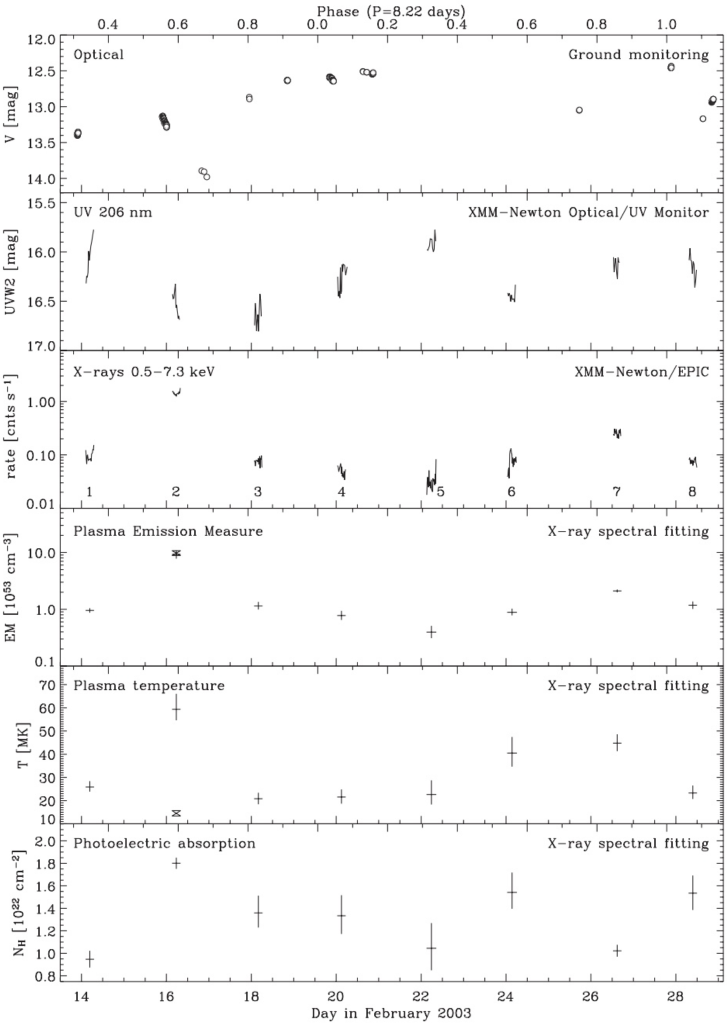

Figure 2.9: Light curves of a flare on AA Tau from Grosso et al. [2007]. The top three panels show the results from optical, UV and X-ray observations respectively. The bottom three panels show the best fit light curves for the emission measure, temperature and column density obtained from spectral fitting.

2.3.3 Other wavelengths

Whilst activity on young stars is typically observed at radio and X-ray wavelengths, observations of these stars at other wavelengths is also relevant. Important information about their disks or confirmations of active accretion can be gained and used to interpret and support the more fruitful X-ray and radio observations of flaring.

2.3.3.1 UV

UV emission from flaring T-Tauri stars has been previously observed, e.g. Grosso et al. [2007]. This emission is usually attributed to the shocks at the base of accretion funnels. The top two panels in Figure 2.9 show the optical and UV light curves respectively for this flare.

2.3.3.2 Infrared

Most of the infrared (IR) emission observed from these stars comes from the dusty circumstellar disks. Variability at infrared (as well as optical Hα) wavelengths have been observed and are useful tools in comparing variable IR light curves to those from X-ray and radio observations. However, variability at these IR wavelengths is suggested to be much slower. Simultaneous, multi-wavelength observations (radio, X-ray, optical and near infrared) have been carried out previously by Forbrich et al. [2007]. These observations enable direct comparison of the different light curves to detect variability across the wavelength bands. However, although there was variability present in the NIR band for many sources, there was no overall multi-wavelength correlation between the observed light curves. Mid-infrared (MIR) observations of young stars have been performed by Kundurthy et al. [2006]. While no specific information about accretion or flares from these stars was discernible (other than confirmation that they were accreting), suggestions were made about other key characteristic of these stars. For example, it was proposed that disk-possessing stars rotated more slowly than their diskless counterparts. Also, for classical T-Tauri stars in particular, the disks are likely to have a flared appearance. IR observations can tell us much about the accretion disks and their relationship with their central star. Observations by Antoniucci et al. [2017] support this, suggesting that NIR observations provide useful information about the region between the star and disk and the processes occurring there.

2.4 Models of T-Tauri stars

There have been numerous models of T-Tauri stars developed over the past few decades. Many of these models focus on the emission generated from accretion onto the stellar surface. Alternatively, some models focus instead on the suggested magnetic loops that connect the star with its disk. Both of these scenarios are frequently modelled in 1D, 2D and 3D using hydrodynamical (HD) or magnetohydrodynamical (MHD) codes. MHD concerns the study of electrically conducting fluids (in this context, an astrophysical plasma) in non-zero magnetic fields. MHD is a broad and diverse area of research and more detail on it can be found in numerous sources, for example: Roberts [1967], Davidson [2002], Galtier [2016].

One-dimensional HD simulations specifically of flaring loops have been performed by Isobe et al. [2003] and Kawamichi and Shibata [2007]. Isobe et al. [2003] modelled a long ($> 10\,\mathrm{R}_\odot$) magnetic loop that connected the central star (with mass and radius of $1\,\mathrm{M}_\odot$ and $4\,\mathrm{R}_\odot$ respectively) to its accretion disk. The results from the simulation were 'observed' to synthesise X-ray spectra based on the instrumental response of ASCA. The spectra were fitted with a two-temperature model, like the observations discussed earlier. They found the larger of the two 'observed' temperatures was significantly lower than the simulated maximum temperature from the HD model. Surface accretion focused 1D HD simulations have been carried out by Sacco et al. [2008], Sacco et al. [2010], Robinson et al. [2017], etc. Sacco et al. [2008] modelled the chromospheric regions heated via accretion shocks on classical T-Tauri stars. The densities and temperatures reported from this work were $10^{11} - 10^{12}\,\mathrm{cm}^{-3}$ and $3\,\mathrm{MK}$ respectively, with a corresponding X-ray luminosity of $7 \times 10^{29}\,\mathrm{erg\,s}^{-1}$. This work was continued by Sacco et al. [2010] where it was suggested that mass accretion rates are typically underestimated in X-ray bands. Their simulations indicated that because of a large amount of absorption in the dense post shock plasma (which is controlled by the magnetic field strength in the shocked region), emission from lower density plasma is preferentially detected leading to this underestimation. Robinson et al. [2017] also looked at this accretion and argued that the short term variability is due to the accretion shocks causing large increases in the accretion rate onto the star. Two-dimensional HD simulations include those performed by de Val-Borro et al. [2011] who looked at mass accretion from a disk onto a binary T-Tauri system.

MHD models of T-Tauri accretion and flares are more often done in 2D and 3D. For example, Orlando et al. [2013] modelled various non-uniform magnetic field strength configurations to see their effect on the shocked plasma. They found the post shock plasma properties to rely heavily on the initial field configuration. Examples of 3D MHD simulations of T-Tauri stars include those by Kulkarni and Romanova [2008] and Long et al. [2012]. Kulkarni and Romanova [2008] modelled Rayleigh-Taylor instabilities at the magnetosphere-disk boundary of a classical T-Tauri star with a dipolar magnetic field. They found these instabilities to occur for a wide range of different field strengths, accretion rates, etc. These instabilities are different to the typical funnels assumed for accretion and are suggested to be more chaotic. An example of the development of these instability led accretion channels (as well as typical accretion funnels) is shown in Figure 2.10. The viscosity parameter, κ, defined in Kulkarni and Romanova [2008] dictates when the instabilities start to appear. Higher κ values indicate the instabilities being the primary method of accretion over typical magnetospheric funneling (e.g. the first plot for $\kappa = 0.02$).

The top row of panels shows how initially, accretion is limited to polar reaching funnel flows. As κ increases, there is also accretion towards the equatorial plane due to the instabilities. The bottom row shows the most unstable of accretion scenarios with the most accretion resulting from Rayleigh-Taylor driven instabilities. Long et al. [2012] similarly modelled this accretion, however this time they focused on the effect

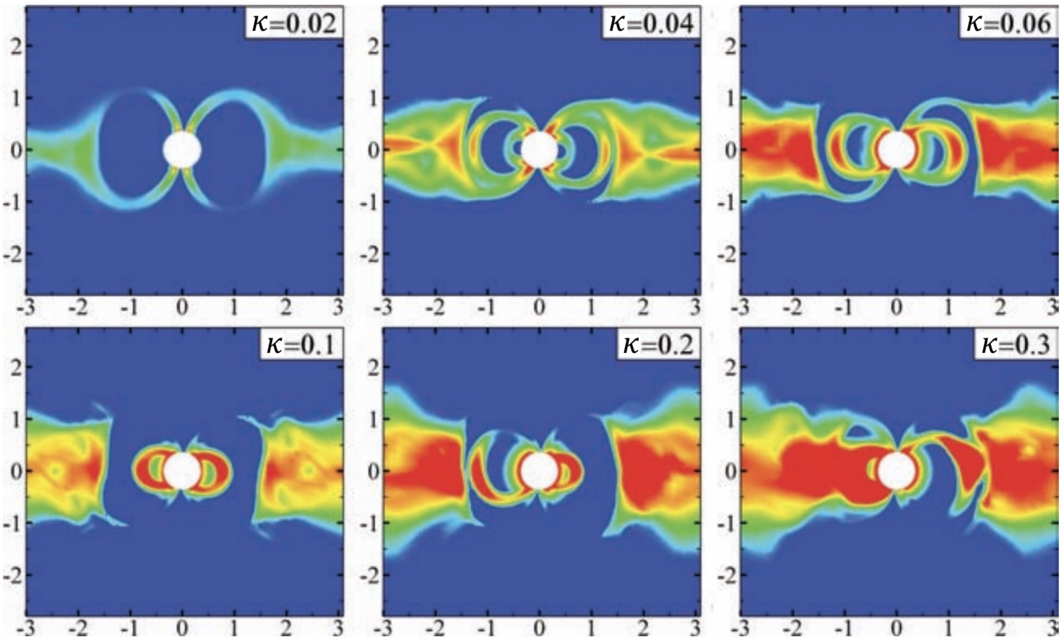

Figure 2.10: 3D MHD simulations of an accreting T-Tauri star. An increasing κ value dictates how dominant the instability led accretion becomes. As this value increases, accretion via magnetospheric funnelling becomes less prevalent and the system becomes more unstable. Figure from Kulkarni and Romanova [2008].

the magnetic field configuration had on the accretion. As previously discussed, T-Tauri stars are likely hosts to multipolar magnetic fields. Long et al. [2012] explored this aspect, varying the dipole and octupole components of the field. They showed that when the dipole component is stronger, matter is accreted towards the stellar poles (like in the first image of Figure 2.10 where a dipole field has been used). For a purely dipolar magnetic field, matter accretes around 20° from the pole. The work by Long et al. [2012], as well as by Alencar et al. [2012], showed that at distances close to the surface the octupole component (in a dipole plus octupole field) dominates and redirects some of the accreting funnel flows to higher latitudes above 20°, as well as nearer the equator tracing the octupolar field lines.

While flaring and accretion are key characteristics of these young stars, other models investigate properties such as T-Tauri winds or their magnetic field. For example, Vidotto et al. [2010] used a 3D time-dependent MHD model to study the effects on the stellar wind of a misaligned rotation axis and magnetic dipole moment vector. Additionally, the effects of this magnetised T-Tauri stellar wind interacting with an orbiting magnetised exoplanet was explored. Unlike the models previously discussed, this work also estimates the radio emission produced from a reconnection event between the two. There remain no models of T-Tauri stars that calculate the radio and X-ray emission generated from flaring events. There are models that predict this emission from flares on the Sun, (discussed in Chapter 4), and these form the basis of this research. Simulators that predict the radio (gyrosynchrotron) emission from solar flares (described in Chapter 4) will be adapted to explore the radio (and X-ray) emission generated from flares on T-Tauri stars. First however, a more in depth examination on what flares are and the physics behind them is presented. This includes discussion on solar flares and how they compare with young stellar flares.

Chapter 3

Solar and T-Tauri flares

Flares are characterised by their increases in emission over a range of wavelengths, thought to be initiated from the sudden release of magnetic energy from magnetic reconnection events. Magnetic reconnection is still a heavily researched area of solar and plasma physics and this section explores the basic theory behind magnetic reconnection as well as the observable phenomena it invokes in a flaring event. The types of emission commonly seen from these flares is discussed as well as some scaling relations that have been developed from observations of solar flares. Solar flares have long been compared to flares on other stars, so the key parameters and timescales from this type of flare are explored and discussed in relation to young stellar flares. A fuller overview of solar flares can be found in the following: Aschwanden [2002], Aschwanden [2006], Benz [2008], Shibata and Magara [2011], etc, with stellar flares also discussed by: Güdel [2002], Benz and Güdel [2010], Huang et al. [2018] etc, where the brief summary given here is based on these works.

There are several types of solar flare which are frequently observed and have common features between them. For example there are long duration event flares (LDE), impulsive flares (also known as compact or confined flares) and also smaller micro and nano flares. Typical characteristic parameters of these types of solar flares are given in

Table 3.1Shibata and Magara [2011].

Table 3.1: Comparison of different properties of three different types of solar flares. Table adapted from Shibata and Magara [2011] where n_e and v_A are the electron density and Alfvén velocity respectively.

	size / 10^4 km	timescale / s	Energy / erg	Field / G	n_e / cm^{-3}	v_A km/s
microflare	0.5 – 4	60 – 600	10^{26} – 10^{29}	100	10^{10}	3000
impulsive	1 – 10	60 – 3×10^3	10^{29} – 10^{32}	100	10^{10}	3000
LDE	10 – 40	10^3 – 10^5	10^{30} – 10^{32}	30	10^9	2000

LDE flares are long lasting and evolve more slowly than impulsive flares, exhibiting features such as plasmoids and helmet streamers. A general model of a solar flare has key phases common to all these flares: a pre-flare phase, a short impulsive phase and a longer lasting gradual phase. The pre-flare phase is not always observed but is characterised by flux emergence from the surface, the build up of magnetic energy and a small degree of coronal heating. The magnetic field structure that emerges carries this magnetic energy, dissipating some of it as the structure expands from a cross-field current generated Lorentz force. In a low resistivity plasma, as two oppositely directed field lines come close to one another, a current sheet forms between them. This current sheet becomes progressively thinner until the magnetic field lines reconnect and the magnetic energy is dissipated [Shibata and Magara, 2011], initiating the impulsive phase. There is sometimes weak soft X-ray emission observed during this pre-flare phase from the heating of plasma [Fletcher et al., 2011].

3.1 Magnetic reconnection

The reconnection of locally oppositely directed field lines leads to the explosive release of magnetic energy from a thinning current sheet, that is converted into kinetic and thermal energy. The dissipation of energy also induces a topological effect, relaxing the field to a lower energy state. After reconnection occurs the flaring loop relaxes to this lower energy state, shrinking in height by a factor of approximately 1.5 [Aschwanden, 2002]. Reconnection is a widely occurring process and can also occur in the Earth's magnetosphere: Souza et al. [2017], in plasma laboratory experiments: Gekelman et al. [1982], Furno et al. [2003], in tokamaks: McClements [2019], etc. A more in-depth overview of magnetic reconnection can be found in the following: Priest and Forbes [2000], Zweibel and Yamada [2009], etc.

Giovanelli [1946] first suggested that particle acceleration and energy release from flares occurred from a neutral X-point triggered by magnetic reconnection. The main problem with this, and subsequent early models, is the time for the current stored to dissipate during a flare. The timescale for diffusion of the magnetic field in the corona is approximately [Priest, 2014]:

$$t_{\mathrm{diff}} \approx \frac{L^2}{\eta} \tag{3.1}$$

where L is the magnetic length scale and η is the magnetic diffusivity:

$$\eta \approx 10^4 {\frac{T}{10^6\,\mathrm{K}}}^{-3/2} \mathrm{cm}^2\,\mathrm{s}^{-1} \tag{3.2}$$

This diffusive timescale is much larger than the timescales reported from solar flares ($10^2 - 10^4$s). One of the most well known models for reconnection, the Sweet-Parker model (Sweet [1958], Parker [1957]), is a simple analytical model of steady reconnection, which incorporates a region of ideal plasma inflow as well as a localised dissipation region with length scale much shorter than the global scale L. A basic diagram showing this type of reconnection is shown in Figure 3.1.

The oppositely directed field lines with field strength B_i move towards each other with inflow velocity, v_i. The current sheet that forms between them has length L and

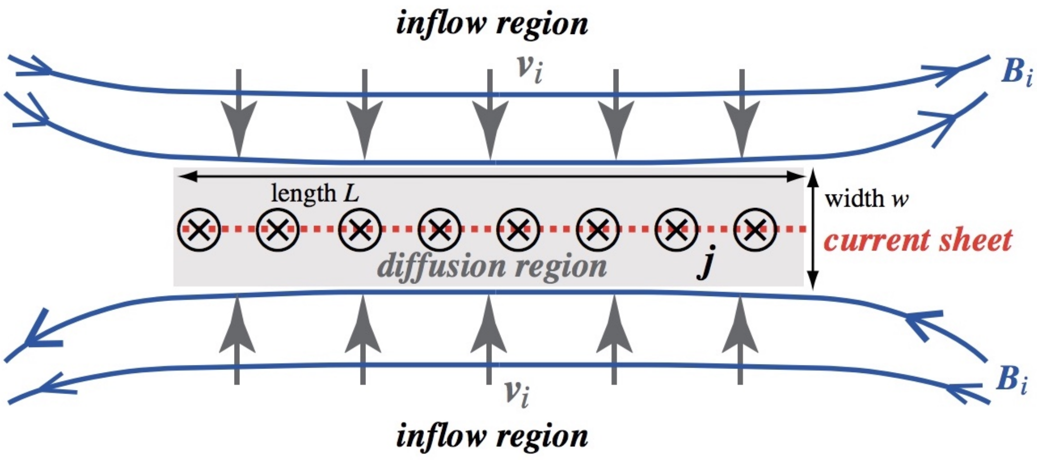

Figure 3.1: Standard model of Sweet-Parker reconnection. A current sheet of thickness, w, and current density, j, forms between two oppositely directed field lines with inflow velocity v_i. Figure from Shibata and Magara [2011].

width w with a component of the electric field perpendicular to the velocity and magnetic field strength. There is an additional outflow velocity, v_o, which is proportional to the Alfvén velocity ($v_A = B/\sqrt{\mu_0 \rho}$) and acts along the field lines. The reconnection rate, R, is calculated as the ratio of this inflow and outflow velocity and is given in terms of the Lundquist number S:

$$R = \frac{v_i}{v_o} \approx \sqrt{\frac{\eta}{L v_A}} \approx \frac{1}{S^{1/2}} \tag{3.3}$$

Based on solar flares values, this gives reconnection timescales of approximately $10^8 - 10^9$s. This is again too slow for reported solar flare reconnection timescales. As such, this model is commonly referred to as the ‘slow reconnection’ model. To further this model, Petschek [1964] suggested that reconnection takes place within a much smaller current sheet, allowing for a faster inflow speed. This is accomplished by incorporating standing slow shocks linked to the current sheet, in which the magnetic field lines change direction. The schematic differences between the Sweet-Parker and Petsheck model are shown in Figure 3.2. Petschek’s work spawned the ‘fast reconnection’ model in which the reconnection rate is:

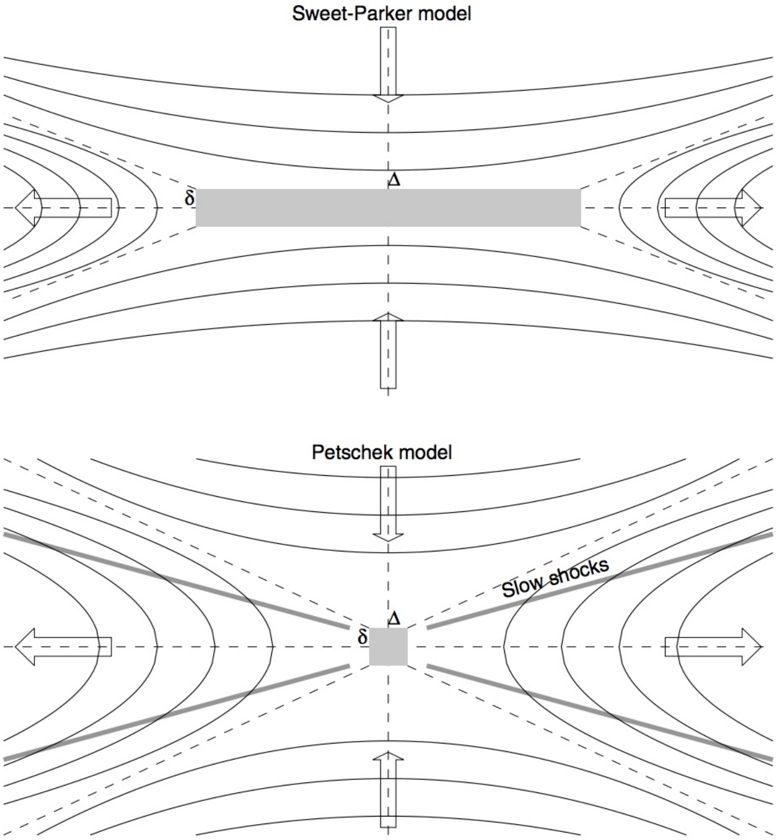

Figure 3.2: Illustration of reconnection in the Sweet-Parker model (top) and Petschek model (bottom). The primary difference is the shorter length scale through which the reconnection of field lines occurs in the latter model. Figure from Aschwanden [2006].

$$R \approx \frac{1}{\ln S} \tag{3.4}$$

This model gives reconnection rates much faster than the Sweet-Parker model that are comparable with solar flares, however the compact geometry of the 'X-point' reconnection leads to its own problems with Petschek reconnection not being replicated in numerical MHD simulations with uniform resistivity (Biskamp [1986], Zweibel and Yamada [2016]).

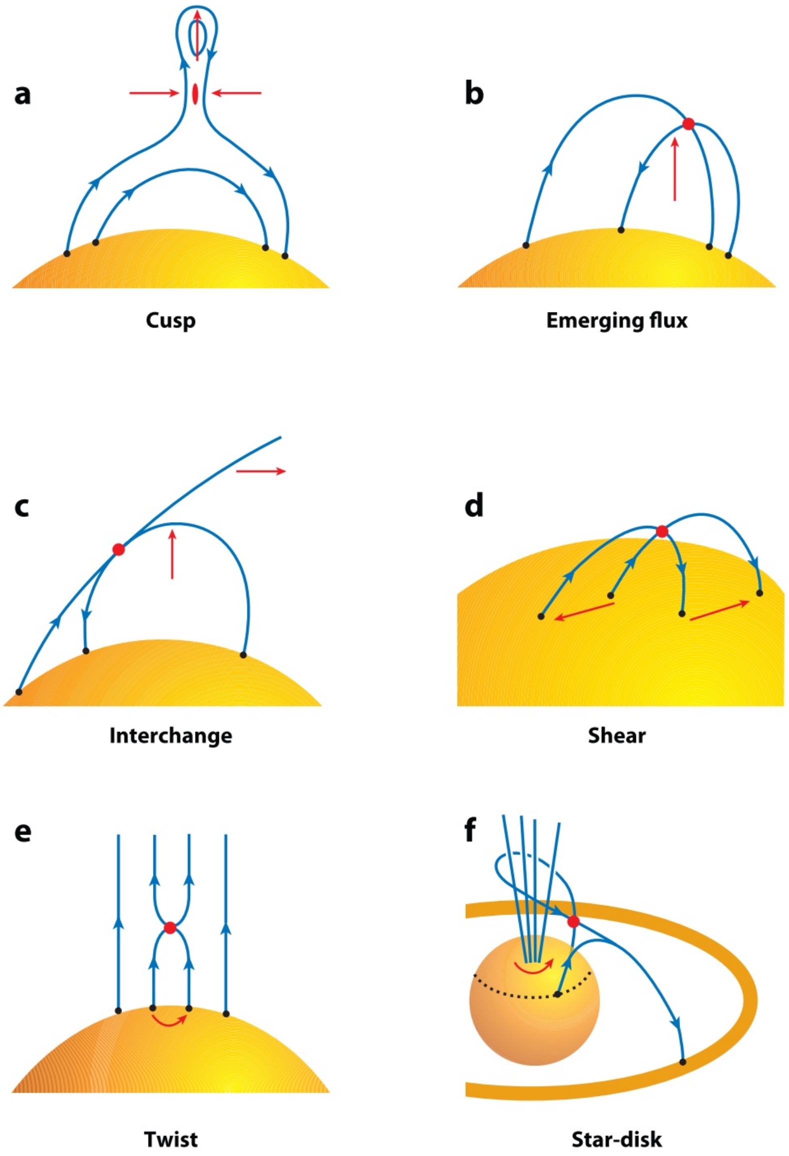

Figure 3.3: Figure from Benz and Güdel [2010] displaying six different large scale magnetic configurations that lead to reconnection. The reconnection sites are shown as red dots and the driving action for reconnection is shown as red arrows. The direction of the field lines are shown as the blue arrows.

Despite a full standard model for the reconnection in solar flares still being required, it is generally agreed that in these flares the most likely scenario for the release of magnetic energy is the dissipation of an enhanced electric current (in a current sheet) when field lines reconnect. The reconnection of these field lines can occur in several proposed scenarios, as is shown in Figure 3.3. Figure 3.3a is a common configuration observed from large flares where one field line is pinched in the middle (e.g. by a wind) forming a cusp and reconnecting. The upper part above the cusp may be ejected as a plasmoid. Figure 3.3b illustrates the interaction of two different field lines, with one emerging and reconnection with the other. This configuration leads to four footpoints as opposed to the typical two. Emission signatures from multiple footpoints has been observed by Aschwanden et al. [1999]. Interchange reconnection shown in Figure 3.3c occurs between closed and open field lines and is more common in regions outside the lower corona. Figure 3.3d displays reconnection from field lines originating from footpoints that do not move in unison that leads to a shearing effect. The footpoints may also rotate around each other, causing the twisting of field lines and the twist reconnection seen in Figure 3.3e.

The circumstellar disks surrounding T-Tauri stars often lead to reconnection led star-disk interactions (Figure 3.3f) which is the focus of this research. The reconnection can be between the star and disk field lines, or from a stellar field line that is connected to the disk becoming sheared and reconnecting if the star is rotating faster, like in Figure 3.3d. In young stars, the idea of binary magnetospheres interacting at periastron has also been suggested as a source for reconnection [Tofflemire et al., 2017].

3.2 Solar flares

The subsequent events that are triggered from the energy release in reconnection are shown in Figure 3.4. The energy release first manifests itself in the heating of plasma, acceleration of particles and mass ejection (in the form of plasmoids) in what is known as the impulsive phase of the flare. This subsequently leads to further plasma heating and chromospheric evaporation during the gradual phase. There are competing theories as to what exactly causes the acceleration of energetic particles during reconnection. Possible acceleration mechanisms include: direct electric field acceleration (e.g. in current sheets), turbulent or stochastic acceleration, acceleration from shocks (e.g. standing or propagating MHD shocks) and betatron acceleration in collapsing magnetic traps [Huang et al., 2018]. These theories and their arguments are not discussed in detail here, as the nature of the emission produced during acceleration is of interest not the acceleration process itself.

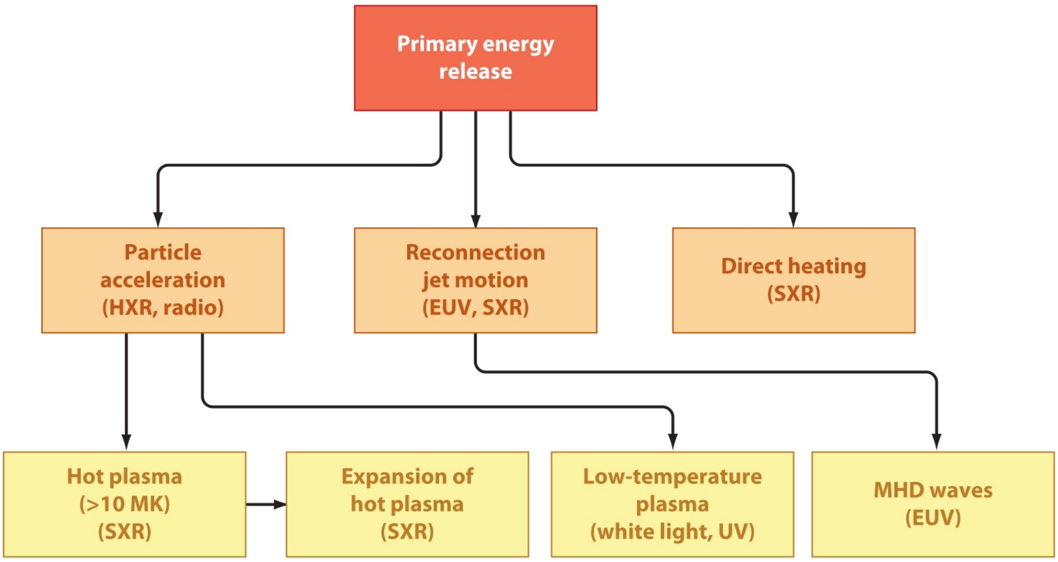

Figure 3.4: Flow of events following the conversion of magnetic energy to thermal and kinetic from a reconnection event. Reconnection jet motion and MHD waves will not be discussed in detail in this research. Figure from Benz and Güdel [2010].

3.2.1 The impulsive phase and non-thermal particles

The impulsive phase is characterised by its radiation signatures. These include non-thermal radio, hard and soft X-ray (HXR and SXR), UV and optical continuum emission (e.g. Benz [2017], Karlickỳ et al. [2019], Wu et al. [2019]). These emissions are indicative of the resulting processes following reconnection (acceleration, heating, etc). The pairing of these processes to the emission produced is seen in Figure 3.4. The impulsive phase typically lasts from seconds to minutes [Fletcher et al., 2011]. Profiles of these emissions are shown in Figure 3.5. This figure describes the emission profiles from solar flares, but similar signatures in X-ray and radio emission have been seen from young stars (see Chapter 2).

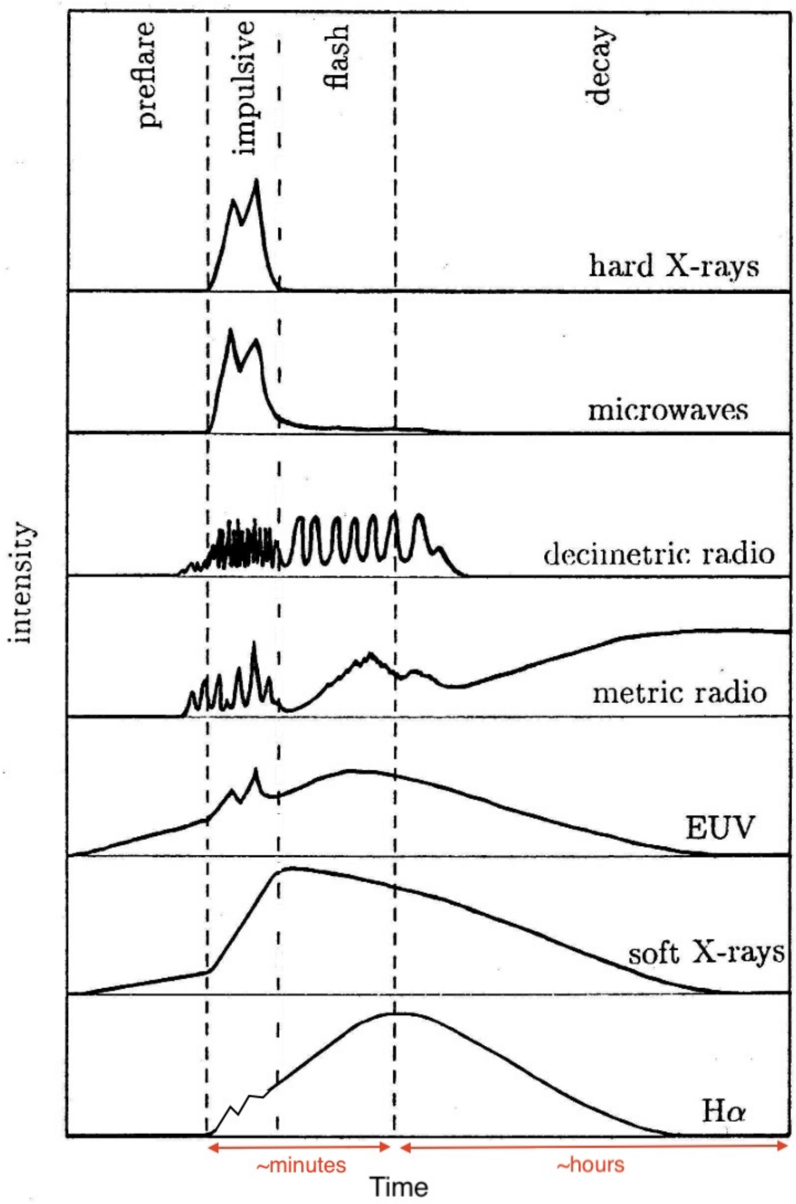

Figure 3.5: Typical emission profiles during the pre-phase, impulsive and decay (gradual) phase of a solar flare. Figure from Benz [2008].

The impulsive phase produces the highest plasma temperatures (and highest energy particles) as well as the most non-thermal radio particles [Benz and Güdel, 2010]. These plasma temperatures are a result of the direct heating of the plasma from the thermal energy produced during reconnection. This thermal energy is seen as both SXR and EUV emission although HXR emission near the coronal loop top has also been observed [Benz and Güdel, 2010]. The high temperatures seen in flares can also be explained by the low plasma beta, β_P, value (the ratio of a plasma's thermal pressure to magnetic pressure) in the coronal regions where reconnection is likely to take place. Optical emission is seen as Hα continuum and peaks towards the end of the impulsive phase in what is sometimes referred to as the 'flash phase'. This occurs before the decay phase [Benz, 2008]. The two main emissions seen during the impulsive phase of a flare however are non-thermal radio and HXR emission. These are both products of particle acceleration. It is thought that both ions and electrons are accelerated after reconnection [Fletcher et al., 2011]. This radio and (soft and hard) X-ray emission are the primary observable emissions from flares both on the Sun and other stars. HXR emission is primarily observed at the footpoints and peaks during the impulsive phase. The particles accelerated in the flare reach energies up to tens of MeV and precipitate onto the chromosphere, causing the high energy emission to be produced as X-ray bremsstrahlung emission (discussed in Chapter 4) [Benz, 2017]. While it is clear from Figure 3.5 that the HXR peaks in the impulsive phase, it is also observed in the gradual phase. However the HXR impulsive emission has a much harder spectrum. This spectrum can be approximated by a power law. This is seen in Figure 3.6 where the observed photon spectrum from an X-ray flare (pink) is best fit with a power-law (as well as thermal) component as there are high energy particles present. There is also sometimes strong white light emission from these footpoints [Fletcher et al., 2011].

Non-thermal radio emission is seen in the form of incoherent microwave emission from mildly relativistic electrons or coherent radiation in the form of decimetric and

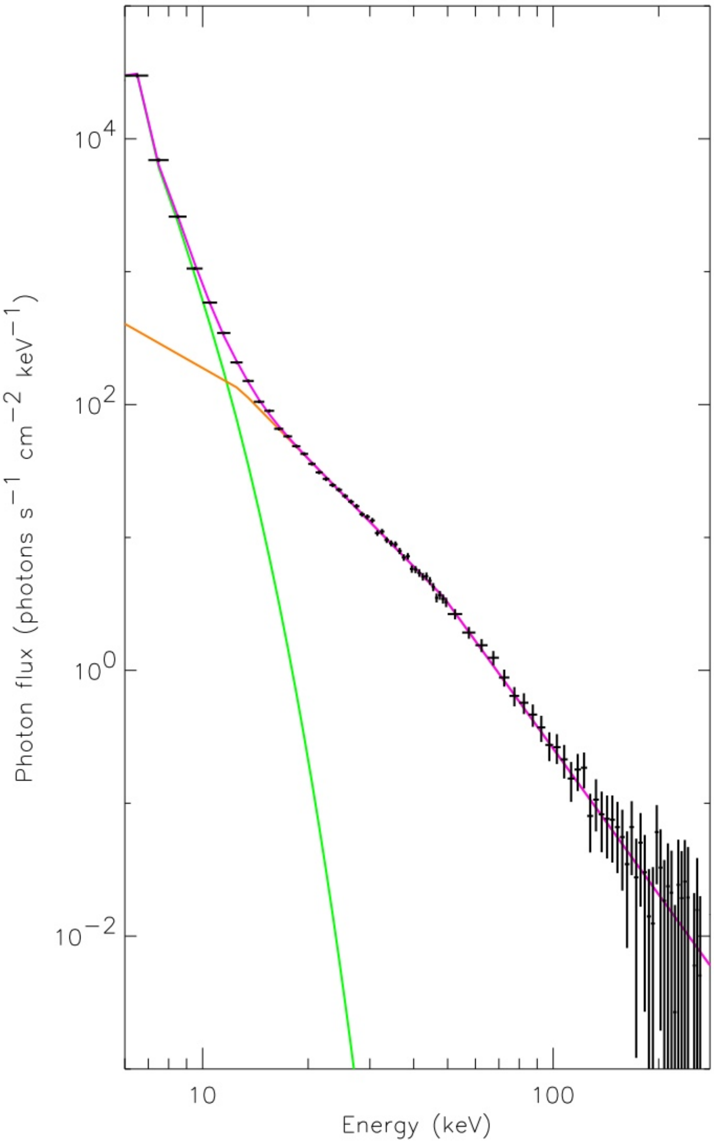

Figure 3.6: Observed X-ray spectrum from a solar flare (black) overlaid with a fitted spectrum (pink). The lower energy, soft X-ray emission is fitted with a thermal component (green) with the HXR spectrum fitted with a power law (orange). Figure from Benz [2008].

metric radio emission from plasma waves [Fletcher et al., 2011]. The incoherent accelerated particles gyrate along the reconnected field lines, emitting gyrosynchrotron radiation before either precipitating onto the surface or being trapped on the field lines. Gyrosynchrotron radiation is discussed in more detail in Chapter 4. The kinematic timescales associated with the accelerated particles that produce HXR and non-thermal radio emission during the impulsive phase are now discussed.

3.2.1.1 Particle acceleration timescales

As discussed in Section 3.1, one of the byproducts of the reconnection of magnetic field lines is the acceleration of non-thermal particles. There are various relevant timescales associated with these electrons once they are injected at the reconnection site. The accelerated electrons have a pitch angle, ψ, which determines their behaviour on the field line. If ψ is less than the critical loss cone angle, ψ_0, the particle is lost. The particle is either lost to space, or lost via impinging on the stellar surface, losing its energy and contributing to the heating of plasma there. These particles are known as free streaming particles with an associated propagation time, t_{prop}, associated with a length l (in the non-relativistic limit):

$$t_{prop} = \frac{l}{v} \approx E^{-1/2} \tag{3.5}$$

This length is the distance travelled once by an electron gyrating along the magnetic field from the reconnection site towards the surface. E is the electron energy and v is the particle velocity. The dependence on energy suggests that particles with higher energies reach the surface first, so the HXR footpoints observed should peak first at higher energies.

In most flaring configurations, there are many particles that fall in the $\psi > \psi_0$ range and so cannot be lost from the system. These particles remain trapped on the field lines. These particles are subject to the frequently used ‘trap plus precipitation’ model [Aschwanden, 1998]. This model describes how the electrons remain magnetically trapped in the corona, eventually either diffusing or being scattered into the loss cone before precipitating onto the surface. As such, there are several time scales associated with this model. Figure 3.7 illustrates the two different behaviours the particles can take in relation to the loss cone.

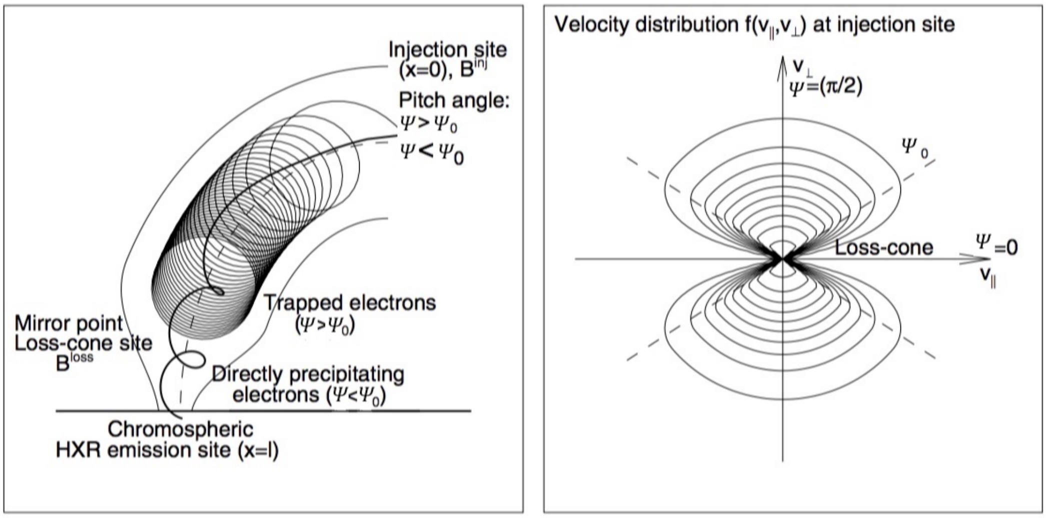

Figure 3.7: Diagram illustrating the particle motion after injection from the reconnection site (left). The particles either free stream directly onto the chromosphere (or are lost to space) or remain trapped on the field line for a time, depending on the particle's pitch angle, ψ. The velocity distribution of a trapped particle and the subsequent loss cone that forms is also illustrated (right). Figure from Aschwanden [1998].

The loss cone angle is defined as:

$$\sin^2\psi_0 > \frac{B_0}{B_m} \tag{3.6}$$

where B_0 is the minimum magnetic field strength at the loop top and B_m is the magnetic field strength at the mirror point. As the particle gyrates along the field line it experiences the mirror force, associated with the changing magnetic field strength [Chen et al., 1984]. This force eventually causes the particle velocity to become zero and its motion to reverse (at the so called mirror point) as it moves into a region of higher field strength along the converging lines. The location of this mirror point depends on the pitch angle of the electron. A smaller pitch angle means a more field aligned electron that will mirror at higher field strength locations. The electrons trapped on the field lines have a bounce period that is defined as the period to bounce back and forth between these mirror points once:

$$t_B = \frac{2\pi L}{v\sqrt{1-\sin^2\psi_0}} \tag{3.7}$$

where L is the loop half length. The particles remain trapped on the field line until they are collisionally scattered into the loss cone and precipitate, in less time than a bounce period, onto the chromosphere. This trapping time is therefore limited to the collisional or deflection time [Aschwanden, 1998]:

$$t_{\text{defl}} = 0.95\times 10^8 \left(\frac{E^{3/2}}{n_e}\right)\left(\frac{20}{\ln\Lambda}\right) \tag{3.8}$$

where lnΛ is the Coulomb logarithm:

$$\ln\Lambda = \ln[8.0\times 10^6(T_e n_e^{-1/2})], T_e > 4.2\times 10^5 K \tag{3.9}$$

This timescale, as opposed to Equation 3.5, has an energy dependence that leads to higher energy electrons being trapped for longer. Therefore the trapped spectrum appears harder than the injected spectrum, with a difference in power law reported as reducing by a factor of 1.5 [Aschwanden, 2006]. This also suggests that trapping timescales for non-thermal radio electrons are higher than for lower energy X-ray electrons. This is seen in observations and is illustrated in Figure 3.8. These collisional deflection times are an upper limit to the trapping time and is known as the weak diffusion limit. A lower limit to these trapping times, in the strong diffusion limit, is controlled by the particle diffusion into the loss cone every bounce period [Kennel, 1969]:

$$t_{trap} > \frac{2t_b}{\psi_0^2} \tag{3.10}$$

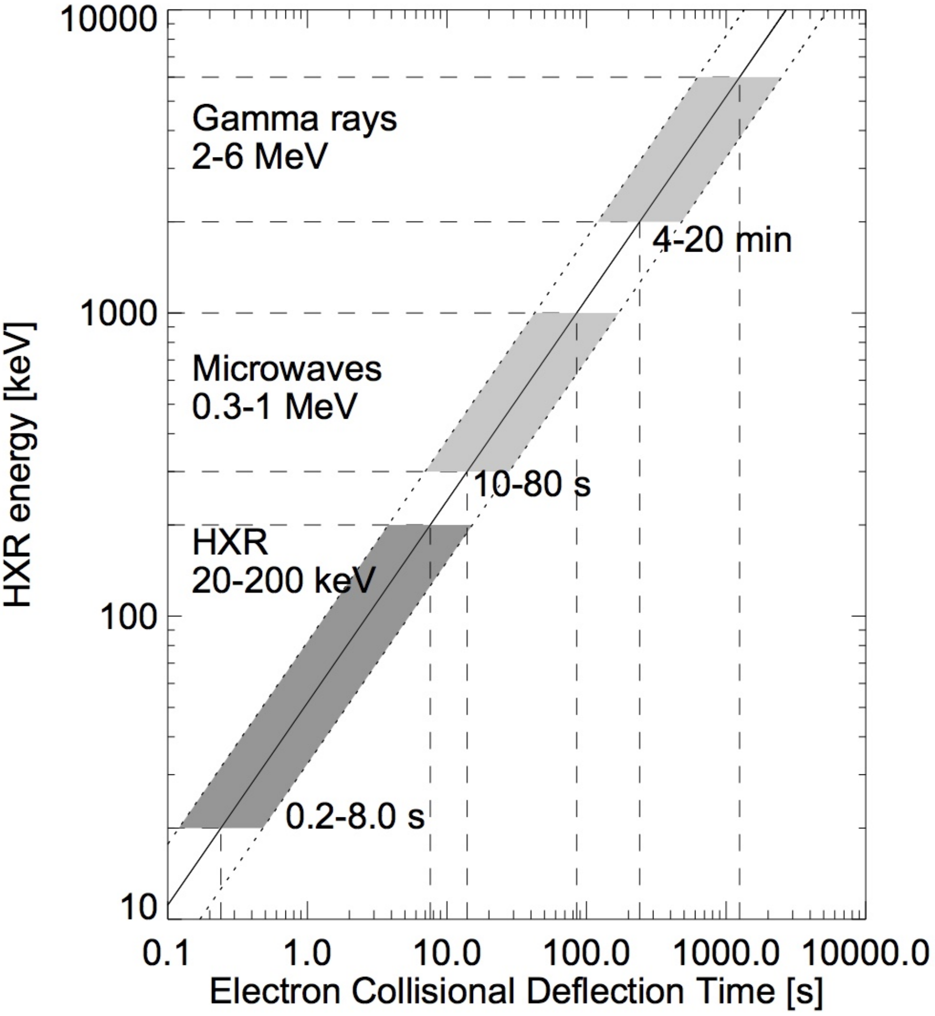

Figure 3.8: Trapping time as a function of electron energy. The shaded areas correspond to densities of n $\approx 10^{11}\,\mathrm{cm}^{-3}$. Particles with microwave energies lead to longer trapping times than corresponding hard X-ray electrons. Figure from Aschwanden et al. [1997].

Once the particles have impinged on the stellar surface the footpoints are observable through HXR emission. The non-thermal radio particles remain trapped for longer, continually producing the gyrosynchrotron emission seen, before precipitating down. The loss of these high energy particles to the chromosphere induce the next stage of a flare: the gradual phase.

3.2.2 Gradual phase

The gradual phase is typically much longer than the impulsive phase. The particles that have been deposited on the surface cause large amounts of heating by collisional energy loss or thermal conduction. This rapid heating causes the upwelling of plasma in a process known as chromospheric evaporation. The heated plasma fills the magnetic loop, producing large amounts of SXR emission (see Figure 3.4). Depending on whether this heating continues, these flare loops may also expand. The expansion of this plasma was first identified by Doschek et al. [1980] and Feldman et al. [1980]. This SXR emission has already been produced earlier in the flare (and continues to be seen above the relaxed loop at the reconnection site) but peaks strongly during the gradual phase (in the plasma filled loop). These loops are also observed at EUV wavelengths. Energy is more slowly released during the gradual phase which is reflected in the emission profile's seen in Figure 3.5. The rise and decline in emission is much gentler, as the heating is done more slowly in this phase as opposed to the sudden reconnection led heating in the impulsive phase. The decline in emission is indicative of cooling in the corona, a key process in the gradual phase. The gradual phase typically occurs on timescales of minutes to hours in solar flares [Benz, 2017]. The cooling of plasma in the magnetic loops is driven by both conduction and radiation [Fletcher et al., 2011]. Radiative losses will dominate when either the temperature is reduced (so the efficiency of conduction led cooling is reduced) or the density is high. Due to the high plasma densities reported in young stellar flares (up to $10^{13}\,\mathrm{cm}^{-3}$, see Section 2.2.3), radiative cooling is therefore expected to dominate over conduction cooling for these flares.

It is reasonable to question the delay between the emission signatures of the impulsive and gradual phase and if they are actually dependent on each other. Neupert [1968] first suggested that the rise phase of the SXR emission during the gradual phase corresponds to the time integral of the impulsive microwave radiation. Neupert [1968] also suggested that the increased thermal SXR emission relative to non-thermal microwave emission is a result of the chromospheric heating that occurs from precipitating accelerated particles. In other words, as the non-thermal input increases, the thermal output subsequently increases. This is now widely accepted to be true in flares and is known as the Neupert effect. The Neupert effect successfully explains the delay in SXR emission relative to microwave (MW) emission and also correlates the soft X-ray emission to HXR flux. The Neupert effect was established using the time integral of the MW emission since the impulsive phase begins at t_0 [Benz, 2017]:

$$F_{SXR}(t) \propto \int_{t_0}^{t} F_{MW}(t')dt' \tag{3.11}$$

This effect helps bridge the two regions and phenomena associated with solar flares: acceleration from high in the corona and plasma heating in the chromosphere. This steady heating in the gradual phase and the filling of magnetic loops has helped to define several scaling relations for the loop lengths as well as X-ray emission measures and densities detectable from these flares. Relations for the primary emission mechanisms (thermal X-ray and non-thermal radio) have also similarly been derived from numerous solar flare observations following the work done by Neupert [1968]. These scaling relations can also then be applied and compared to model and observation results from young stellar flares.

3.3 Scaling relations for flares

3.3.1 Emission measures and temperature

The soft X-ray emission measurable during the gradual phase from the flaring loops can be used to determine quantities like the size of the loop and the density of particles through the relation for emission measure (EM):

$$EM = \int n_e^2 dV \approx n_e^2 V \approx n_e^2 L^3 \tag{3.12}$$

where L and V are the length and volume of the flaring region respectively. Continued heating generated from precipitating high energy particles leads to sustained chromospheric evaporation and SXR emission. This in turn leads to the increase in size of the flaring loop, L. The density of the plasma filling the loop, n_e, can then be calculated from the observed emission measure.

Another detectable quantity is the flaring temperature. In order to compare measurements for solar and stellar flares, it is important to understand how this quantity is measured (and to be aware of the fact that a single temperature may be an oversimplification). For young stellar flares, these quantities are derived from spectral fitting of X-ray observations (see Chapter 2). However, in solar flares these parameters are preferentially derived from spectral line ratios. For example, Feldman et al. [1995a] used the Bragg Crystal Spectrometer (BCS) to obtain the spectral line ratio of Li-like dielectronic recombination lines in Fe, Ca and S to a He-like line to obtain the maximum electron temperatures and emission measures [Feldman et al., 1995b]. They also used the ratio of broadband fluxes from the Geostationary Operational Environmental Satellites (GOES) to determine these parameters. The filter ratio method used takes the ratio of X-ray fluxes at different wavelengths to derive the EM and temperature using the equation:

$$F_k = P_k(T)EM(T) \tag{3.13}$$

where P_k is the temperature response function of filter k and F_k is the observed flux in the same filter. The temperatures and emission measures derived from measured GOES fluxes from over 900 solar flares is shown in Figure 3.9.

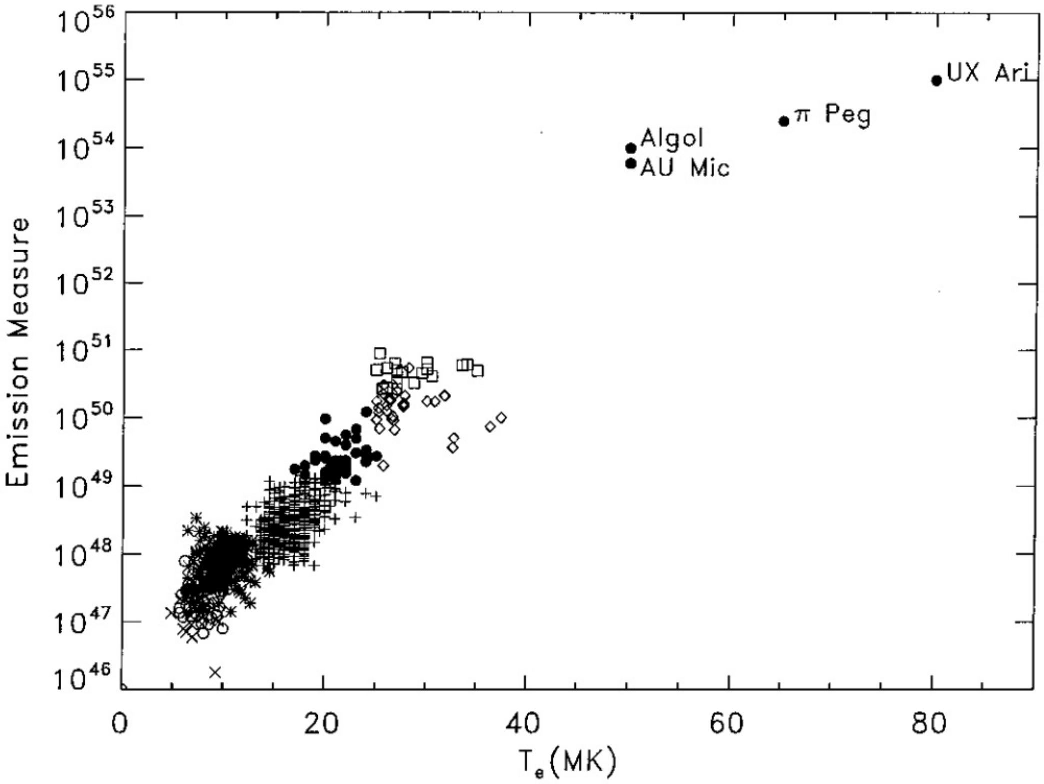

Figure 3.9: Figure from Feldman et al. [1995b] of solar flare temperatures and emission measures. Different symbols denote flares obtained from various sources, full references listed in Feldman et al. [1995b]. The high temperature and emission sources in the upper right region are all large flares from main sequence stars from Garcia and McIntosh [1992].

These emission measures and temperatures derived from observations have been used to support scaling relations derived from numerical models. Yokoyama and Shibata [1998] performed MHD simulations of magnetic reconnection, balancing the reconnection led heating and cooling of the system from conduction (where the conduction coefficient is $\propto \mathrm{T}^{5/2}$). The model assumes the emission measure is calculated as in Equation 3.12, where the volume of the flaring loop, V, is equal to L^3 where L is the length of the loop. An upper limit to the gas pressure is also set to maintain loop stability and confine the plasma to the loop. This is done by equating the gas pressure to the magnetic pressure within the loop. From this, they calculated several relationships between the EM and temperature, as well as the loop length and magnetic field. These relationships were based off the maximum temperature, which is the maximum temperature throughout the whole simulation. This maximum temperature does not necessarily coincide with the maximum emission measure, so the distinction should be made clear. The peak temperature during flare observations is often represented by the temperature measured when the peak emission measure is taken. The temperature is likely to have a maximum slightly before the peak emission measure, due to the intense heating caused by reconnection initially. Indeed, Yokoyama and Shibata [1998] showed the peak temperature (i.e. when the emission measure peaks) is three times lower than the maximum temperature during their simulated flare. Yokoyama and Shibata [1998] also assumed that the plasma filling the loop during chromospheric evaporation has a gas pressure smaller than the magnetic pressure of the loop so the loops can maintain stability. These simulations resulted in the following scaling relations for solar flares [Shibata and Yokoyama, 1999]:

$$T_{\mathrm{peak}} \approx 10^7 \left(\frac{B}{50\,\mathrm{G}}\right)^{6/7} \left(\frac{n_o}{10^9\,\mathrm{cm}^{-3}}\right)^{-1/7} \left(\frac{L}{10^9\,\mathrm{cm}}\right)^{2/7} \mathrm{K} \tag{3.14}$$

where the maximum temperature $T_{max} = 3 \times T_{\mathrm{peak}}$, n_o is the pre-flare coronal density, L is the reconnected loop length and B is the magnetic field strength in the loop.

$$EM \approx 10^{48} \left(\frac{B}{50\,\mathrm{G}}\right)^{-5} \left(\frac{n_o}{10^9\,\mathrm{cm}^{-3}}\right)^{3/2} \left(\frac{T}{10^7\,\mathrm{K}}\right)^{17/2} \mathrm{cm}^{-3} \tag{3.15}$$

$$EM \approx 10^{48} \left(\frac{L}{10^9\,\mathrm{cm}}\right)^{5/3} \left(\frac{n_o}{10^9\,\mathrm{cm}^{-3}}\right)^{2/3} \left(\frac{T}{10^7\,\mathrm{K}}\right)^{8/3} \mathrm{cm}^{-3} \tag{3.16}$$

These scaling relations for B and L are shown in Figure 3.10. The solar flares from Feldman et al. [1995b] are also plotted. The scaling relations fit well with the observed trend in emission measure and temperature.

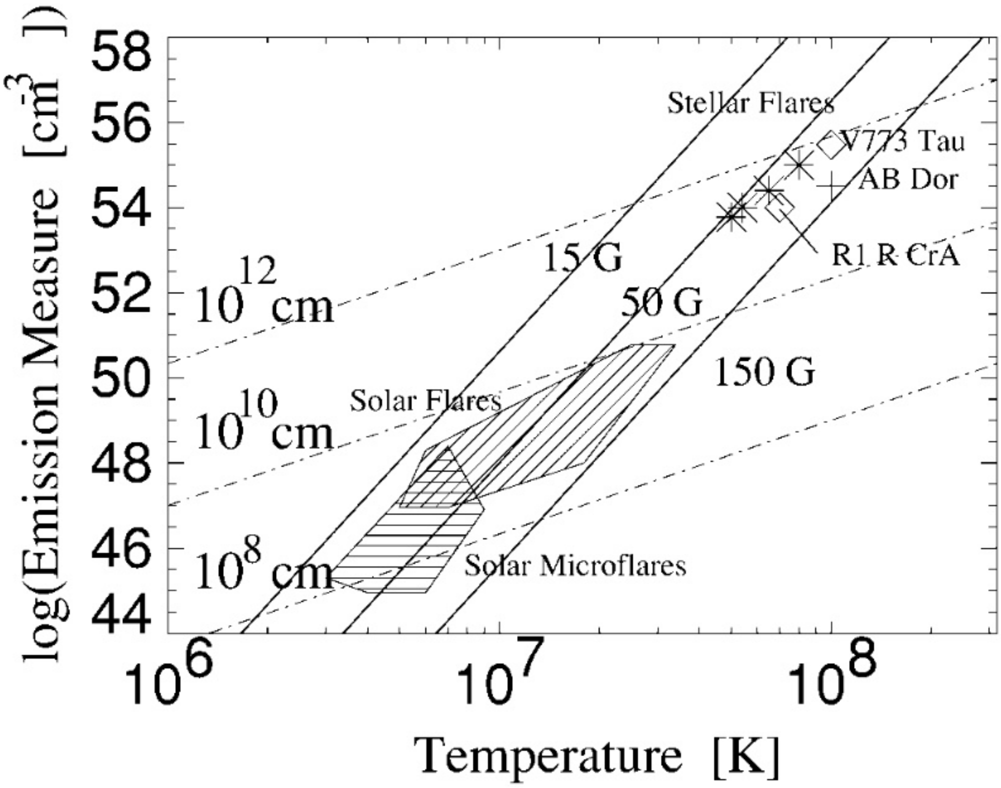

Figure 3.10: Emission measure and temperature plot from Shibata and Yokoyama [1999] showing a range of solar and stellar flares taken from Feldman et al. [1995b]. The scaling relations of Equation 3.15 and Equation 3.16 are overlaid as the solid and dashed lines respectively.

The relations also show how the temperature increases as the loop expands for a fixed field strength. This is suggested to be due to the conduction cooling becoming less efficient as the loop size increases. The loop length scaling relations overlaid in Figure 3.10 suggest possible loop lengths between $10^8 - 10^{10}$ cm for solar flares, agreeing well with observed solar loop lengths of $10^9 - 10^{10}$ cm. The scaling relations also appear to fit for the young stellar flares in the upper right region of Figure 3.10, as discussed in Chapter 2. These flares are expected to have larger loop lengths capable of reaching out to the inner edge of the circumstellar disk around $10^{10} - 10^{12}$ cm which these relations support. Fortunately, there have been a wealth of X-ray observations of young stellar flares since these relations were developed. In order to see how well the Shibata and Yokoyama [1999] scaling laws apply to T-Tauri stars, we collected this temperature and emission measure data from literature for these stars and plotted them in a similar manner to Figure 3.10. These observations are displayed on Figure 3.11 which show the same results from Figure 3.10 overlaid with recent T-Tauri flare observations. Only class II and III observations have been included. Where a source was fitted with a 2-temperature model, only the higher temperature (and emission measure) was used.

The young stellar flares do not seem to fit as well with the scaling relations as first thought from Figure 3.10. The distribution is far flatter, with a wider range in temperatures than for solar flares but a smaller spread in emission measures. The solar flare temperature range also falls within the reported T-Tauri temperature range. There are T-Tauri flares with the same temperatures as seen in solar flares but far higher emission measures. Based on the scaling relation this suggests these stellar flares have larger loops containing more thermal SXR emitting plasma, but maintain similar temperatures. There appears to be no significance of the type of young stellar object measured. The class II and III sources both have a similar temperature and emission measure range. The presence of a disk apparently has little effect on the emission measures and temperatures measured from these flares. There is also no discernible skew in results

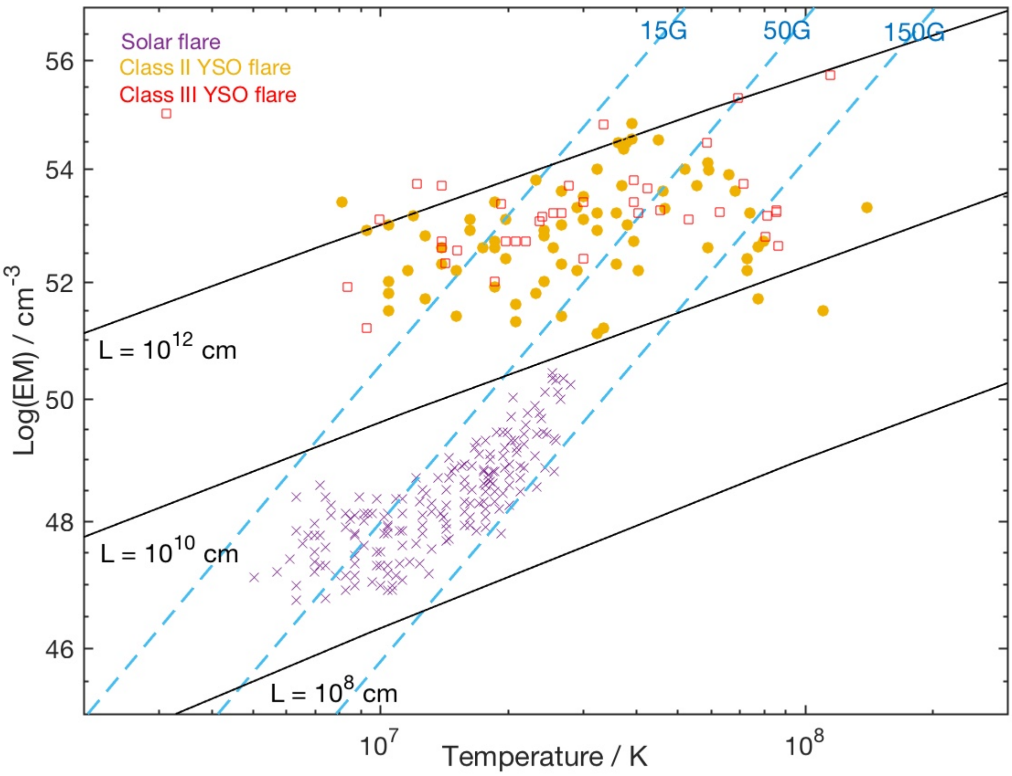

Figure 3.11: Flare peak temperatures and emission measures for flares on both the Sun (purple cross) and T-Tauris. Solar flare data is gathered from Feldman et al. [1995b] and Shibata and Yokoyama [1999]. The yellow circles represent class II (CTT) flares and red squares show class III (WTT) flares. TTS flare data is from Tsuboi et al. [1998], Imanishi et al. [2001], Imanishi et al. [2003], Franciosini et al. [2007], Giardino et al. [2006], Giardino et al. [2007], Güdel et al. [2007], Grosso et al. [2007], Argiroffi et al. [2006], Getman et al. [2011], Schulz et al. [2015] and Tsuboi et al. [2016].

when the specific star forming region that some of these flares are from is highlighted. Although the young stellar flare parameters are obtained through spectral fitting of X-ray observations, and the solar flare data is obtained through spectral line ratios, it is not thought that the differing methods would be the reason for any disagreements with the data. When the lower value from the 2-temperature fit is used, the profile remains the same, with a large dispersion in T-Tauri flares, albeit shifted slightly to lower temperatures.

The large loops predicted for T-Tauri stars when these relations were first derived are still applicable to these newer collated results. The newer observations still mostly fall within the $10^{10} - 10^{12}$ cm range predicted by these scaling relations. The relation for magnetic field however, predicts a range of magnetic fields, with a considerable portion below 15 G. This might be expected from the larger loop lengths only, as they extend further into the magnetospheres. However, the strong magnetic field strengths (see Chapter 2) of young stars would not give the weak field strengths for smaller loop lengths predicted by these relations. These scaling relations are therefore useful for giving a range of possible loop length values, however are less reliable for calculating magnetic field strength values. The loop length range given by these relations is over two orders of magnitude, and can be refined more with other methods for calculating these lengths directly from observations of flares.

3.3.2 Loop lengths

Despite the loop length scaling relation agreeing well with these observations of solar flares there are other methods for deriving the sizes of flaring loops using light curve data. One of these methods was laid out by Reale et al. [1997], hereafter referred to as the Reale method. The decay phase of X-ray light curves can be used to determine the loop length, as generally the larger the loop the longer the decay time of the gradual phase. However, when there is sustained heating this increases the decay time and overestimates the size of the magnetic loop. To combat this, the Reale method uses both light curve decay times as well as a calculated slope from an EM-T diagram. The emission measure and temperature, as already discussed, are measured during and correspond to the gradual phase of a flare. By combining these observations, Reale et al. [1997] derived an expression for the loop length:

$$L = \frac{\tau_{LC}\sqrt{T}}{\phi F(\zeta)} \tag{3.17}$$

where τ_{LC} is the (1/e folding time) light curve decay time, T is the maximum flare temperature, $\phi = 3.7\times10^{-4}\,\mathrm{cm^{-1}\,s\,K^{1/2}}$, ζ is the slope in the $\sqrt{EM} - T$ diagram in the decay phase and $F(\zeta)$ is the correction function:

$$F(\zeta) = \frac{c_a}{\zeta/\zeta_a - 1} + q_a \tag{3.18}$$

where c_a, ζ_a and q_a are dimensionless parameters obtained with a non-linear fitting procedure for each light curve. This expression ensures the loop length calculated is still proportional to the flare decay time but if there is sustained heating the correction function increases and the length is not overestimated. The main issue with this method for calculating loop lengths, is the relatively small number of data points available for light curves of flares. This is especially true for young stellar flares. For example, the emission measure-temperature plot for a flare on the young stellar object V827 Tau is shown in Figure 3.12 with only three data points [Giardino et al., 2006]. V827 is a weak-lined T-Tauri star in the Taurus star forming region with a radius of $\approx 2\,\mathrm{R_\odot}$. The values used in the above equations are obtained from the light curve as: $c_a = 0.51$, $\zeta_a = 0.35$, $q_a = 1.36$, $\zeta = 0.73$, $\tau_{LC} = 18.5\,\mathrm{ks}$. Using these quantities, the loop length is predicted to be $2.5 - 3.5\,\mathrm{R_\odot}$. The flaring density is calculated from this (assuming the loops radius $= 0.1L$) as $n_e = 1.3\times10^{11}\,\mathrm{cm^{-3}}$. As V827 is a WTT there is likely to be little interaction of this loop with a circumstellar disk however the loop is still considerable in size. Other loop lengths calculated using this method are shown in Table 3.2.

These loop lengths are all calculated from light curves like in Figure 3.12. That is, they are all calculated from relatively few data points with large error bars. Therefore, while it is easy to conclude that stellar flares in young stars are capable of producing loop lengths that can reach the inner edge of the circumstellar disk, these are still only estimates of the true loop size in flares. Additionally, it predicts the size of the loop

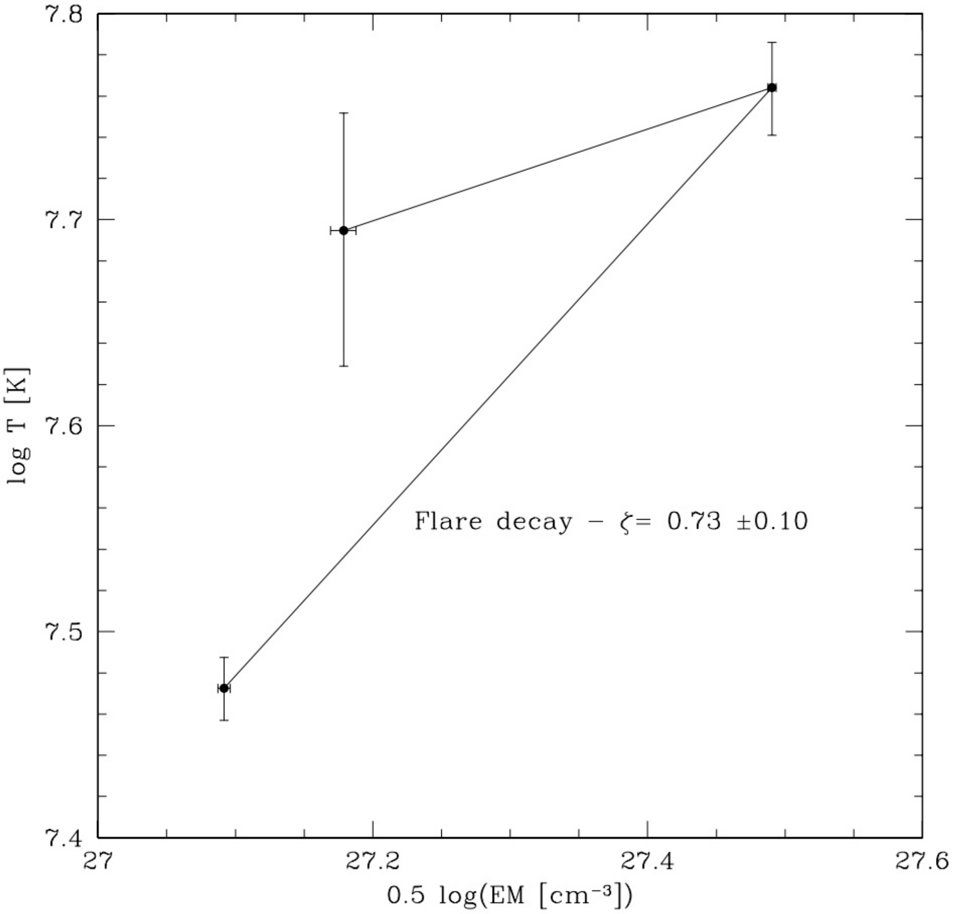

Figure 3.12: Emission measure and temperature plot for the flare observed by Giardino et al. [2006] on the weak-lined T-Tauri star V827 Tau.

based on prolonged heating in the decay or gradual phase of a flare, not the original loop that reconnects. In general, the Reale method for calculating loop lengths delivers smaller loop lengths than the Shibata and Yokoyama [1999] scaling relations. Namekata et al. [2017] argues that the latter of these methods generates more accurate results as well as not requiring time evolution data. Which method is more accurate remains an open question, but both approaches support the possibility of star-disk interactions via flaring magnetic loops. There is lots of information to be gained from X-ray observations of stellar flares. The loop lengths, emission measures, temperatures

Table 3.2: Loop lengths from YSOs calculated using the Reale method [Reale et al., 1997] where ζ is the slope in the $\sqrt{EM} - T$ plot.

ζ	L (10^{10} cm)	L/R_*	Reference
0.35	7.2	0.4	Favata et al. [2005]
0.46	13.7	0.6	Favata et al. [2005]
1.29	48.3	2.5	Favata et al. [2005]
0.79	198	18.0	Favata et al. [2005]
4.02	323	10.1	Favata et al. [2005]
0.60	64	4.2	Favata et al. [2005]
1.63	92	5.1	Favata et al. [2005]
<0.46	65	5.6	Favata et al. [2005]
6.53	162	11.8	Favata et al. [2005]
1.68	173	5.1	Favata et al. [2005]
0.36	3.7	0.3	Favata et al. [2005]
1.48	35	1.6	Favata et al. [2005]
2.96	76	12.0	Favata et al. [2005]
0.90	40	3.8	Favata et al. [2005]
0.70	51	3.0	Favata et al. [2005]
<0.57	110	55.0	Favata et al. [2005]
<0.58	3.7	0.4	Favata et al. [2005]
<0.70	82	6.7	Favata et al. [2005]
0.83	12	1	Franciosini et al. [2007]
0.67	2.4	2	Franciosini et al. [2007]
0.9	7	0.5	Franciosini et al. [2007]
0.73	2.5-3.5	1.25-1.75	Giardino et al. [2006]
0.36	7.5	0.25	Favata et al. [2001]
1.4	64	3.7	Getman et al. [2006]

and densities are valuable parameters to inform us about these flares. The thermal X-ray emission in general from these flares can also be compared with the non-thermal radio emission to explore the connection between the two flaring radiation mechanisms through the Güdel-Benz relation.

3.3.3 The Güdel-Benz relation

The link between particle acceleration and plasma heating that occurs in solar flares can be explored by looking at the primary emission both of these processes produce. The work established by Neupert [1968] linking the microwave emission and SXR emission in these processes has been built on in recent years. The Güdel-Benz relation was first proposed by Güdel and Benz [1993] to similarly relate the non-thermal radio (particle acceleration) and thermal X-ray (plasma heating) emission produced in flares from active stars:

$$\frac{L_{\mathrm{X}}}{L_{\mathrm{R}}} \approx 10^{15.5} [\mathrm{Hz}] \tag{3.19}$$

where $\mathrm{L_X}$ [erg s^{-1}] and $\mathrm{L_R}$ [erg s^{-1} Hz^{-1}] are the X-ray and radio luminosities respectively. Observations of the peak X-ray and radio luminosity from several solar flares as well as main sequence flares is shown in Figure 3.13 from Benz and Güdel [2010]. The Güdel-Benz (GB) relation is overlaid as the dashed line. This relation clearly holds over several orders of magnitude as well as for various types of flares from microflares on the Sun to large main sequence stellar flares.

In order to see how well the GB relation fits with flares on young stars, we collected data from literature where these stars were observed at X-ray and radio wavelengths. Only data from sources that were confirmed to be flaring and determined to be either class II or III in nature were included. These results are shown in Figure 3.14 along with the previous results for solar microflares and main sequence flares from Figure 3.13. It is clear there is a significant deviation from the relation for these observed T-Tauri flares. While there are a couple of sources which fall on the relation, the majority lie in a region of larger than expected radio luminosity (when compared with the GB relation). However, the sources do show how these T-Tauri flares are more powerful than their solar counterparts. The luminosities of these flares are several orders of magnitude larger than for solar flares. Dzib et al. [2015] suggested a modified version of the GB relation for these star forming regions:

$$\frac{L_{\mathrm{X}}}{L_R} \approx 0.03 \cdot 10^{15.5} [\mathrm{Hz}] \tag{3.20}$$

which is shown as the red dashed line in Figure 3.14. This modified relation gives a

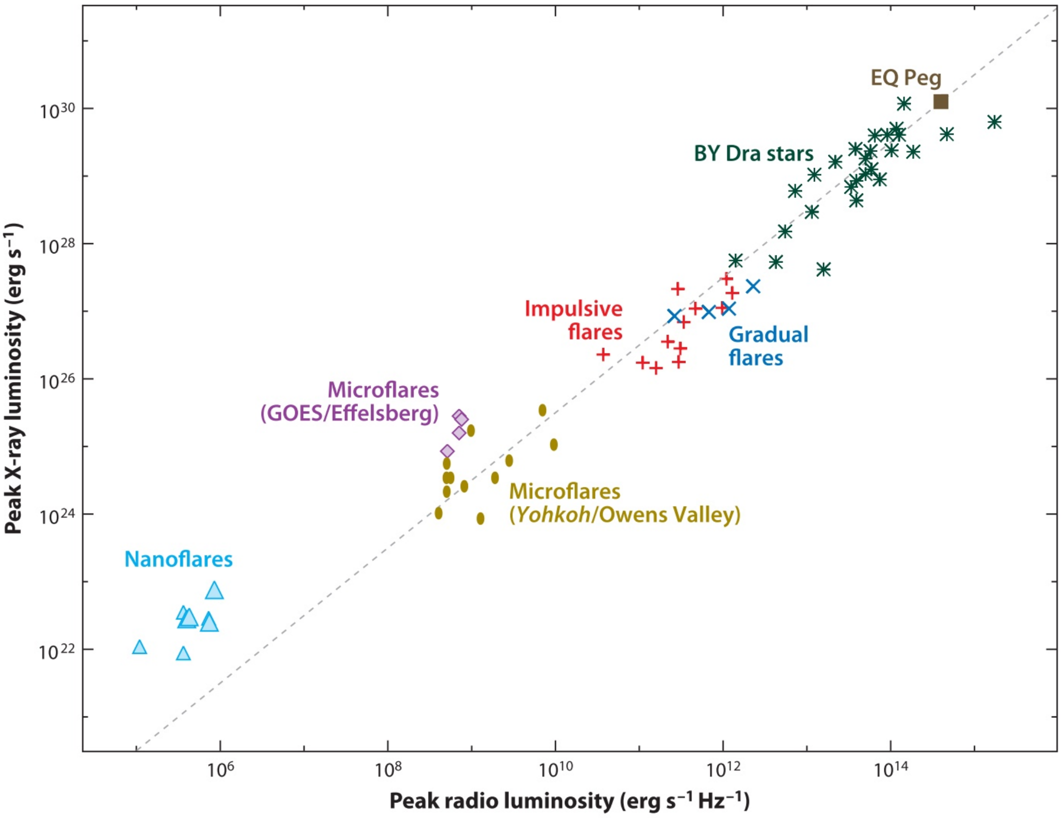

Figure 3.13: Peak radio and X-ray luminosities from flares on the Sun (nano, micro, impulsive and gradual) and main sequence stars. The Güdel-Benz relation is shown as the dashed line. Figure from Benz and Güdel [2010].

better fit for the observational data however it is unclear why the data does not fit with the original GB relation.

The observed radio luminosities in Figure 3.14 were taken at 7.5 GHz with the values corrected to the most recent distance estimates to the sources. These sources were also observed at 4.5 GHz and show a very similar distribution. The difference in observing frequency between these two bands does not appear to make a significant difference. The full list of radio and X-ray bands from which all these sources were detected is given in Table 3.3. The X-ray bands used are broader for the T-Tauri data than the solar and main sequence flares however still cover approximately the same (lower energy) range. The differing X-ray bands are not expected to cause any effect

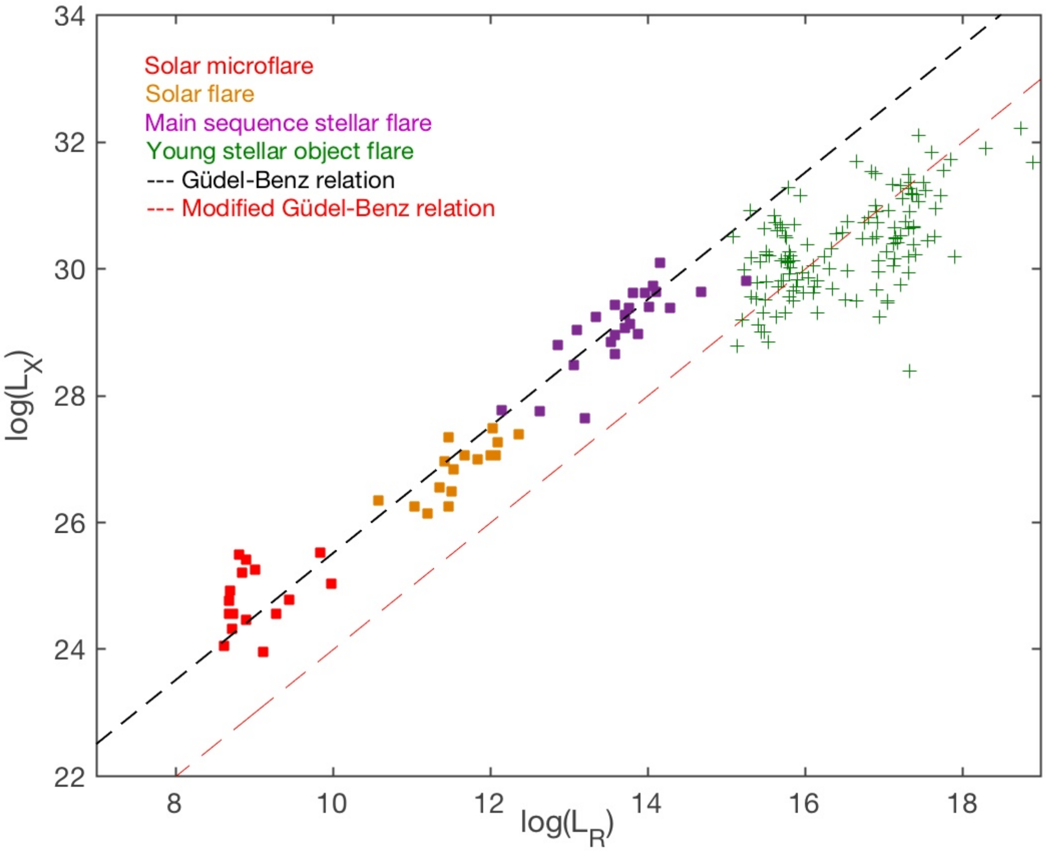

Figure 3.14: X-ray [erg s^{-1}] and radio [erg s^{-1} Hz^{-1}] luminosities of solar and main sequence flares (from Figure 3.13) and the luminosites from the collated T-Tauri literature sources (green crosses). The original and modified Güdel-Benz relations are shown as the dashed black and red lines respectively. References for observations are given in Table 3.3.

that would lead to this significant deviation from the relation for all T-Tauri sources.

To investigate the deviation, properties of the observational data are examined. Firstly, the luminosities of the separate class II (blue) and III (green) sources are looked at in Figure 3.15. The solid blue and green circles represent the mean value of the class II and class III flares respectively with their variances indicated by the error bars. The general distribution between the class II and III sources does not indicate that either class has a dramatic effect on the deviation from the relation. However, looking at the mean values of the class III sources suggest a slight increase in their non-thermal radio

Table 3.3: X-ray bands and radio frequencies of observational data from Figure 3.14. The star forming region (i.e. the different literature source) from which the T-Tauri sources are observed is shown in the first column. Radio references; [a] Ortiz-León et al. [2015], [b] Dzib et al. [2013], [c] Dzib et al. [2015], [d] Kounkel et al. [2014], [e] Güdel and Benz [1993], [f] Güdel [1992], [g] Benz and Güdel [1994]. X-ray references; [h] Kuhn et al. [2010], [i] Giardino et al. [2006], [j] Pillitteri et al. [2010], [k] Imanishi et al. [2003], [l] Güdel et al. [2007], [m] Tsujimoto et al. [2002], [n] Skinner et al. [2003], [o] Ramírez et al. [2004], [p] Getman et al. [2006].

Object	Radio frequency / GHz	X-ray band / keV
TTS (Serpens)	7.5 [a]	0.5 – 8.0 [h,i]
TTS (Taurus)	7.5 [b]	0.3 – 10 [j,k]
TTS (Ophiuchus)	7.5 [c]	0.3 – 10 [l]
TTS (Orion)	7.5 [d]	0.3 – 10 [m,n,o,p]
Main sequence star	8.5 [e,f]	0.1 – 2.4, 0.2 – 4.0 [e,f]
Solar flare	8 – 9 [g]	0.1 – 2.4 [g]

emission. There is no significant difference in the thermal X-ray emission between these two types of T-Tauri star. A two sample Kolmogorov-Smirnov (K-S) test was also carried out to explore the relationship between the two classes. First, the test is performed between the X-ray luminosity of the class II and class III stars. The test indicates that there is a probability of 16% that the two samples are drawn from the same population. In other words there is no statistically significant evidence that the X-ray luminosity is different between these two groups of objects. For the radio luminosity case, the probability that the two groups are from the same population is smaller, 7%, but still formally insignificant [Waterfall et al., 2019].

The effect of the star forming region each source resides in is investigated in Figure 3.16. Each literature reference from which this observational data is taken is shown here and represents the different star forming regions which are observed. Dzib et al. [2015] observed the Ophiuchus complex, Dzib et al. [2013] observed the Taurus-Auriga complex, Ortiz-León et al. [2015] observed the Serpens regions and Kounkel et al. [2014] observed flaring T-Tauri sources from the Orion region. The furthest of these regions, the Orion region [Kounkel et al., 2014], show the highest radio luminosities for all flares. As this is by far the furthest region considered it would be expected

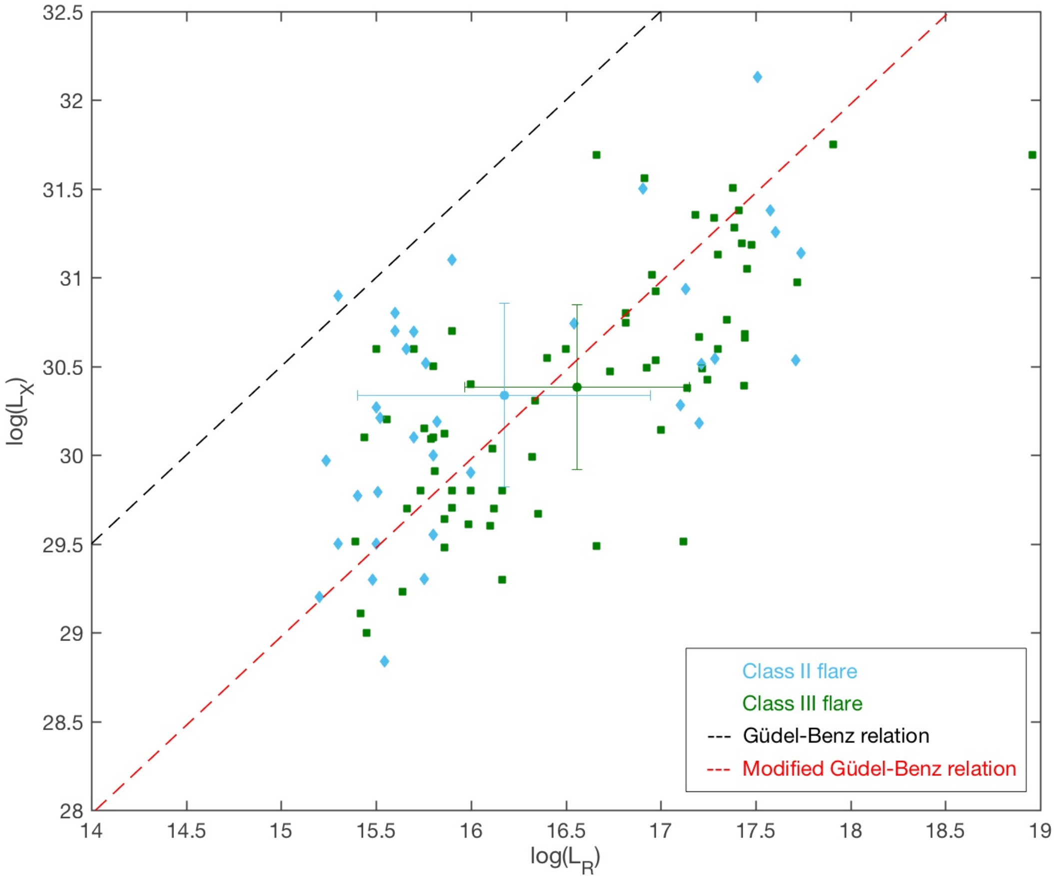

Figure 3.15: X-ray [erg s^{-1}] and radio [erg s^{-1} Hz^{-1}] luminosities of the observed T-Tauri flares from Figure 3.14. The sources are now differentiated by their class (class II: blue, class III: green). The solid blue and green circles represent the mean value of the class II and class III sources, respectively, with their variances indicated by the error bars.

that only the most luminous sources would be detected. This is an example of the Malmquist bias, where brighter sources are preferentially detected and observing regions that are further away will therefore lead to the detection of only the brightest sources. In the case of the Orion sources, no flares with luminosities lower than approximately $\log L_R$ [erg s^{-1} Hz^{-1}] = 17 are detected. The other (closer) star forming regions observed detect flares down to $\log L_R$ [erg s^{-1} Hz^{-1}] = 15.3. This distance bias is the same for all main sequence flares too, however they fit with the GB relation whereas the young stellar flares do not.

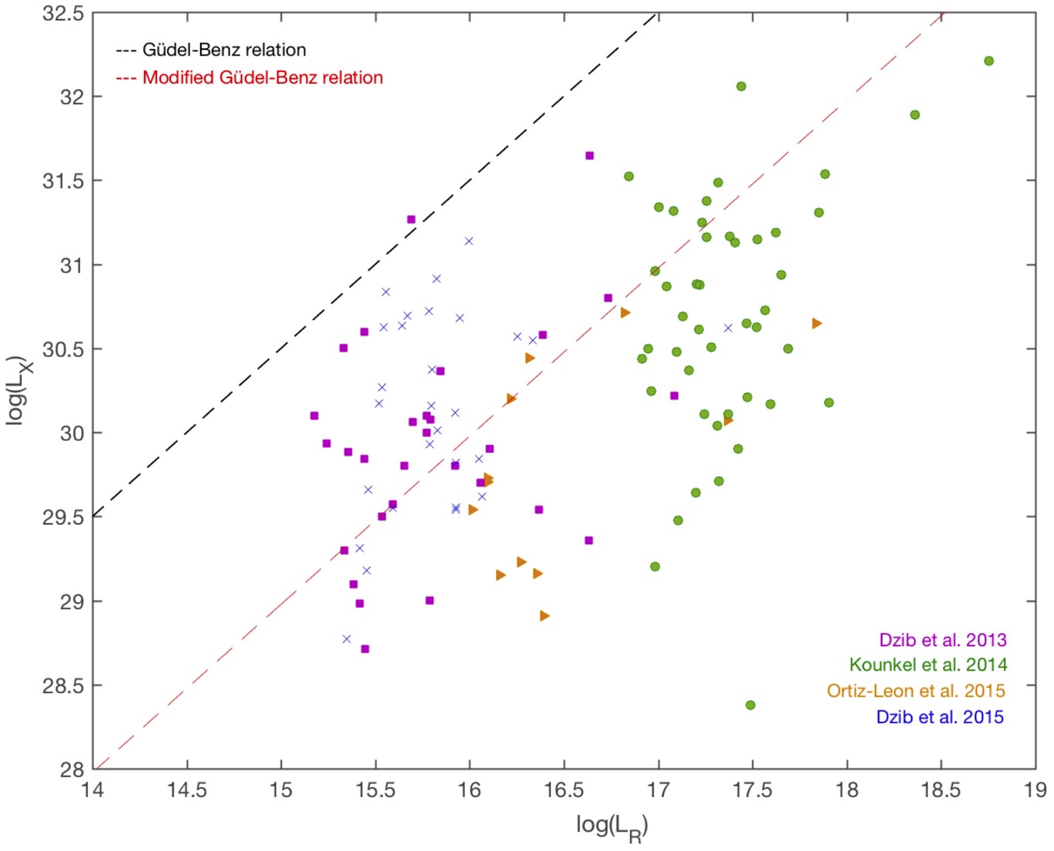

Figure 3.16: X-ray [erg s^{-1}] and radio [$\text{erg s}^{-1}\,\text{Hz}^{-1}$] luminosities of the observed T-Tauri flares from Figure 3.14. The sources are now differentiated by their original literature reference (and therefore star forming region). The references for these observations are given in Table 3.3.

The peak temperature of these flares (taken from the higher temperature component of a 2-temperature fit, where available) is shown in Figure 3.17. Again, there is no evidence for flares of a certain temperature producing more radio or X-ray emission or causing a noticeable deviation from the relation. There is an even spread in all five temperature ranges considered, with the highest luminosity X-ray and radio flares having no specific temperature range limit. It was previously stated that Getman et al. [2008] found that classical T-Tauri stars experienced hotter flares than their weak-lined counter parts, however no such statement can be made here.

The class, temperature, location and frequency band that these sources are observed

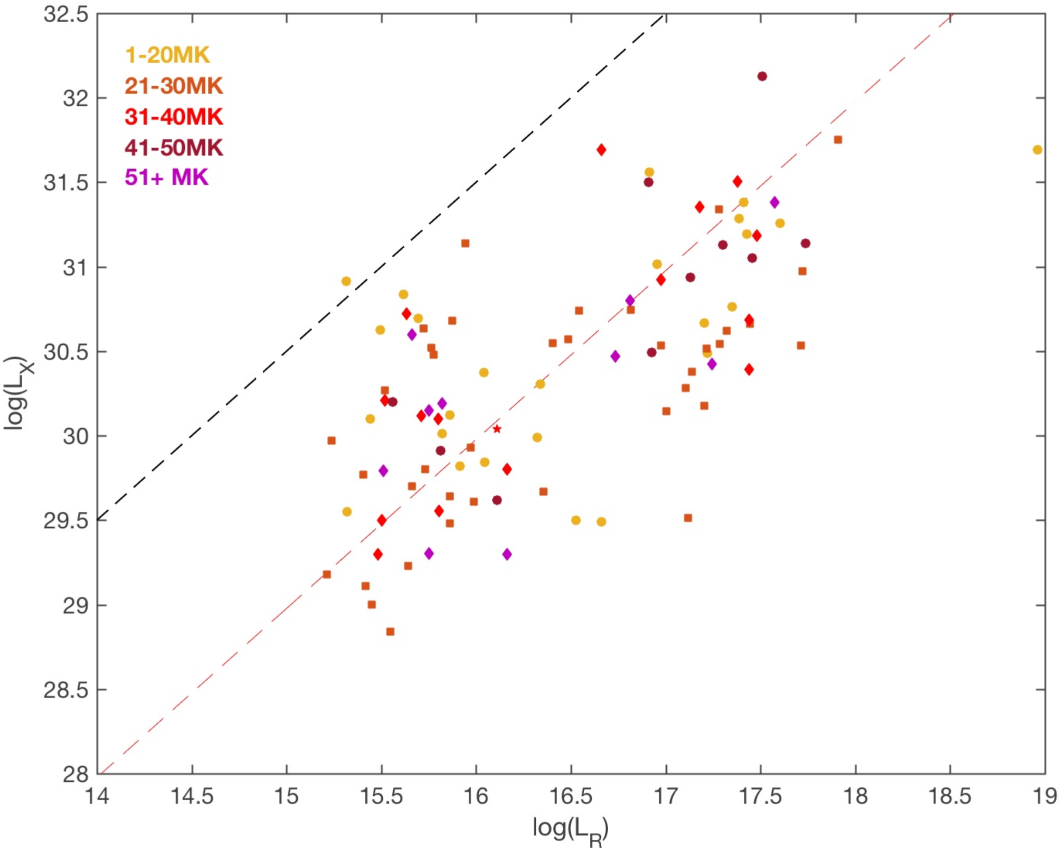

Figure 3.17: X-ray [erg s^{-1}] and radio [erg s^{-1} Hz^{-1}] luminosities of the observed T-Tauri flares from Figure 3.14. The sources are now colour-coded according to their peak flaring temperature, determined from the X-ray observations (see Table 3.3).

in do not reveal why their is a large deviation between the GB relation and the emission produced in T-Tauri flares. To further investigate this, simulations of flaring emission from T-Tauri stars is required and is carried out in Chapter 5 and Chapter 6.

3.4 Comparing flaring timescales

It is useful to know how the timescales involved in these flares vary between the Sun and T-Tauri stars. The extended magnetic loops predicted in T-Tauri stars will affect the timescales discussed in Section 3.2.1.1. Values of these timescales for both types of flare are now explored. The T-Tauri values will be revisited in Chapter 6 when the variation of gyrosynchrotron emission in time is modelled.

3.4.1 Reconnection time

The Sweet-Parker reconnection time (Section 3.1) can be approximated as:

$$\tau_{rec} = \sqrt{\tau_D \tau_A} \tag{3.21}$$

where τ_A and τ_D are the Alfvén and diffusive timescales given as:

$$\tau_A = \frac{L}{v_A} = \frac{L\sqrt{\mu_0 \rho}}{B} \tag{3.22}$$

(where ρ is the mass density mn) and:

$$\tau_D = \frac{L^2 \mu_0}{\eta} \tag{3.23}$$

The ratio of solar to stellar reconnection time (for the Sweet-Parker model) is therefore calculated using (Sweet [1958], Parker [1957]):

$$\frac{\tau_{rec\odot}}{\tau_{rec*}} = \left(\frac{\tau_{D\odot}\tau_{A\odot}}{\tau_{D*}\tau_{A*}}\right)^{\frac{1}{2}} = \left(\frac{L^3 n^{\frac{1}{2}}}{BT^{-\frac{3}{2}}}\right)^{\frac{1}{2}}_{\odot} \left(\frac{BT^{-\frac{3}{2}}}{L^3 n^{\frac{1}{2}}}\right)^{\frac{1}{2}}_{*} \tag{3.24}$$

While the Sweet-Parker reconnection model leads to reconnection times far slower than is observed, this equation can still be used to give a general idea of the difference in timescale between the reconnection on the two different types of star using the well known Sweet-Parker model. Using Equation 3.24 and the typical parameters for a solar flare ($n_\odot = 10^9$ cm^{-3}, $T_\odot = 10^7$ K, B$_\odot$ = 100 G), a sample of possible reconnection times is given in Table 3.4.

The subscripts denote whether the value is for the Sun ($\odot$) or the T-Tauri star ($_*$).

Table 3.4: Ratio of solar to stellar reconnection time for a variety of different flares using the Sweet-Parker reconnection model, calculated using Equation 3.24.

$L_\odot$ / cm	T_* / K	n_* / cm^{-3}	L_* / cm	B_* / G	$\tau_{rec\odot}/\tau_{rec*}$
10^9	10^7	10^{11}	10^{11}	50	0.0002
10^9	10^7	10^{11}	10^{11}	100	0.0003
10^9	10^7	10^{11}	10^{11}	500	0.0007
10^{10}	10^7	10^{11}	10^{11}	50	0.0003
10^{10}	10^7	10^{11}	10^{11}	100	0.0005
10^{10}	10^7	10^{11}	10^{11}	500	0.001
10^9	5×10^7	10^{11}	10^{11}	50	0.0001
10^9	5×10^7	10^{11}	10^{11}	100	0.0002
10^9	5×10^7	10^{11}	10^{11}	500	0.0003
10^9	10^7	10^{10}	10^{11}	50	0.0002
10^9	10^7	10^{10}	10^{11}	100	0.0003
10^9	10^7	10^{10}	10^{11}	500	0.0007
10^9	10^7	10^{11}	10^{10}	50	0.004
10^9	10^7	10^{11}	10^{10}	100	0.005
10^9	10^7	10^{11}	10^{10}	500	0.01

This table illustrates how for the more powerful and large T-Tauri flares the reconnection is much slower. This effect is increased by decreasing the loop top field strength, increasing the flare temperature and increasing the loop length (all in T-Tauri flares).

3.4.2 Propagation time

It has already been discussed how the free streaming propagation time of electrons when they are accelerated after reconnection is proportional to $E^{-1/2}$ from Equation 3.5. This equation is used in Table 3.5 to calculate this propagation time for various parameter values covering both solar and T-Tauri flares. The free streaming propagation time is calculated for non-relativistic energies as well as in the mildly relativistic regime. It should be noted that while electron energies around 1 MeV should be treated as mildly relativistic, the calculated non-relativistic propagation time is also included in the table just for completeness and comparison purposes.

From Table 3.5 it is clear that the higher energy particles have shorter propagation

Table 3.5: Free streaming time for particles accelerated during reconnection that have angles within the loss cone. The γ propagation time indicates that the timescale has been calculated in the mildly relativistic regime. The non-relativistic propagation time is also included for completeness and comparison purposes. Calculated from Equation 3.5.

Energy / keV	Loop length / cm	Propagation time / s	γ Propagation time / s
10	10^9	0.02	0.17
100	10^9	0.05	0.06
1000	10^9	0.02	0.04
10	10^{10}	0.17	1.71
100	10^{10}	0.53	0.61
1000	10^{10}	0.17	0.35
10	10^{11}	16.87	17.12
100	10^{11}	5.34	6.09
1000	10^{11}	1.69	3.54
10	10^{12}	168.73	171.19
100	10^{12}	53.36	60.87
1000	10^{12}	16.87	35.43

times (as expected). It is also evident that the larger loop lengths lead to longer propagation times. This suggests there will be larger delays between the initial reconnection and HXR footpoint emission in T-Tauri flares. The non-thermal radio emission may also be higher as the particles gyrate and emit over a longer scale. However, despite the stronger surface field strengths of T-Tauri stars the loop top field strength will be far lower in the case of the larger loops. This will lead to small loss cone angles as defined by Equation 3.6 which is important when considering the bounce period.

3.4.3 Bounce time

For the case of a large loop, where the loop top field strength is much smaller than the field strength of a mirror point, the resulting small loss cone angle should lead to shorter bounce periods according to Equation 3.7. Typical bounce period values for solar and stellar flare electrons are given in Table 3.6. Again, a non-relativistic and mildly relativistic time period is shown.

A smaller loss cone angle does lead to smaller bounce periods and therefore shorter

Table 3.6: Bounce period values for different flare configurations. The γ bounce period indicates that the timescale has been calculated in the mildly relativistic regime. The smaller loop length value are more suggestive of solar flares. Calculated from Equation 3.7.

Loop length / cm	Energy / keV	ψ_0 / degrees	Bounce period / s	γ bounce period / s
10^9	10	5	1.06	1.08
10^9	10	20	1.13	1.15
10^{11}	10	5	106.42	107.97
10^{11}	10	20	112.82	114.46
10^9	1000	5	0.11	0.22
10^9	1000	20	0.11	0.24
10^{11}	1000	5	10.64	22.35
10^{11}	1000	20	11.28	23.69

bounce timescales of particles in T-Tauri flares. Increasing the particle energy (and therefore velocity) leads to a shorter bounce period as expected. Increasing the loop length increases the overall travel distance between mirror points and therefore leads to an increase in bounce period.

3.4.4 Deflection time

The upper limit to how long these particles remain trapped on the field lines is dictated by the deflection time in Equation 3.8 and calculated values are shown in Table 3.7.

Table 3.7: Collisional deflection (trapping) time of electrons in a range of flare scenarios calculated from Equation 3.8.

Energy / keV	Electron density / cm^{-3}	Temperature / K	Deflection time / s
10	10^9	10^7	2.78
100	10^9	10^7	87.75
1000	10^9	10^7	2775.03
10	10^9	10^6	3.11
100	10^9	10^6	98.20
1000	10^9	10^6	3105.27
10	10^{10}	10^7	0.29
100	10^{10}	10^7	9.27
1000	10^{10}	10^7	293.09
10	10^{11}	10^7	0.031
100	10^{11}	10^7	0.98
1000	10^{11}	10^7	31.05

An increase in particle energy leads to longer deflection times. This may be due to the high velocity of these particles, which may bounce back and forth before they are able to be collisionally scattered into the loss cone. Decreasing the temperature of the plasma itself increases the deflection time as the other particles have slower velocities leading to less collisions. In a similar way, increasing the density decreases the deflection time as there are more particles to knock the accelerated electrons into the loss cone.

Aside from the changing magnetic field strength (which affects the loss cone angle of the trapped electrons) and the deflection into the loss cone via coulomb collisions, there are other scattering mechanisms that affect the transport of accelerated electrons from a flare. These include the non-collisional scattering of electrons via waves, turbulence, etc [Aschwanden, 1998]. However, the upper limit of the trapping and transport of these electrons in solar flare loops is suggested to be controlled by coulomb collisions [Aschwanden, 2006]. Modelling these electrons and how they behave both over time and within the loop are important elements in simulating flares. Flaring emission from these stars, with a focus on the non-thermal electrons at the peak of the flare as well as over time, is investigated in Chapter 5 and Chapter 6. However, a more in-depth review of the radio emission produced in flares with a focus on gyrosynchrotron radiation is now given. Included in this next chapter is discussion on how this gyrosynchrotron emission can be calculated and how the simulators used in our models work.

Chapter 4

Gyrosynchrotron emission

4.1 Radio emission

Radio astronomy is an essential tool in understanding astrophysical processes. Other observations, e.g. optical, lack the wide frequency range and ability to detect the numerous astronomical sources which emit in the radio. One area of radio astronomy research involves flares on both the Sun and young stars. In particular, the detection of gyrosynchrotron (GS) radiation, a type of non-thermal radio emission, enables us to determine several important features of flares. For example, the detection of circular polarised radio emission provides information on the magnetic field in these regions. The peak fluxes and frequencies obtainable from emission spectra can also provide information on parameters like the flaring densities.

This chapter will explore the theory behind this gyrosynchrotron radiation and why it is of particular importance in this research on T-Tauri flares. A short review of other types of radio emission (including thermal gyrosynchrotron), and the circumstances and frequencies in which they're observed is given, as well as a brief revision of radiation fundamentals.

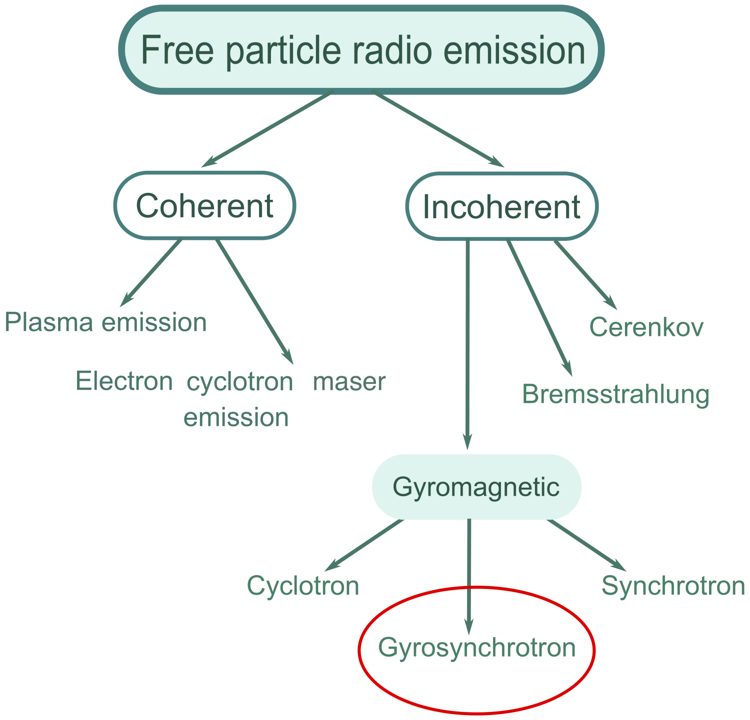

Figure 4.1: Types of free particle radio emission.

4.1.1 Types of radio emission

Nearly every source emits at radio frequencies. However, there are several different radio emission mechanisms to consider when observing objects at radio wavelengths. One has to consider whether the emission is thermal or non-thermal in nature, from incoherent or coherent sources, or from free or bound state particles.

Gyrosynchrotron (GS) radiation, the focus of this research, is produced by the acceleration of mildly relativistic electrons gyrating around magnetic field lines. As such it is a free particle, incoherent, non-thermal process. Other examples of both coherent and incoherent free particle radio emission processes are shown in Fig 4.1.

The two most common coherent radio emission mechanisms are plasma emission and electron cyclotron maser emission. These two emission processes can produce brightness temperatures far higher than their incoherent counterparts. This is due to the electrons working ‘coherently’ or ‘in phase’ with each other to produce the emission, rather than individually. Both these processes are not of importance in this thesis, where the focus is on incoherent non-thermal emission and is therefore not discussed in more detail. A more in-depth review of these coherent processes can be found in various sources including: Aschwanden [2006], Melrose [2017], etc.

Another free particle, incoherent mechanism is that of Cherenkov radiation. Cherenkov radiation occurs when a free particle, travelling in a particular medium, has a greater velocity than the speed of light. Similarly to sound waves that are produced when a moving object exceeds the speed of sound, the light is radiated in a cone shape.

Bremsstrahlung radiation, also called free-free emission (a primarily, although not necessarily, thermal emission), is discussed in Section 4.4.1. An overview of types of gyromagnetic emission is given in Section 4.4.2 with a more in-depth look into gyrosynchrotron radiation discussed in Section 4.5.

As mentioned previously, it is important to be able to diagnose which emission mechanisms is being detected. Figure 4.2 shows how some of these different mechanisms depend on frequency for height above the solar surface. In general, the higher radio frequencies are used to detect the incoherent processes. It is clear again that gyromagnetic (and in particular gyrosynchrotron) emission is key in tracing the active processes occurring between the chromosphere and corona. It is important to note however, that despite being able to see further at higher frequencies, the deepest regions remain optically thick at even the highest (upwards of 100 GHz) radio frequencies. Additionally, GS emission is highly dependent on the plasma parameters discussed in Chapter 2 and Chapter 3 (i.e. flaring densities and temperatures) as well as the viewing angle from which the radiation is calculated.

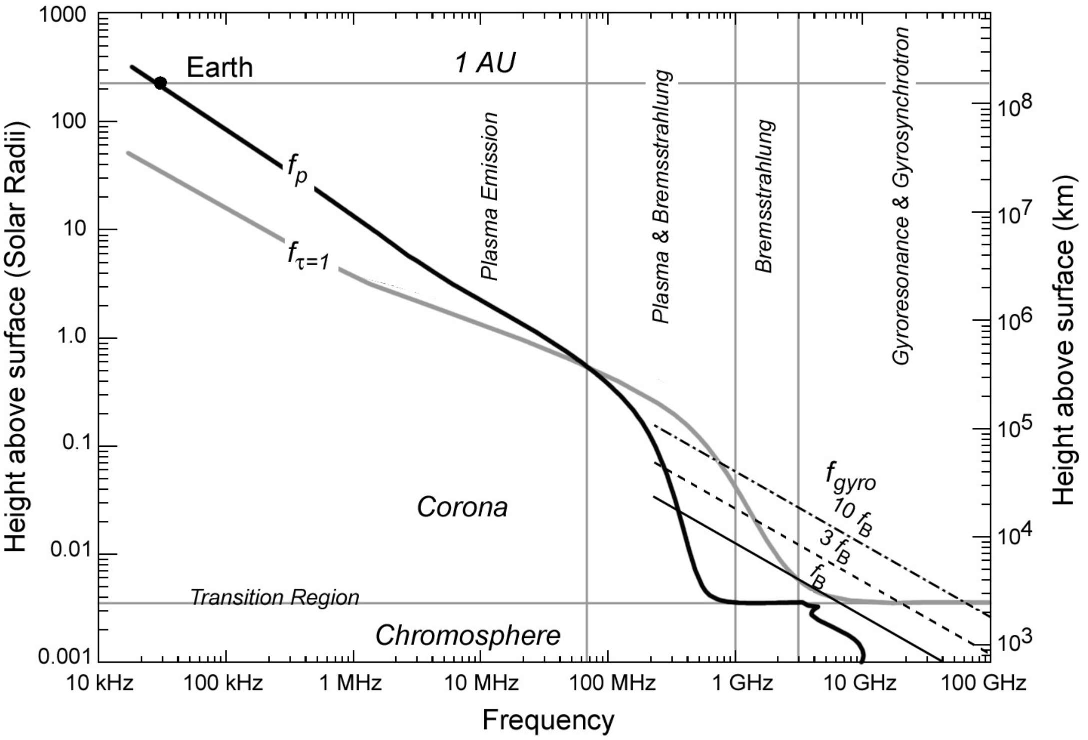

Figure 4.2: Figure from Gary and Hurford [2004] showing frequency ranges of different radio emission mechanisms at different heights from the solar surface. f_p and f_B are the plasma frequency and gyrofrequency respectively (defined in Section 4.4.2.1).

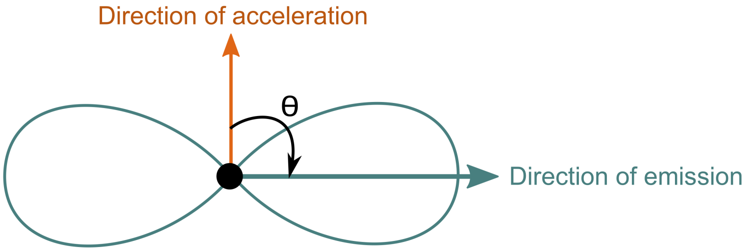

Figure 4.3: Dipole emission radiated from a non-relativistic charged particle.

4.1.2 Protons or electrons?

The incoherent radio emission mechanisms rely on the acceleration of individual electrons via different processes (see Chapter 3). Going forward, any mention of any accelerated radiating particle (especially in the context of gyrosynchrotron radiation) will refer to electrons not protons. To explain why this is appropriate, consider the Larmor equation. This equation describes the power radiated from an accelerating charged particle in a vacuum per unit solid angle, Ω:

$$\frac{\mathrm{dP}}{\mathrm{d}\Omega} = \frac{e^2 a^2}{4\pi c^3} sin^2\theta \tag{4.1}$$

where e is the particle charge, a is the acceleration, c is the speed of light and θ is the angle between the direction of acceleration and emission. The radiation produced from these particles is emitted in a dipole configuration, see Figure 4.3. Looking at this pattern, it is clear there is no emission in the direction of acceleration. The most emission occurs (as in the figure) in a direction perpendicular to this acceleration vector. To find the total power radiated, Equation 4.1 is integrated over all solid angles to give:

$$\mathrm{P} = \frac{2}{3}\frac{e^2 a^2}{c^3} \tag{4.2}$$

Using $F = ma$ and $P \propto a^2 \propto \frac{1}{m^2}$, as the electron rest mass is approximately 2000 times less than that of a proton, it therefore follows that accelerated electrons radiate more power than other charged particles.

4.2 Radiative transfer

Before discussing the variety of specific radiation mechanisms responsible for radio emission in more detail it is necessary to examine some fundamentals of radiation. This section explores these, and highlights the parameters of importance in radio observations, e.g. absorption, emissivity, polarisation, etc.

Radiation emitted from a source is detected by an observer. This radiation has a specific intensity at a frequency ν, I_ν, which is conserved along the path from source to observer in the absence of any intervening medium (i.e. in a vacuum - free space). This is described by the following equation, where s is the distance along this path and the specific intensity of a source is measured in cgs units of [$\mathrm{ergs\,cm^{-2}\,s^{-1}\,Hz^{-1}\,sr^{-1}}$]:

$$\frac{\mathrm{d}I_\nu}{\mathrm{d}s} = 0 \tag{4.3}$$

However, when the radiation passes through a medium this intensity is not conserved. There are two processes that can occur: absorption and emission. Both these processes must be taken into account when deriving the equation that defines radiative transfer as a whole. The fraction of specific intensity lost due to absorption within some distance ds is defined as:

$$\frac{\mathrm{d}I_\nu}{I_\nu} = -\kappa \mathrm{d}s \tag{4.4}$$

where κ is the absorption coefficient. Integrating this intensity over the source's projected area gives the flux density, S_ν with cgs units of [$\mathrm{ergs\,cm^{-2}\,s^{-1}\,Hz^{-1}}$]. This flux density can be integrated over all frequencies to give the total flux, S [$\mathrm{ergs\,cm^{-2}\,s^{-1}}$]. One important quantity in radiative transfer is the opacity or optical depth of the medium which is absorbing the radiation. This optical depth, τ, is related to the absorption coefficient by:

$$\mathrm{d}\tau = -\kappa \mathrm{d}s \tag{4.5}$$

where $\tau > 0$. It is therefore possible to identify whether a source is optically thin or thick to radiation according to the following condition:

$$\tau \ll 1 : \text{optically thin}$$
$$\tau \gg 1 : \text{optically thick}$$

The specific intensity measured from optically thick regions, where $\tau \gg 1$, depends on the average energy of the electrons. However, the intensity of radiation from optically thin sources depends on the magnetic field as well as the energy and density distributions of these electrons [Dulk, 1985]. Similarly, the coefficient for emission is:

$$j_\nu = \frac{\mathrm{d}I_\nu}{\mathrm{d}s} \tag{4.6}$$

which is combined with Equation 4.4 to give the equation for radiative transfer:

$$\frac{dI_\nu}{ds} = -\kappa I_\nu + j_\nu \tag{4.7}$$

which can be rearranged (using Equation 4.5) to give:

$$\frac{\mathrm{d}I_\nu}{\mathrm{d}\tau_\nu} = S_\nu - I_\nu \tag{4.8}$$

where S_ν is the source function: $S_\nu = j_\nu/\kappa_\nu$. At radio frequencies, it is common to see these equations written in terms of the brightness temperature. To derive this expression we must first consider both Kirchoff's and Planck's law. Kirchoff's law for a system in thermal equilibrium at temperature T states that:

$$B_\nu(T) = \frac{j_\nu}{\kappa_\nu} \tag{4.9}$$

This law applies to any system in local thermal equilibrium (LTE) as well. B_ν(T) is the spectrum of radiation at temperature T at a frequency ν in equilibrium. In thermal equilibrium, this spectral radiance is equal to the specific intensity, I_ν. Planck's law defines this spectral radiance as:

$$B_\nu(T) = \frac{2h\nu^3}{c^2}\frac{1}{e^{\frac{h\nu}{k_BT}} - 1} \tag{4.10}$$

where h is the Planck constant, k_B is the Boltzmann constant and c is the speed of light in the medium. At radio frequencies, $h\nu \ll k_BT$ which reduces Equation 4.10 to:

$$B_\nu(T) = I_\nu \approx \frac{2v^2 k_B T_b}{c^2} \tag{4.11}$$

where T_B is the brightness temperature (temperature of a black body in thermal equilibrium). Similarly, the source function can be rewritten in terms of the effective temperature, T_{eff}, as $S_\nu = \frac{2v^2 k_B T_{\text{eff}}}{c^2}$. For a non-thermal electron distribution, T_{eff} is a function of both the frequency and polarisation mode. Equation 4.8 can therefore be written as:

$$\frac{\mathrm{dT_b}}{\mathrm{d}\tau_\nu} = T_{\text{eff}} - T_b \tag{4.12}$$

which is solved as:

$$T_b = T_{\text{eff}}[1 - \mathrm{e}^{-\tau_\nu}] \tag{4.13}$$

where, for an optically thick source ($\tau \gg 1$), $T_b = T_{\text{eff}}$. For an optically thin source

$(\tau \ll 1)$, $T_b = T_{\text{eff}}\tau_\nu$. The brightness temperature cannot exceed the effective temperature. The effective temperature is also associated with the average energy of the emitting electrons, which is in turn related to the brightness temperature observed. When there are more lower energy emitting electrons this brightness temperature is therefore reduced. This is generally attributed to increased Compton scattering from the more numerous lower energy electrons. As such, the temperatures observed from incoherent emission is usually no higher than 10^{10} K in stellar sources [Dulk, 1985]. The brightness temperature is therefore a useful tool in identifying the mechanism that produces radio emission.

4.3 Polarisation

A transverse electromagnetic wave propagating through a medium has electric field components in the X, Y and Z direction. Traditionally, the Z direction acts in the direction the wave is propagating perpendicular to the XY plane (in which the electromagnetic field oscillates). The radiation emitted is unpolarised if the direction of this electric field oscillates randomly in time. If there is zero phase difference between the X and Y components (that act perpendicularly to each other) then the light is linearly polarised and confined to one plane along the Z direction. If these two components have a phase difference not equal to zero or 90°, and are not equal in magnitude, then the light is elliptically polarised. If the X and Y components of the electric field are equal in magnitude with a phase difference of 90° then the radiation is circular polarised. The electric field vector in this case rotates in a circle in either a clockwise or anticlockwise direction. This direction, as viewed from the source toward the observed, dictates whether the polarisation is left-handed (anticlockwise) or right-handed (clockwise). The difference in these three types of polarisation is shown in Figure 4.4. The left and right circular polarisation are described in terms of the Stokes V and

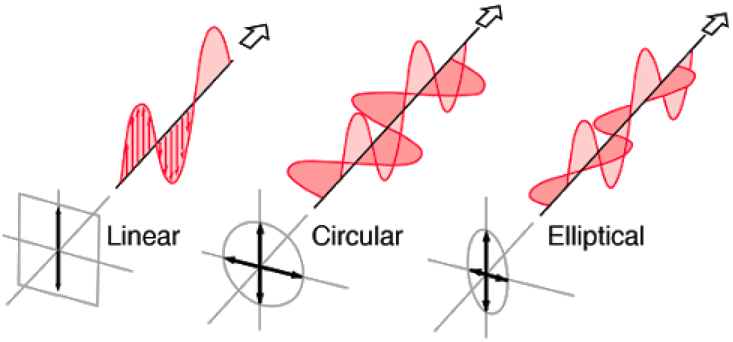

Figure 4.4: Diagram of linear, circular and elliptical polarisation from: `http://hyperphysics.phy-astr.gsu.edu/hbase/phyopt/polclas.html`.

Stokes I parameters. The Stokes V parameter is the difference between the right and left polarisation states ($V = R - L$). The Stokes I parameter (or intensity) is the sum of these states ($I = L + R$). The observed fraction of circular polarisation (CP) is given as the ratio of these parameters: $CP = V/I$.

In a magnetised plasma, the circular polarisation can be affected by what is known as Faraday rotation. The Faraday effect is when the plane of the polarised radiation is rotated as it propagates in a direction parallel to the magnetic field. The degree of rotation is determined by the magnitude of the field strength and the rotation is caused by the left and right circular polarised radiation propagating at different velocities to each other. In solar and stellar flares, where the magnetic field is non-zero, Faraday rotation affects the polarisation state. As the radiation propagates through the corona, most of the linear or elliptically polarised light is depolarised due to the Faraday effect. This leads to circular polarisation being the dominant polarisation state detectable in these active environments [Huang et al., 2018], except when the propagation direction is almost perpendicular to the magnetic field [Dulk, 1985].

For propagating waves in magnetised plasmas there are different modes to describe their motion perpendicular or parallel to the magnetic field. The wave modes that describe propagation perpendicular to the magnetic field are called the ordinary (O) and extraordinary (X) modes. Circular polarisation is often described in terms of these O and X modes, where the O and X mode are designated based on the sense of circular polarisation, e.g. left handed circular polarisation corresponds to the X-mode when the source's magnetic field is directed away from the observer. The O-mode has a dispersion relation equal to that in an unmagnetised plasma, while the X-mode has a more complex dispersion relation dependent on an upper hybrid frequency (see Aschwanden [2006]). The degree of circular polarisation can be determined by the relative intensities in the O and X-mode: $\mathrm{CP} = (\mathrm{I_X} - \mathrm{I_O})/(\mathrm{I_X} + \mathrm{I_O})$ [Huang et al., 2018].

For gyrosynchrotron emission, the circular polarisation is in the O-mode and X-mode in the optically thick and thin regions respectively [Huang et al., 2018]. Gyrosynchrotron emission can be large in this optically thin limit, as the X-mode has a larger emissivity [Dulk, 1985]. In general, the degree of polarisation can inform us about the magnetic field strength and direction. For small magnetic field viewing angles (i.e. directed along the field) the degree of polarisation is large. Various incoherent emission processes, and how the polarisation detectable from each of these varies, are discussed next.

4.4 Incoherent emission processes

Incoherent emission concerns any emission process where the electrons emit individually and do not act collectively. The emission produced in this way can be either thermal or non-thermal in nature depending on the electron distribution. The three main types of non-thermal emission are generated from the acceleration of electrons along magnetic field lines, the so called gyromagnetic emission (see Figure 4.1). Bremsstrahlung emission is not produced in this way, however it can still be both thermal or non-thermal in nature. However, only the thermal description of Bremsstrahlung emission is discussed here. Thermal Bremsstrahlung is applicable at radio wavelengths, whereas non-thermal is of more significance in X-ray and gamma ray emission from flares.

4.4.1 Bremsstrahlung

Bremsstrahlung emission is produced from electrons that are accelerated (decelerated) within a Coulomb field. As fast moving electrons move through a region containing ions, the electrons are deflected from the ions via the Coulomb force [Aschwanden, 2006]. This deflection results in the acceleration of particles leading to the emission of bremsstrahlung radiation. The angle of the deviation depends on the velocity of the electron and a quantity known as the impact parameter. This impact parameter, b, is a measure of the distance between the ion and electron. The maximum value of this impact parameter is determined by the Debye length, λ_D:

$$\lambda_D = \left(\frac{k_B T}{4\pi n_e e^2}\right)^{0.5} \approx \frac{v_{th}}{\omega_p} \approx b_{max} \tag{4.14}$$

where v_{th} and ω_p are the thermal velocity and plasma frequency respectively. n_e is the electron number density and e is the electron charge. The minimum value of the impact parameter depends on the energy of the electron. Assuming a Maxwellian distribution, the emissivity and absorption coefficients for thermal bremsstrahlung emission are given by the following:

$$j_\nu = \frac{\pi^2 Z^2 e^6 n_e n_i}{4c^3 m_e^2}\left(\frac{2m_e}{\pi k_B T}\right)^{0.5} \ln\left(\frac{b_{max}}{b_{min}}\right) \tag{4.15a}$$

$$\kappa_\nu = \frac{1}{\nu^2 T^{3/2}}\left[\frac{Z^2 e^6}{c} n_e n_i \frac{1}{\sqrt{2\pi (m_e k_B)^3}}\right]\frac{\pi^2}{4}\ln\left(\frac{b_{max}}{b_{min}}\right) \tag{4.15b}$$

where n_i is the ion number density and m_e is the electron rest mass. The absorption coefficient is also sometimes calculated by using a Gaunt factor which is proportional to the logarithm of the ratio of b_{min} and b_{max} and differs depending on the energy of the electrons. For example (from Güdel [2002]):

$$\kappa_\nu \approx 0.01 n_e^2 T^{-3/2} \nu^{-2} \times \begin{cases} \ln(5 \times 10^7 T^{3/2}/\nu) & \text{for T} < 3.2 \times 10^5\text{K}, \\ \ln(4.7 \times 10^{10} T/\nu) & \text{for T} > 3.2 \times 10^5\text{K}. \end{cases} \tag{4.16}$$

In the optically thick limit, the polarisation of bremsstrahlung emission is zero. The optically thick flux is $\propto \nu^{-2}$. In the optically thin limit, the polarisation is predominately in the X-mode (Dulk [1985], Güdel [2002]). This X-mode circular polarisation degree is given by:

$$r_c \approx 2cos\theta(\nu_g/\nu) \tag{4.17}$$

where θ is the viewing angle (angle between the magnetic field and line of sight) and ν_g is the electron gyrofrequency. Bremsstrahlung emission is also called free-free emission or braking radiation. It is commonly observed in radio emission from the Sun, both in quiet and active regions [Aschwanden, 2006].

4.4.2 Gyromagnetic emission

Gyromagnetic, also known as magnetobremsstrahlung, radiation is an incoherent emission mechanism. It involves the acceleration of energetic particles around field lines. If the field strength or temperature (velocity) is low enough (or the density is high enough), free-free emission will dominate over gyromagnetic emission. Whereas bremsstrahlung emission is driven by the Coulomb force, gyromagnetic emission is driven by the

Lorentz force. Emission can be produced from both thermal and non-thermal electrons and both cases are discussed here. There are three types of gyromagnetic emission to be discussed: cyclotron (or gyroresonance), gyrosynchrotron and synchrotron. The key difference separating these emissions is the speed of the electrons involved. Electrons in a magnetic field experience the Lorentz force, given by:

$$\mathbf{F} = \frac{e}{c}(\mathbf{E} + \mathbf{v} \times \mathbf{B}) \tag{4.18}$$

where **E**, **v** and **B** are the electric field strength, electron velocity and magnetic field strength respectively. As we are dealing with electrons in a magnetised plasma, the electric field can be ignored when looking at gyromagnetic emission (except for when dealing with current sheets). The electrons experiencing the Lorentz force are accelerated in a direction perpendicular to both the velocity vector and magnetic field.

4.4.2.1 Cyclotron

Cyclotron emission (also known as gyroresonance emission) occurs when these electrons move at non-relativistic velocities, i.e. where the Lorentz factor, $\gamma = (1-(\mathrm{v/c})^2)^{-0.5}$, is ≈ 1. The electrons gyrate around the field lines at a fixed frequency that is only dependent on the magnetic field strength. This is known as the electron gyrofrequency and is given by:

$$\nu_g = \frac{eB}{2\pi m_e c} \approx 2.8\,\mathrm{B}\ [\mathrm{MHz}] \tag{4.19}$$

where B is given in Gauss. The electron gyrofrequency should not be confused with the plasma frequency, ν_p, as both are frequently used in equations for gyromagnetic emission:

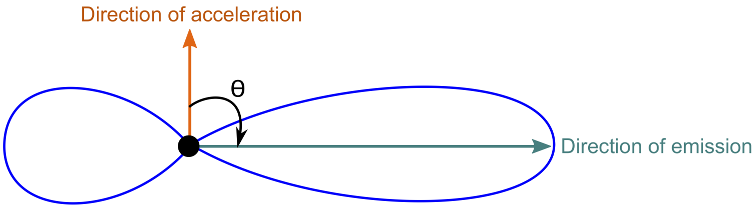

Figure 4.5: Emission pattern produced from a relativistic charged particle. The dipole emission of the non-relativistic case is shown in Figure 4.3.

$$\nu_p = \left(\frac{n_e e^2}{\pi m_e} \right)^{0.5} \tag{4.20}$$

where n_e is the number density of electrons. The non-relativistic electrons radiate power sinusoidally as they gyrate (see Figure 4.3). This emission is typically seen as spectral lines, rather than continuum emission since the radiation is emitted with frequency ν_g. As the velocity increases (up to $\gamma \approx 2$), this dipolar shape changes, see Figure 4.5, becoming asymmetric and peaking more strongly.

This is a relativistic effect, giving rise to harmonics of the gyroresonance emission lines. The radiated power (gyromagnetic emission) peaks more strongly at a harmonic frequency $\nu = s\nu_g$, where s denotes the harmonic number ($s = 0,\ 1,\ 2...$). Cyclotron harmonics are limited to s $<$ 10 due to the non-relativistic speeds and lower electron energies.

To calculate the emission radiated by electrons requires integrating over a velocity distribution. At relativistic velocities, a power law distribution in energy is often assumed. Analytical expressions for these are given where possible, however exact solutions to the emissivity and absorption equations are time consuming for certain types of radiation (e.g. gyrosynchrotron). For cyclotron emission in particular, a thermal electron distribution is typically assumed. As the average electron energy is low, there are many collisions and a Maxwellian distribution is most appropriate. The following equations for the absorption and emissivity coefficients are given for a distribution of thermal electrons [Dulk, 1985]:

$$\kappa_\nu(s,\theta) = \frac{\pi^2}{4c}\frac{1}{n_\sigma\frac{\partial}{\partial\omega}(\omega n_\sigma)}\frac{\nu_p^2}{\nu}\frac{s^2}{s!}\left(\frac{s^2\beta_o^2\sin^2\theta}{2}\right)^{s-1}\frac{1}{\beta_o|\cos\theta|}\exp\left[-\frac{(1-s\nu_g/\nu)^2}{2n_\sigma^2\beta_o^2\cos^2\theta}\right](1-\sigma|\cos\theta|)^2 \tag{4.21}$$

$$j_\nu(s,\theta) = n_\sigma^2\frac{k_B T\nu^2}{c^2}\frac{\partial}{\partial\omega}(\omega n_\sigma)\kappa_\nu(s,\theta) \tag{4.22}$$

where n_σ is the index of refraction, $\beta_o = k_B T/mc^2$ and σ indicates the polarisation mode (+1 for O-mode, -1 for X-mode which dominates). These equations, taking $\theta = \pi/3$, can be approximated as [Güdel, 2002]:

$$\kappa_\nu(s) \;=\; 1020(1 \pm 0.5)^2\frac{n_e}{\nu T^{1/2}}\frac{s^2}{s!}\left(\frac{s^2 T}{1.6\times10^{10}}\right)^{s-1}\exp\left[-\frac{(1-s\nu_g/\nu)^2}{8.4\times10^{-11}T}\right] \tag{4.23}$$

$$j_\nu(s) = \frac{k_B T\nu^2}{c^2}\kappa_\nu(s) \tag{4.24}$$

4.4.2.2 Gyrosynchrotron

For the mildly relativistic case the harmonics s = 10 – 100 are produced. The increased velocities and electron energies lead to stronger peaks in emission and these higher harmonics. The Lorentz factor is $2 < \gamma < 3$ and the electrons produce gyrosynchrotron radiation. This emission is the most appropriate to study here as it is produced ubiquitously in flaring coronal regions of active stars. Due to Doppler broadening, it is observed as continuum emission. However, it is also the hardest type of gyromagnetic emission to derive the absorption and emissivity coefficients for. The distribution of electrons is also important to consider. Due to the mildly relativistic speeds, the electrons are often and best described by a power law distribution in energy with an isotropic pitch angle distribution. A general form of this power law is given by:

$$n(E) = (\delta - 1)E_o^{\delta-1} N E^{-\delta} [\mathrm{cm}^{-3}\,\mathrm{erg}^{-1}] \tag{4.25}$$

where N is the total electron number density ($\mathrm{N} = \int_{E_o}^{\infty} n(E)d(E)$), δ is the power law index and E_o is the lower energy cut off, generally taken to be 10 keV in solar flares [Aschwanden et al., 2019]. The exact and approximate equations for gyrosynchrotron emission are explored more in Section 4.5. In the mean time, empirical expressions for non-thermal electrons based on numerical calculations done by Dulk [1985] are:

$$\begin{aligned}
\kappa_\nu &\approx \frac{N}{B} 1.4 \times 10^{-9} 10^{-0.22\delta} (\sin\theta)^{-0.09+0.72\delta} \left(\frac{\nu}{\nu_g}\right)^{-1.30-0.98\delta} && \text{(4.26a)}\\
j_\nu &\approx 3.3 \times 10^{-24} 10^{-0.52\delta} NB (\sin\theta)^{-0.43+0.65\delta} \left(\frac{\nu}{\nu_g}\right)^{1.22-0.90\delta} && \text{(4.26b)}\\
T_{\mathrm{eff}} &\approx 2.2 \times 10^{9} 10^{-0.31\delta} (\sin\theta)^{-0.36-0.06\delta} \left(\frac{\nu}{\nu_g}\right)^{0.5+0.085\delta} && \text{(4.26c)}\\
r_c &\approx 1.26 \times 10^{0.035\delta} 10^{-0.071\cos\theta} \left(\frac{\nu}{\nu_g}\right)^{-0.782+0.545\cos\theta} && \text{(4.26d)}\\
\nu_{peak} &\approx 2.72 \times 10^{3} 10^{0.27\delta} (\sin\theta)^{0.41+0.03\delta} (NL)^{0.32-0.03\delta} B^{0.68+0.03\delta} && \text{(4.26e)}
\end{aligned}$$

where θ is the angle between the line of sight and the magnetic field. These expressions, from Dulk [1985] are valid for: $2 < \delta < 7$, $\theta > 20^\circ$ and $10 < \nu/\nu_g < 100$. Figure 4.6 shows the spectra for these quantities obtained numerically for the X-mode from a power law distribution. It is clear that the absorption (plot b) and emissivity (plot a) decrease for: increasing frequency, decreased viewing angle and increased power law index. The effective temperature (plot c) increases for: increasing frequency, increased viewing angles and decreased power law index. The degree of circular polarisation (plot d) decreases for: increasing frequency, increasing viewing angle

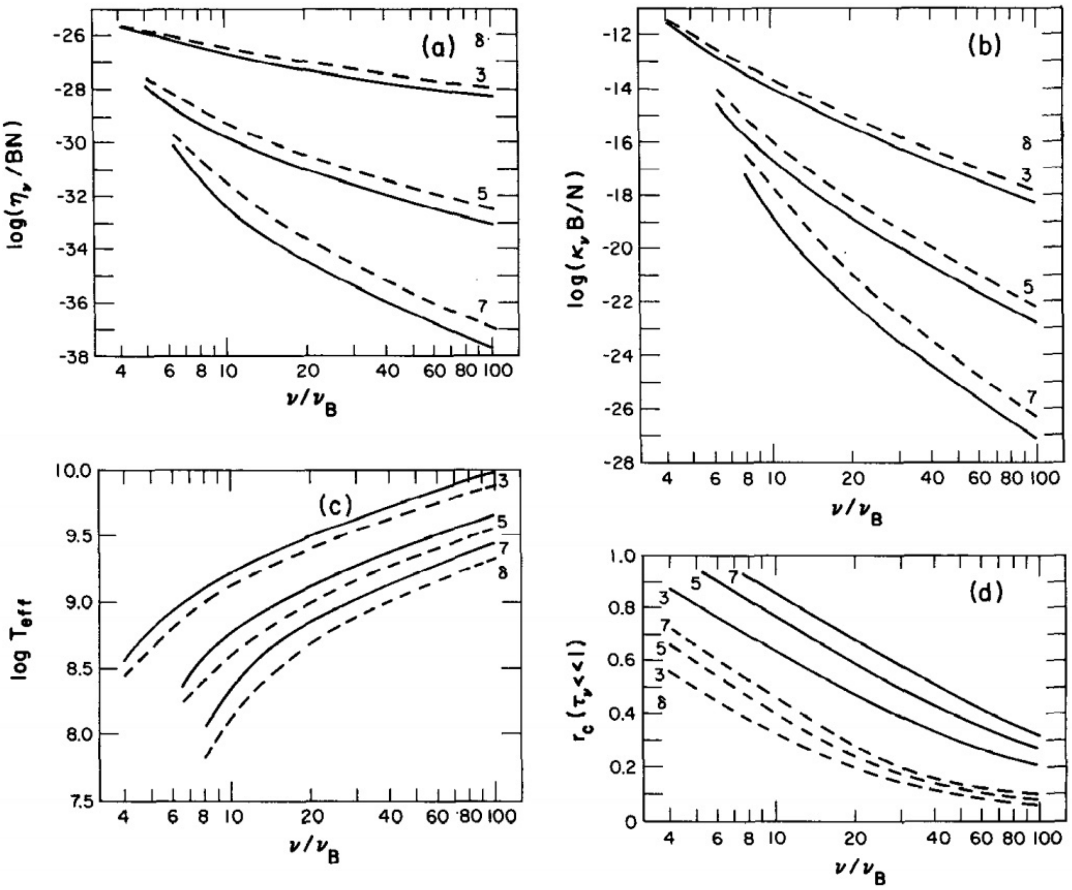

Figure 4.6: Spectra showing results for the emissivity coefficient, absorption coefficient, effective temperature and degree of circular polarisation respectively (a-d respectively) for power law electrons from Dulk [1985]. The solid and dashed lines correspond to $\theta = 40°$ and $80°$ respectively. The different solid lines represent the spectra for varied power law index (specified on the line). ν_B in this case is equivalent to ν_g in Equation 4.19.

and decreasing power law index. These equations can be simplified (with $\theta = \pi/3$) as (from Güdel [2002]):

$$\kappa_\nu \approx 10^{-0.47+6.06\delta} N B^{0.3+0.98\delta} \nu^{-1.3-0.98\delta} \tag{4.27a}$$

$$j_\nu \approx 10^{-31.32+5.24\delta} N B^{-0.22+0.9\delta} \nu^{1.22-0.9\delta} \tag{4.27b}$$

$$r_c \approx 10^{3.35+0.035\delta} (\nu/B)^{-0.51} \tag{4.27c}$$

$$\nu_{peak} \approx 10^{3.41+0.27\delta} (NL)^{0.32-0.03\delta} B^{0.68+0.03\delta} \tag{4.27d}$$

Estimates for values of the peak frequency from a gyrosynchrotron spectra can be taken from Equation 4.27d. Some examples of these are shown in Table 4.1. The total electron number density, N, as discussed for stellar flares can lie around 10^{11} cm^{-3} but has been quoted around 10^9 cm^{-3} for solar flares [Shibata and Magara, 2011]. The magnetic length scale, as discussed in Chapter 3, Section 3.3.2 on loop lengths, can be as large as several times the stellar radii. The surface field strengths are of the order of several kG but at the site of reconnection these field strengths are much smaller. These estimates for peak frequency are typically tens of GHz, as expected for flares that produce GS emission [Waterfall et al., 2019]. These approximate equations will be revisited later on in Chapter 5 when the modelled peak frequency will be compared with the estimates.

Table 4.1: Estimated peak frequencies of flaring emission, calculated from Equation 4.27d.

N / cm^{-3}	L / cm	B / G	ν_{peak} / GHz
10^9	10^9	10	13.5
10^9	10^9	100	7.9
10^9	10^{11}	10	3.9
10^9	10^{11}	100	22.9
10^{11}	10^{11}	10	11.2
10^{11}	10^{11}	100	66.1

The gyrosynchrotron radiation from thermal electrons, as well as power-law electrons, should also be considered. Analytical expressions have been derived previously for gyrosynchrotron emission from thermal electrons by Petrosian [1981] but the more simplified expressions from Dulk [1985] are given here:

$$\kappa_\nu \approx \frac{N}{B} 50 T^7 \sin^6\theta B^{10} \nu^{-10} \tag{4.28}$$

$$j_\nu \approx 1.2 \times 10^{-24} NBT \left(\frac{\nu}{\nu_g}\right)^2 \kappa_\nu \tag{4.29}$$

When looking at spectra, the spectral power is $\propto \nu^2$ in the optically thick region, with $\propto \nu^{-8}$ in the optically thin region. This is seen in the spectral slope of Figure 4.7. When modelling gyrosynchrotron radiation a common effect that must be taken into account is the Razin effect. The Razin effect is the suppression of gyrosynchrotron emission in a dense magnetised plasma [Kuznetsov et al., 2011]. In this case, free-free emission will likely dominate. The Razin effect can also suppress the absorption coefficient in addition to the emissivity [Ramaty, 1969]. The Razin effect is caused by the presence of a dense thermal plasma. This thermal plasma can lead to the refractive index of the emitting region being less than one, and subsequently the phase velocity of the electromagnetic radiation being greater than the speed of light [Dulk, 1985]. This leads to the GS emission being suppressed and is prevalent at low frequencies, according to the following condition [Simon, 1969]:

$$\nu_{\mathrm{R}} \approx \frac{20 n_e}{B} \tag{4.30}$$

For example, for an electron density of $10^{10}\,\mathrm{cm}^{-3}$ and field strength 100 G, the Razin cut-off frequency is approximately 2 GHz. Low frequency emission is also affected by free-free absorption (by ambient electrons), reabsorption of gyrosynchrotron emission (by the GS emitting electrons), as well as the Razin effect [Ramaty, 1969].

4.4.2.3 Synchrotron

For ultra relativistic speeds ($\gamma >> 1$) the electrons emit synchrotron radiation (at harmonics s$\gg$100). As the electron velocities are so high, collisions are rare. These electrons are therefore best described by a power law distribution where there are larger numbers of higher energy particles. Again, the emission is broad and generates continuum spectra. The absorption and emissivity coefficients for a power law distribution of electrons are given by [Dulk, 1985]:

$$\kappa_\nu = \frac{N}{B}(\delta-1)E_o^{\delta-1}h(\delta)\frac{2\pi e m^5 c^{10}}{9}\frac{1}{\sin\theta}\left[\frac{m^2c^4}{3\sin\theta}\frac{\nu}{\nu_g}\right]^{-(\delta+4)/2} \tag{4.31a}$$

$$j_\nu = \frac{NB}{2}(\delta-1)E_o^{\delta-1}g(\delta)\frac{\sqrt{3}e^3}{8\pi mc^2}\sin\theta\left[\frac{2m^2c^4}{3\sin\theta}\frac{\nu}{\nu_g}\right]^{-(\delta-1)/2} \tag{4.31b}$$

where $h(\delta)$ and $g(\delta)$ involve products of gamma functions and all other parameters are as before. For the optically thick case, the spectral index is equal to 2.5 at low frequencies. Synchrotron emission is often seen in extreme astrophysical sources, e.g. neutron stars and black holes [Ipser and Price, 1982].

A schematic of spectra generated for the thermal free-free, thermal gyrosynchrotron, non-thermal gyrosynchrotron and synchrotron emission is shown in Figure 4.7. The power law index on the latter two emission spectra are varied between $\delta = 3$ and $\delta = 6$. A smaller power law index leads to the non-thermal spectral tail being 'picked up' from the larger number of higher energy electrons present. This power law index is an important parameter when modelling the gyrosynchrotron emission from stellar flares and is explored when simulating a T-Tauri flare in Chapter 5 and Chapter 6.

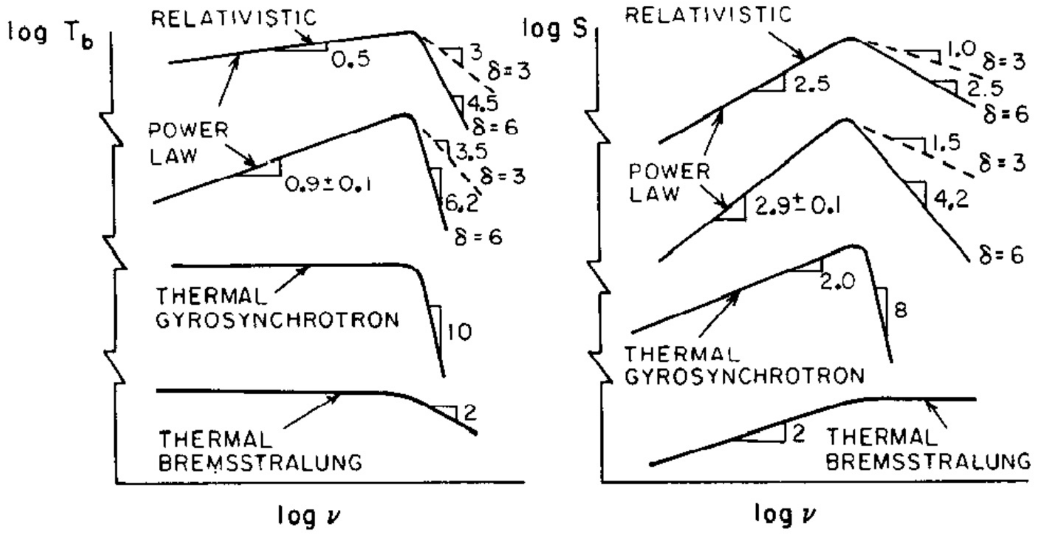

Figure 4.7: Spectra from Dulk [1985] of brightness temperature (left) and flux density (right) for all the incoherent radio emission processes discussed: synchrotron (labeled as relativistic), gyrosynchrotron (labeled as power law), thermal gyrosynchrotron and thermal bremsstrahlung.

4.5 Calculations of gyrosynchrotron radiation

4.5.1 Exact equations

The exact equations for the gyrosynchrotron emissivity and absorption coefficients have long been known [Ramaty, 1969] and are given below for an eigenmode σ [Fleishman and Kuznetsov, 2010]:

$$j_\nu^\sigma = \frac{2\pi e^2}{c^2}\frac{n_\sigma \nu^2}{1+T_\sigma^2} \times \sum_{s=-\infty}^{\infty}\left[\frac{T_\sigma(\cos\theta - n_\sigma\beta\mu)+L_\sigma\sin\theta}{n_\sigma\sin\theta}J_s(\lambda)+J_s'(\lambda)\beta\sqrt{1-\mu^2}\right]^2$$
$$\times F(\mathbf{p})\delta\left[\nu(1-n_\sigma\beta\mu\cos\theta)-\frac{s\nu_g}{\gamma}\right]\mathrm{d}^3\mathbf{p} \quad (4.32)$$

$$\kappa^{\sigma} = -\frac{2\pi e^2}{n_\sigma(1+T_\sigma^2)} \times \sum_{s=-\infty}^{\infty} \left[\frac{T_\sigma(\cos\theta - n_\sigma\beta\mu)L_\sigma\sin\theta}{n_\sigma\sin\theta} J_s(\lambda) + J_s'(\lambda)\beta\sqrt{1-\mu^2}\right]^2$$
$$\frac{1}{\beta}\left[\frac{\partial F(\mathbf{p})}{\partial p} + \frac{n_\sigma\beta\cos\theta - \mu}{p}\frac{\partial F(\mathbf{p})}{\partial\mu}\right] \delta\left[\nu(1 - n_\sigma\beta\mu\cos\theta) - \frac{s\nu_g}{\gamma}\right] \mathrm{d}^3\mathbf{p} \quad (4.33)$$

where p is the electron momentum and $\beta = \mathrm{v/c}$. n_σ is the refractive index and T_σ and L_σ are the transverse and longitudinal components of the polarisation vector respectively. $\mu = \cos\psi$ where ψ is the electron pitch angle and γ is the Lorentz factor. The Bessel function and its derivative are given by $J_s(\lambda)$ and $J_s'(\lambda)$ respectively. The electron distribution function $F(\mathbf{p})$ is normalised as [Fleishman and Kuznetsov, 2010]:

$$\int F(\mathbf{p})d^3\mathbf{p} = 2\pi \int_{p_1}^{p_2} p^2 dp \int_{-1}^{1} F(p,\mu)d\mu = n_e \quad (4.34)$$

The summations involved in these exact equations from Ramaty [1969] become extremely time consuming as higher order harmonics (i.e. gyrosynchrotron, s>10) are included. As a result, several approximations and simplifications have been developed over the years. The most frequently used of these approximations, and their benefits and drawbacks, are now discussed.

4.5.2 Approximations to the exact equations

Dulk and Marsh [1982] developed an approximation for the gyrosynchrotron emissivity and absorption for an isotropic power-law distribution of electrons in solar and stellar flares. The empirical formulae derived from these approximations are given in Dulk [1985] and are seen in Equations 4.26a – 4.26e. These approximations have been widely used and are accurate to within 30% for the harmonics s = 20 – 100 and viewing angle $\theta = 30 - 80^\circ$. One of the main drawbacks of these approximations is the exclusion of any thermal plasma effects. As there is a large degree of heating involved with flares (see Chapter 3), and associated free-free emission, a more accurate approximation including these thermal effects is necessary for modelling the gyrosynchrotron emission from flares.

Another frequently used approximation is known as the Petrosian-Klein (PK) approximation. This approximation combines the work of Petrosian [1981] and Klein [1987] to give a fast approximation that satisfies a wider range of parameters. The work published initially by Petrosian [1981] delivered a faster numerical approximation for the coefficients for an isotropic power law distribution. However they again ignored the thermal contribution from the surrounding plasma through which the gyrosynchrotron emission radiates. Furthering this work, Klein [1987] incorporated the effect of the surrounding plasma (both when tenuous and dense). This allowed for the inclusion of effects like the Razin effect where the lower harmonics of gyromagnetic radiation are suppressed. These two methods were combined into the PK approximation which generates accurate emission intensities. It holds for harmonics above s = 3 – 4 and for a wide range of viewing angles. When the gyrosynchrotron emission is calculated in vacuo, it holds for smaller values of θ. There are several key assumptions of the PK model that aim to simplify the time consuming solving of the exact equations. The first simplification is replacing the summations from Ramaty [1969] and Equations 4.32 and 4.33 with an integral (Klein [1987], Fleishman and Kuznetsov [2010]):

$$\sum_{s=-\infty}^{\infty} U(s) \simeq \int_{\infty}^{\infty} U(s) ds \tag{4.35}$$

This integral can then be solved analytically using the Dirac delta function. The next approximation involves the Bessel function. The Carlini approximation for the Bessel function of the first order, $J(s)$, and its derivative, $J'(s)$, was initially used in calculating the gyrosynchrotron emission from flares [Melrose, 1980]. However the approximation given by Wild and Hill [1971] holds for a wider range of situations involving mildly relativistic electrons. These approximations are:

$$J_s(sx) \approx \frac{1}{\sqrt{2\pi s}} \frac{Z^s(x)}{a(s,x)} \tag{4.36a}$$

$$J'_s(sx) \approx \frac{b(s,x)}{\sqrt{2\pi s}} \frac{Z^s(x)}{x} \tag{4.36b}$$

where (with all symbols as previously defined),

$$Z(x) = \frac{x\exp(\sqrt{1-x^2}}{1+\sqrt{1-x^2}} \tag{4.37a}$$

$$a(s,x) = \left[(1-x^2)^{3/2} + \frac{A}{s}\right]^{1/6} \tag{4.37b}$$

$$b(s,x) = \left[(1-x^2)^{3/2} + \frac{B}{s}\right]^{1/6} \tag{4.37c}$$

$$A = 0.503, B = 1.193 \tag{4.37d}$$

$$x = \frac{\lambda}{s} = \frac{n_\sigma \beta \sin\theta \sqrt{1-\mu^2}}{1 - n\beta\mu\cos\theta} \tag{4.37e}$$

A third simplification concerns the integral over pitch angle, $\mu = \cos\psi$. The pitch angle ψ is the angle between the magnetic field and velocity vectors. This integral is calculated using Laplace's method of approximate asymptotic integration. This method uses a best-fit Gaussian function in place of the original integral. If the Gaussian peak and width is known this Gaussian function is then evaluated analytically. Finding the best-fit Gaussian relies on knowing the peak and width, which is simplified in this approximation by using a simple analytical solution.

Again, this model has large limitations for work in flares. It is designed primarily for isotropic distributions of electrons, like the work by Dulk and Marsh [1982]. While an isotropic distribution of electrons is a reasonable assumption (and is what is used later on in the models of Chapter 5 and Chapter 6), there is evidence of anisotropic electron distributions being common in solar flares (Fleishman and Melnikov [2003], Kuznetsov et al. [2011]). Additionally, this approximation is inaccurate at low frequencies and for polarisation calculations. Due to the known inaccuracies at low frequencies, a final simplification made in the PK approximation is to ignore the longitudinal components, L_σ, of the polarisation vectors. This simplification is suitable for when the gyrosynchrotron emission is calculated at high frequencies only, when in vacuo or when only an isotropic distribution is considered.

4.5.2.1 Fast gyrosynchrotron codes

The last approximation to be discussed builds on the PK approximation to produce fast and accurate codes for calculating GS emission from a wide range of flaring scenarios. These codes, outlined and developed by Fleishman and Kuznetsov [2010], are considered a modern development of the PK approximation, utilising some of the simplifications discussed earlier as well as adjusting others to allow for modelling anisotropic pitch angle distributions. Further benefits of the Fleishman and Kuznetsov [2010] approximation is an improved accuracy for an isotropic distribution over the PK approximation (while maintaining a similar computational speed) and an overall faster computation of the gyrosynchrotron emission, two to three orders of magnitude faster than using the exact equations. The equations are derived using the same assumptions from the PK approximation where the summation is replaced with an integral (Equation 4.35) and the Bessel functions are approximate as Equation 4.36. The longitudinal components of the polarisation vectors are this time included however, to not limit the validity of the gyrosynchrotron emission calculated at low frequencies. Additionally, the peak position from the Gaussian function used to replace the pitch angle integral is calculated differently. In the PK approximation, the peak value is calculated via a simplified analytical solution to a transcendental equation that describes the Gaussian peak, μ_0. This is adequate for an isotropic distribution, and after comparing with Gaussian fits for anisotropic distributions, Fleishman and Kuznetsov [2010] proved this Laplace method to be a reasonable approximation for those distributions too. To improve the accuracy at low frequencies, the first approximation was removed at low harmonics. That is to say, instead of an integral being used in the small (less time consuming) harmonic number, the original summation was used. Fleishman and Kuznetsov [2010] explored the merits of different versions of a final model, combining one, some or all of the discussed approximations. For example, they refer to one model as 'hybrid' which incorporates the approximations of the Bessel functions and Laplace integration method but no integral over harmonics (instead using the original method of summation). They discuss the relative merits of each of these models, which boil down to either increased speed or increased accuracy. The model with all the above approximations included is known as the 'continuous' model and reports the fastest computation speeds. This set of codes allow for the fast computation of gyrosynchrotron emission from a 3D model (from solar flares) over a range of pitch angle distributions.

This work forms the basis for two simulators that calculate the gyrosynchrotron emission from a flaring plasma: the GS simulator [Kuznetsov et al., 2011] and the GX simulator [Nita et al., 2015]. These simulators aim to ease the 3D modelling of this emission, allowing for anisotropic distributions (if needed) as well as a non-uniform spatial distribution of electrons.

4.5.3 Modelling of gyrosynchrotron emission

More recently, there has been an increase in the number of models that explore the generation of gyrosynchrotron emission from solar flares with both isotropic and anisotropic electron distributions. For example, Simões and Costa [2006] developed a model for the gyrosynchrotron emission from solar flares, based on the exact equations and work by Ramaty [1969] and Ramaty et al. [1994]. They initially modelled this emission with an isotropic distribution of electrons but argue that anisotropic distributions must be taken into consideration to incorporate established effects such as magnetic mirroring and the trapping of particles according to the loss cone. Indeed, Fleishman and Melnikov [2003] suggested that these anisotropic distributions could lead to vast differences in the calculated polarisation and intensity of the gyrosynchrotron emission. This led to further modelling by Simoes and Costa [2010] where the gyrosynchrotron emission from an anisotropic pitch angle distribution in solar flares was calculated.

Osborne and Simões [2019] have recently developed a 3D model to calculate the GS emission within a spatially varying atmosphere. The model (known as 'Thyr') is applied to solar flares, where they have improved on the resolution in the lower coronal regions from previous models. Indeed, many of the models discussed so far are focused primarily on emission generated away from the chromosphere. This is due to the dense chromospheric plasma being optically thick to non-thermal radio emission and so holding less interest for gyrosynchrotron models. However, the heating of material near the chromosphere can lead to large amounts of free-free emission which needs to be taken into account when calculating the total (GS plus free-free) radiation produced, which this model allows for.

These 3D models developed by Simões and Costa [2006] and Osborne and Simões [2019] are useful tools but lack the ability to consider a range of flaring scenarios. For example, they only consider an isotropic pitch angle distribution, or have overly long computation times. The fast gyrosynchrotron codes produced by Fleishman and Kuznetsov [2010] remain the most useful tool for modelling the gyrosynchrotron and thermal emission for young stellar flares, where the parameters can vary greatly compared to in solar flare models. The fast GS codes have been employed in two simulator tools, the GS and GX simulator which are now discussed.

4.5.3.1 GS simulator

The GS simulator [Kuznetsov et al., 2011] was designed to model the microwave from a 3D dipole magnetic loop. The loop is thickest at its apex, becoming narrower at the footpoints. The loop is populated with a thermal plasma with a constant density and temperature. The non-thermal electron density included can either be constant or vary along the loop according to:

$$n_e \propto \exp[-\varepsilon^2(\varphi - \pi/2)^2] \tag{4.38}$$

ε defines the distribution along the loop, with $\varepsilon = 0$ for the constant case. A higher ε value leads to more confinement of energetic electrons around the loop's apex, characteristic of an injection site from magnetic reconnection. φ defines the magnetic latitude (the angular distance north or south of the magnetic equator). As the magnetic latitude increases, the electrons have a more concentrated distribution around the loop top. The non-thermal electrons have a distribution function equal to:

$$F(E, \mu) = u(E)g(\mu) \tag{4.39}$$

where $u(E)$ denotes the distribution over energy, E, and $g(\mu)$ describes the pitch angle distribution over $\mu = \cos(\psi)$ where ψ is the pitch angle (as before). The available pitch angle distributions in this simulator are for the isotropic ($g(\mu) = 1$) and anisotropic (defined by a loss cone) cases. Due to the loss cone and magnetic mirroring effect, the anisotropy of the electrons is most noticeable around the converging field lines at the footpoints.

The energy distributions available include (but are not limited to): thermal, power law, thermal/non-thermal (TNT), etc. A power law distribution is commonly used for non-thermal particles, similar to that described in Equation 4.25 for some predefined range in energy. This simulator uses the ‘strong coupling’ model, where both the left and right handed polarisation vectors propagate independently of each other [Kuznetsov et al., 2011]. The symmetric dipole loop can be viewed from any angle and the GS simulator then computes the emission (gyrosynchrotron plus free-free) along this line of sight. The simulator uses the fast gyrosynchrotron codes by Fleishman and Kuznetsov [2010] described earlier, allowing for the fast computation of emission. While the distribution can be set as isotropic, the anisotropy of electrons was initially investigated using this model. It was found that even when using non-extreme values for some of the parameters there was still a difference in emission compared to the isotropic case. The outputs of this simulator are spectra and images of the microwave emission.

4.5.3.2 GX simulator

An extension of this GS simulator is the GX simulator, developed by Nita et al. [2015] and again used for 3D modelling of flares. This simulator provides the same calculation of the gyrosynchrotron (as well as X-ray) emission as the GS simulator but increases the ease of this 3D modelling. The GX simulator offers the ability to easily change the parameters involved as well as being able to choose different magnetic field configurations other than a simple dipole loop. Additionally, the GX simulator can calculate the intensity for many lines of sight. The general process involved with using the GX simulator to calculate the microwave emission from a flaring flux tube is now outlined.

Step one: The magnetic field

A 3D magnetic field model is imported into the simulator. This can be done by either importing a 3D Cartesian configuration directly or from importing a photospheric magnetic field map. A magnetic field configuration can then be extrapolated from the map for use in the simulator. The Cartesian coordinate system (x, y, z) is defined with the z axis extending outwards from the stellar surface with x and y lying on the surface in a West and North direction respectively. Once the magnetic field structure has been imported it is contained within a data cube along with a background plasma.

Step two: The background plasma

The ambient, coronal plasma is defined as hydrostatic with a uniform base pressure. The base temperature, T_0 within the corona is constant and can be altered manually. A coronal base thermal density, n_0 can also be chosen. This background density is set to scale with height within the corona according to:

$$n(z) = n_0 \exp\left[-\frac{h/R}{6.7576 \times 10^{-8} T_0}\right] \tag{4.40}$$

where $n(z)$ is the coronal thermal density, h is the height above the surface relative to the stellar radius, R, and $z = h/R$. As this simulator is designed for modelling solar flares, the radius is automatically set as being equal to the solar radius. The thermal distributions available for this plasma are: free-free only, thermal and a kappa distribution. A kappa distribution combines a thermal and non-thermal distribution with a smooth transition between them at low energies and is often used to describe astrophysical plasmas. The default emission mechanism in the corona is set as free-free but can be changed within the simulator.

Step three: The flux tube

Next, a flux tube is constructed from one of the field lines imported in step one. The flux tube consists of several field lines, centred around the chosen one. The spacing of these flux tube field lines can be altered manually and the arrangement of them around the central line can either be circular or elliptical. The ellipse semi axes are given by the parameters a and b.

The creation of this flux tube also creates a modifiable 'cross-section' (which is either circular or elliptical). The location of this cross-section is initially at the distance along the field line $s_l = 0$ where the magnetic field is a minimum (not to be confused with the total length of the central field line, l, or the harmonic number from before). In a simple dipole loop this would be at the loop's apex. This cross-section can be moved along the loop to any position between the footpoints. As this cross-section is moved closer to the footpoints, the convergence of the field lines leads to an altered appearance of the flux tube to insure the field lines are contained within the cross-section region. This is illustrated in Figure 4.8. The first image (A) shows what a simple flux tube may look like. The red line is the initial line the flux tube is based on, with the yellow lines being the new magnetic field lines comprising the rest of the flux tube. The flux tube is viewed side on (perpendicular to the field) so that the cross section appears here as the straight red line in the centre of the loop. The second image (B) shows the effect of the flux tube shape on adjusting the position of this cross section. The third image (C) shows the effect on the flux tube when increasing the size of the cross section (showed by slightly rotating the flux tube to see the cross section circle). The fourth image (D) shows how the flux tube changes when the cross section is changed from circular (A, B, C) to elliptical (D). The semi-major axes can also be adjusted.

It is possible to have multiple flux tubes within the same data cube, or multiple data cubes across the stellar surface containing flux tubes. Only the non-thermal GS emission from the flux tube is calculated as that is the only location of the non-thermal electrons. Outside of the flux tube (but within the data cube) the thermal plasma contributes to the free-free emission. Outside the data cube, the emission is treated as propagating in vacuo.

Step four: The thermal flux tube plasma

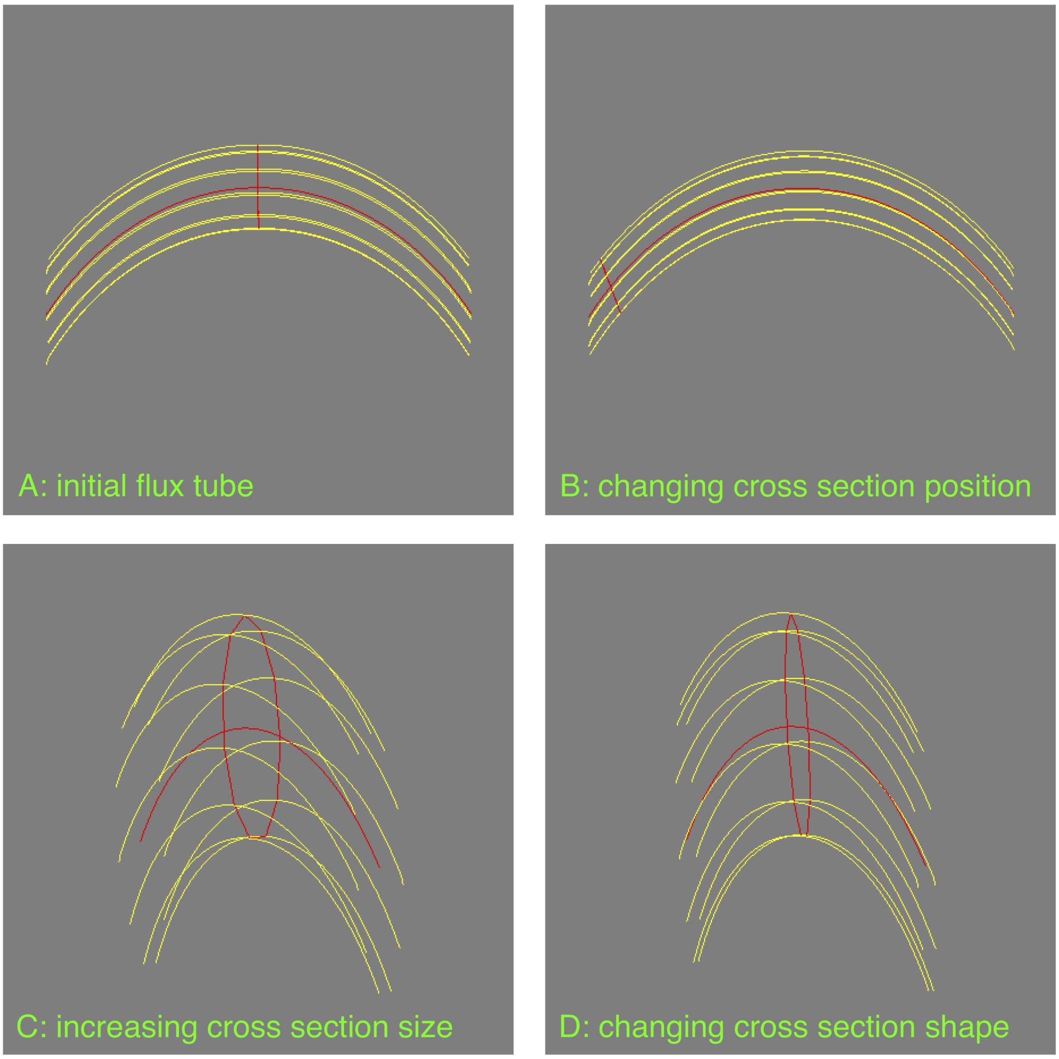

Figure 4.8: Visualisation of a flux tube within the GX simulator and its appearance when varying the cross section (red circle). The field lines comprising the flux tube are shown in yellow.

Now the flux tube is defined, the simulator requires it to be populated with both a thermal and non-thermal distribution of particles. The thermal (super-hot compared to the background coronal temperature) plasma is the ‘flaring’ plasma and has a spatial distribution of:

$$n_{th}(x,y,z) = n_0 n_r(x/a, y/b) n_z[z(s_l)/R] \tag{4.41}$$

where n_0 is the ‘loop top’ thermal density. n_r and n_z are the radial and vertical distribution of thermal electrons within the flux tube respectively. x/a and y/b are the cartesian coordinates x and y of the cross section parameter (described above) normalised by the semi-axes parameters a and b. This cross section is assumed to be at $s_l = 0$. R is the solar radius and $z(s_l)$ is the (x, y, z) coordinate corresponding to the point where the central field line intersects the cross section.

The default radial distribution takes a Gaussian form:

$$n_r(x,y) = \exp\left[-\left(p_0\frac{x}{a}\right)^2 - \left(p_1\frac{y}{b}\right)^2 - \left(p_2\frac{x}{a}\right)^2 - \left(p_3\frac{y}{b}\right)^2\right] \tag{4.42}$$

where p_i (i = 0,1,2,3) are adjustable, dimensionless parameters. The vertical distribution, n_z has a similar form to Equation 4.40:

$$n_z[z(s_l)/R] = \exp\left[-\frac{z(s_l)/R}{6.7576 \times 10^{-8} T_0}\right] \tag{4.43}$$

where T_0 is the flux tube temperature.

Step five: The non-thermal electrons

Next, the non-thermal particles are added to the flux tube. This is the most important part of the simulator and controls the gyrosynchrotron emission. As such, there are many parameters which can be altered and varied to easily see the effect they have on the generated emission. The four main parameters that control the non-thermal electrons are the number density, spatial distribution, power-law distribution and energy distribution.

The non-thermal spatial distribution is similar to that of Equation 4.41 except for the replacement of the loop top non-thermal density with the parameter n_b (n_0 for thermal). n_s is now the distribution centred along the central field line:

$$n_s(s) = \exp\left(-\left[q_0\left(\frac{s_l - s_0}{l} + q_2\right)\right]^2 - \left[q_1\left(\frac{s_l - s_0}{l} + q_2\right)\right]^4\right) \tag{4.44}$$

where q_0 and q_1 are dimensionless scaling factors, and q_2 is the location of the energetic electrons injection. This longitudinal distribution allows for the electrons to be confined around this injection site [Nita et al., 2015].

The non-thermal electrons have the following pitch angle distributions options: isotropic (with $g_\mu = 0.5$ from Equation 4.39), exponential loss-cone (symmetric loss cone with exponential boundaries), Gaussian loss-cone (symmetric loss cone with Gaussian boundaries), Gaussian and super-Gaussian (distribution decreases more rapidly from its maximum). The electron energy distributions available are: free-free only, thermal, single power law, double power law, TNT, kappa, power law over momentum, power law over Lorentz factor, TNT over momentum and TNT over Lorentz factor. Examples of what some of these distributions look like can be seen in Figure 4.9 [Oka et al., 2018]. The addition of the power law to a thermal distribution leads to more higher energy particles being included, indicative of the higher energy non-thermal particles produced in the mildly-relativistic gyrosynchrotron emission. The larger ‘power law’ tail seen between Figure 4.9b and c is the result of a changing power law index. A smaller index will lead to the raising of this tail and more higher energy particles being introduced.

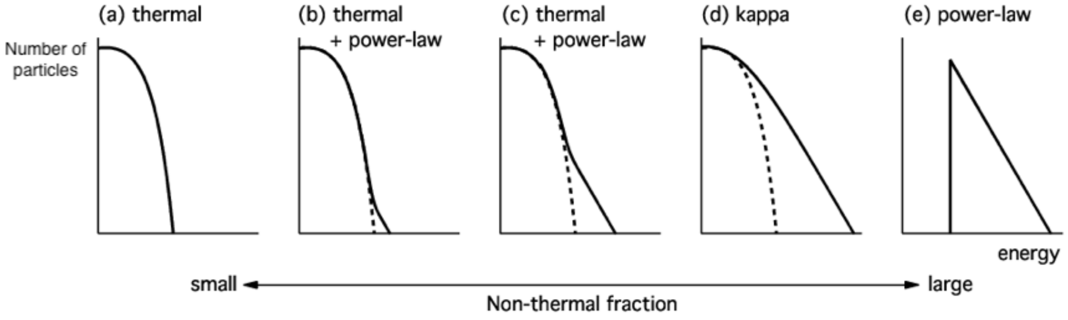

Figure 4.9: Particle spectra for different energy distributions. From left to right, the distributions show the effect of an increased number of non-thermal (higher energy) particles. The difference between (b) and (c) is a decreased power law index in (c) leading to more higher energy particles. Figure from Oka et al. [2018].

Step six: Calculating the emission

The GX simulator calculates the radio emission according to the fast gyrosynchrotron codes by Fleishman and Kuznetsov [2010] that are also used in the GS simulator [Nita et al., 2015]. These codes account for both the free-free emission from the thermal flux tube electrons and background plasma, as well as the non-thermal GS emission from the non-thermal flux tube electrons. The simulator calculates the radiated intensities (both left, I_L, and right, I_R) by numerical integration of the radiation transfer equation (Equation 4.7) along all selected lines of sight. Any line of sight can be chosen by altering the 3D orientation of the model, however the simulator is capable of solving the radiative transfer across multiple lines of sight simultaneously to produce emission maps at a particular frequency. The GX simulator can solve the radiative transfer equation for a range of radiation processes, e.g. EUV, microwave, HXR, SXR, etc. It is used in this work to calculate the microwave and SXR emission over a $1 - 100\,\mathrm{GHz}$ frequency range.

The simulator (and fast gyrosynchrotron codes) also calculates different combinations of the intensities. The emission maps produced in Chapter 5 are shown as a total power: $I_L + I_R$. The circular polarisation can also be calculated and given as (I_L

− I_R)/(I_L + I_R). These quantities are calculated automatically in the exact-coupling regime. However this can be changed to either strong coupling (like in the GS simulator) or weak coupling. The polarised emission is assumed to be entirely circularly polarised [Nita et al., 2015]. Despite the non-thermal particles being confined to the loop within the data cube, the GX simulator works along the entire line of sight. This allows for the computation of parameters (e.g. most importantly the polarisation) outside the data cube region.

The GX simulator also calculates both soft and hard (thin-target) X-ray emission. As well as free-free X-ray emission, free-bound continuum emission is also of importance in flares. The emission generated from free-bound mechanisms is effected by the varying abundances present. The GX simulator uses typical solar abundances in the following equations to calculate the X-ray emission, but these abundances can differ between different stellar regions. This free-bound emission is important at the lowest X-ray energies, where the free-bound to free-free emission ratio is largest. However, **?** argue that free-bound emission may also contribute at higher electron energies where free-free bremsstrahlung is usually assumed to dominate, in particular in high temperature sources (10-30 MK) where there is a larger than originally thought abundance of Fe ions [Kontar et al., 2011].

The photon flux, $I(\varepsilon)$, for photon energy ε (in keV) for the soft X-ray emission is calculated as [Nita et al., 2015]:

$$I(\varepsilon) = 8.1 \times 10^{-39} \frac{n_e^2 V}{\varepsilon\sqrt{T}} exp\left(-\frac{\varepsilon}{k_B T}\right) \tag{4.45}$$

where the photon flux is given in units of photons cm^{-2} keV^{-1} s^{-1}. V is the volume of each voxel. Similarly, the thin target hard X-ray spectrum is calculated as:

$$I(\varepsilon) = \frac{n_p V}{4\pi r^2} \int_{\varepsilon}^{\infty} \sigma(E,\varepsilon) F(E) dE \tag{4.46}$$

where $F(E)$ is the electron flux spectrum [photons $\mathrm{cm}^{-2}\,\mathrm{keV}^{-1}\,\mathrm{s}^{-1}$] and σ is the bremsstrahlung X-ray cross-section. r is taken as the distance to the source, which in this case (and every case in the GX simulator) is 1AU.

Step seven: Outputs

Once all these parameters have been defined and a rendering package chosen (either microwave, soft or hard X-ray) the emission maps and spectra can be generated. As the 3D model is moveable, any line of sight can be chosen. This is demonstrated in Chapter 5 where the GS emission and circular polarisation from several different view points is calculated. While the GX simulator focuses on emission produced in the corona rather than closer to the surface this is not a disadvantage in our research. The GX simulator remains a suitable tool for modelling the variable gyrosynchrotron emission produced in flares on young stars. The adaptation of the GX simulator to accommodate this scenario and the subsequent results are discussed in the following chapter.

Chapter 5

Time-independent modelling of a T-Tauri flare

In this chapter the GX simulator is used to model a flaring flux tube comprised of field lines originating from a T-Tauri star. This flux tube, and the surrounding corona, are given conditions akin to those seen from T-Tauri flares. This chapter first explores a general flaring flux tube generated from a simple dipolar configuration and the results that the GX simulator can generate. Then, we take a more in-depth look at GS and X-ray results from a flux tube that reaches a radius from which disk accretion is possible. The parameters used in these models are varied to see the effect on the GS emission and spectra. The emission is not calculated over time, rather just for the case of maximum flaring parameters. In other words, this model predicts the non-thermal radio and thermal X-ray emission from the peak of a range of T-Tauri flares which are then compared to the GB relation. The GX simulator is downloadable via the solar software (SSW) distribution website: `www.lmsal.com/solarsoft/`.

5.1 Adapting the 3D GX simulator

The parameters that can be adapted in the GX simulator have been laid out in the previous chapter. The stellar radius and mass cannot be altered in this simulator and have the same value as for the Sun. The parameters that are altered in this work to fit a T-Tauri flare are:

- Coronal temperature
- Coronal density
- Flux tube non-thermal density
- Flux tube thermal density
- Flux tube temperature
- Magnetic field strength
- Magnetic field configuration
- Power law index of non-thermal electrons
- Width of flux tube

5.1.1 Magnetic field

The magnetic field is the first thing to adjust within the simulator. It is loaded into the simulator as a set of 3D Cartesian coordinates. For initial investigation purposes, the field is set to a simple dipolar configuration:

$$B_x = \frac{3}{2} B_{dipole} \left(\frac{R}{r}\right)^3 \left(\frac{xz}{r^2}\right) \tag{5.1}$$

$$B_y = \frac{3}{2} B_{dipole} \left(\frac{R}{r}\right)^3 \left(\frac{yz}{r^2}\right) \tag{5.2}$$

$$B_z = B_{dipole} \left(\frac{R}{r}\right)^3 \left(\frac{3z^2 - r^2}{2r^2}\right) \tag{5.3}$$

Where r is the distance from the centre of the star (r = 0), R is the stellar radius and B_{dipole} is the dipolar polar field strength. This polar surface field strength value is related to the equatorial field strength as:

$$B_{\mathrm{dip}_{\mathrm{equator}}} = \frac{1}{2} B_{\mathrm{dip}_{\mathrm{polar}}} \tag{5.4}$$

The initial equatorial surface field strength that will be used is 1 kG, so the polar value is initially set at 2 kG. Henceforth, unless stated otherwise, the magnetic field strength value quoted will be that of the equatorial value. Once the field configuration is imported, a flux tube is defined to be comprised of closed magnetic field lines with both footpoints anchored to the stellar surface. The appearance of this flux tube within the simulator is seen in Figure 5.1.

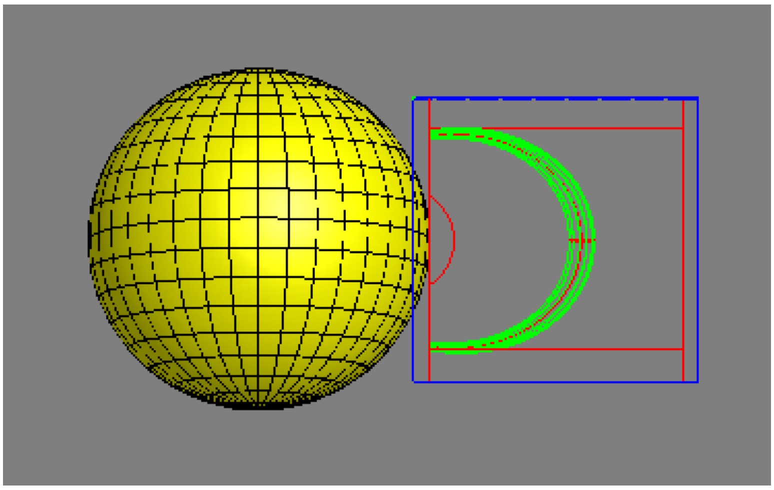

Figure 5.1: Appearance of a flux tube comprised of dipolar field lines (green) within the GX simulator.

The flux tube is large, with a loop length of 1.7×10^{11} cm and height of approximately 6.9×10^{10} cm above the surface. The central object (the Sun) is to scale compared with the loop in Figure 5.1.

5.1.2 Other parameters

The system can now be adapted further by altering the values for the parameters listed above. To start with, the model is given values as listed in Table 5.1, under the 'normal value' column. The other values listed will be trialled and the results discussed. The coronal density and temperature are not varied from their given normal values of $10^{10}\,\mathrm{cm}^{-3}$ and 7×10^{6} K respectively. The flux tube width is kept at $0.15\,\mathrm{R}_{\odot}$. The electron pitch angle distribution is isotropic with the energy distribution set as a single power law with an initial power law index of $\delta = 3.2$:

$$n(\varepsilon)d\varepsilon = A\varepsilon^{-\delta}d\varepsilon \tag{5.5}$$

for $\varepsilon_0 < \varepsilon < \varepsilon_{max}$ where A is a normalisation constant. The energy range is defined in the GX simulator as $10\,\mathrm{keV} < \varepsilon < 100\,\mathrm{MeV}$ [Nita et al., 2015].

Table 5.1: Adapted parameter values for initial model. Values given are for the 'normal' model and then the range within which the parameter is varied.

Parameter	Normal value	Range considered
Field (B) / kG	1.0	1.0 – 2.0
Flux tube thermal density (n_0) / cm^{-3}	5.0×10^{11}	2.5×10^{11} – 1.0×10^{13}
Flux tube temperature (T) / K	3×10^{7}	10^{7} – 1.5×10^{8}
Flux tube non-thermal density (n_b) / cm^{-3}	2.5×10^{11}	0 – 5.0×10^{11}

5.2 Calculations of radio emission from a flaring flux tube

Figure 5.2 shows the emission map results (gyrosynchrotron plus free-free) from the normal model at four different frequencies: 1, 5, 20 and 50 GHz. Unless otherwise stated, the emission maps and spectra are produced for the viewing angle seen in Figure 5.1. This viewing angle is facing the flux tube, where the line of sight is perpendicular to the magnetic field. The intensities are calculated along multiple lines of sight covering this orientation by integration of the radiative transfer equation. At low frequencies (< 5 GHz) the footpoints are not visible because of the dominating fluxes nearer the loop top and optical depth effects. There is lots of background thermal emission from the corona which is most intense at the base of the corona. At these low frequencies, and in the optically thick regime, these footpoints are obscured by absorption and the flux is dominated by the emission from the loop top region.

The highest intensity below 5 GHz comes from the very top of the loop where the non-thermal particle density is highest. At higher frequencies, the emission throughout the loop becomes optically thin and the footpoints can now be seen. The highest flux is still concentrated near the top of the loop at 20 GHz however at 50 GHz the highest emission comes from the footpoints. Indeed, 50 GHz (well within the optically thin regime) shows the highest fluxes overall, peaking at 1.4×10^5 solar flux units (where $1\,\mathrm{sfu} = 10^4$ Janskys). The fluxes are calculated at a distance of 1AU. Although the flux tube non-thermal density peaks at the top of the loop, the highest densities should be at the footpoints. This is due to the large coronal densities here and the large thermal density (larger than non-thermal) within the loop itself which accounts for a large degree of free-free emission. The spectra for this model is discussed next in comparison with the changing field strength.

One important result of this frequency dependent behaviour is the emission map

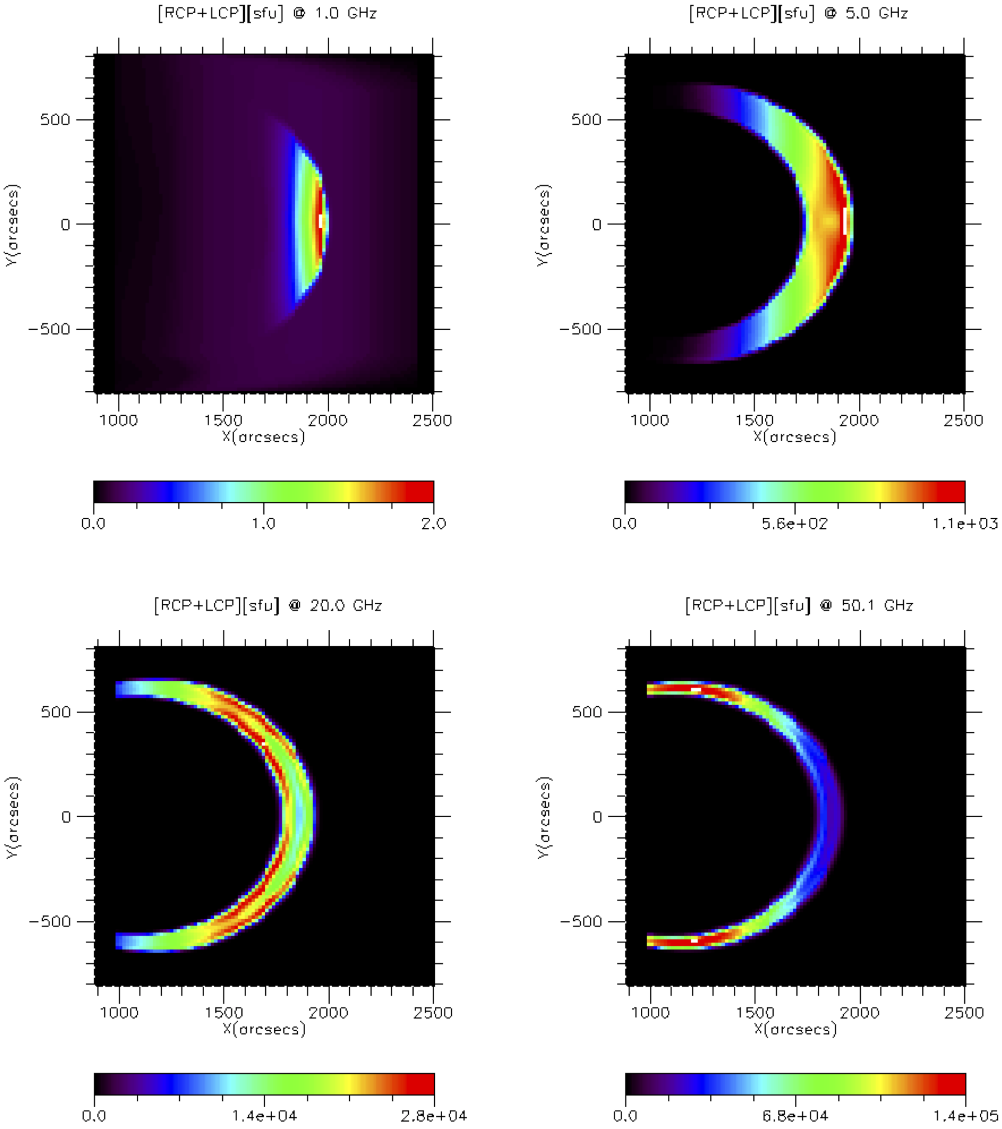

Figure 5.2: Emission maps of the radio flux from a flaring flux tube with parameters from Table 5.1. The flux from the system is shown at four different frequencies: 1, 5, 20 and 50 GHz. The colour bars are given in solar flux units, where 1 sfu = 10^4 Jy.

pattern at 20GHz. The thermal flux tube density is distributed evenly throughout the loop and the non-thermal flux tube density is localised around the apex of the loop. Moving between the optical depth limits (seen as thick at <5 GHz and thin at >50 GHz) sees the contribution from the denser thermal plasma becoming more dominant than the contribution from the non-thermal electrons. This is seen in the 20GHz emission map as the brightening of the loop edges when compared with the central portion around the loop's apex (as well an increase in the footpoint emission). This effect is seen in later emission maps, where if a thermal parameter (e.g. temperature or thermal flux tube density) is increased or non-thermal parameter (e.g. non-thermal flux tube density or field strength) is decreased then the emission from the apex of the loop top becomes more reduced in intensity at 20GHz compared to the region where the thermal density dominates. When there are zero non-thermal particles present (as discussed later in Section 5.2.4, Figure 5.10), there is no loop brightening effect seen at 20GHz. This indicates how the presence of non-thermal particles causes the 'dimming' of the loop apex compared to the edges where the higher thermal density emission is now less absorbed as the frequency moves from the optically thick to thin limit.

5.2.1 Field strength

The emission map and spectral results for increasing the surface field strength from 1 kG to 2 kG are shown in Figure 5.3 and Figure 5.4 respectively. Figure 5.3 shows the effect on flux throughout the loop at 20 GHz for both field strengths. The 1 kG map has already been seen in Figure 5.2 but is shown here for an easier comparison. When the field strength is increased the flux increases over the whole loop top region. However the maximum flux value remains the same between the 1 kG and 2 kG case. Both spectra have a turnover point at high frequencies after which the flux decreases with increasing frequency according to the value of the power law index, δ. This is characteristic of a gyrosynchrotron emission spectra, as is seen in Figure 4.7. The frequency of this turnover point can be approximated by Equation 4.26e.

Movie S2 from Fleishman et al. [2020] explores how changing the field strength affects the peak flux and frequency. As the surface field strength increases in that model, the frequency of the peak intensity moves to higher frequencies but the overall change

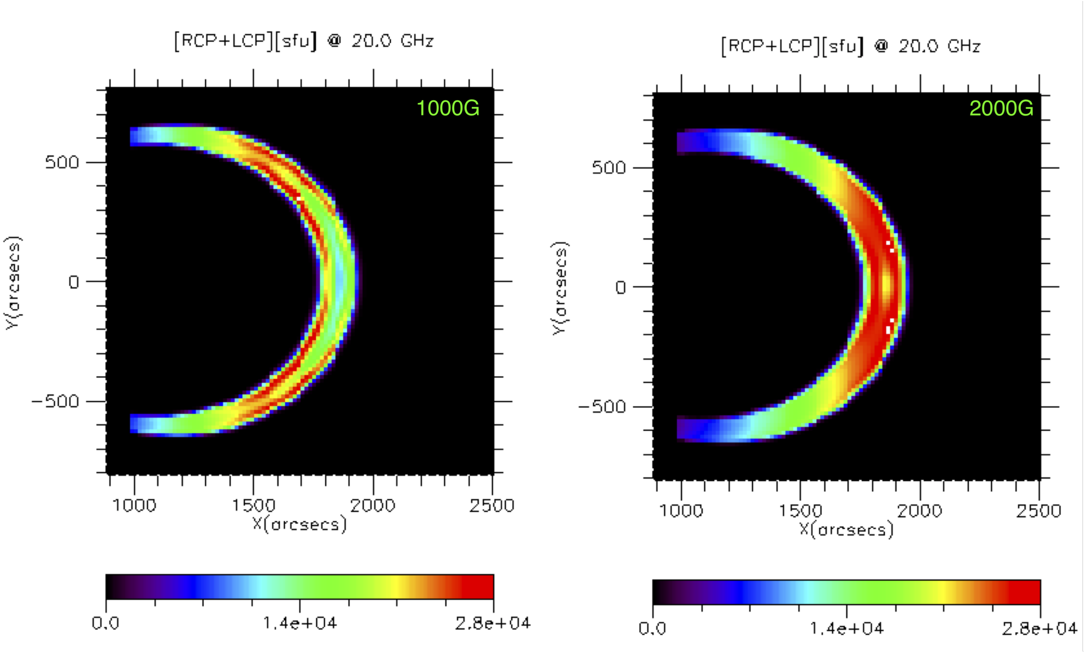

Figure 5.3: 20 GHz emission map images of the flux tube with surface field strength 1 kG (left) and 2 kG (right).

in peak flux is minimal for small changes in field strength. This peak moving to more optically thin regions allows for more of this loop top flux to be visible. Looking at the spectra in Figure 5.4, it is clear the 2 kG spectra does have a peak at a higher frequency than the 1 kG case. However, the peak value of the flux is different between the two spectra. Looking at Figure 5.3 it is clear there is a larger region that is of higher flux in the 2 kG case, leading to this increased integrated flux overall when comparing the spectra for these large differences in field strength. This supports the observations of increased fluxes from T-Tauri stars when compared with solar flares, as these stars are reported to have much larger surface field strengths. The increased field strength shifts the spectra to higher frequencies, causing slightly more lower frequency emission between 2-18 GHz for the 1 kG case. At the low frequencies (<2GHz) there is a lower flux for the 1kG case. This is due to the Razin effect, where at low frequencies the gyrosynchrotron emission is suppressed (see Chapter 4). The frequency where Razin suppression becomes prevalent is determined by the magnetic field strength and electron density. In this case, as the magnetic field strength is increased, the frequency where suppression occurs decreases. So for a lower field strength there is more suppression of the gyrosynchrotron emission (than a higher field strength at the same frequency) and the flux is reduced.

In general, both spectra have a similar shape. The flux rises over several orders of magnitude with increasing frequency. They both peak at high frequencies.

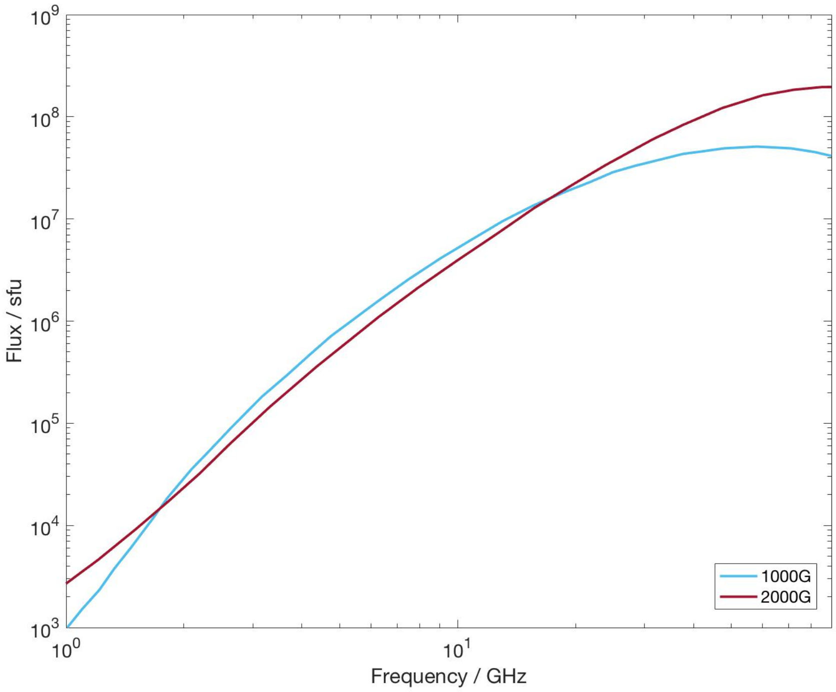

Figure 5.4: GS spectra for the changing field strength case over the frequency range $1 - 100$ GHz. Flux is given in sfu. The blue and red line denote the 1 kG and 2 kG case respectively.

5.2.2 Flux tube thermal density

Figure 5.5 shows the emission maps produced at 5 and 20 GHz for the case of minimum (2.5×10^{11} cm^{-3}, same as normal non-thermal density value) and maximum

($10^{13}\,\mathrm{cm}^{-3}$) thermal flux tube density (from Table 5.1). The effect of changing frequency on the minimal flux tube density is similar to that discussed from Figure 5.2. However, the difference in flux throughout the loop between 5 and 20 GHz behaves differently for the maximum thermal density case (bottom two plots). The footpoints are obscured in the lower frequency case (as seen before) but the highest fluxes appear this time on the outer edges of the loop top rather than inside the apex itself. This is due to the (now very dense) thermal electrons not being constrained around the loop top in the same way the non-thermal electrons are, allowing them to spread out along the loop more giving these higher flux regions. In the minimum case, the GS emission from the non-thermal electrons constrained at the loop top dominates. Similarly, at higher frequencies when the footpoints are visible, these regions still have the highest fluxes.

When comparing the emission maps for the minimum and maximum density cases, the peak flux is smaller when the density is larger at all frequencies. This can also be seen in movie S2 from Fleishman et al. [2020]. As the thermal density increases the emission becomes lower overall, moving to a lower peak value and lower frequencies. The greater amount of thermal GS and free-free emission from this increased thermal density shifts the optically thick/thin transition region to lower frequencies, also resulting in a smaller observed flux. This effect is seen in the spectra for the minimum, normal and maximum cases shown in Figure 5.6.

For a system that has both thermal and non-thermal particles, the higher the thermal density is, the lower the flux is at higher frequencies. The spectra itself flattens out at higher frequencies, as the effect from the non-thermal GS emission becomes less dominant. As explored by Fleishman et al. [2015], a purely thermal spectra from a flare is flat at high frequencies as the flux is controlled by the free-free and thermal GS emission, not non-thermal GS. The higher flux seen in the lower thermal density spectra of Figure 5.6 is due to the GS emission from non-thermal electrons becoming

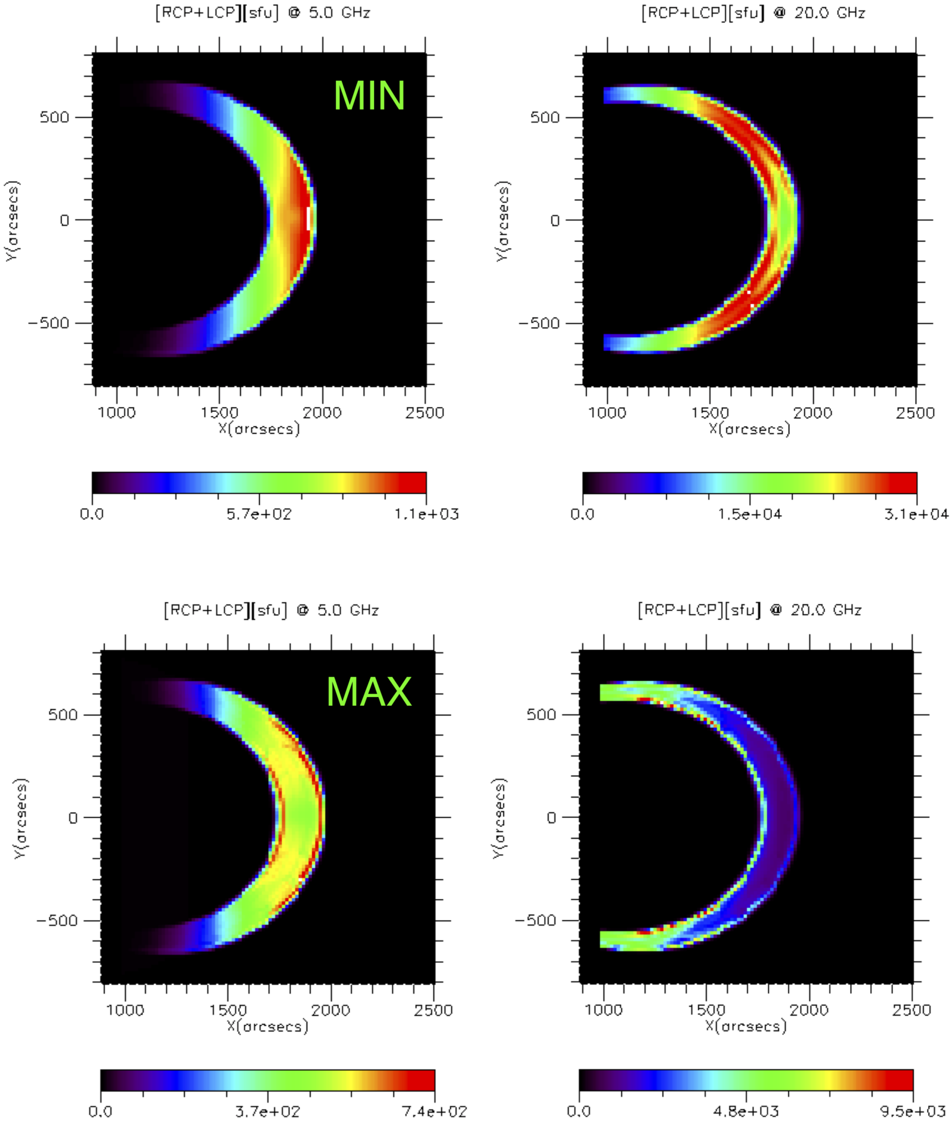

Figure 5.5: Emission maps for the flux tube with minimum thermal density (2.5×10^{11} cm^{-3}, top) and maximum thermal density (10^{13} cm^{-3}, bottom). Both cases are shown for 5 GHz (left) and 20 GHz (right).

more dominant. The point at which the thermal spectra plateaus is determined by the thermal density and is illustrated in Figure 5.7. For these spectra, the thermal density is varied without any non-thermal particles in the system. The purely thermal GS emission produced plateaus below 100 GHz unless the thermal density is greater than

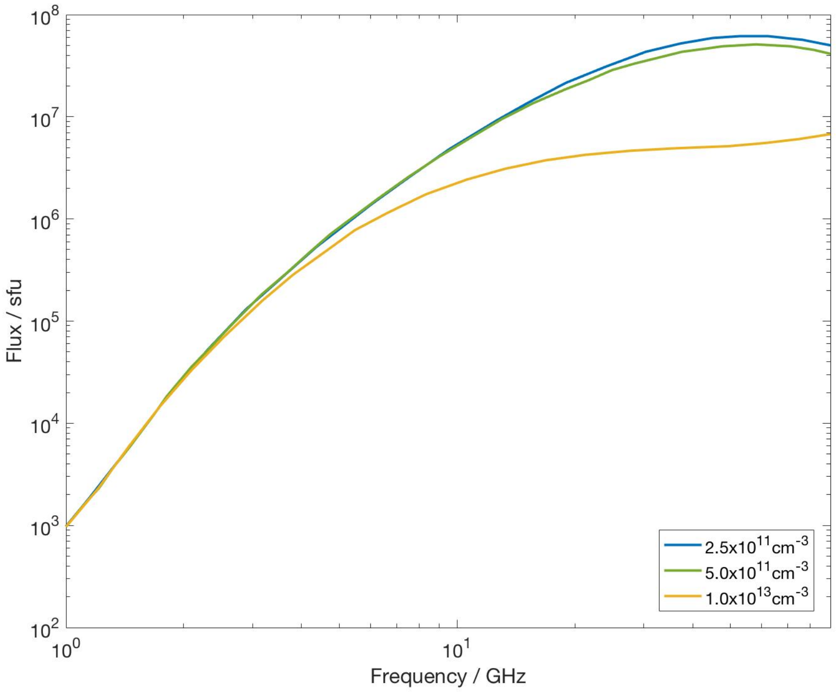

Figure 5.6: Spectra results for the minimum (blue), normal (green) and maximum (yellow) cases of varying flux tube thermal density.

10^{12} cm^{-3}.

These purely thermal spectra behave the same at low frequencies. There is a steady increase in flux between 1 and 5 GHz for all densities. Past 5 GHz, the lowest density spectra flatten out up to 100 GHz. However as the thermal density rises the high frequency spectra rise to higher fluxes and do not plateau within this frequency range. The introduction of non-thermal particles is therefore responsible for the high frequency bumps seen in plots such as Figure 5.6. In short, anything that increases the generation of non-thermal gyrosynchrotron emission (i.e. the non-thermal density, field strength, power-law index) is expected to affect the higher frequency region of the spectra and push it to a larger peak flux.

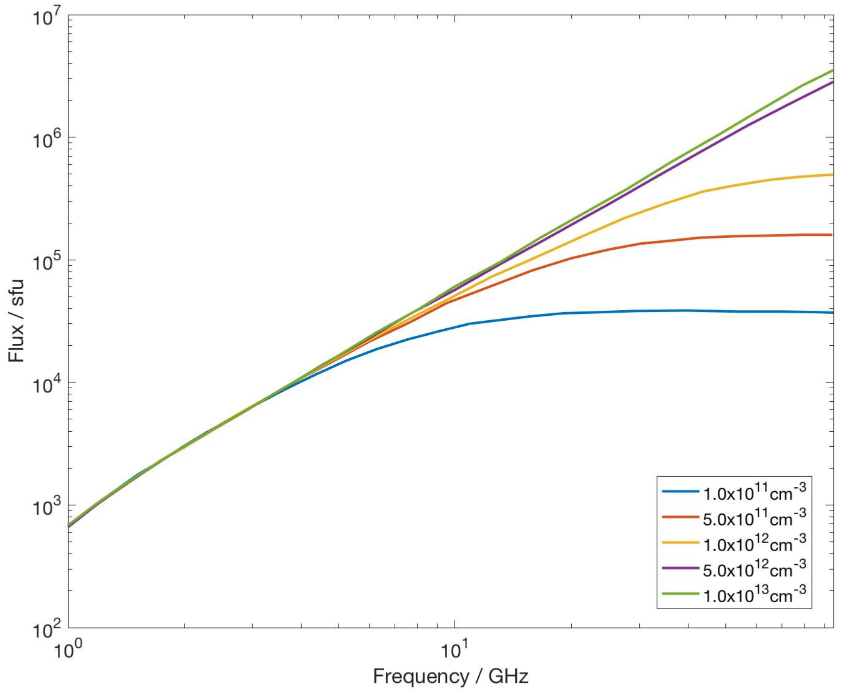

Figure 5.7: Spectral results of varying the flux tube thermal density with no non-thermal particles present over the frequency range $1 - 100$ GHz.

5.2.3 Flux tube temperature

Figure 5.8 shows the effect of varying the flux tube temperature between 10^7 (minimum) and 1.5×10^8 K (maximum). Similar optical depth effects as before are seen with regards to increasing frequency and the visibility of footpoints and throughout the loop. The peak fluxes are similar between the minimum and maximum cases, with a slightly lower flux for the higher frequency (20 GHz) case.

5.2.4 Flux tube non-thermal density

The non-thermal flux tube density controls the amount of non-thermal gyrosynchrotron emission produced. This non-thermal GS emission is produced by the accelerated electrons in a flare and is therefore of most importance in this work. For that reason, a wider range of values is now explored. Figure 5.9 shows the emission maps for the

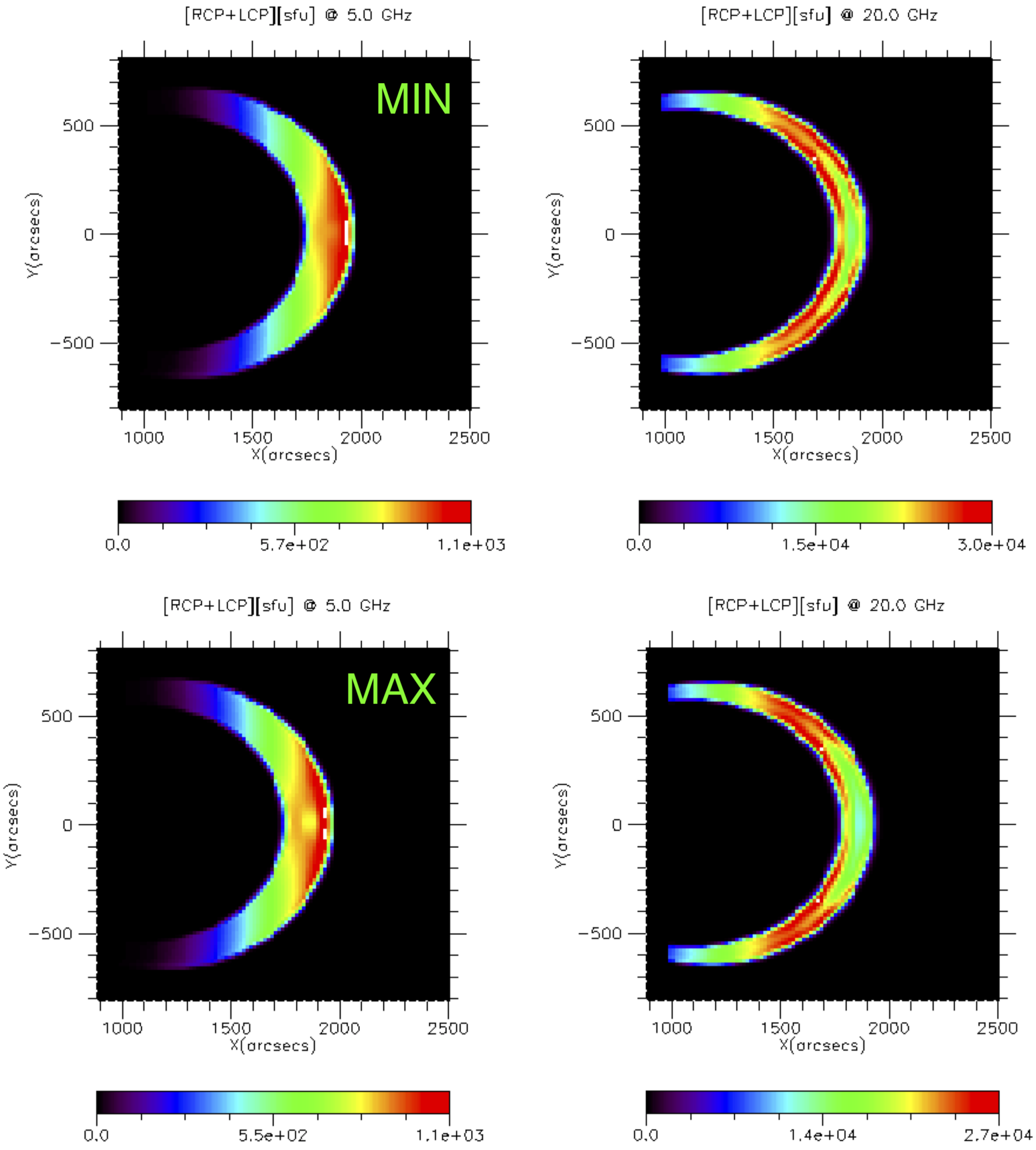

Figure 5.8: Same as Figure 5.5 but with varying flux tube temperature instead of density.

middle (5.0×10^{10} cm^{-3}) and maximum values (5.0×10^{11} cm^{-3}) of non-thermal density considered. The maximum value was chosen so as the non-thermal density never increases above the normal flux tube thermal density value. The same frequencies (5 and 20 GHz) are shown as for all previous emission maps. The 'middle' non-thermal density values have a more even peak flux throughout the loop top for 5 GHz. This is a result of the thermal density of electrons dominating in emission as they are not confined to the apex. The opposite is then seen in the 5 GHz maximum case, where the large non-thermal density of constrained electrons around the loop top dominates in the GS emission produced. As the frequency increases, the rest of the loop's emission becomes optically thin and (for the middle case) the more dominant thermal density emission becomes favourable towards the footpoints. As before, for the maximum density case, the emission is still dominated by the non-thermal GS producing particles which are constrained to the loop top.

The increase in non-thermal density overall leads to larger peak flux values in the GS emission, as expected. This is clear at 20 GHz but less clear at 5 GHz where there is more absorption within the optically thick limit. Additionally, for these low frequency and high field strength conditions, the Razin effect is prevalent and suppresses the gyrosynchrotron emission. This can be illustrated further by considering the case of zero non-thermal particles shown in Figure 5.10. The fluxes are overall much lower than the previous emission maps at both frequencies. The only flux contributing is that from the free-free emission from the thermal particles in the flux tube and corona. Indeed, at low frequencies the background thermal density is registering on the emission map and is comparable to the emission from the flux tube itself. At higher frequencies the unobscured thermal emission in the optically thin regime can be seen. The denser thermal particles are evenly distributed throughout the loop and are not constrained to the apex. Comparing the peak fluxes between the previous 20 GHz plots and this one, it is clear that the non-thermal GS emission accounts for most of the overall flux produced. This is illustrated in the following spectra in Figure 5.11 for all four cases (zero, middle, normal and maximum).

The purely thermal (zero non-thermal particle) case produces a spectra that is much lower in overall emission compared with the other cases. Past the spectral peak, the spectra is flat. This effect was discussed earlier to be due to the free-free emission

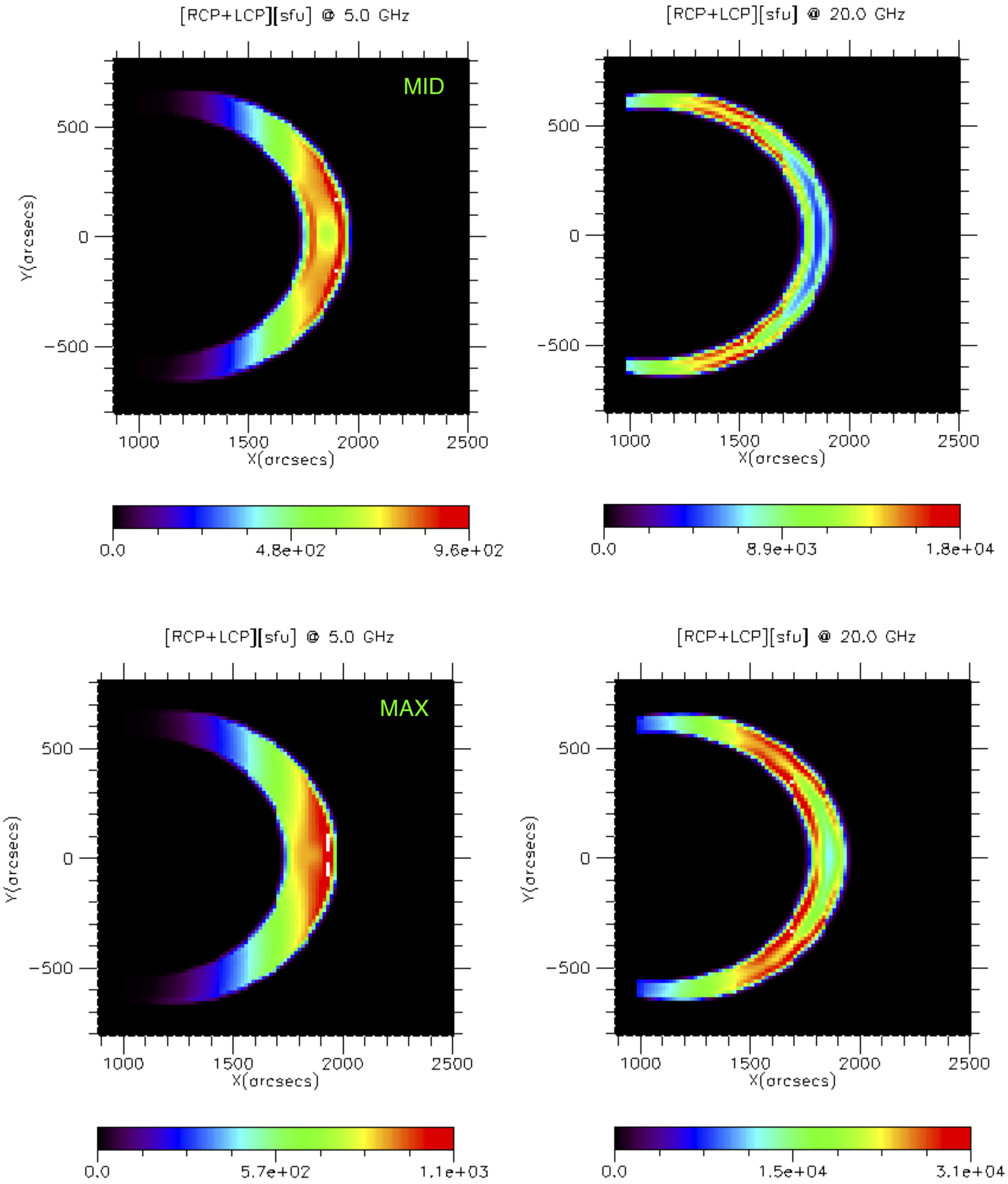

Figure 5.9: Emission maps at 5 and 20 GHz (left and right plots respectively) for varying the non-thermal flux tube density between $5.0 \times 10^{10}\,\mathrm{cm}^{-3}$ (top plots) and $5.0 \times 10^{11}\,\mathrm{cm}^{-3}$ (bottom plots).

which causes a flat spectrum above 10 GHz when the thermal density isn't too high. Indeed, the spectra itself has a much shallower gradient, indicating the presence of

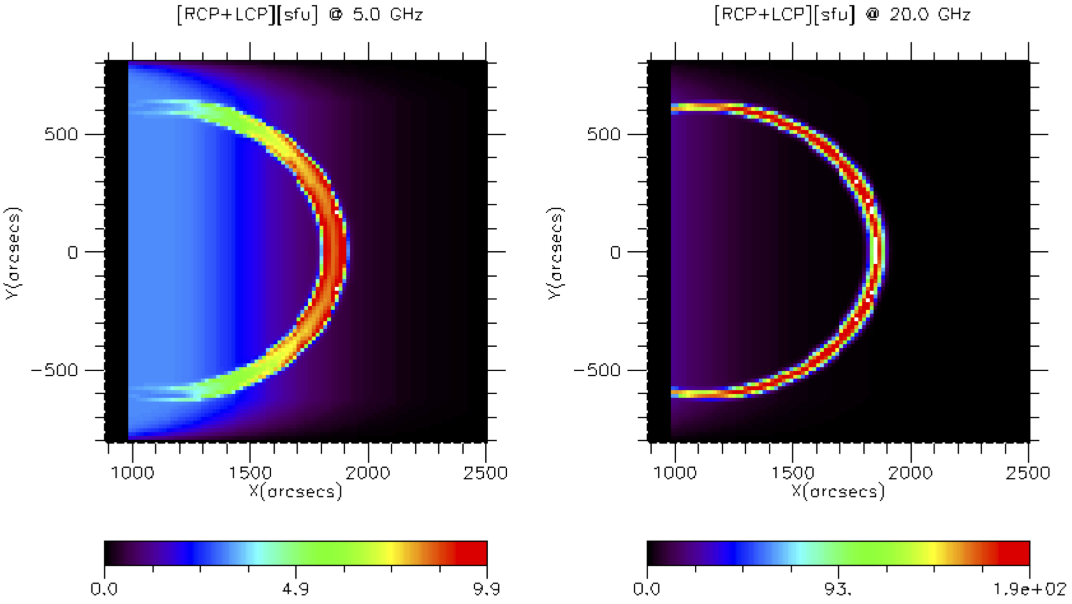

Figure 5.10: GS emission maps at 5 and 20 GHz (left and right) for the case where there are zero non-thermal particles.

free-free emission. A steeper gradient indicates the GS emission is produced from non-thermal (in this case, power law) electrons (see Figure 4.7). The other three spectra show a pattern that would be expected from increasing non-thermal density. As it increases, the peak flux also increases and shifts to higher frequencies. The overall flux is highest for the larger densities, with this effect most dominant at high frequencies.

5.2.5 Viewing angles

The angle from which the flux tube is viewed plays an important role in the intensity of emission produced. This viewing angle, in relation to the magnetic field direction, also affects the degree of circular polarisation as well as the flux. To investigate this, three different view points of the flux tube are considered. These are illustrated in Figure 5.12. All the plots so far have been for viewing angle A, where the emission is calculated facing the flux tube. This direction calculates the emission from a line of sight that is perpendicular to the magnetic field direction. The other two viewing

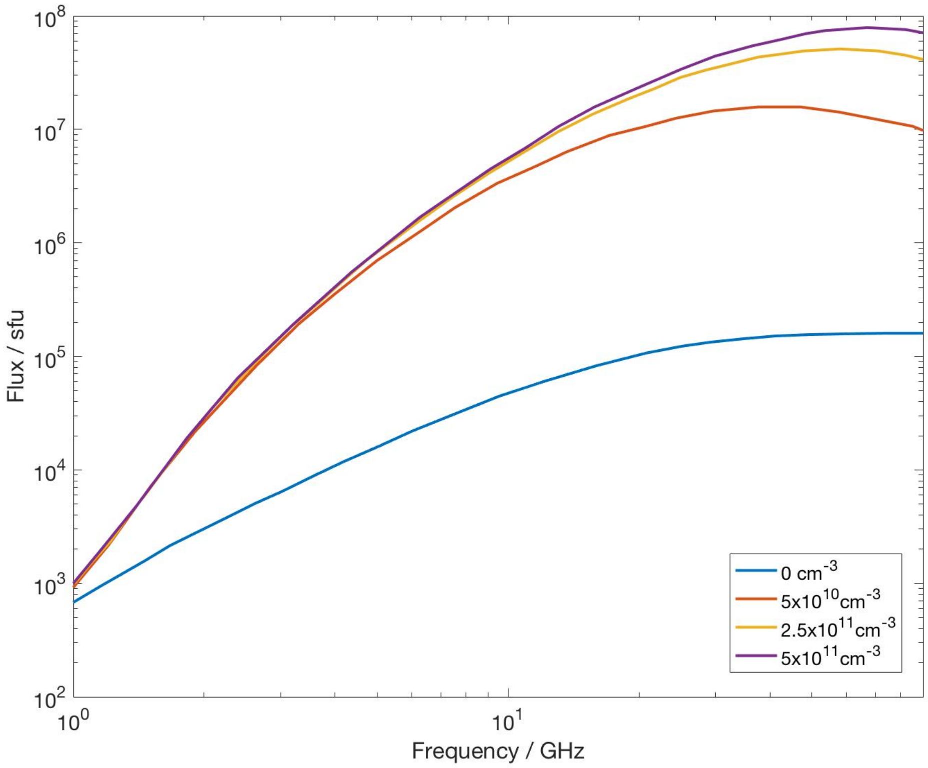

Figure 5.11: Spectra results for varying the non-thermal density between 0 (blue) and 5×10^{11} cm^{-3} (purple).

angles, view B and C, are directed top down and side on respectively. These two angles are both along the magnetic field lines and should therefore generate the highest fluxes. To show a more contrasting comparison, the emission maps are now produced at 1.6 and 20 GHz for each of the three view points. These are displayed in Figures 5.13, 5.14 and 5.15 respectively. All the emission maps and spectra are generated for a field strength of 2 kG.

View A in Figure 5.13 shows what we have already discussed. The only difference is the lower fluxes at the lower frequency of 1.6 GHz (as would be expected). Comparing these maps with view B (Figure 5.14) and C (Figure 5.15) it is clear that the peak flux is indeed lower overall when the viewing angle is perpendicular to the magnetic field direction. However, because the flux tube is being viewed side on, there is a larger

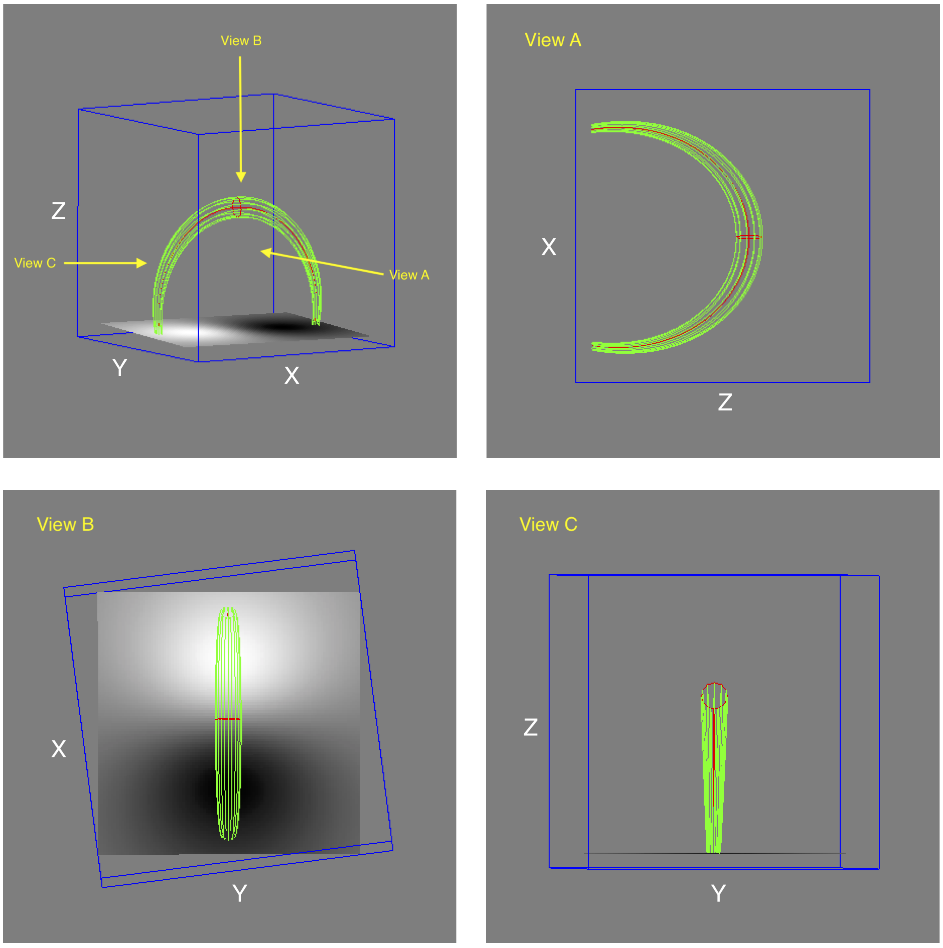

Figure 5.12: Illustration of the three different viewing angles of the flux tube considered within the GX simulator.

emitting volume to be considered and the integrated flux across all frequencies is likely to still be larger. Figure 5.14 shows the emission maps for the top down viewing angle of view B. At low frequencies the emission is concentrated at the very top of the loop, however at higher frequencies the high fluxes are found almost throughout the entire region being viewed. This illustrates how the GS producing non-thermal electrons are constrained at this loop top. Figure 5.15 shows the side on viewing angle (view C). Again, this viewing angle is useful in illustrating how the non-thermal GS emission peaks at the top of the loop from the constrained non-thermal electrons. The peak emission is similar to that of viewing angle B, i.e. larger than for view A.

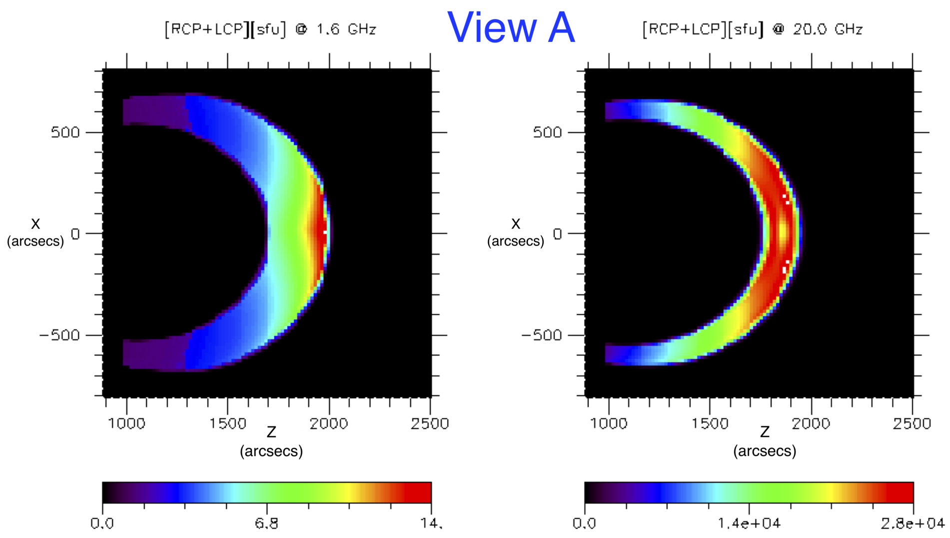

Figure 5.13: 1.6 and 20 GHz GS emission maps of view A.

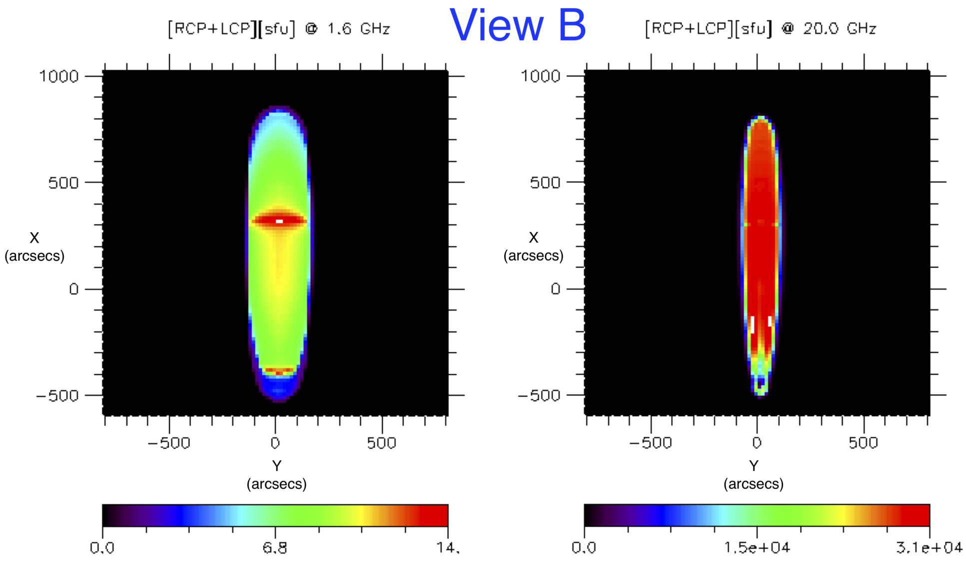

Figure 5.14: 1.6 and 20 GHz GS emission maps of view B.

The spectra for these three viewing angles is shown in Figure 5.16. As suggested above, view A has the largest integrated flux at higher frequencies due to the more numerous lines of sight passing through the flaring flux tube from this orientation. The profile of spectra A is very similar, just of a higher magnitude, to view C. View B however has a similar general profile to C except for being shifted to a lower frequency

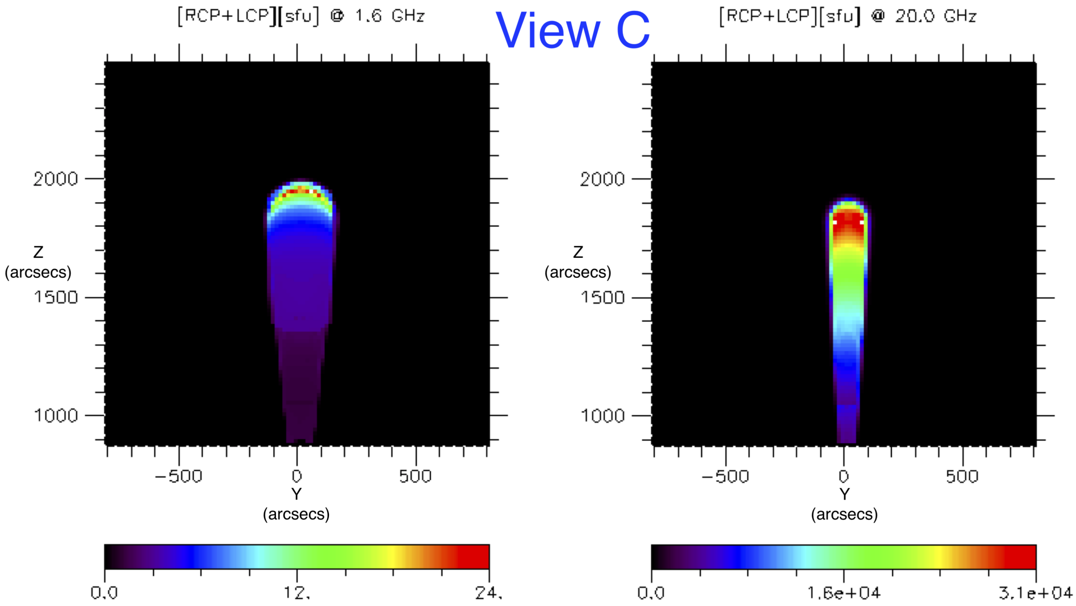

Figure 5.15: 1.6 and 20 GHz GS emission maps of view C.

peak flux. This leads to the flux below 10 GHz being similar to view A, but the peak flux occurring at the lowest frequency for all three cases. As is seen in movie S2 from Fleishman et al. [2020], decreasing the viewing angle between the line of sight and magnetic field (as has been done in the case of View B) can result in the spectra shift seen here.

The viewing angle with respect to the field lines also has a large effect on the circular polarisation. This is seen in Figure 5.17. When the line of sight is orientated in the direction of the field lines, the degree of polarisation is larger as is the case for view B and C. From Dulk [1985], it is shown that the circular polarisation decreases with increased viewing angle. This explains the behaviour seen in view A, which has a lower peak degree of circular polarisation than view B and C. The circular polarisation also decreases for increasing frequency in View B, which has been seen in Figure 4.6. Optical depth effects, as well as Faraday rotation, can explain the unpolarised emission of view B and C at high frequencies.

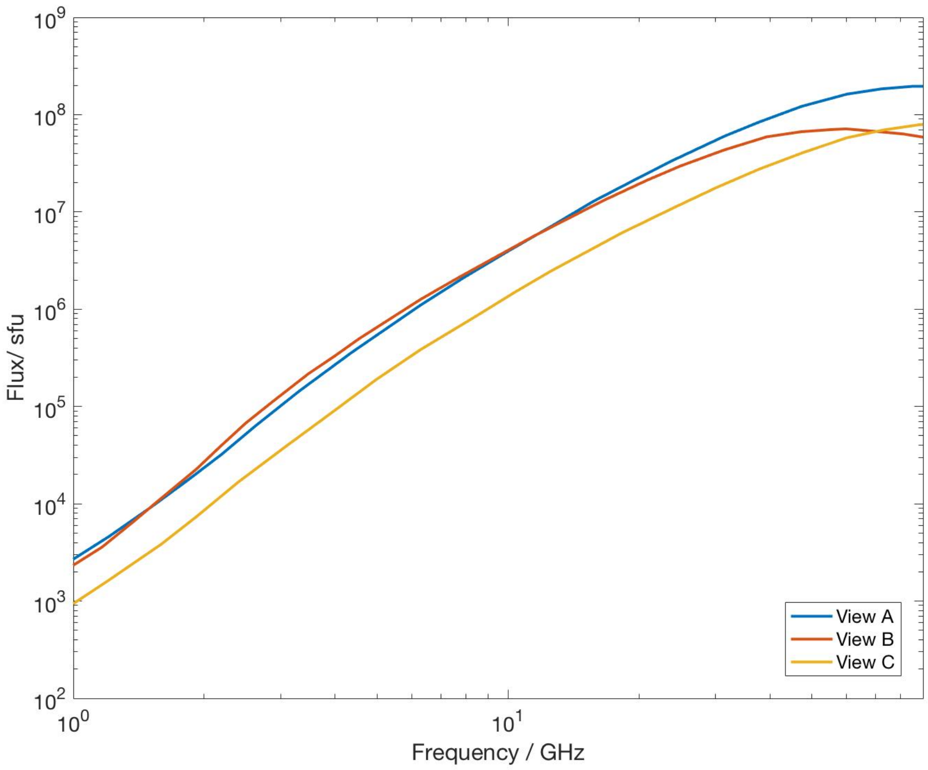

Figure 5.16: Spectra results for the three different viewing angles.

5.2.6 Revisiting the scaling relations

Using the scaling relations derived by Shibata and Yokoyama [1999] the emission measure from this model can be estimated and compared to Figure 3.11. The field strength at the loop top is approximately 92 G and the loop length has already been stated as 1.7×10^{11} cm. The preflare coronal density is assumed to be the background coronal density at the loop top. This is estimated from Equation 4.40, with $\mathrm{n}_0 = 10^{10}\,\mathrm{cm}^{-3}$, to be $n_z \approx 1.2 \times 10^9\,\mathrm{cm}^{-3}$. These values are then applied (with T = 30 MK) to Equations 3.15 and 3.16. Equation 3.15 gives an emission measure of $7.14 \times 10^{50}\,\mathrm{cm}^{-3}$ and Equation 3.16 gives $1.1 \times 10^{53}\,\mathrm{cm}^{-3}$. The first of these emission measures is low for a T-Tauri flare, falling in the lower range for the observed emission measures from Figure 3.11. The low field lengths predicted by this scaling relation have already been

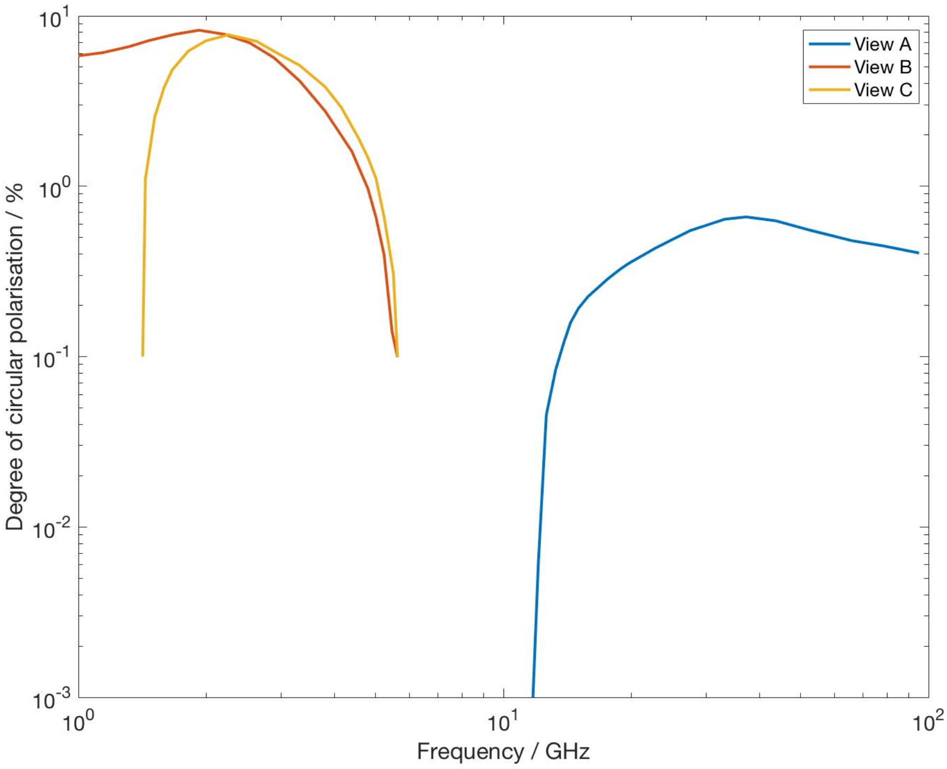

Figure 5.17: Degree of circular polarisation for the three viewing angles over the $1 - 100$ GHz frequency range.

discussed and it was suggested that the scaling relation for loop lengths are more accurate for T-Tauri flares. This is reflected in the latter of these calculated emission measures. A value of $1.1 \times 10^{53}\,\text{cm}^{-3}$ for this flaring loop places the star well within the range shown from observations of T-Tauri flares. Applying these values to Equation 4.27d, the peak frequency is estimated as approximately 78 GHz for a density of $2.5 \times 10^{11}\,\text{cm}^{-3}$ and a viewing angle of 90°. For comparison, the frequency of the peak flux obtained from the normal model (e.g. the yellow spectra from Figure 5.11) is 58 GHz.

5.3 Calculations of radio and X-ray emission from an extended flux tube

The capabilities of the GX simulator have been explored and the effects of varying some flaring parameters has been discussed. However, to better simulate a flare on a T-Tauri star several adjustments to this model need to be made. The first is the field configuration. It has been discussed in Chapter 2 how these young stars often have multipolar field configurations. A commonly reported configuration is that of a dipole plus octupole component [Johnstone et al., 2013]. Therefore the imported field structure is altered to incorporate this. Also, in order to simulate emission from a flux tube interacting with the circumstellar disk, the flux tube must be moved to an appropriate distance away from the star. This is now adjusted so the flux tube's loop top is situated at $4\,R_{\odot}$. Other changes in parameter value ranges to be varied is discussed in this section but in general the standard value is the same as in Table 5.1, with the exception of the dipolar surface field strength component. This improved model of a T-Tauri star interacting with its disk will also have several more of the parameters mentioned at the start of this chapter varied. For example, the flux tube width and the power law index will be varied to see the effect on the overall radio flux. The X-ray flux will now be incorporated as well, so the results from this model can be compared with the Güdel-Benz relation in Chapter 3. The results from this time independent model are also reported in Waterfall et al. [2019].

5.3.1 Model parameters

5.3.1.1 Changing to a multipolar configuration

The 3D cartesian coordinate system describing the model's magnetic field has now been modified to include an octupole component as follows:

$$B_x = \frac{3}{2}B_{\rm dip}\left(\frac{R}{r}\right)^3\left(\frac{xz}{r^2}\right) + B_{\rm oct}\left(\frac{R}{r}\right)^5\left(\frac{35xz^3 - 15xzr^2}{8r^4}\right) \tag{5.6}$$

$$B_y = \frac{3}{2}B_{\rm dip}\left(\frac{R}{r}\right)^3\left(\frac{yz}{r^2}\right) + B_{\rm oct}\left(\frac{R}{r}\right)^5\left(\frac{35yz^3 - 15yzr^2}{8r^4}\right) \tag{5.7}$$

$$B_z = B_{\rm dip}\left(\frac{R}{r}\right)^3\left(\frac{3z^2 - r^2}{2r^2}\right) + B_{\rm oct}\left(\frac{R}{r}\right)^5\left(\frac{3r^4 - 30z^2r^2 + 35z^4}{8r^4}\right) \tag{5.8}$$

Where the component $B_{\rm oct}$ is the octupole surface polar field strength. This is related to the equatorial value as:

$$B_{{\rm oct}_{\rm equator}} = \frac{3}{8}B_{{\rm oct}_{\rm polar}} \tag{5.9}$$

As before, any mention of the octupole surface field strength from now on refers to the equatorial value. These multipolar fields have been reproduced in magnetic maps of accreting T-Tauri stars [Hussain et al., 2009] and are also used in models simulating these environments (Long et al. [2012], Gregory et al. [2010]). The choice of a dipole plus octupole configuration has been chosen based on research done by Gregory et al. [2010], however different components (e.g. quadrupole) can also be added. The dipole surface field strength value is now altered to 2 kG (from 1 kG) with an octupole component of 0.5 kG, adopted from the values reported by Donati et al. [2010] for the classical T-Tauri star AA Tau.

The flux tube is now positioned so its loop top is at $4\,R_\odot$. This extends the total loop length to approximately 6.9×10^{11} cm ($\approx 10\,R_\odot$). As discussed in Section 3.3.2, this loop length fits within the range predicted by the scaling relations from Figure 3.11 and falls within the upper range of values from flaring loop lengths on other T-Tauri stars predicted by Reale et al. [1997] in Table 3.2. Despite the addition of the octupole component to the field configuration, this ends up making minimal difference to the results overall. The octupole component's dependence on the distance from the star, *r*, renders it almost negligible at these distances. As such (and for simplicity), only the dipolar component is varied.

A limitation of the GX simulator is the computation volumes it is capable of. It is designed to model smaller scale solar flare loops, not the extended flaring loops of T-Tauri stars. As such, the footpoints of this model are excluded and only the emission from a volume centred around the loop top is calculated. As we are only modelling the emission in a time-independent manner, i.e. the GS emission from the peak of the flare when the particles are injected, the emission from these footpoints is thought to make minimal difference. Indeed the footpoint emission from the initial model results in Section 5.2 makes little difference to the flux overall. In a time dependent model the footpoint emission would need to be included to give a more realistic picture, incorporating the effects of the radiating non-thermal particles propagating towards these regions.

5.3.1.2 Other parameters

The rest of the normal values for the model parameters are shown in Table 5.2. The standard values for flux tube thermal density, flux tube temperature and flux tube non-thermal density all remain unchanged with the range in which these parameters are to be varied also shown in Table 5.2. The power law index (still at 3.2) will also now be varied, along with the flux tube width. This width is initially set at $1\,R_\odot$ (based on the assumption that flux tube width, $w = 0.1\,L$, [Isobe et al., 2003]). The coronal density and temperature are not varied and are set as the same values as before: $10^{10}\,cm^{-3}$ and 7×10^6 K respectively. The electron pitch angle distribution is kept as isotropic.

Table 5.2: Standard parameter values for the new model and the range in which they will be varied.

Parameter	Normal value	Range considered
Dipolar field (B) / kG	2.0	0.5 – 7.0
Flux tube thermal density (n_0) / cm^{-3}	5.0×10^{11}	2.5×10^{11}-1.0×10^{12}
Flux tube temperature (T) / K	3×10^{7}	10^{7}-1.5×10^{8}
Flux tube nonthermal density (n_b) / cm^{-3}	2.5×10^{11}	$0 - 5.0\times10^{11}$
Power law index (δ)	3.2	2 – 7
Flux tube width (w) / $R_\odot$	1	0.5 – 2

5.3.2 Initial results

The spectra generated for the model described by the parameters in Table 5.2 is shown in Figure 5.18. The peak flux is approximately 8×10^7 sfu occurring around 30 GHz. The field strength at this location is around 35 G, drastically reduced from the surface value because of the distance, causing the shift in peak to a lower frequency than in Figure 5.4. However, the flux tube is much thicker than the initial one, generating more gyrosynchrotron emission.

To compare these radio fluxes with thermal X-ray emission and other T-Tauri flare observations, the fluxes are converted to luminosities. The result from this standard model is shown as the black dot in Figure 5.19. The observations of class II and III flares from Figure 3.15 are kept for comparison. The X-ray and radio luminosities of this normal model are $\log L_X$ [erg s^{-1}] = 30.5 and $\log L_R$ [erg s^{-1} Hz^{-1}] = 16.3 respectively. These values agree well with observational results, lying below the GB relation. This further supports the idea there is an overproduction of non-thermal radio emission when compared with flares on other active stars. To investigate the effect the different model parameters have on these two emissions, the normal values are now varied one at a time. This also enables us to see if a change in any of them brings the results closer to the GB relation, and what this would physically mean for the flare.

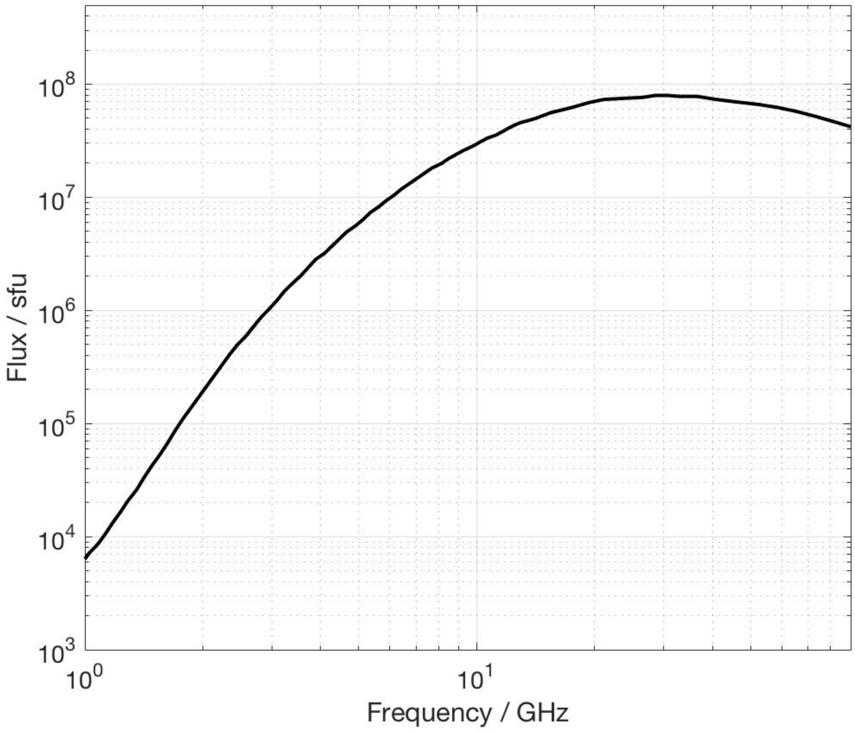

Figure 5.18: GS spectrum for the model with parameters equal to the normal values from Table 5.2. The frequency range is $1-100$ GHz and the flux is given in solar flux units (sfu) calculated at a distance of 1AU.

5.3.3 Varying the parameters

5.3.3.1 Surface field strength

The dipolar surface field strength component is varied between 1 kG and 6 kG initially and the spectral results are shown in Figure 5.20. As expected, the larger the field strength the larger the peak in flux and corresponding frequency of the peak. For example, for a 1 kG surface strength the peak flux and frequency are 1.01×10^7 sfu and 16.26 GHz respectively. Conversely, for 4 kG these values are 5.01×10^8 sfu and 51.32 GHz. The higher field strengths lead to more GS emission, agreeing with the higher luminosities seen in the more active T-Tauri flares compared to main sequence stars.

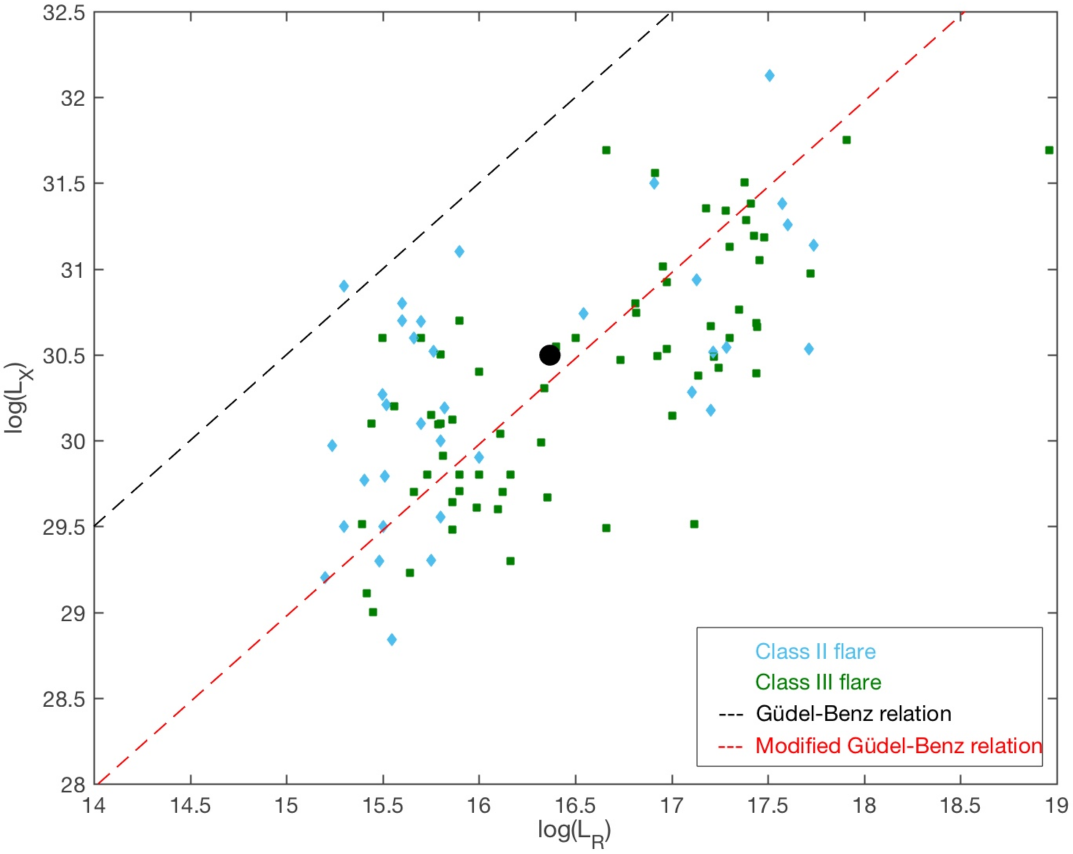

Figure 5.19: Logarithmic plot of the non-thermal radio [erg s^{-1} Hz^{-1}] and thermal X-ray [erg s^{-1}] luminosity showing the class II (blue) and III (green) observations of T-Tauri flares as well as the standard model result (black dot). The original and modified GB relations are shown as the black and red dashed lines respectively.

The behaviour of these peak fluxes and frequencies as the field strength varies is shown by the black points in Figure 5.21. The red points illustrate a change in non-thermal density which is discussed next. Between 1 and 7 kG the peak flux is measured at 1 kG intervals. The factor by which this peak flux changes becomes smaller and smaller as the field strength increases. For example, the flux changes by a factor of 10 between $1-2$ kG but also $2-6$ kG. The frequencies of these peaks are far more evenly spread between different field values, however below 1000 G the frequencies of the peaks remain similar as there is less non-thermal GS emission shifting the peak.

Overall, the frequencies of the peaks for changing field strengths are far larger than

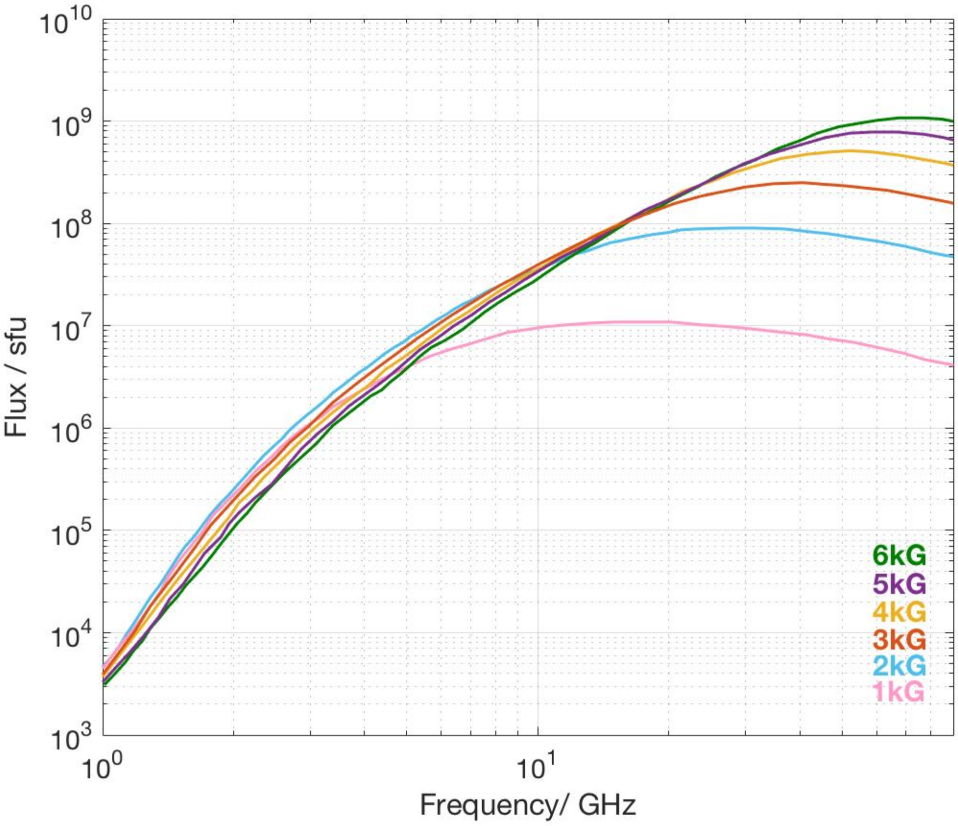

Figure 5.20: Spectra results for varying the surface dipolar field strength between 1 and 6 kG.

for the increasing non-thermal densities and if detected observationally could indicate these large field values. Indeed, even for field strengths of 2 kG which is considered typical for a T-Tauri star, the peak frequency is around 30 GHz. This is far higher than these regions are commonly observed at, for example many YSO surveys have been conducted with the VLA at 4.5 and 7.5 GHz (see Section 3.3.3). The effect of changing field strength on the model results when compared with the GB relation is seen in the following figures. For example, in Figure 5.22. As the surface field strength increases (the black points) between 1 kG and 4 kG the peak radio emission moves to a higher value (as seen in Figure 5.20). However, this does not alter the X-ray emission.

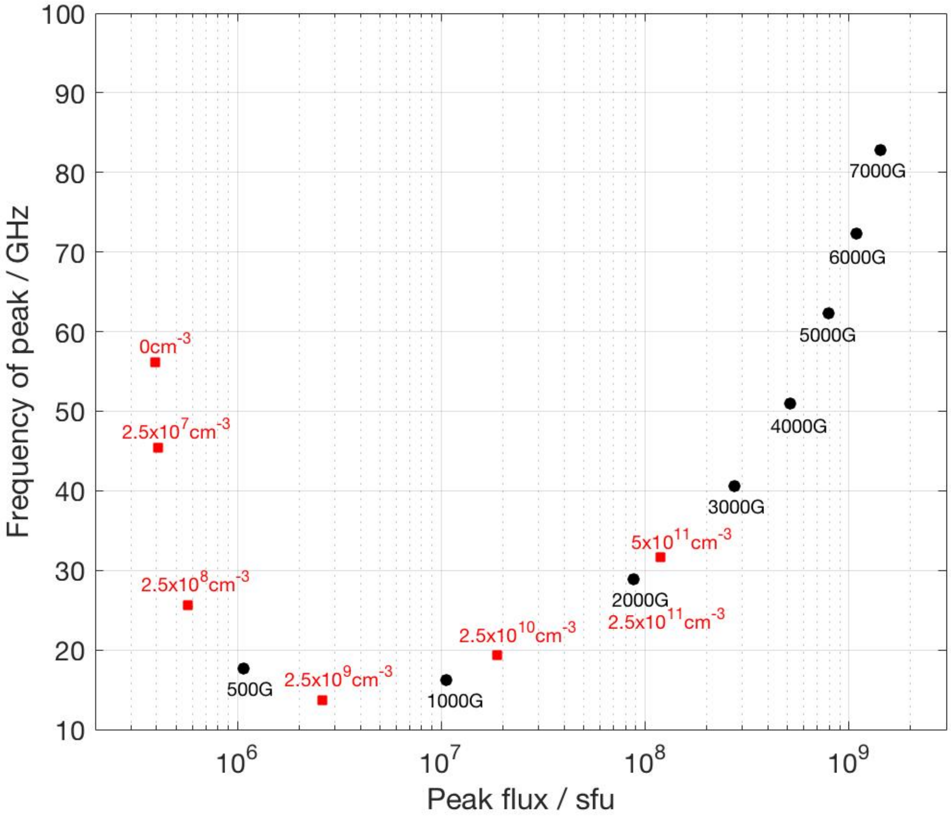

Figure 5.21: Peak fluxes and corresponding frequencies of models where the surface field strength (black) and non-thermal flux tube density (red) has been varied. The frequency of the peak is given in GHz and the peak flux is given in sfu.

Therefore, an increased field strength leads to an even larger deviation from the Güdel-Benz relation.

5.3.3.2 Non-thermal density

The flux tube non-thermal density is the critical component in this model. It leads to the generation of gyrosynchrotron radio emission, emitted by the gyration of particles accelerated during reconnection. The variable nature of this emission is explored in Chapter 6, but the initial modelling of this parameter and its effect on the radio and X-ray emission helps constrain the values of this parameter at the peak of the flare as well as comparing it with flare observations. There are two factors to consider when

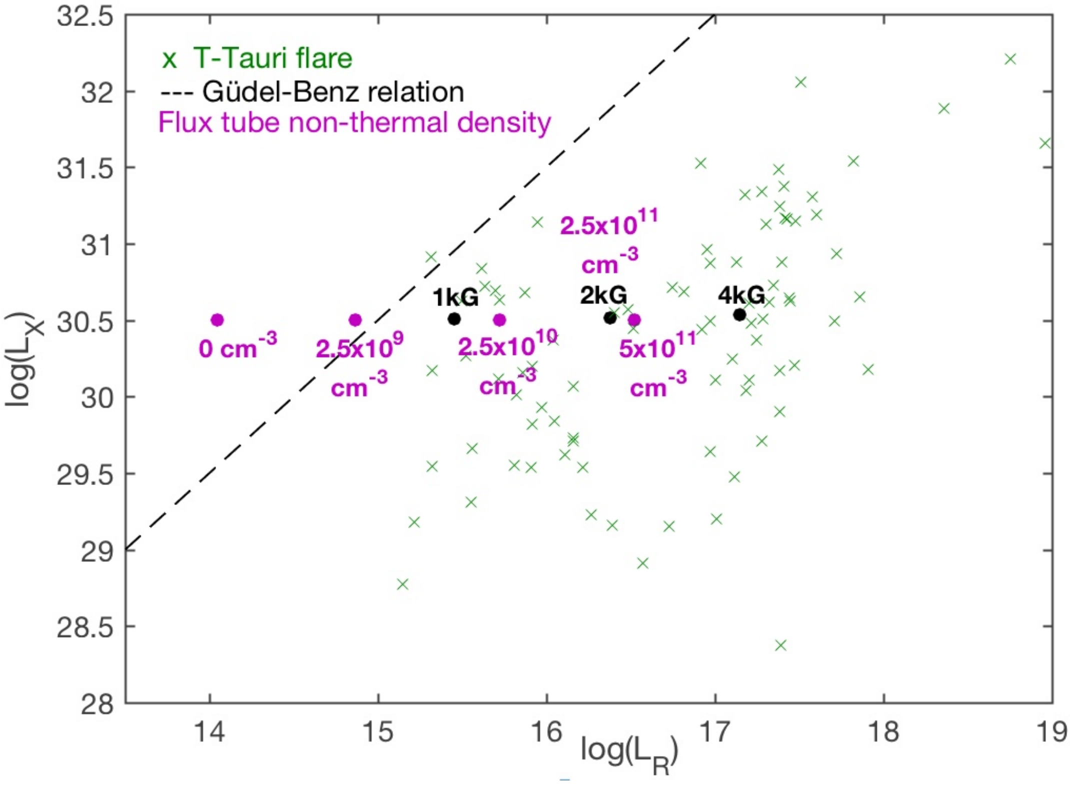

Figure 5.22: Radio and X-ray luminosity plot of the observed T-Tauri flares overlaid with model results for flaring T-Tauri stars with varying surface field strength (black) and flux tube non-thermal density (purple). The GB relation is shown again as the dashed line. The T-Tauri flare observations are shown in green and are no longer separated by class.

choosing the non-thermal density: the magnitude of this value in general, and the ratio of this value with the thermal density.

Initially, the non-thermal density was set as 50% of the thermal density. As the exact non-thermal and thermal emitting regions of T-Tauri flares are unable to be resolved from observations, this seemed a reasonable initial assumption. It is still assumed that the non-thermal density does not exceed the thermal density, as there is considerable heating and thermal particles along the entire flux tube. The result of varying this ratio of non-thermal to thermal plasma density is displayed in Figure 5.23. The purely thermal spectra, with zero non-thermal particles, is shown in black and has the same shape as before (discussed in Section 5.2.4). As the fraction of non-thermal particles increases, the peak flux moves to higher values and higher frequencies. When the non-thermal and thermal densities are equal, the peak of the spectra moves out of the frequency range. At frequencies below 10 GHz, the 0.1 and 1 (orange and blue) ratio spectra are almost identical, indicating that the ratio of non-thermal to thermal particles becomes most distinguishable at higher frequencies. It is therefore key to observe these flares at higher frequencies (above 10 GHz), as this is where the non-thermal particle effects become more dominant. Indeed, the flux in Figure 5.23 is calculated here in mJy to illustrate how the non-thermal density leads to larger and more easily detectable fluxes. The purely thermal (i.e. non-flaring) case has fluxes around 10^{-4} mJy, far more faint than their flaring counterparts.

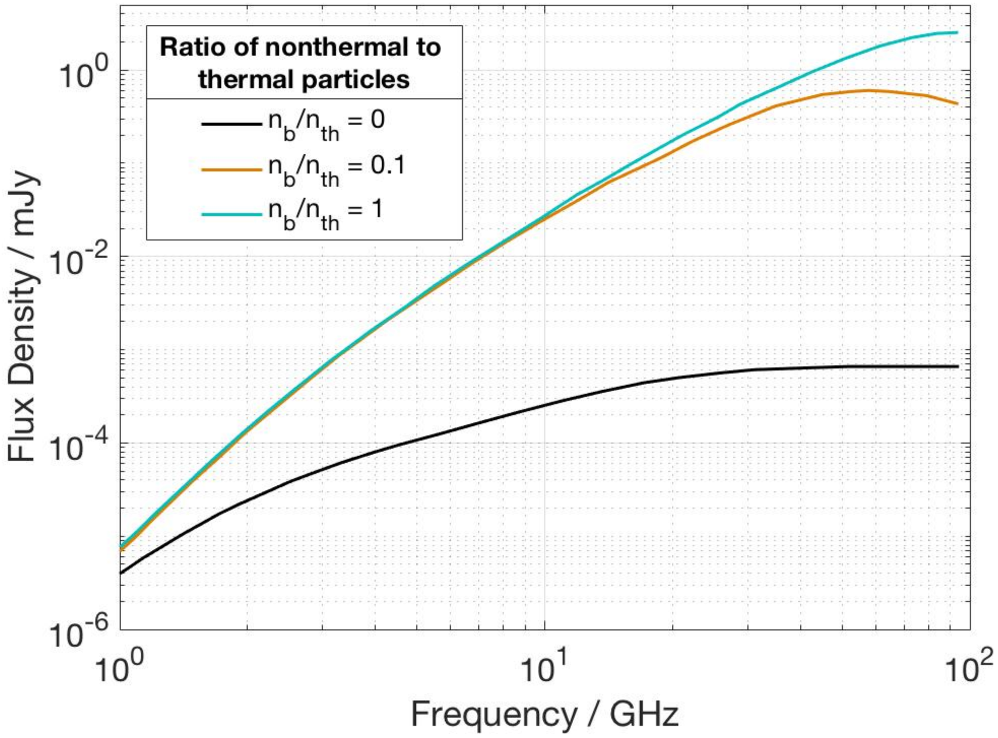

Figure 5.23: Spectra for a varying non-thermal to thermal density ratio where the flux is calculated in mJy at a distance of 140 pc.

Figure 5.24 takes a closer look at how changing the magnitude of this non-thermal density affects the spectra. As before, zero non-thermal particles lead to flat spectra at high frequencies and no non-thermal GS emission. As the non-thermal density is gradually increased, the non-thermal GS component becomes more dominant. The spectra is ‘picked up’, increasing in flux at all frequencies as well as their peak moving to higher frequencies at the highest non-thermal densities. When the non-thermal density is still small compared with the thermal density, there is still an increase in flux from the GS emission, however the thermal component still dominates. This is translated to the spectra as the initial decrease in frequency of the peak flux. As already mentioned, higher frequency observations are critical in understanding the contribution from non-thermal particles to the emission. This is highlighted in this figure, when the dominating thermal component affects the lower flux and frequency emission.

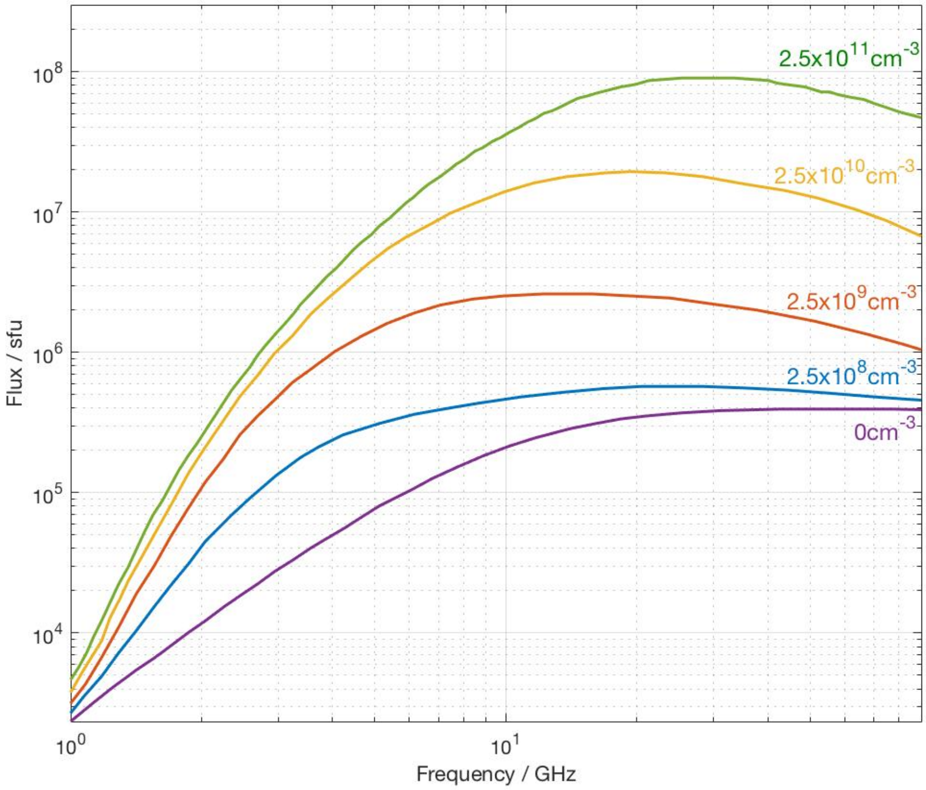

Figure 5.24: Spectra results for varying the flux tube non-thermal density. The flux is again given in sfu.

The effect of changing the non-thermal density is further illustrated by the red points in Figure 5.21. For the purely thermal case, the peak flux is at its lowest but the frequency is high. As is seen in Figure 5.7, for an increasingly high thermal density this peak flux is expected to move to even higher frequencies but not reach the high flux values the non-thermal particles can generate. As the density increases, the frequency of the peak first decreases as the flux increases. However, as the non-thermal component increases above 0.01 times that of the thermal value, the peak of the frequency starts to increase as the non-thermal component becomes more dominant. Flux calculations from single frequency observations may dictate whether the emission is likely to be thermal or non-thermal in origin if the observed flux is sufficiently high.

The effect on the radio and X-ray luminosity of varying this non-thermal density is shown in Figure 5.22. The similar behaviour of the non-thermal density and surface field strength on the peak flux has already been seen in Figure 5.21, so a similar effect is expected for the GB plot. Indeed, it is clear the increasing non-thermal density acts along the same line as the increasing surface field strength. That is; as the non-thermal density increases the radio emission becomes larger, the X-ray emission remains the same, and the model results move away from the Güdel-Benz relation. The X-ray emission measured here is the soft X-ray (SXR) emission generated by a free-free mechanism that depends on the thermal properties of the system. When the thermal density is varied later on, this results in an expected change in X-ray luminosity. At zero and the lowest non-thermal densities, the results lie on the other side of the GB relation. These low (or zero) densities are not representative of flares on T-Tauri stars, which are thought to produce large amount of non-thermal emission following reconnection. Therefore those specific results are not representative of these impulsive flaring events, but are shown here to emphasise the effect of non-thermal particles on radio luminosities. Observations of quiescent phases on T-Tauri stars are expected to fall on this side of the relationship too. The lack of change in the thermal (soft) X-ray emission is expected, as the non-thermal particles introduced into the system produce emission at gyrosynchrotron frequencies.

5.3.3.3 Thermal density

In contrast to the non-thermal density, the variation of the flux tube thermal density is expected to predominately affect this soft X-ray emission. We have already seen in the initial model and its variations that increasing the thermal density leads to a slight decrease in peak flux at radio frequencies. The results of varying this thermal density between the values listed in Table 5.2 in comparison with the T-Tauri flare observations and GB relation are shown in Figure 5.25. The variation of thermal density values is paired with the variation of the field strength between $1 - 4\,\mathrm{kG}$ to obtain a range of possible luminosity values constrained by these parameters.

As the thermal density increases (for any field strength) the X-ray emission increases, pushing the model closer to the GB relation. However, only for the highest thermal density and lowest field strength does the result fall above the GB relation. While a flare from a star with a low field strength may produce results closer to the GB relation, the high thermal densities also required for this to be the case are not realistic for a flare. The combination of both non-thermal and thermal emission is ubiquitously seen from these flares and a thermal density of this magnitude (indicating large amounts of heating and X-ray emission) is likely to also be paired with a non-thermal density similar to this. Inclusion of such a non-thermal density would push this result back away from the GB relation, as indicated in Figure 5.22. The increase in X-ray emission is caused by the heating effects from the increased thermal density. The slight decrease in peak radio luminosity with increasing density is suggested to be due to the dominating thermal emission (as in Figure 5.6). The red numbers overlaid on each model results are the frequencies of the peak in radio emission. As the field strength decreases the frequency of the peak decreases but this value does not

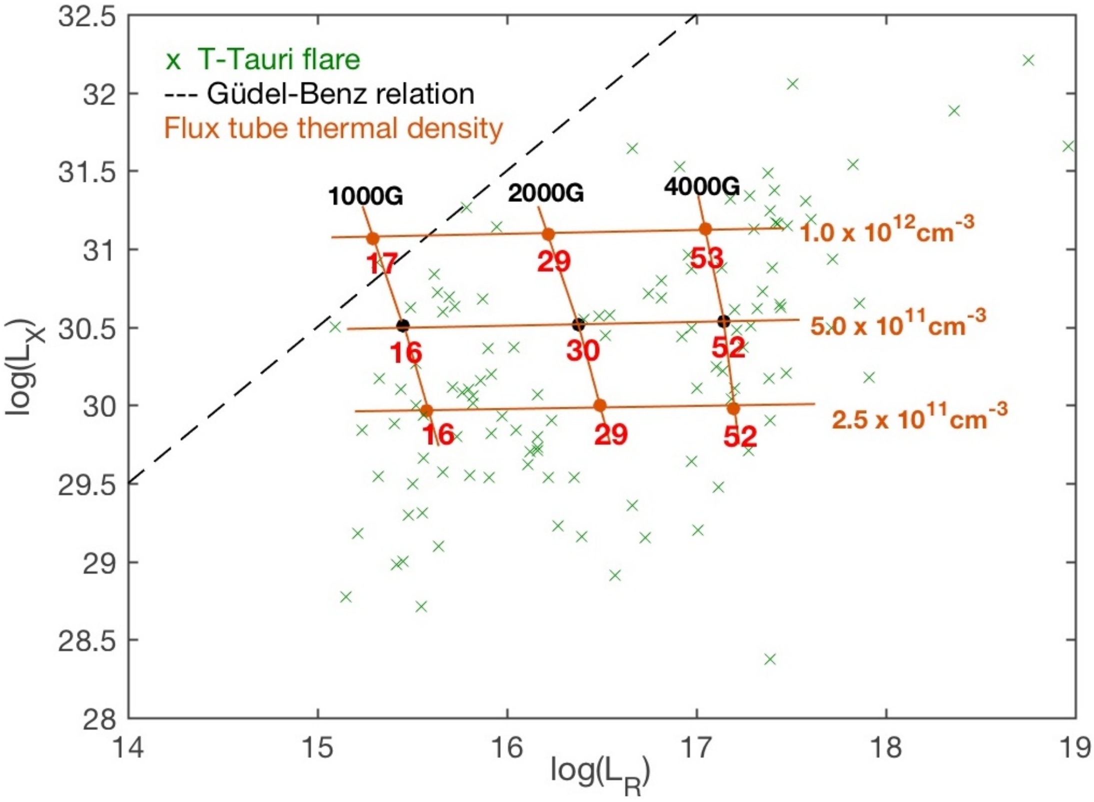

Figure 5.25: Plot showing how varying the thermal flux tube density affects the radio and X-ray luminosity with regard to the GB relation. The changing thermal density is shown by the orange points, with the changing surface field strength shown in black. The red numbers by each model point are the frequencies of the peak radio flux in each model.

change similarly for decreasing thermal density. As the thermal emission increases, the non-thermal GS emission becomes less dominant. The non-thermal components (e.g. non-thermal density and field strength) control this peak and therefore leads to a reduction in the peak flux value. The reduction in peak radio luminosity between thermal density values is most drastic for the lower field strengths, demonstrating how this effect is more prevalent when the parameters affecting non-thermal emission have a less dominant role.

5.3.3.4 Temperature

Results from altering the flux tube temperature between the minimum and maximum range typically observed from T-Tauri flares are shown in Figure 5.26. Again, the magnetic field strength has also been varied between $1-4\,\mathrm{kG}$ to constrain the luminosity range in a grid. The frequencies of the peak radio luminosities are again overlaid for each model result.

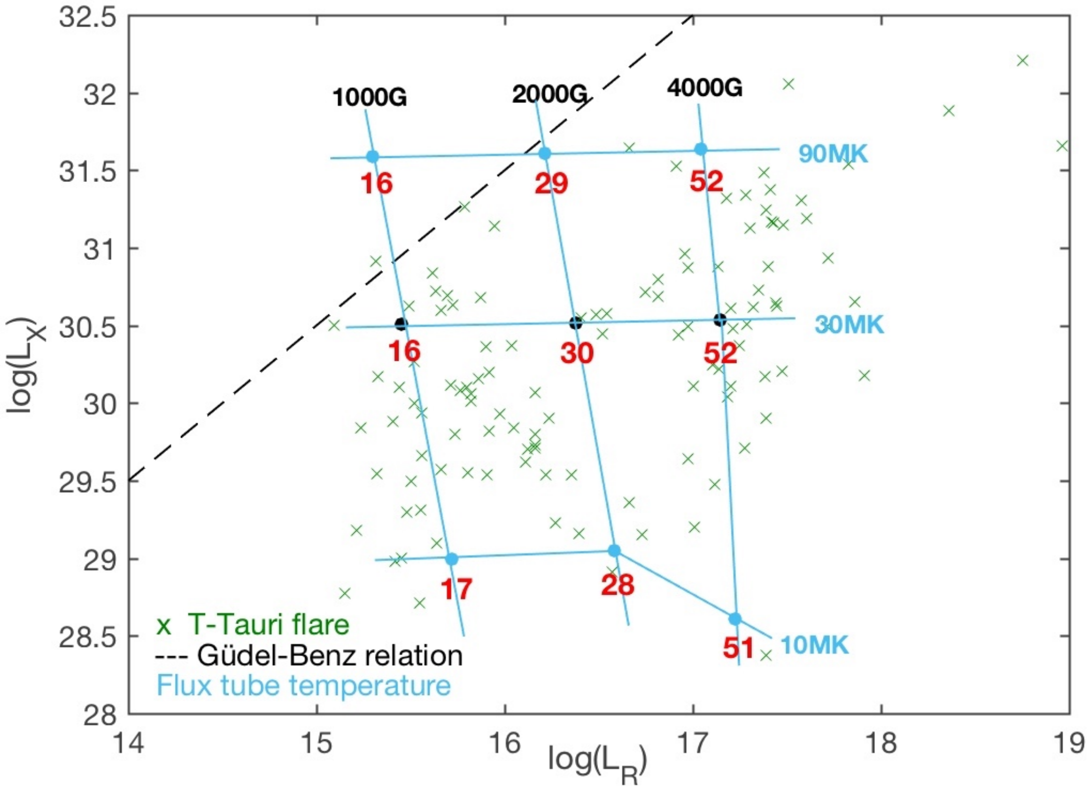

Figure 5.26: Plot showing how varying the flux tube temperature affects the radio and X-ray luminosity with regard to the GB relation. The changing temperature is shown by the blue points, with the changing surface field strength shown in black. The red numbers by each model point are the frequencies of the peak radio flux in each model.

Similar trends are observed as for the varying thermal density, as expected. Increasing the temperature does not lead to an increase in the radio luminosity, instead causing more thermal emission in the form of X-rays. The decrease in radio luminosity is again most prevalent at lower field strengths where there is less non-thermal emission. The highest flux tube temperatures (90 MK) produce models closest to the GB relation, with the lowest field strength model (1 kG) for this case falling above the relation. Again, a flare with such a high temperature but no corresponding increase in non-thermal density is not assumed to represent flaring from a star-disk interaction on a T-Tauri star. The spread in the grid for temperature variation is much larger than for thermal density, however the results still all agree well with observations.

5.3.3.5 Flux tube width

Varying the width of the flux tube alters the size of the emitting region. As such, these results in Figure 5.27 show how the size of the flux tube affects both the thermal and non-thermal emission. As the flux tube width increases for a fixed field strength, the X-ray and radio emission both increase as both the thermal and non-thermal emitting volumes are consequently increased. For varying flux tube width, the models move parallel to the GB relation. It is only the individual thermal and non-thermal parameters that affect the movement towards or away from the GB relation. Additionally, as the width increases, the frequency of the peak radio flux also increases. This is expected from the increase in non-thermal radio emission.

5.3.3.6 Power law index

The non-thermal electrons are given a single power law distribution in energy, with a power law index of δ as given by Equation 5.5. The range of power law index values appropriate for gyrosynchrotron emission is $2 < \delta < 7$ [Dulk, 1985]. A standard value of 3.2 is chosen for this model (as suggested by the GX simulator) but is now varied between these values. A value of 3 or lower is often applied to the impulsive phase of solar flares (Benz and Güdel [2010], Fletcher et al. [2011]).

The resulting spectra from this power law index range is shown in Figure 5.28. As discussed in Chapter 4, a higher power law index reduces the number of higher energy

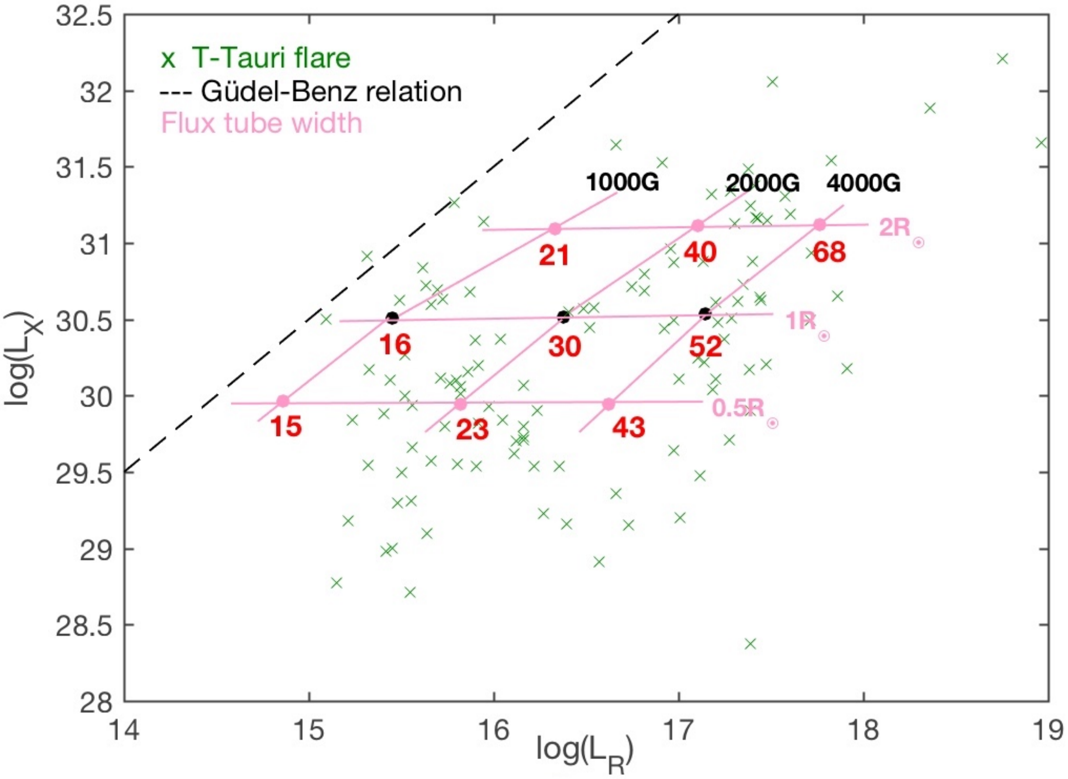

Figure 5.27: Plot showing how varying the flux tube width affects the radio and X-ray luminosity with regard to the GB relation. The changing width is shown by the pink points, with the changing surface field strength shown in black. The red numbers by each model point are the frequencies of the peak radio flux in each model.

electrons and for the highest values the particle spectra appears approximately thermal. This is illustrated in Figure 5.28, with the highest value of delta ($\delta = 7$) producing a spectra very similar to that of the zero non-thermal particle spectra from Figure 5.24. As the power law index decreases, the contribution of emission from higher energy non-thermal particles increases and the spectral peak moves to higher fluxes and frequencies. At the smallest power law index values the contribution of GS emission from the non-thermal particles dominates and the peak moves above 100 GHz.

This time-independent model has provided some useful insight into the parameters involved in a flare. Each of these parameters affects the flux over a range of frequencies, how high it peaks, as well as the frequency of that peak. There is some

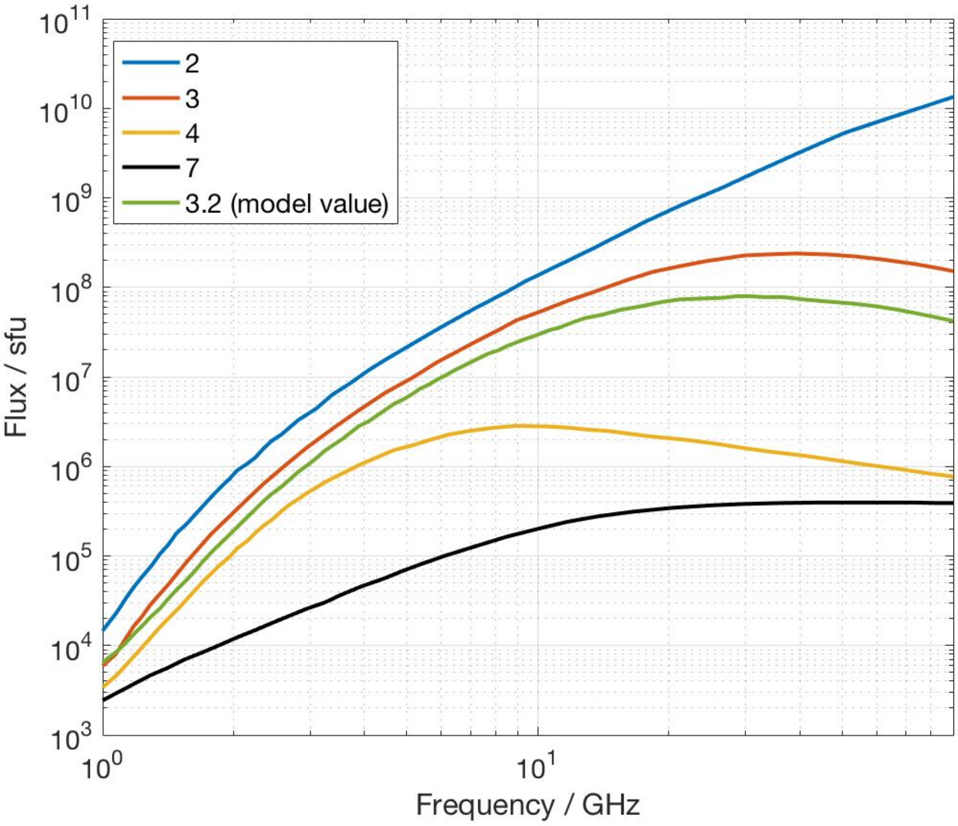

Figure 5.28: Spectra for varying the power law index between $\delta = 2$ and $\delta = 7$.

degeneracy between these variables however. The non-thermal density, magnetic field strength and power law index all produce similar effects on the gyrosynchrotron emission when varied. These effects are focused on the overall peak radio flux, as well as at what frequency this peak occurs. In contrast, the thermal parameters (flux tube thermal temperature and density) control the thermal X-ray emission and also the behaviour of the spectra at lower frequencies within the considered parameter ranges. This model has enabled us to see the effect on constraining some of these parameter values with regard to observations of T-Tauri flares and the GB relation. Nearly all the models agree with the observational results and show an overproduction of radio emission when compared with this relation. It is thought to be an overproduction of non-thermal radio, not underproduction of X-ray, because of the behaviour of the models when the parameters are varied. That is to say, it is the non-thermal density values varied that cause the increase in radio emission seen but that easily fall within the observed range of densities seen from T-Tauri flares. Conversely, there is no reason to suggest that if the non-thermal radio emission from a flare was as predicted there would be a suppression (or underproduction) of X-ray emission. The deviation is more likely to be from an increased radio flux, possibly generated from more frequent reconnection events in the large magnetospheres where the non-thermal particles have longer loop lengths to emit along. Decreasing the thermal parameters (and causing a smaller X-ray flux) while not simultaneously decreasing the non-thermal parameters is not indicative of a flare where both emissions are significant and co-dependent. To produce results that fall on or above the GB relation requires thermal values that are far higher than is currently reported in these flares. These thermal values are thought to be unrealistic as the flares they are a result of would also produce large amounts of non-thermal emission following on from the theory of reconnection and particle acceleration. Drastically increasing the thermal component, and not the non-thermal component, is not indicative of a reconnection driven flaring process occurring.

The results of this model suggest that more comprehensive observations of these flares are needed. In particular, multi-frequency and simultaneous X-ray and radio observations are required to better constrain the nature of the flaring emission. Future missions such as Athena [Barcons et al., 2017] and the high time cadence proposed for the SKA [Fuller et al., 2015] will hopefully fulfil this, with this model providing a useful guide to interpreting any observations. While this model is useful in investigating the peak emissions from a flare, the radio emission observed in T-Tauri flares is known to vary similarly to solar flare emission, i.e. peaking sharply and then decaying slowly over time. To investigate this, a model that calculates the gyrosynchrotron emission from a flaring T-Tauri star over a period of hours is now developed. The emission over the whole star and disk as well as the flux tube will be calculated, so as not to exclude the propagation and loss effects of the particles over time.

Chapter 6

Time dependent modelling of a T-Tauri flare

In Chapter 5 the 3D GX simulator was used to calculate the radio and X-ray emission from a region representing a flaring magnetic loop from a T-Tauri star interacting with its circumstellar disk. Parameter ranges for variables defining the flaring flux tube (e.g. densities and temperatures) were investigated and all the models were compared to the GB relation. Nearly all results agreed with the observations of T-Tauri flares and suggested these events over produce radio emission when compared with flares on other stars. This radio emission will now be investigated further. Several components of the original model will be changed and are outlined in the following sections. The key difference is that of the time variability of the radio emission. Before, only the peak values of a flare and the emission at that instant were calculated. Now, the gyrosynchrotron emission is calculated over a period of 8 hours. The gyrosynchrotron emission is calculated with a simpler form of the 3D GX simulator, which still uses the fast gyrosynchrotron codes developed by Fleishman and Kuznetsov [2010] but this time acting along singular lines of sight (LOS). Outputs from a 3D magnetohydrodynamic (MHD) model (e.g. temperature, magnetic field) of flaring activity on a classical

T-Tauri star performed by Orlando et al. [2011] are combined with a flux tube model and the fast gyrosynchrotron codes are then used to calculate the GS emission. The flux tube, populated with a distribution of non-thermal electrons, is added to the model in order to simulate the variable gyrosynchrotron emission produced by the system over time. The gyrosynchrotron emission will now be calculated in the $1 - 1000\,\mathrm{GHz}$ frequency range.

A diagram describing what will be simulated is shown in Figure 6.1. The MHD data is generated from a T-Tauri star surrounded by an accretion disk. A flux tube is created that interacts with the inner edge of the disk. This interaction occurs in a high temperature region that represents the reconnection site, from which the non-thermal particles within the flux tube gyrate down from. We are therefore still simulating a similar classical T-Tauri flaring scenario as in Chapter 5, but this time with a more comprehensive model of the entire flux tube and how the non-thermal particles within it are distributed in space and over time.

6.1 Fast GS simulations

As discussed in Chapter 4, the 3D GX simulator described by Nita et al. [2015] implements the fast gyrosynchrotron codes developed by Fleishman and Kuznetsov [2010]. These codes allow for the computation of GS emission by solving the radiative transfer equation along singular lines of sight and have been adapted here in a model which will now be referred to as the 'fast GS simulations'. There are many advantages of using this more flexible model over the 3D GX version. Firstly, as we are dealing with MHD data from a T-Tauri star over time this data can be directly imported into the routine. The 3D GX simulator instead takes single values of a parameter (e.g. flux tube temperature) each time. The emission maps of the flux tube that the 3D GX simulator

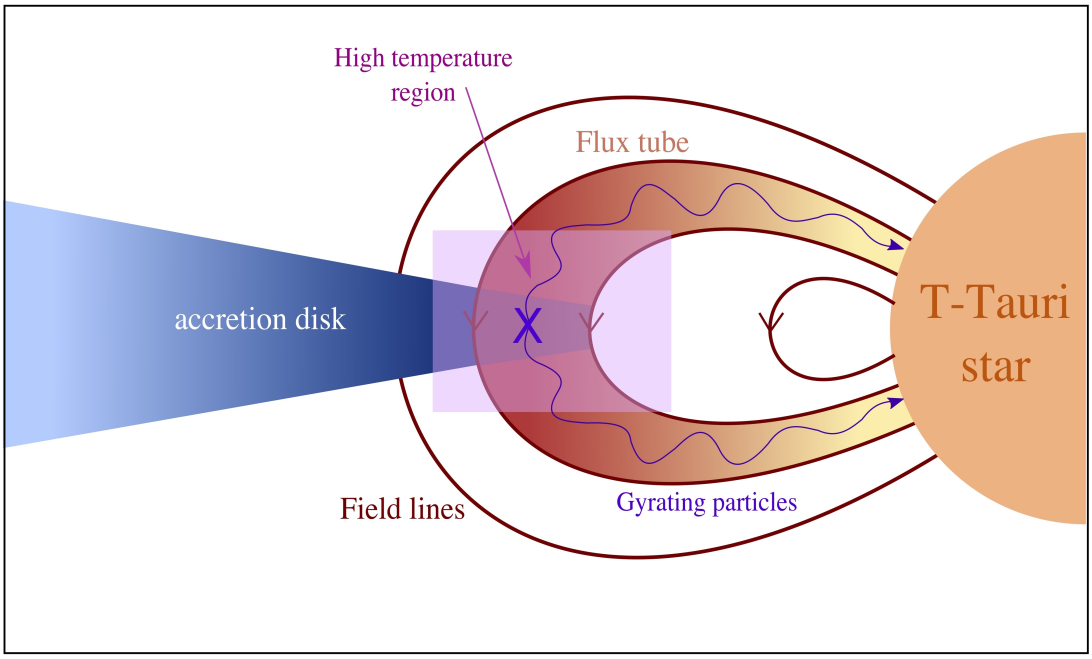

Figure 6.1: Diagram depicting a star-disk interaction between a classical T-Tauri star and its accretion disk. A magnetic flux tube links the stellar surface to the inner edge of the disk and non-thermal particles gyrate towards the surface from the reconnection of field lines at the high temperature X-point within the loop's apex.

produces are ultimately unnecessary when comparing radio emission results to observations as these regions are not able to be resolved and are discarded in the fast GS simulations, saving on computation time. The fast GS simulations is in general a more malleable and beneficial model for our use, and we are more easily able to calculate the emission from a T-Tauri star (not the Sun with a T-Tauri flux tube) hundreds of parsecs away.

Both this model and the 3D GX simulator are derived from the same fast gyrosynchrotron codes despite their different main uses. Two models are developed with approximately the same flaring parameters to investigate how the spectra from each simulator differs because of this. These results are shown in Figure 6.2. The spectrum from the 3D simulator is calculated from a single pixel at the apex of a flux tube with a loop top field strength of 180 G. The thermal and non-thermal flux tube densities were set at $10^8\,\mathrm{cm}^{-3}$ and $5\times10^7\,\mathrm{cm}^{-3}$ respectively. The lower density values were chosen over those in Chapter 5 so the spectrum would be shifted to lower frequencies so the behaviour in the optically thin limit could be seen. The same parameters were set in the fast GS simulation. The 3D simulator also includes emission from a background with predefined temperature and density, whereas the fast GS simulation does not for this basic model. The spectra generally have the same profile up to 10 GHz, peaking around the same frequency but with different peak fluxes. An exact match was not expected due to the different natures of the simulators. At high frequencies, above 10 GHz, the 3D simulator continues producing high fluxes whereas the fast GS simulation version drops off rapidly. This is due to the increased free-free emission from the background component which is detectable at these higher frequencies.

The 3D MHD data that will be used in the fast GS simulation describes a CTT star surrounded by an accretion disk. Figure 6.3 illustrates how the simulator is used related to this set up. The gyrosynchrotron emission (including free-free emission) is calculated along singular lines of sight along either the X, Y or Z direction. These lines of sight are made up of individual nodes of specific length and cross section which can be altered within the simulator. The LOS can be chosen to pass through any region, and the emission over entire planes (i.e. integrating the emission over all lines of sight) will eventually be calculated. The results obtained from this model will be calculated along all three LOS. The emission is not calculated along an inclination angle specific to any T-Tauri star. This allows for more flexibility in interpreting the results from multiple LOS, not limiting us to one inclination angle. The X and Y LOS are angled edge on parallel to the disk. The Z LOS acts perpendicular to the plane of the disk. This multiple but generic LOS approach will also inform us about how the circular polarisation is affected from the different angles.

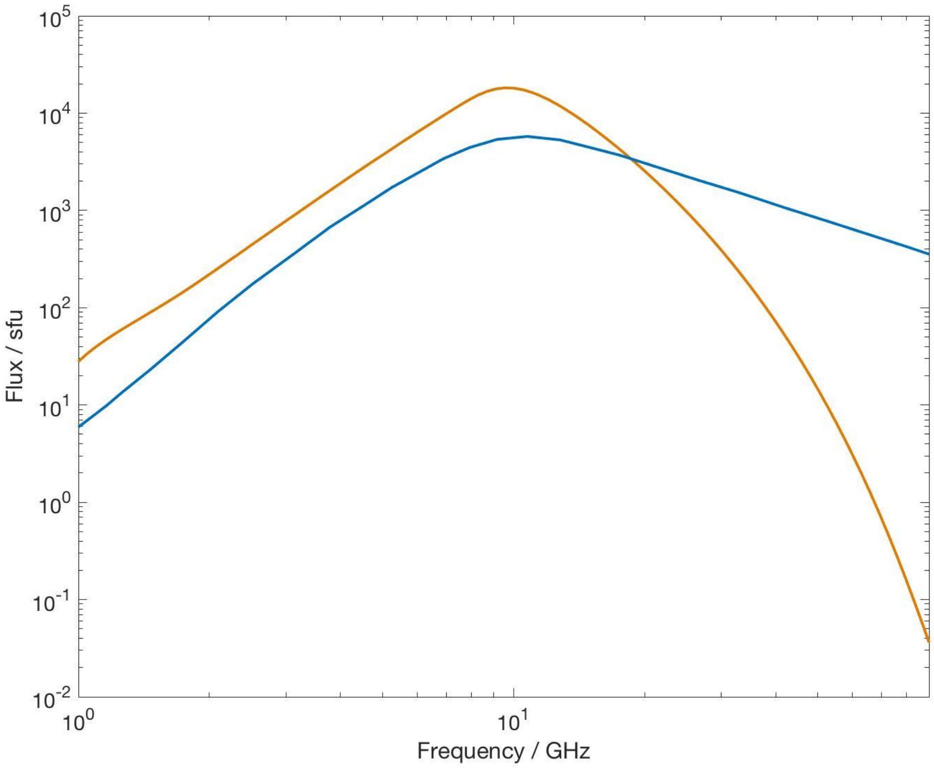

Figure 6.2: Comparing the radio spectra generated by the fast GS simulations (orange) and 3D GX (blue) simulator from models with similar flaring parameters. The frequency range is $1 - 100\,\mathrm{GHz}$ and the flux is given in solar flux units.

6.2 3D MHD data

The data used in this model originates from the 3D ideal MHD simulation performed by Orlando et al. [2011]. A classical T-Tauri star with a mass of $0.8\,\mathrm{M}_\odot$, radius of $2\,\mathrm{R}_\odot$ and dipolar surface field strength of 1 kG aligned with the rotation axis is used. The stellar corona is initially isothermal with density $10^8 - 10^9\,\mathrm{cm}^{-3}$ and temperature 4 MK. The star is surrounded by a thick, dense, quasi-keplerian disk. The disk is initially isothermal ($8 \times 10^3\,\mathrm{K}$) with a truncation radius of $2.86\,\mathrm{R}_*$. The corotation radius, defined as the radius around the star at which a Keplerian orbit has the same angular velocity as the star's surface, is $9.2\,\mathrm{R}_*$. The star itself rotates with a period of 9.2 days about an axis coincident with the normal to the disk mid-plane.

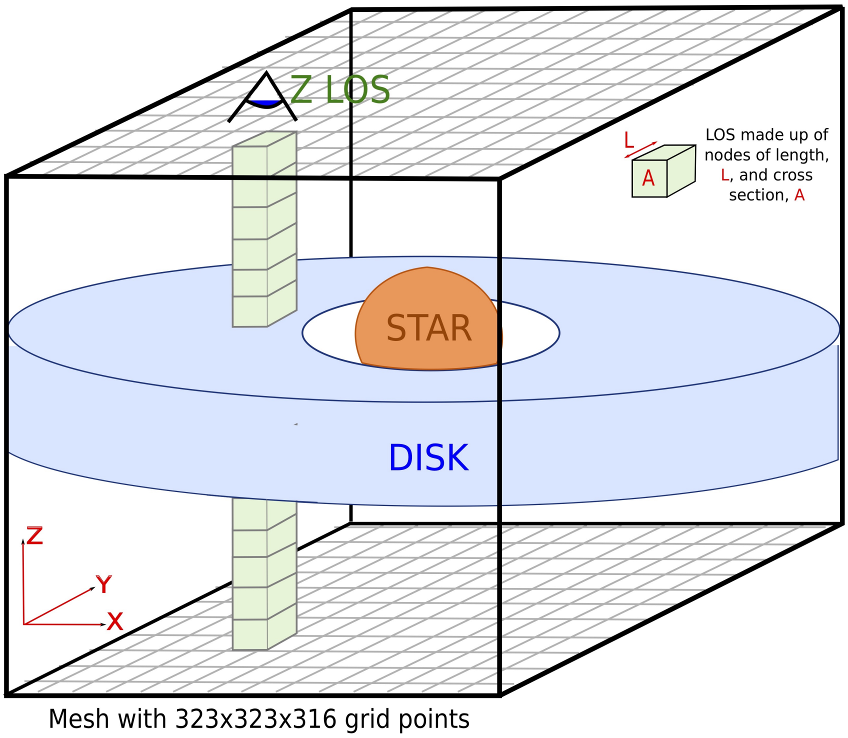

Figure 6.3: Diagram displaying how the fast GS simulation works. The MHD data is provided in (323x323x316) 3D arrays. The fast GS simulation calculates the emission along singular lines of sight within these arrays and can be chosen to pass through any point in the X, Y and Z directions.

The model takes into account the disk viscosity, gravitational force, magnetic field orientated thermal conduction, and radiative losses from optically thin plasma. The model uses a transient heating component to simulate a flaring event, which is allowed to evolve through the system over time. The heat pulse is switched off after 300 s and is initiated at a radius of 5 R_* from the stellar surface, just past the surface of the accretion disk. The heat pulse leads to the generation of a hot flaring loop between the disk and the star, a result of heating propagating along the field lines toward the star. This hot loop can be seen in the temperature plots of Figure 6.4. All three panels show the central star, the dipolar field lines, the cold accretion disk and the hot loop joining the star and disk. The first panel shows the loop edge on along the Y LOS (but not obscured by the disk in this case). The second panel shows the Z LOS, looking down onto the disk. The third panel shows the star and disk system with the flaring loop at a different inclination. These 3D views of the system and flaring loop were taken 1.2 hours after the initial heat pulse was triggered. The density and temperature vary throughout the simulation time, with the heat pulse leading to accretion funnels being formed onto the star.

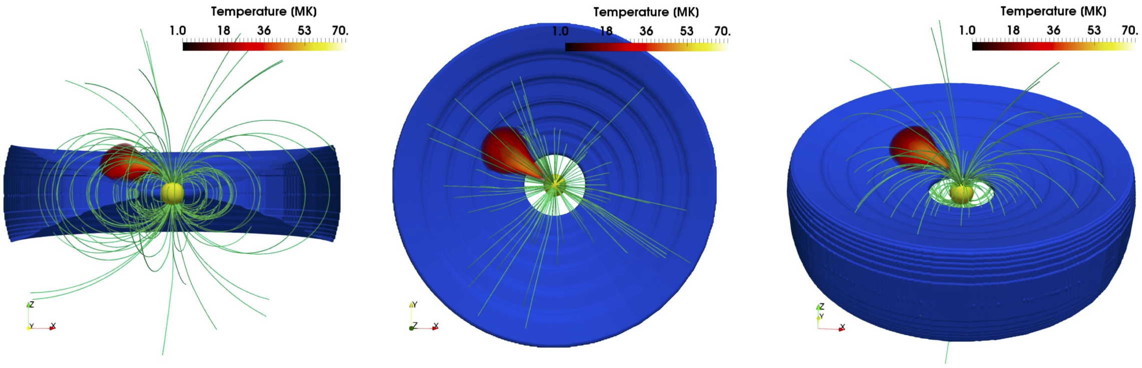

Figure 6.4: Illustration of the hot flaring loop that develops in the MHD simulation 1.2 hours after the heat pulse is switched on. Three different views of the star and disk system are shown.

6.2.1 Density and temperature evolution

Figure 6.5 shows the evolution of the density and temperature throughout the system at 24, 3144 and 9917 s after the heat pulse is switched on. From the temperature plot at 24 s it is shown how the heat pulse from which this loop evolves is initially confined to a small area. This heat pulse is used to simulate a flaring event in this ideal MHD model. The reconnection of field lines is not modelled, but the sudden and intense heating localised to one region is instead used to represent the flare initiation. As the heat is conducted to the surrounding disk regions, some of the disk material evaporates. Some of this material is funnelled through the loop and contributes to accretion onto the star. Most of this material however is not confined to the field lines and propagates

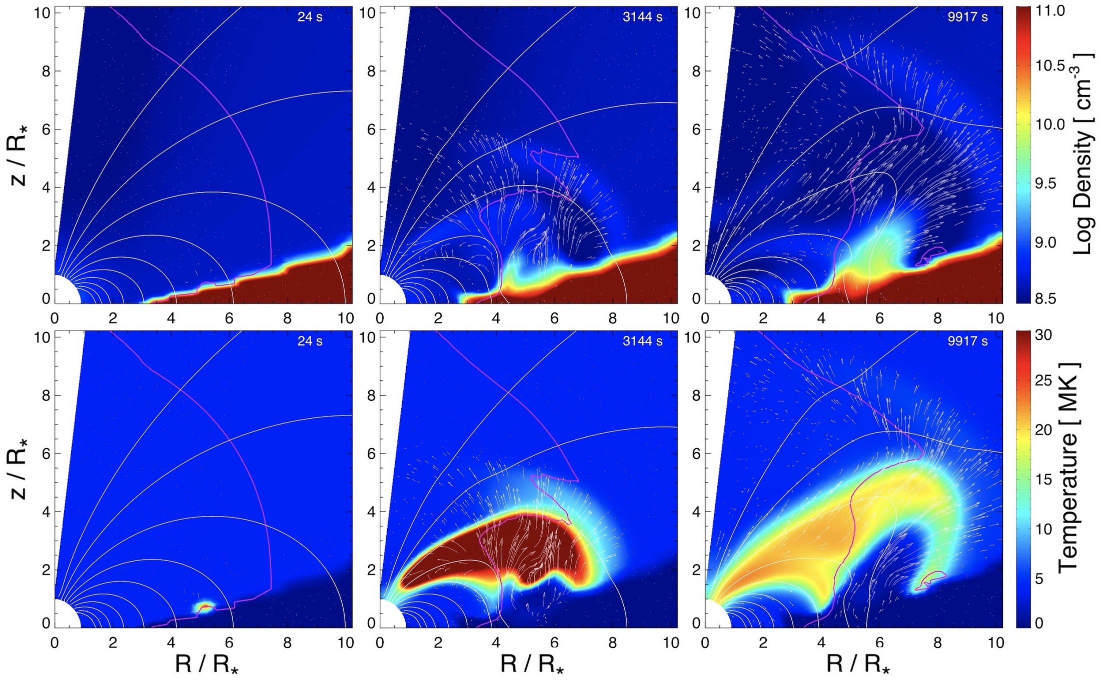

Figure 6.5: Density (top) and temperature (bottom) evolution at 24, 3144 and 9917 s after the heat pulse is switched on. The white lines are sample field lines, the white arrows show the velocity field and the pink line denotes the β_P (plasma beta, the ratio of the plasma's thermal pressure to magnetic pressure) < 1 area. The plots display the temperature and density from a plane perpendicular to the XY plane that passes through the middle of the hot flaring loop that develops.

away into the corona. This is observed in the velocity field of Figure 6.5. The larger structure of the loop originating at the heat pulse region is clear at the later time shots in these profiles.

The results from this model provided a flaring loop length, maximum temperature and peak X-ray luminosity that were all comparable to observations of T-Tauri flares (Favata et al. [2005], Orlando et al. [2011]). The length of the flaring loop that develops is approximately 10^{12} cm which agrees with the larger loops predicted by the scaling relation in Figure 3.11. The peak X-ray luminosity is $\log L_X$ [erg s^{-1}] = 32.8 which is at the higher end of observations of X-ray emission observed from T-Tauri flares according to Figure 3.14. Figure 6.6 shows the evolution of the emission measure and temperature over time. The temperature peaks first, as described in Section 3.3.1, dropping by nearly an order of magnitude by the time the emission measure peaks. The temperature rises quickly and peaks around nearly 1000 MK whilst the heat pulse is still active. This is far larger than typical T-Tauri flaring temperatures reported from observations. However, the plasma temperature drops quickly due to thermal conduction and radiation when this is switched off. When the emission measure peaks the temperature is around 100 MK, which is more consistent with observations of the hottest X-ray flares [Tsuboi et al., 1998].

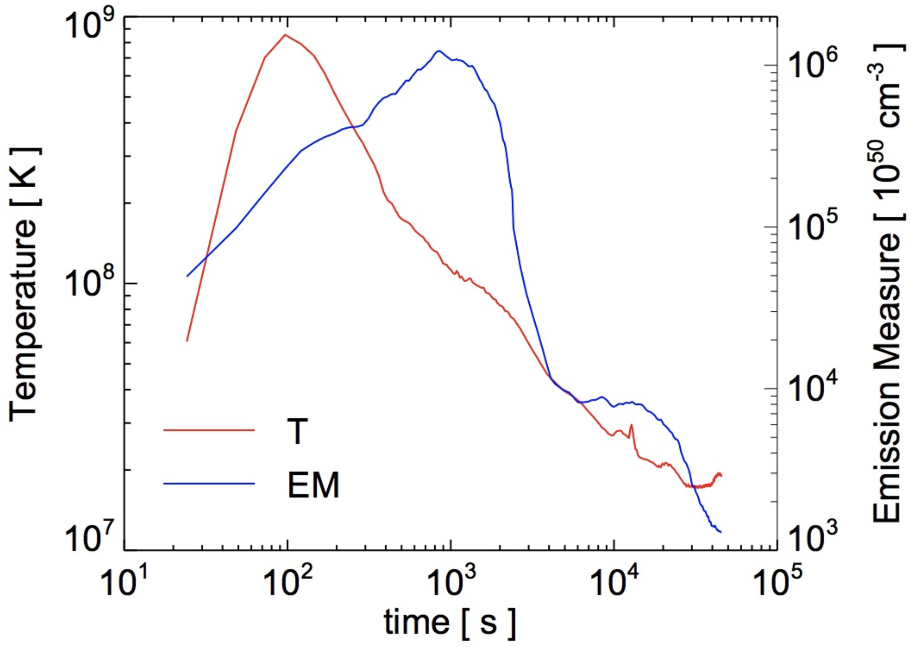

Figure 6.6: Figure from Orlando et al. [2011] of the emission measure and temperature over time (in s) in the 3D MHD model. The temperature (red) is given in K and the emission measure is given in units of 10^{50} cm^{-3}.

Figure 6.7 shows the evolution of the temperature between 96 and 9917 s. Each panel is a slice in a certain plane. The X LOS image shows the YZ plane at the point along the X axis where the heat pulse is initiated. The Y and Z LOS images are the same, but in the XZ and XY plane respectively. All three images are shown at both times, and all in the same plane that passes through the centre of the heat pulse site.

It is clear from these images that the peak temperature drops significantly between 96 and 9917 s in that region. The high temperature material is highly localised in the early time shot for all lines of sight. After the heat pulse is switched off there is significant heating of the coronal environment including the development of the hot loop, clear in the X and Y LOS images at 9917 s. Along all LOS the disk remains cold compared to the surrounding coronal material.

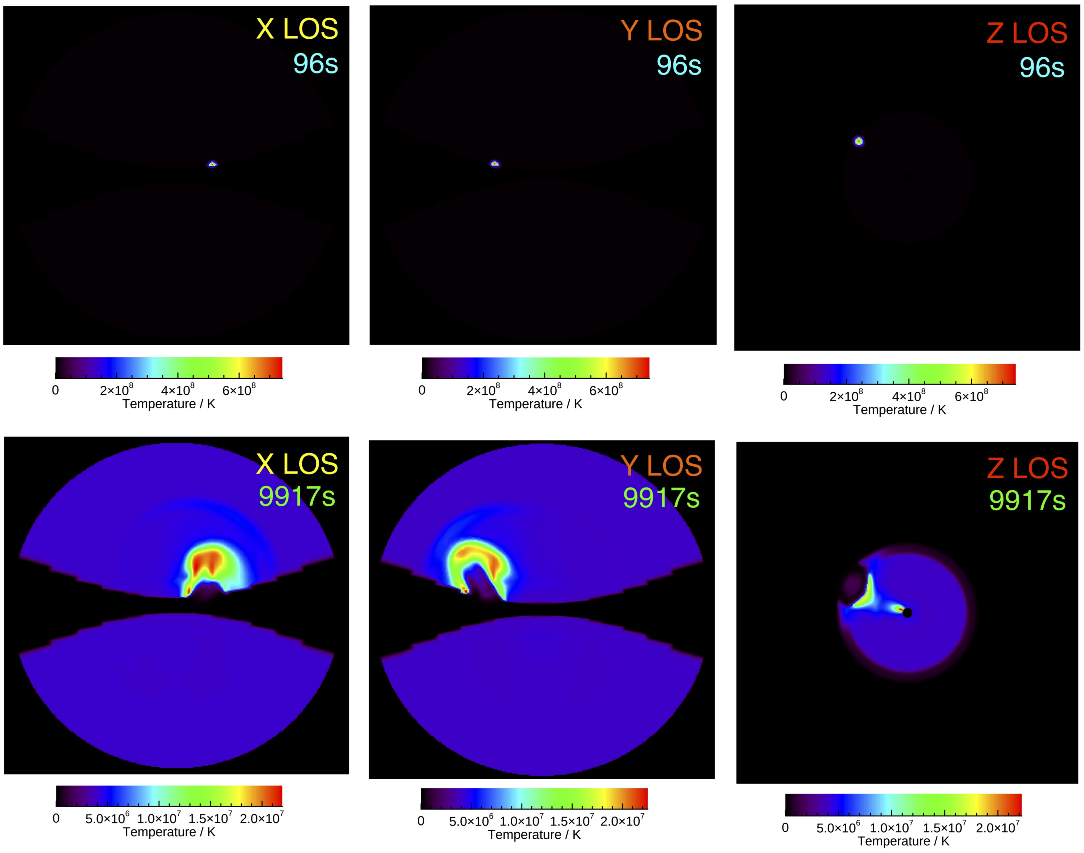

Figure 6.7: Temperature plots in the X, Y and Z planes that pass through the heat injection site at 96 and 9917 s. The colour bars indicate the temperature range for each individual plot, measured in K.

The exact behaviour of the temperature through the LOS passing through the heat pulse site is shown in Figure 6.8 for the same LOS's and time shots as in Figure 6.7. All temperature profiles are shown varying along the LOS which is made up of either 323 or 316 grid points. The total grid domain for each data set has a size of (323x323x316).

So, for example, the temperature profile along the X LOS runs from 0 to 323 grid points where the heat pulse injection site is located at 116 grid points. The corresponding Y and Z injection site grid points are at 195 and 168 respectively. Each profile is therefore generated according to these coordinates, e.g. the X LOS temperature profile is taken for the Y-Z coordinates (195,168). Both time shots (96, 9917) are taken according to these coordinates for comparison.

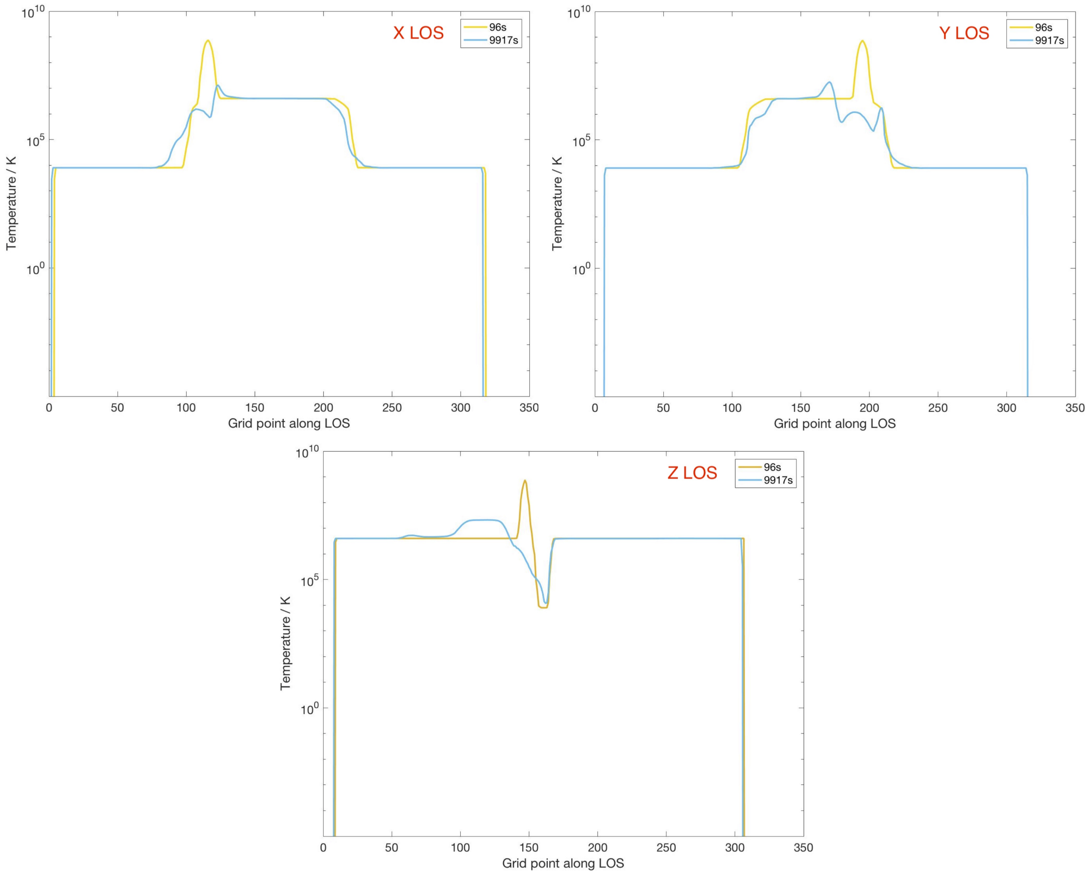

Figure 6.8: Temperature profiles (in K) along the X, Y and Z lines of sight that pass through the heat pulse site at 96 s (yellow) and 9917 s (blue). The X-axis denotes the number of grid points, or how far along the line of sight the temperature is taken at.

For the X LOS in Figure 6.8 the temperature is highly peaked around the injection site at 96 s. The secondary plateau like increase in temperature signifies the temperature increase of the corona, decreasing again to below 10^4 K in the cold disk. As the X

LOS passes through the disk parallel to its plane, the temperature remains at this value for the majority of the way along the LOS. Only rising when within the truncation radius or heat pulse region. At 9917 the temperature peaks closer to the star but at a much lower magnitude. The temperature distribution is more spread out around the initial injection site as more material is heated over the simulation period. The corresponding Y LOS image is very similar, however the profiles are mirrored to reflect the opposing LOS chosen.

The Z LOS passes from the corona into the top of the disk and beneath it. Therefore unlike the X and Y LOS there are not the two plateaus in temperature seen after the primary peak in temperature (from the corona and then disk). Instead, the temperature profile mainly shows the behaviour of the coronal temperature. At 96 s, it rises sharply in the injection site region and then drops sharply as the LOS is in the vicinity of the cold disk. In the outer region of this LOS it is again showing the temperature profile of the warmer corona (see Figure 6.3). At 9917 s the distribution is more spread out, due to the heating of the upper area of the disk material where the heat pulse was. The peak of the temperature at this later time is flatter and lower in magnitude, occurring higher in the corona due to the cooling via conduction and evaporation of heated material through the system.

6.2.2 Spectra with no added fluxtube

The temperature, thermal density and magnetic field are the components of this model that are supplied by the 3D MHD data. The other parameters, such as the non-thermal electron density, will be set individually and are discussed later. Beforehand, it is worthwhile considering how the GS emission calculated from this 3D MHD data alone behaves in time. As we are not adding any non-thermal particles to the system, we call this run the purely thermal case. The GS spectra at 96 and 9917 s are shown in Figure 6.9. The flux units are shown in mJy, calculated for a distance of 140 pc (approximately that of the Taurus star forming region [Mooley et al., 2013]). From now on, any result is from the integration over all LOS in the plane specified. These thermal spectra are produced by integrating over every Z LOS. In general unless otherwise specified, the results will always be generated from the Z LOS where there is less obscuration from the dense disk material.

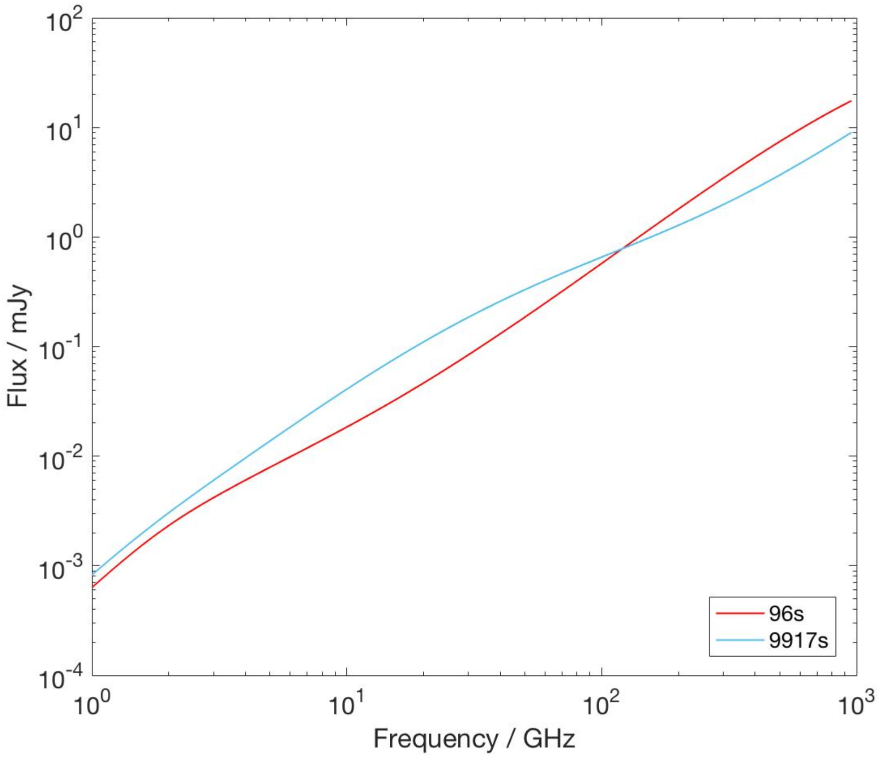

Figure 6.9: GS spectra of the MHD data at 96 s (red) and 9917 s (blue) along the Z LOS. The entire plane has been considered, i.e. the emission calculated by integrating over all lines of sight. The flux is calculated in mJy for a distance of 140 pc.

In general, both spectra show the same behaviour. They both steadily increase in flux over several orders of magnitude between 1 and 1000 GHz. Below 100 GHz there is slightly more flux produced at later times. This is due to the increase in heated material through the system (as seen in Figure 6.7 and 6.8). Most of this emission originates in the coronal region and so is not obscured in the optically thick region of the disk. However, at high frequencies (between 100 and 1000 GHz) the dense disk material is optically thick to the free-free emission and produces high fluxes. The highest of these fluxes is for the 96 s spectra. This is a result of the higher densities present nearer the start of the simulation closer to the period when the heat pulse is still active. This spectra behaviour has been seen before in the highest density cases in Chapter 5 where the thermal flux tube density was varied with no non-thermal particles present. As the flux tube density rose (to values similar to that of the disk) the spectra did not peak or plateau but instead rose sharply over the frequency range. The spectra for the thermal case at other times are not shown here but display similar flux profiles.

In solar physics, sub-THz observations are useful in examining flaring plasma [Stepanov and Zaitsev, 2016]. Solar flare observations in this high frequency range show a similar behaviour as above, characterised by high fluxes and a rising spectrum with increasing frequency. Sub-THz solar flares have been modelled previously (e.g. by Kontar et al. [2018]), also assuming a free-free emission mechanism, and were found to agree well with existing observations at these frequencies. The magnitude of the flux values differ between the two types of flare however, with sub-THz solar flares reaching 10^4 sfu compared with this more powerful T-Tauri flare reaching around 10^9 sfu at sub-THz frequencies.

6.3 Flux tube model

To model the gyrosynchrotron radiation emitted from this flaring T-Tauri star over time, a flux tube populated with non-thermal electrons is added to the simulation. The magnetic flux tube that contains these non-thermal electrons is defined by the magnetic field lines that thread the initial injection site region. These field lines are selected and then traced to the footpoints on the stellar surface. At all times, the flux tube is comprised of these same field lines. The flux tube that contains these field lines is then populated with a density of non-thermal electrons. A visualisation of sample field lines that make up this flux tube is shown in Figure 6.10. Four different time shots are shown, but the field lines chosen are exactly the same, anchored at their footpoints on the stellar surface.

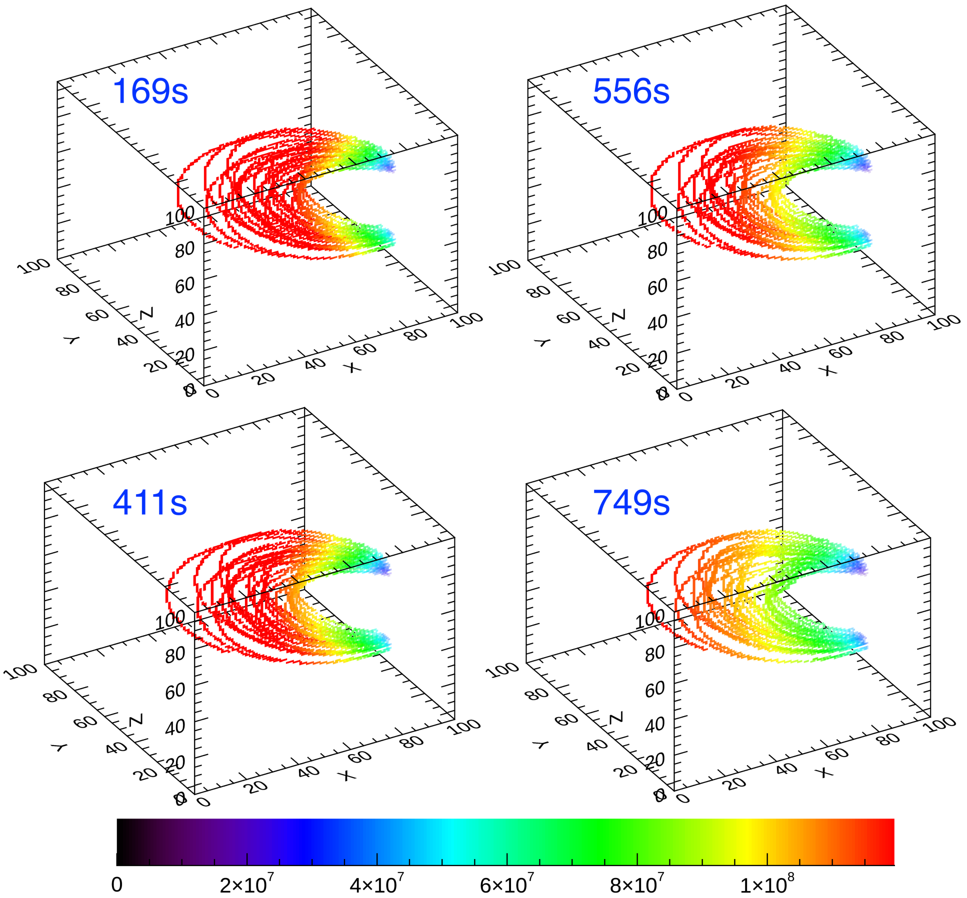

Figure 6.10: 3D visualisation of sample field lines within the flux tube and how the non-thermal particle density is distributed at four different time shots after the heat pulse is switched on. The colour bar units are cm^{-3}.

The density of the non-thermal electrons is set to vary along the loop, according to the simple Gaussian:

$$n = n_o e^{-\frac{l^2}{s^2}} \tag{6.1}$$

where n is the non-thermal particle density (cm^{-3}), n_o is the loop top density, l is the distance from the loop top to a footpoint, i.e. the loop half length, and s is the confinement length scale. Such a distribution is used for modelling solar flare non-thermal electrons, e.g. Fleishman et al. [2018]. Varying this s factor controls the distribution of particles along the magnetic field lines. A smaller value of s leads to more confinement near the loop top. A standard value of s is chosen so the electron number density is smallest at the footpoints but so that there are still particles present there. The s factor is initially set as being equal to l (the loop half length) but is varied in Section 6.5.2. This density distribution is shown in terms of the field lines within the flux tube in Figure 6.10. These are sample field lines to illustrate the electron distribution along the loop with regards to the relevant field lines. In the simulation, the flux tube itself does not have any empty gaps between the field lines where there are no non-thermal electrons present.

The value of the non-thermal density along the loop is dictated by the loop top density n_0. This loop top density is set to be 10% of the thermal density at that point up to 300 s. After that, the loop top density value is set to be 10% of the thermal density at that location at 300 s. This value, as seen in Figure 6.5, is lower than previously used in Chapter 5 however the ratio of thermal to non-thermal particles is more important than the absolute value here. The non-thermal electrons have an electron energy distribution defined by a single power law as in Equation 5.5. As before, the power law index, δ, is set at 3.2 throughout the simulation with the energy range still $10\,\text{keV} < \varepsilon < 10\,\text{MeV}$. The electron pitch angle distribution is assumed to be isotropic. This power law index is varied later in Section 6.5.1.

6.3.1 Electron lifetimes

The simulation itself in Orlando et al. [2011] runs for 48 hours however we are concerned with the period of initial flare activity so only consider the data up to approximately 9 hours. There are 23 time shots of data ranging from 24 to 31688 seconds after the heat pulse is initiated. There are 6 time stamps of data available before the heat pulse is switched off at 300 s, the rest falling after this period when the flare loop develops. We do not consider time periods after 9 hours as we are concerned with the variability in radio emission due to the presence of non-thermal electrons. These non-thermal electrons are likely to be lost from the flux tube before this time and the system will relax to the state seen in Figure 6.9.

This is illustrated by examining some of the timescales associated with electrons in a flare, laid out in Chapter 3. To calculate the bounce time, we have to consider the loss cone angle determined by the magnetic field strength. The surface field strength is 1 kG and the magnetic field strength at the heat pulse injection site is approximately 7 G. From Equation 3.6 this gives an angle of 4.79°. This can be used in the equation for bounce period, from Equation 3.7 to give the approximate bounce period range 1060 – 106 s for the energy range 10 keV – 1 MeV. These non-thermal electrons will eventually decay away from the system, lost to either the surface or space. The particles will move into the loss cone via a pitch angle scattering mechanism, e.g. Coulomb collisions, non-collisional wave scattering, turbulence, etc. Coulomb deflection times give an upper limit to the trapping time of electrons in solar flares (see Chapter 3). The trapping, or deflection time, from Equation 3.8 will therefore give a better idea of how long these particles may remain on the field lines. For a 1 MeV electron, the trapping time for electrons within this corona is approximately 2000 s. This value will be used as a phenomenological constant in the model to simulate the effect on the emission and light curves as the particles are slowly lost. To parameterise this, an exponential time decay component is added after 300 s of the form:

$$e^{-\frac{t-300}{t_0}} \tag{6.2}$$

where t (> 300) is the time (in seconds) during the simulation and t_0 is the value representing the trapping or decay time constant. Initially t_0 is set as 2000 to ensure all non-thermal particles have decayed away by the end of the simulation. This parameter is varied later on in Section 6.5.3 to see its effect on the light curves. With this time decay component, the complete equation governing the non-thermal electrons within the flux tube after the heat pulse is switched off is:

$$n = n_0 e^{-\frac{l^2}{s^2}} \cdot e^{-\frac{t-300}{t_0}} \tag{6.3}$$

The results from the fast GS simulations calculating the GS emission from this MHD data with the added flux tube are now discussed.

6.4 Initial results

6.4.1 Spectra

The gyrosynchrotron emission spectra for the X, Y and Z LOS are shown in Figure 6.11. Each LOS spectra shows the variation in GS emission over a 1 – 1000 GHz frequency range for seven different time shots. The fluxes are given in units of mJy, calculated at a distance of 140 pc. The GS emission is calculated for each of the X, Y and Z planes with temperature, thermal density and magnetic field described by the MHD data and the non-thermal density and electron distribution dictated by the flux tube described previously. Outside the flux tube the non-thermal density is zero. The time decay component of Equation 6.2 is added after 300 s. As previously stated, from

300 s onward the non-thermal electron loop top density is taken as 10% of the thermal density at 300 s at that loop top point. For this model, this loop top non-thermal density, n_{o}, is set as $1.78 \times 10^{8}\,\mathrm{cm}^{-3}$ from 300 s onward.

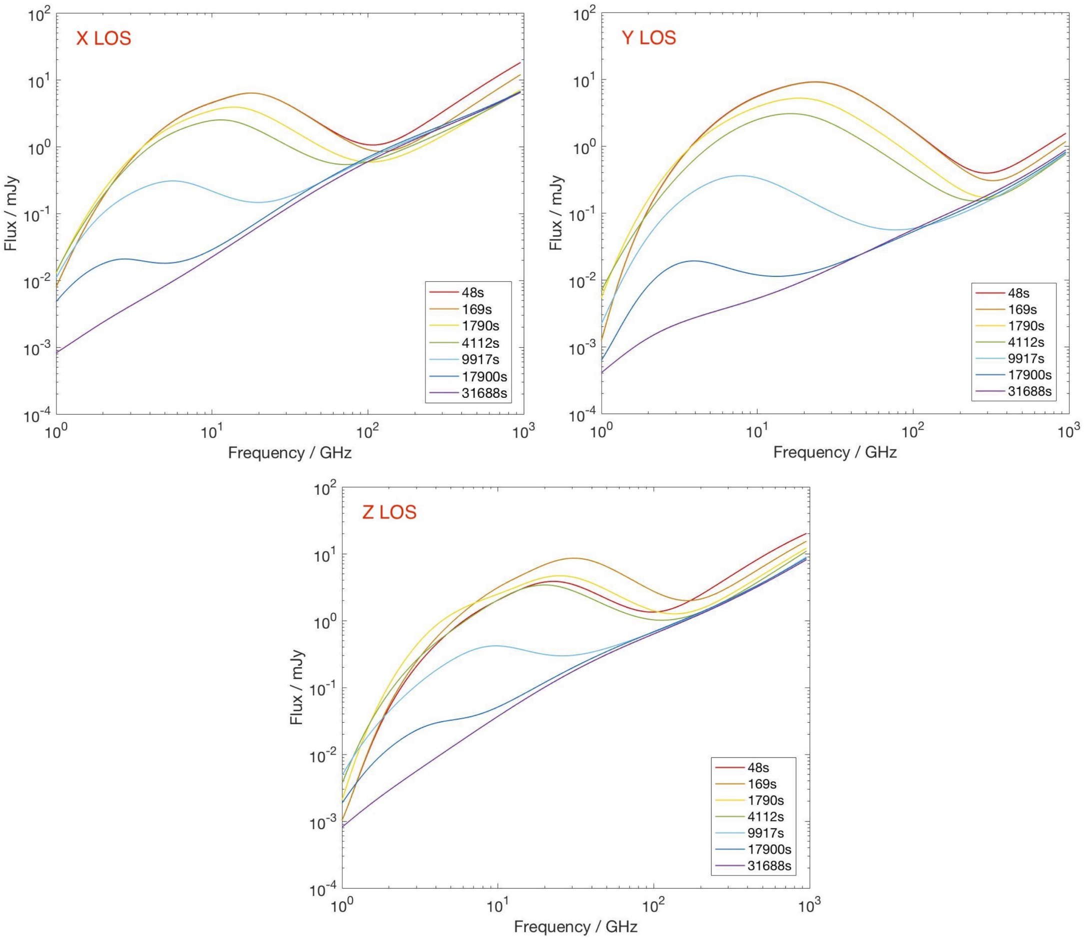

Figure 6.11: GS spectra along the X, Y and Z LOS (covering the entire plane) at 48, 169, 1790, 4112, 9917, 17900 and 31688 s after the heat pulse is switched on. The frequency range is $1 - 1000$ GHz and the flux is given in mJy, calculated for a distance of 140 pc.

The main similarity between all three LOS is the spectral profile at the end of the simulation (31688 s). By this time, all of the non-thermal particles that were initially trapped have decayed away. This results in a spectral profile similar to that of Figure 6.9 where no non-thermal particles were added. This 31688 s spectra has the lowest fluxes at all frequencies. However, the exact magnitude of the fluxes at this time varies between the lines of sight. The Z LOS has the largest fluxes at 31688 s for all frequencies, due to the increased thermal emission from viewing the entire disk plane. All three sets of spectra have a prominent bump in the mid frequency range before 31688 s due to the presence of non-thermal particles. This non-thermal induced bump moves to lower peak fluxes with time, i.e. as the non-thermal density is reduced. This non-thermal peak also moves to lower frequencies as its peak flux values decreases. At higher frequencies (in the sub-THz range), the flux is dominated by the background free-free emission from the original MHD model (i.e. where no population of non-thermal electrons has been added). This can be seen and is discussed in Figure 6.9. The magnitude of these spectra differ between the three lines of sight but these general trends remain the same.

For the X LOS, the bump caused by the non-thermal particles has the highest flux at 169 s with a value of 6.33 mJy. This peak flux occurs at 18 GHz. The spectra for 48 and 169 s are very similar however, both showing similar profiles and peak values below 100 GHz. Over time, this non-thermal bump moves to lower frequencies, with the 17900 s spectra having a shallow peak at 2 GHz. In general, for increasing time the flux will be decreased for any given frequency. Additionally, as the time increases and the non-thermal density decreases then the lower the non-thermal induced peak will be and the frequency of this peak will be reduced. At 1000 GHz the highest intensity is therefore at 48 s, at 18.1 mJy, and decreases with time. At 1 GHz the lowest flux is for 31688 s with a value of 0.823 mJy.

The Y LOS spectra behave similarly. The same trend is seen with regard to the non-thermal bump's behaviour in time. The peak flux for all times occurs at 48 s with a value of 9.12 mJy at 24 GHz. Again, this is very similar to the 169 s spectra. The lowest total intensity at 1 GHz is also at 31688 s with a smaller value of 0.408 mJy compared to the X LOS. The highest total intensity at 1000 GHz is again for 48 s, with a value of 1.55 mJy. However, whereas for the X LOS this high frequency flux dominated over that of the non-thermal bump, the 1000 GHz flux in the Y LOS is smaller than that of the non-thermal bump. In general, the Y LOS spectra appear shifted to higher frequencies when compared relatively to the X LOS spectra. This is due to an increased level of GS emission, a result of the differing magnetic field orientation between the lines of sight. As has been shown in Chapter 5, Figure 5.14, looking top down along the magnetic field lines (as the Y LOS approximately does) produces far higher GS fluxes. This increased emission from a varying magnetic field (or increased non-thermal density) causes an increase in peak radio flux and corresponding frequency (also seen in Figure 5.21).

The Z LOS spectra shows slightly different behaviour at early times than for the X and Y LOS spectra. Instead of the 48 and 169 s spectra having similar flux values, the spectra rises between the two times instead peaking more strongly at 169 s. This is due to the orientation relative to the disk. The heat pulse acts on the system until 300 s, leading to the steady increase in temperature and density before it is switched off. As the heat pulse is not obscured by the disk in the Z LOS this effect is seen in the GS spectra with the peak flux occurring at 8.57 mJy (and 30 GHz) at 169 s, the last time shot before the electrons start to decay away. After this peak the spectra behave as before, declining in flux with the non-thermal peak moving to lower frequencies.

The flux values at 7.5GHz when the flare peaks (≈ 169 s) are consistent with values observed in the T-Tauri flares from Section 3.3.3 (all taken at 7.5GHz). Additionally, a radio flare observed by Furuya et al. [2003] was determined to peak at 68 mJy when observed at 150 GHz. This is larger than the peak values determined here, however the radio flare observed was noted to be extreme while we are modelling a ‘typical’ flare from one of these stars. Increasing the non-thermal density, associated with a more powerful flare, would result in higher peak fluxes at higher frequencies. This trend of reduced peak flux and corresponding frequency for the Z LOS is displayed in the complete light curves of Figure 6.12. The flux (blue line) increases sharply (impulsive phase) and peaks at 314 s and then decreases more slowly (decay phase) once the time decay constant is added. The frequency of the peak follows this trend (orange line), peaking around 30 GHz. The lowest frequency peaks are observed for the latest times and lowest fluxes around 7 GHz. Most observations of T-Tauri flares do not take place at frequencies around 30 GHz, instead favouring lower (below 10 GHz, e.g. Osten and Wolk [2009], Dzib et al. [2013]) or higher frequency bands (above 100 GHz, e.g. Furuya et al. [2003]).

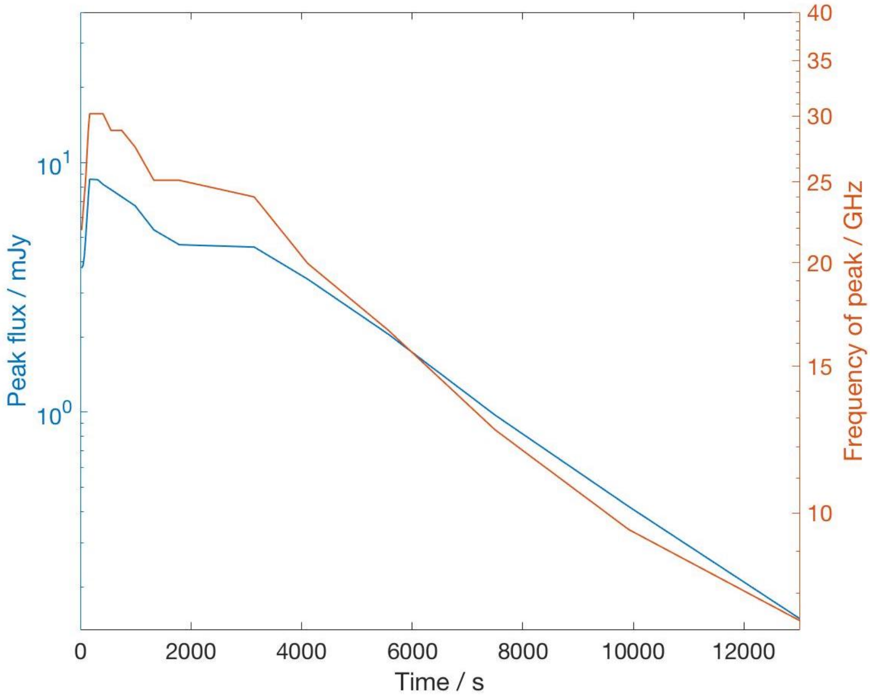

Figure 6.12: The variation of peak flux (blue) and corresponding frequency (orange) along the Z LOS in time, measured from 24-31688 s.

From this model it is evident that the peak of this flare occurs early on, at detectable flux levels from distant regions and in bands not commonly observed in. Future observations that wish to investigate these flares and their impulsive phases should take this into account and consider multi-frequency approaches over time. To emphasise this, predicted multi-frequency radio light curves from this model are shown in the top panel of Figure 6.13.

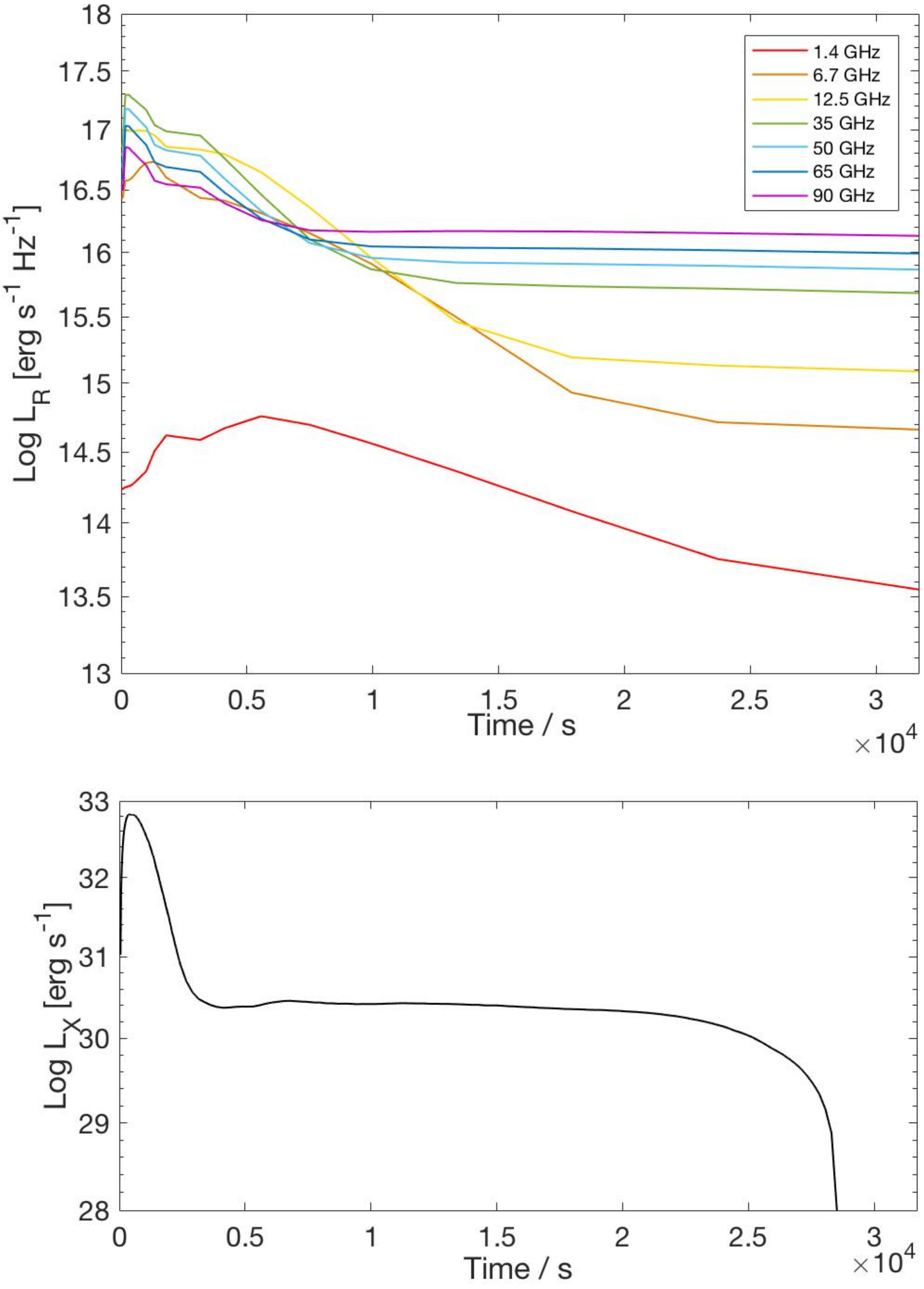

Figure 6.13: Radio luminosity light curves in seven different frequency bands generated from this model (top). The X-ray light curve taken from the MHD model by Orlando et al. [2011] is shown in the bottom plot. Both light curve plots are aligned in time.

The frequencies of the light curves chosen correspond to different observatories. The lower frequency bands (1.4, 6.7, 12.5 GHz) represent planned SKA bands [Braun et al., 2017] while the higher frequencies correspond to ALMA bands (Wootten and Thompson [2009], Huang et al. [2016]). The fluxes are converted into radio luminosities for easy comparison with results in Chapter 5 and the Güdel-Benz relation in Section 3.3.3. The X and Y LOS light curves are similar and are not shown here. At early times, the radio luminosity peaks in the higher frequency bands, dropping sharply and flattening out after 10^4s. At late times when the non-thermal particle population is reduced, the highest luminosites are still observed at the highest frequencies. This is because there is still a large amount of thermal emission from the dense disk. Above 35 GHz, the radio luminosity never drops below approximately $\log L_R$ [$\mathrm{erg\,s^{-1}\,Hz^{-1}}$] = 16. The overall change in luminosity at high frequencies over time is smaller when compared with the 35 GHz curve, as this mid frequency range responds the most to the varying non-thermal effects. The peak radio luminosity across all light curves occurs in this 35 GHz band at $\log L_R$ [$\mathrm{erg\,s^{-1}\,Hz^{-1}}$] = 17.3. When compared to the Güdel-Benz relation plots in Chapter 3 and 5, this agrees well with the observations and model results of radio luminosities from T-Tauri flares. Therefore this model also suggests an overproduction in radio luminosity. Comparisons between these light curves and those in Chapter 2 (for example the light curve of a 100MK flare from Figure 2.8) show similar variability. Both light curves have a sharp peak in intensity over a period of minutes followed by a gradual decline in intensity over a period of hours.

To compare the X-ray luminosity with these results the X-ray light curve generated from the MHD data (in the 0.6 – 12 keV band) by Orlando et al. [2011] is shown in the lower panel of Figure 6.13. The X-ray luminosity peaks around 500 s, after the heat pulse is switched off and after the peak in radio luminosity while the heat pulse is still switched on. This agrees with patterns observed in solar flares (e.g. Benz [2008], and discussed in Chapter 3). During the impulsive phase the microwaves peak sharply and drop off, with the X-ray emission peaking later during the gradual phase due to the sustained heating of the flaring plasma (as expected from the Neupert effect). The flare induced in the MHD model is only partially confined to the magnetic field and causes a large amount of evaporation of the disk material that is not trapped in the star-disk loop (as detailed in Section 6.2). This rapid loss of material causes the sharp decline in X-ray emission seen to follow the peak at 500 s. For the purposes of comparison with the radio luminosities this X-ray peak value of $\mathrm{LogL_X}$ [$\mathrm{erg\,s^{-1}}$] = 32.8 is the most important factor of this light curve. It is comparable to peak values of the largest X-ray flares on young stars [Favata et al., 2005] and leads to a result on the Güdel-Benz plot of Figure 3.14 that is just below the GB relation in the upper rightmost section of observed flares (despite the magnitude of the non-thermal density being much lower than trialled in Chapter 5).

6.4.2 Polarisation

It has been seen how the orientation of the star along each line of sight affects the GS emission in Chapter 4 and Chapter 5. This orientation, with regards to the direction of the magnetic field, also strongly affects the circular polarisation. The degree of circular polarisation (CP) is an important quantity to consider as it is often observable from young stellar flares and occurs in regions that produce GS emission. It can therefore be used to help determine whether non-thermal emission is present in a flaring source. As well as the degree of CP from a source depending on the magnetic field viewing angle (and field strength) it can also vary according to the pitch-angle anisotropy of the non-thermal electrons [Fleishman and Melnikov, 2003]. A stronger magnetic field strength along a LOS will produce a larger degree of CP however the frequency at which it is observed will affect the optical depth and the degree of CP observed. Monitoring the CP can therefore give us a diagnostic of the magnetic geometry of the T-Tauri star.

The CP for this model is calculated along all 3 LOS for the $10 - 1000\,\text{GHz}$ frequency range. These results are shown in Figure 6.14.

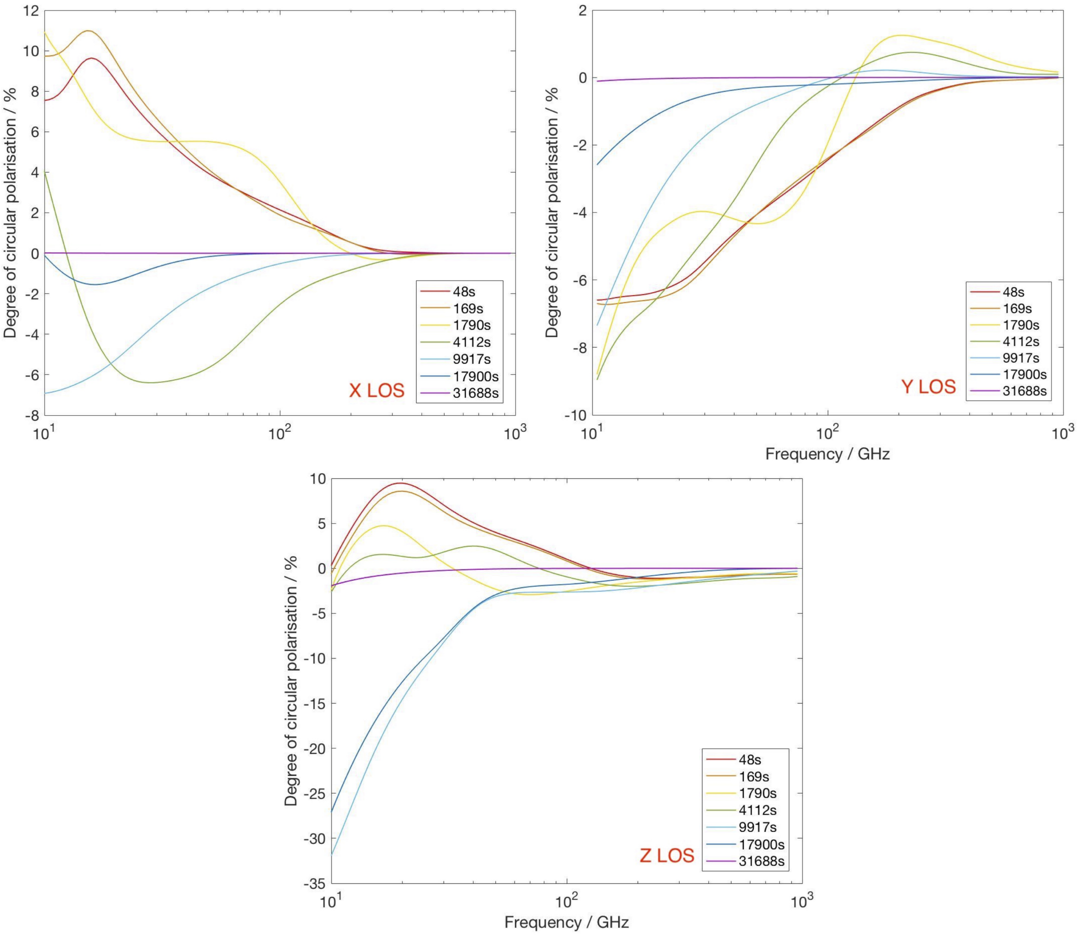

Figure 6.14: Degree of circular polarisation for increasing time steps in along the X, Y and Z LOS that cover the entire plane. The frequency range used is $10 - 1000\,\text{GHz}$.

Figure 6.14 shows a complexity in the degree of CP in both time and frequency. As time progresses the degree of CP moves towards zero as non-thermal particles are lost. There is zero CP by 31688 s for all frequencies and all three lines of sight. This enforces the results from the spectra discussed earlier, where as the non-thermal particles are lost the spectra returns to a thermal profile. The CP also approaches zero at high frequencies for all three lines of sight. Again, this is to be expected when looking at the spectra. The high frequency emission in the spectra is a result of the thermal emission from the disk, not the non-thermal flux tube. No circular polarisation is detected below 10 GHz for the X and Y LOS. In these optically thick regions (i.e. the low frequency range) the sense of polarisation is either in the O-mode or there is no polarisation at all. In the case of the X and Y LOS, it is the latter. There is no polarisation in these directions at low frequencies because it is obscured by the dense disk. In the Z LOS however, the flare is visible looking down on the disk and the emission is polarised in the O-mode.

In the optically thin region, i.e. at frequencies greater than 10 GHz, the sense of polarisation corresponds to the X-mode and is detectable across all three LOS when non-thermal particles are present. This frequency range is where the differences between the magnetic field orientation on the CP is most apparent. Looking at the magnetic field orientation in Figure 6.10, the Y LOS looks down the magnetic field lines from the loop top the most. The X LOS is angled more across the field lines and the Z LOS looks down onto them. With regards to Chapter 5 and the view points discussed there, this corresponds to approximately View B, A and C respectively. As the Y LOS is orientated in this way the degree of CP generally does not reverse in sign over time. A change in sign of polarisation corresponds to absorption effects or the radiation passing through a region of opposite field direction. A change in sign of polarisation has also been seen looking across flux tubes over time in solar flares from the rise to decay phase [Huang et al., 2018] which agrees with the change in sign observed for both the X and Z LOS.

6.5 Varying the parameters

The results obtained so far are consistent with both observations of T-Tauri stars and previous model results. Some key parameters of the model are now varied to see their effect. These parameters include the distribution of particles within the loop, the decay rate of the non-thermal electrons and the power law index. Parameters like the magnetic field strength and flux tube non-thermal density are not varied as this is comprehensively explored in Chapter 5.

6.5.1 Power law index

The first parameter to be varied is the power law index, δ, from Equation 5.5. Instead of changing the power law index once for all times, the index is allowed to increase linearly from its initial value of 3.2 to a value of 6 by the end of the simulation. This is to simulate the effect the spectrum of the non-thermal electrons has on the GS emission, not just the general number density of them. A power law spectrum of electrons has a larger number of higher energy electrons than for a thermal spectra (see Figure 4.9). The number of higher energy electrons depends on the power law index and is higher for a smaller index value. Therefore, at the peak of a flare the index should have the smallest value and increase in time to reflect the loss of these higher energy particles. As these non-thermal particles are lost, the particle spectrum will become steeper over time [Benz, 2008]. This is reflected in the GS spectra in Figure 6.15 which shows the effect of changing the power law index.

As the power law index increases to $\delta = 6$, the non-thermal bump drops in peak flux value more quickly. This effect is also seen in Figure 5.28 as well as movie S2 from Fleishman et al. [2020] where the spectral peak moves to a lower intensity as the power law index is increased. As the simulation time increases and the power law index reaches $\delta = 6$, the spectrum once again returns to a thermal profile. The emission is from lower energy particles associated with a thermal distribution. The addition of an increasing power law index therefore results in the spectral peak being reduced faster and pushed to lower frequencies as the contribution of higher energy particles is reduced.

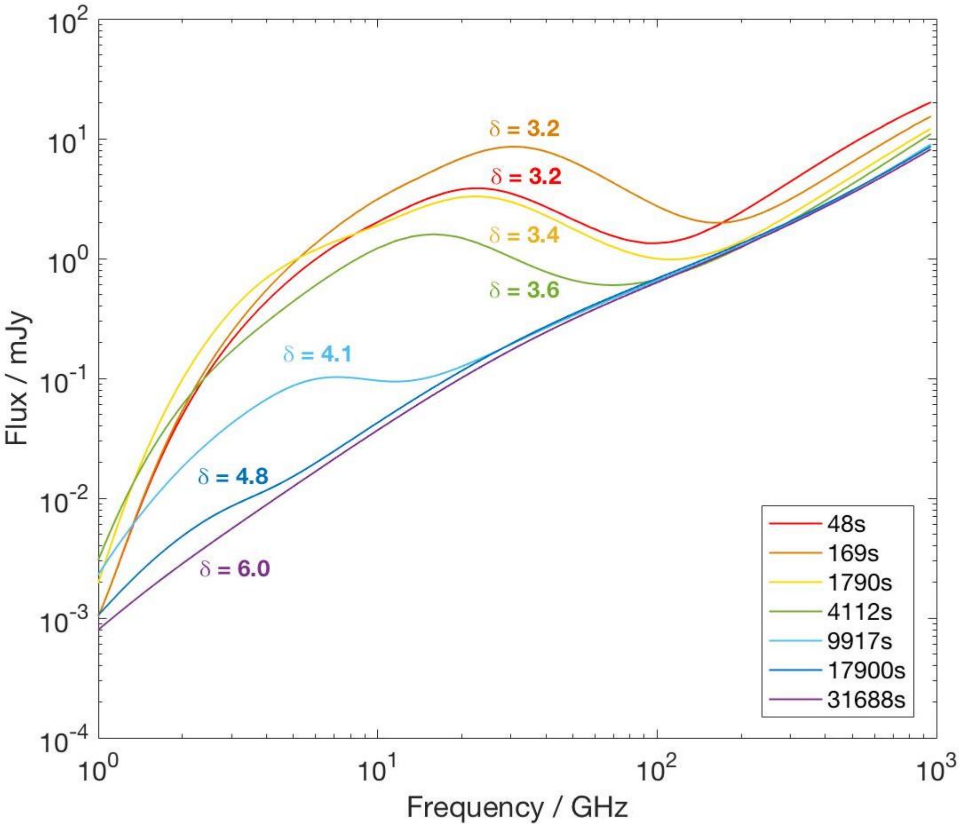

Figure 6.15: Spectra results for changing the power law index with time along the Z LOS. The index is changed linearly from its initial value of 3.2 while the heat pulse is switched on, to a value of 6 when the simulation is over.

6.5.2 Distribution along the loop

The distribution along the loop is controlled by the s factor defined in Equation 6.1. Initially, this s factor is equal to half the loop length, l. Figure 6.16 shows the spectra over time when varying the s factor to be 0.3 and 1.5 times this loop half length (while conserving the number density of electrons within the loop). Also shown in Figure 6.16 are the volume plots illustrating how the densities may vary along sample field lines at 4112 s within the flux tube. Smaller values of s lead to more confinement near the loop top. The density at the loop top is still the highest overall throughout the loop.

Kuznetsov et al. [2011] also varied this distribution of electrons over the loop and found that a more confined distribution around the apex led to the spectral peak moving

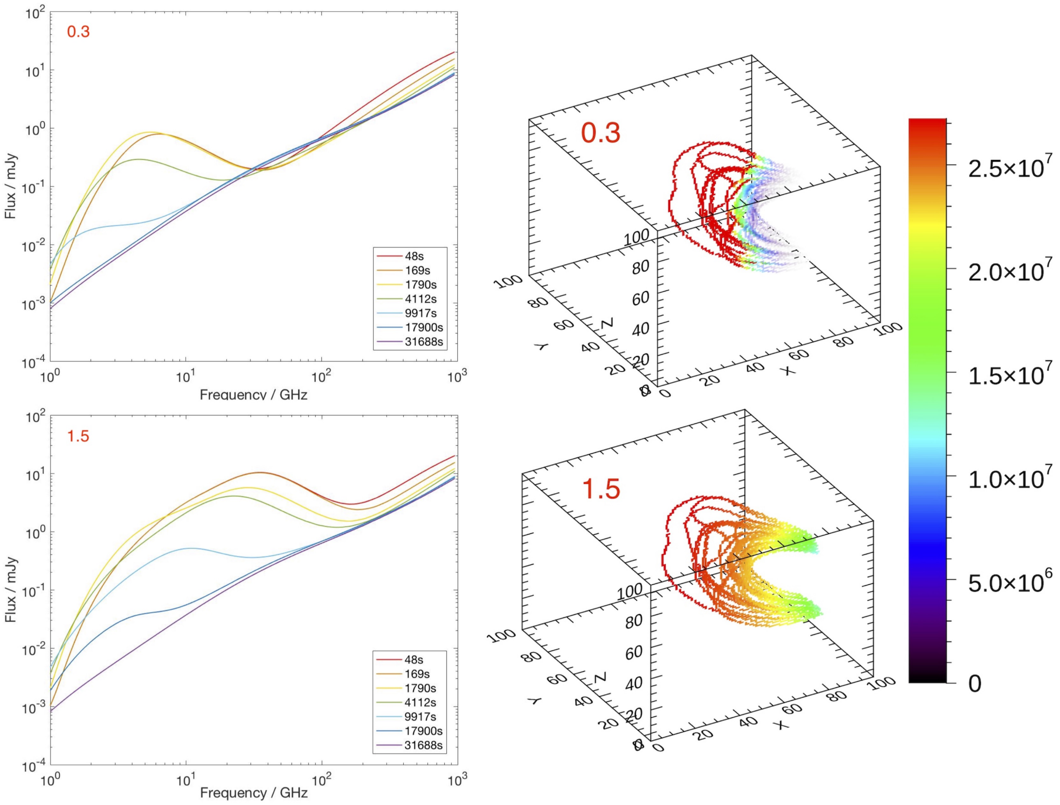

Figure 6.16: Spectra showing how the distribution of non-thermal particles along the loop affects the GS emission in time. Two scenarios are considered: $s=0.3$ (top) and 1.5 (bottom). A 3D visualisation of sample field lines within the flux tube at 4112 s is also shown to illustrate how the electrons are more confined in the $s=0.3$ case.

to lower fluxes and corresponding frequencies. This same effect is seen in the results from Figure 6.16. For the more compact distribution of $s=0.3$, the GS flux peaks at lower values than normal and at smaller frequencies as a consequence of this smaller emitting volume. The $s=1.5$ plot has higher peak fluxes of the non-thermal bump at earlier times but shows the same pattern as before with the peak moving to smaller values and frequencies as time progresses. The more confined distribution relaxes to a thermal state more rapidly. The effect of varying the time decay constant on this non-thermal radio emission over time is explored next.

6.5.3 Time constant

The phenomenological constant, t_o, from Equation 6.2 is now varied to see the effect on the radio light curves produced in this model. The constant has an initial value of 2000 but is now varied between 500 and 1000. A smaller value represents a smaller trapping time leading to the particles being lost more quickly from the system. In reality, this trapping time varies according to the energy of the electron but here it is chosen to be constant and simulate the eventual decay of all non-thermal particles from the system. The light curves for these two decay constants at three different frequencies is shown in Figure 6.17. The frequency bands chosen are taken from Figure 6.13 (6.7, 35 and 90 GHz) and the fluxes are converted into luminosities for easy comparison with the $t_\mathrm{o} = 2000$ light curves from this figure.

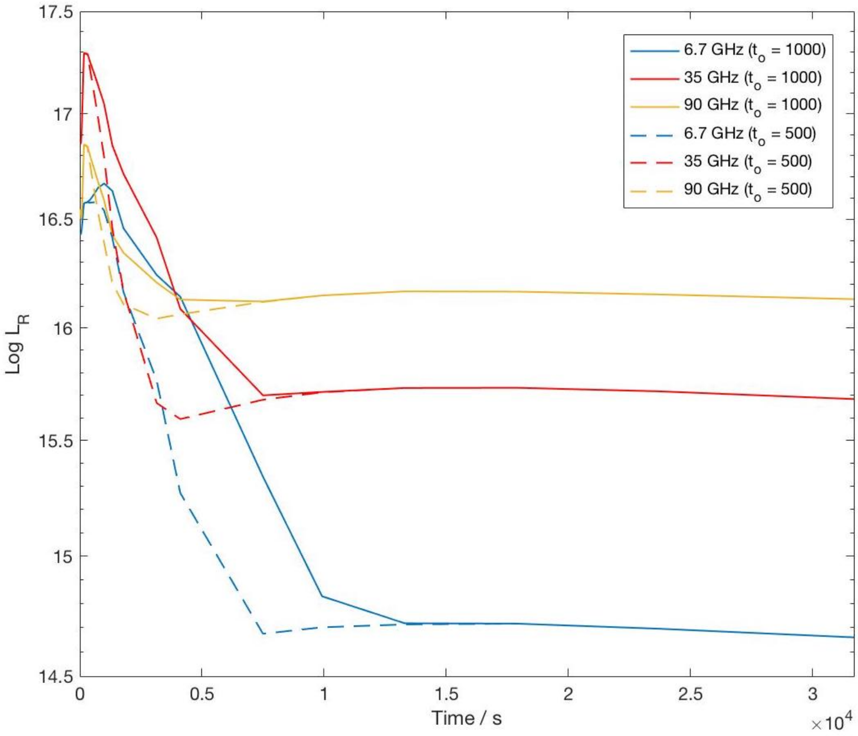

Figure 6.17: Radio luminosity light curve results of changing the time decay constant to $t_\mathrm{o} = 500$ (dashed lines) and 1000 (solid lines). Three different frequency bands are shown: 6.7, 35 and 90 GHz (blue, red, yellow lines respectively).

As expected, the smaller value of 500 s leads to a more rapid drop in radio luminosity as the electrons are lost faster and the non-thermal GS emission decreases. The choice of time decay constant has no effect on the peak luminosity as the luminosity peaks during the heat pulse before the time decay component is added. For all frequencies the luminosity peaks and then plateaus at some time when the non-thermal particles are lost. The difference between this peak and plateau value is larger in magnitude in lower frequency bands. Therefore, generating radio light curves from low frequency observations may be more useful in distinguishing when non-thermal emission is occurring. As before, the peak radio luminosities occur for 35 GHz and moves to lower values and frequencies with time.

This model has provided results for the gyrosynchrotron emission produced from a flaring classical T-Tauri star over a period of approximately 9 hours. The results provide the first multi-frequency intensity and polarisation predictions for this scenario over the $1 - 1000$ GHz frequency range. The resulting peak emission has been compared with the results from Chapter 5 as well as the GB relation in Figure 3.14 and generally agrees. There still appears to be an overproduction in non-thermal radio emission when compared with flares on the Sun and main sequence stars. The model has combined MHD data, along with a radiative transfer simulator to calculate the GS spectra, light curves and circular polarisation along three different lines of sight relative to the star and disk system. Most notably, the frequency at which the spectra peak in each LOS is greater than 10 GHz. This further supports the idea of higher frequency observations being necessary in this star forming regions, as suggested in Chapter 5. Additionally, as the frequency of the peak has been found to decrease with time, multi-frequency observations over time will also be beneficial and this model will provide a useful guide in interpreting those observations.

Chapter 7

Conclusions

The X-ray and non-thermal radio emission from a flaring T-Tauri star has been investigated here for a range of different scenarios. Varying magnetic field configurations, flux tube arrangements, flaring parameter values and viewing angles have all been considered and the gyrosynchrotron emission calculated over a wide range of frequencies ($1 - 1000\,\mathrm{GHz}$). This has led to the first predictions of multi-frequency intensity and circular polarisation for a T-Tauri star undergoing a flare.

These predictions have been compared to observations of flaring T-Tauri stars at both X-ray and radio wavelengths. Observations of class II and III flares from several different star forming regions have been collated and compared to the Güdel-Benz relation. This relation, which relates the thermal X-ray and non-thermal radio emission produced in flares, holds for flares on the Sun as well as other active main sequence stars. The combination of T-Tauri flare observations from multiple sources suggest that this relation does not hold for flares on these young stars. The observed flares appear to peak at radio luminosities far greater than the GB relation predicts. Separating the observed TTS flares by class shows that there is no difference in the X-ray emission between the two classes however the radio emission is slightly higher in class III flares on average. However, in general there is a wide spread of luminosities between both classes of flare and a more detailed comparison and analysis of any evolutionary trends would be required to confirm this increased radio emission in weak-lined T-Tauri stars. The large flaring flux tubes reported in these magnetospheres would lead to longer trapping and bounce times of energetic particles that gyrate along the field lines and therefore more sustained non-thermal radiation. There could also be far more frequent and powerful reconnection events as these stars are far more active than the Sun with larger surface field strengths. There is also the difference in what triggers the reconnection between solar and T-Tauri stars to be considered. Main sequence and solar flares are thought to be triggered via an instability or loss of equilibrium in the corona, whereas magnetic energy release can occur at much higher altitudes in young stellar flares due to different interactions. For example, many of these stars are also part of binary systems, and the reconnection between their magnetospheres could lead to an increase in radio emission. Additionally, in the case of classical T-Tauri stars, interaction of the star with its accretion disk could also generate large amounts of non-thermal emission from reconnection events.

The models used in this paper have sought to investigate this non-thermal radio emission from star-disk interactions. The models have predicted the radio emission from the peak of the flare, as well as the variable emission over a simulation period of 9 hours. Both model's results match the observed distribution of radio and X-ray luminosities.

The 3D GX simulator is first used in Chapter 5 to calculate the radio and X-ray emission from a flaring loop situated at $4\,\mathrm{R}_\odot$ from the stellar surface. The flux tube loop is given flaring parameters (temperatures, densities, etc) that have been reported from X-ray observations of flares. The energy release process induced in magnetic reconnection is not modelled, and the flux tube is treated only as a source of high energy particles and intense plasma heating from which the emission is predicted using the GX simulator. The initial radio and X-ray luminosities from this model again suggest a result that agrees well with observations and lies beneath the GB relation. This flaring flux tube is then modified and a range of scenarios with different parameter values is considered. The flaring parameters that are varied are the: surface magnetic field strength, power law index for the non-thermal electrons, flux tube width, flux tube thermal density, flux tube non-thermal density and flux tube temperature. The range of values chosen all reflect the typical minimum and maximum quantities reported in literature. The flux tube thermal density and temperature heavily affect the thermal X-ray emission, as expected. They also cause a slight decrease in peak radio luminosity when increased. The magnetic field strength and flux tube non-thermal density both cause large increases in peak radio luminosity and minimal change in X-ray emission when they are increased. There is some near degeneracy with the peak fluxes obtained when varying these two parameters, with an increase in either causing similar changes to the spectrum. The only model results that are able to predict luminosities that fall on or above the GB relation describe flares with very small non-thermal to thermal density ratios or weak surface field strengths. These flares are unrealistic in the case of T-Tauri stars as they are known to possess strong field strengths and produce large amounts of non-thermal radio emission. The frequency at which all the model spectra peak depends on the parameter that is changed, with the magnetic field strength and non-thermal density having the greatest effect on this frequency change. Nearly all the results peak above 10 GHz, with some of the more extreme conditions investigated peaking above 100 GHz. These results suggest that high multi-frequency observations would be beneficial in learning more about these T-Tauri flares, as well as simultaneous radio and X-ray observations. This model provides a useful guide to interpreting observations of T-Tauri flares, demonstrating how the peak flux and corresponding frequency varies depending on the parameters of the flare.

The second model used in Chapter 6 explores the time dependency of the radio emission produced during a flare. Data was obtained from a 3D MHD model of a flaring classical T-Tauri star and combined with a model of a flux tube that connected the surface of the star to the flaring site at the inner edge of the accretion disk. The gyrosynchrotron emission from this system is then calculated using the 1D GS simulator.

The 3D ideal MHD model uses a transient heat pulse to represent the initiation of a flare from the inner edge of the disk. The magnetic field lines that thread this heat pulse location are used in defining a magnetic flux tube that has two footpoints on the stellar surface and its apex at the ‘injection’ site. The flux tube is given a Gaussian distribution of non-thermal electrons that is allowed to decay away (given some time decay constant) after the heat pulse is switched off at 300s. The total simulation time is 31688s. The GS spectra generated from this model is produced for this entire time period as well as for three different viewing angles. The frequency range used extends to 1000 GHz. This is done to cover the sub-millimeter range, enabling comparison to existing and future observations of T-Tauri flares (e.g. the non-thermal flare from Mairs et al. [2019]). The magnitude of the non-thermal density in the flux tube is smaller than considered in the first model. However, the ratio between non-thermal and thermal densities is kept the same as before and still led to peak radio luminosities that agree with both the observations of T-Tauri stars and the results from the first model in Chapter 5 (where the peak radio luminosity from the standard result in the first model is $\mathrm{LogL_R} = 16.3$, and in this second model is $\mathrm{logL_R} = 17.3$). The light curves generated from this model show how the peak flux decreases with time after the heat pulse is switched off, but also how the frequency of the peak moves to lower frequencies with elapsed time. Again, at the peak of the flare the frequency of the peak flux is around 30 GHz. This agrees with the result from the first model and continues to support the need for higher multi-frequency observations of these flares.

The circular polarisation is investigated for all three lines of sight, at all times and for the frequency range $10 - 1000$ GHz. The degree of circular polarisation is shown to have a complex behaviour over time and frequency, and varied considerably depending on which time step, frequency and orientation line of sight was considered. These results provide useful multi-frequency predictions and diagnostics for observations of circular polarisation however careful interpretation and comparison with this model would be essential given the complexity.

As in the first model, some of the parameters are varied to see the effect on the radio emission over time. The flaring quantities themselves, like the densities and temperatures, are not altered. Instead, the variables that describe the flux tube and the population of non-thermal electrons over time are varied in this model. These include the time decay constant, power-law index and the spatial distribution of electrons within the flux tube. Increasing the power-law index sees the spectra more rapidly relax to a thermal state with time. Similarly, decreasing the time decay constant reduces the trapping time of the particles so they are all lost from the flux tube more quickly. This time decay constant is the least well constrained of all the parameters used in these models and more observations would be needed to further assess the period within which these particles are trapped in these extended loops.

These intensity and circular polarisation predictions are all testable through future observations. In particular, multi-frequency observations over time will allow for comparison to these model results. Where multi-frequency observations are not possible, observations in frequency bands around 30 GHz will be most useful in investigating the non-thermal emission as this is where both of these models peaked in flux. Observatories like ALMA [Fuller et al., 2015] and the ngVLA [McKinnon and Selina, 2018] will be fundamental in high frequency observations of T-Tauri flares while the upcoming SKA will inform us about the low frequency emission [Braun et al., 2017]. Additionally, simultaneous X-ray and radio observations between radio observatories and future X-ray missions such as Athena [Barcons et al., 2017] will hopefully aid in finding trends between these two emissions with regards to the GB relation. Possible next steps in modelling these flares include the use of a resistive MHD model to simulate the energy release itself via magnetic reconnection. The more physically sophisticated and complete modelling of these flares is vital to provide further constraint of flaring parameters, as well as for interpreting and comparing any results with observations.

Bibliography

S.H.P. Alencar, J. Bouvier, F.M. Walter, C. Dougados, J-F. Donati, R. Kurosawa, M. Romanova, X. Bonfils, G.H.R.A. Lima, S. Massaro, et al. Accretion dynamics in the classical T-Tauri star V2129 Ophiuchi. *Astronomy & Astrophysics*, 541: A116, 2012.

P. Andre, D. Ward-Thompson, and M. Barsony. Submillimeter continuum observations of ρ Ophiuchi A - The candidate protostar VLA 1623 and prestellar clumps. *The Astrophysical Journal*, 406:122–141, 1993.

S. Antoniucci, B. Nisini, K. Biazzo, T. Giannini, D. Lorenzetti, N. Sanna, A. Harutyunyan, L. Origlia, and E. Oliva. High-resolution TNG spectra of T-Tauri stars-Near-IR GIANO observations of the young variables XZ Tauri and DR Tauri. *Astronomy & Astrophysics*, 606:A48, 2017.

C. Argiroffi, F. Favata, E. Flaccomio, A. Maggio, G. Micela, G. Peres, and S. Sciortino. XMM-Newton survey of two Upper Scorpius regions. *Astronomy & Astrophysics*, 459(1):199–213, 2006.

M. Aschwanden. *Physics of the solar corona: an introduction with problems and solutions*. Springer Science & Business Media, 2006.

M.J. Aschwanden. Deconvolution of directly precipitating and trap-precipitating electrons in solar flare hard X-rays. I. Method and tests. *The Astrophysical Journal*, 502 (1):455, 1998.

M.J. Aschwanden. Particle acceleration and kinematics in solar flares. In *Particle acceleration and kinematics in solar flares*, pages 1–227. Springer, 2002.

M.J. Aschwanden, R.M. Bynum, T. Kosugi, H.S. Hudson, and R.A. Schwartz. Electron trapping times and trap densities in solar flare loops measured with Compton and Yohkoh. *The Astrophysical Journal*, 487(2):936, 1997.

M.J. Aschwanden, T. Kosugi, Y. Hanaoka, M. Nishio, and D.B. Melrose. Quadrupolar magnetic reconnection in solar flares. I. Three-dimensional geometry inferred from Yohkoh observations. *The Astrophysical Journal*, 526(2):1026, 1999.

M.J. Aschwanden, E.P. Kontar, and N.L.S. Jeffrey. Global energetics of solar flares. VIII. The low-energy cutoff. *The Astrophysical Journal*, 881(1):1, 2019.

X. Barcons, D. Barret, A. Decourchelle, J.W. den Herder, A.C. Fabian, H. Matsumoto, D. Lumb, K. Nandra, L. Piro, R.K. Smith, et al. Athena: ESA's X-ray observatory for the late 2020s. *Astronomische Nachrichten*, 338(2-3):153–158, 2017.

M. Barsony. Class 0 protostars. In *Clouds, Cores, and Low Mass Stars*, volume 65, page 197, 1994.

A. O. Benz. Flare observations. *Living Reviews in Solar Physics*, 5, 2008. doi: 10.12942/lrsp-2008-1.

A.O. Benz. Flare observations. *Living reviews in solar physics*, 14(1):2, 2017.

A.O. Benz and M. Güdel. The soft X-ray/microwave ratio of solar and stellar flares and coronae. 1994.

A.O. Benz and M. Güdel. Physical processes in magnetically driven flares on the Sun, stars, and young stellar objects. *Annual Review of Astronomy and Astrophysics*, 48: 241–287, 2010.

N.H. Bian, J.M. Watters, E.P. Kontar, and A.G. Emslie. Anomalous cooling of coronal loops with turbulent suppression of thermal conduction. *The Astrophysical Journal*, 833(1):76, 2016.

D. Biskamp. Magnetic reconnection via current sheets. *The Physics of fluids*, 29(5): 1520–1531, 1986.

R. Braun, A. Bonaldi, T. Bourke, E. F. Keane, and J. Wagg. Anticipated SKA1 science performance. *SKA-TEL-SKO-0000818*, 2017.

L. Carkner, E. Mamajek, E. Feigelson, R. Neuhäuser, R. Wichmann, and J. Krautter. Radio emission from ROSAT-discovered young stars in and around Taurus-Auriga. *The Astrophysical Journal*, 490(2):735, 1997.

F.F. Chen et al. *Introduction to plasma physics and controlled fusion*, volume 1. Springer, 1984.

M. Choi, K. Tatematsu, K. Hamaguchi, and J-E. Lee. Centimeter polarimetry of the R Coronae Australis region. *The Astrophysical Journal*, 690(2):1901, 2008.

G. Costa, S. Orlando, G. Peres, C. Argiroffi, and R. Bonito. Hydrodynamic modelling of accretion impacts in classical T-Tauri stars: radiative heating of the pre-shock plasma. *Astronomy & Astrophysics*, 597:A1, 2017.

P.A. Davidson. An introduction to magnetohydrodynamics, 2002.

M. de Val-Borro, G.F. Gahm, H.C. Stempels, and A. Pepliński. Modelling circumbinary gas flows in close T-Tauri binaries. *Monthly Notices of the Royal Astronomical Society*, 413(4):2679–2688, 2011.

J-F. Donati, M.B. Skelly, J. Bouvier, S.G. Gregory, K.N. Grankin, M.M. Jardine, G.A.J. Hussain, F. Ménard, C. Dougados, Y. Unruh, et al. Magnetospheric accretion and spin-down of the prototypical classical T-Tauri star AA Tau. *Monthly Notices of the Royal Astronomical Society*, 409(4):1347–1361, 2010.

G.A. Doschek, U. Feldman, R.W. Kreplin, and L. Cohen. High-resolution X-ray spectra of solar flares. III-General spectral properties of X1-X5 type flares. *The Astrophysical Journal*, 239:725–737, 1980.

G.A. Dulk. Radio emission from the Sun and stars. *Annual review of astronomy and astrophysics*, 23(1):169–224, 1985.

G.A. Dulk and K.A. Marsh. Simplified expressions for the gyrosynchrotron radiation from mildly relativistic, nonthermal and thermal electrons. *The Astrophysical Journal*, 259:350–358, 1982.

S.A. Dzib, L. Loinard, A.J. Mioduszewski, L.F. Rodríguez, G.N. Ortiz-León, G. Pech, J.L. Rivera, R.M. Torres, A.F. Boden, L. Hartmann, et al. The Gould's Belt Very Large Array Survey. I. The Ophiuchus Complex. *The Astrophysical Journal*, 775 (1):63, 2013.

S.A. Dzib, L. Loinard, L.F. Rodríguez, A.J. Mioduszewski, G.N. Ortiz-León, M.A. Kounkel, G. Pech, J.L. Rivera, R.M. Torres, A.F. Boden, et al. The Gould's Belt Very Large Array Survey. IV. The Taurus-Auriga complex. *The Astrophysical Journal*, 801(2):91, 2015.

F. Favata, G. Micela, and F. Reale. Coronal structure geometries on Pre-main sequence stars. *Astronomy & Astrophysics*, 375(2):485–491, 2001.

F. Favata, E. Flaccomio, F. Reale, G. Micela, S. Sciortino, H. Shang, K.G. Stassun, and E.D. Feigelson. Bright X-ray flares in orion young stars from COUP: Evidence for star-disk magnetic fields? *The Astrophysical Journal Supplement Series*, 160(2): 469, 2005.

E.D. Feigelson and T. Montmerle. High-energy Processes in Young Stellar Objects. *Annual Review of Astronomy and Astrophysics*, 37(1):363–408, 1999.

U. Feldman, G.A. Doschek, R.W. Kreplin, and J.T. Mariska. High-resolution X-ray spectra of solar flares. IV-General spectral properties of M type flares. *The Astrophysical Journal*, 241:1175–1185, 1980.

U. Feldman, G.A. Doschek, J.T. Mariska, and C.M. Brown. Relationships between temperature and emission measure in solar flares determined from highly ionized iron spectra and from broadband X-ray detectors. *The Astrophysical Journal*, 450: 441, 1995a.

U. Feldman, J.M. Laming, and G.A. Doschek. The correlation of solar flare temperature and emission measure extrapolated to the case of stellar flares. *The Astrophysical Journal Letters*, 451(2):L79, 1995b.

M. Felli, G.F. Gahm, R.H. Harten, R. Liseau, and N. Panagia. Radio emission from young stars. *Astronomy and Astrophysics*, 107:354–361, 1982.

G.D. Fleishman and A.A. Kuznetsov. Fast gyrosynchrotron codes. *The Astrophysical Journal*, 721(2):1127, 2010.

G.D. Fleishman and V.F. Melnikov. Gyrosynchrotron emission from anisotropic electron distributions. *The Astrophysical Journal*, 587(2):823, 2003.

G.D. Fleishman, G.M. Nita, and D.E. Gary. Energy partitions and evolution in a purely thermal solar flare. *The Astrophysical Journal*, 802(2):122, 2015.

G.D. Fleishman, G.M. Nita, N. Kuroda, S. Jia, K. Tong, R.R. Wen, and Z. Zhizhuo. Revealing the evolution of non-thermal electrons in solar flares using 3D modeling. *The Astrophysical Journal*, 859(1):17, 2018.

G.D. Fleishman, D.E. Gary, B. Chen, N. Kuroda, S. Yu, and G.M. Nita. Decay of the coronal magnetic field can release sufficient energy to power a solar flare. *Science*, 367(6475):278–280, 2020.

L. Fletcher, B.R. Dennis, H.S. Hudson, S. Krucker, K. Phillips, A. Veronig, M. Battaglia, L. Bone, A. Caspi, Q. Chen, et al. An observational overview of solar flares. *Space science reviews*, 159(1-4):19, 2011.

J. Forbrich, T. Preibisch, and K.M. Menten. Radio and X-ray variability of young stellar objects in the Coronet cluster. *Astronomy & Astrophysics*, 446(1):155–170, 2006.

J. Forbrich, T. Preibisch, K.M. Menten, R. Neuhäuser, F.M. Walter, M. Tamura, N. Matsunaga, N. Kusakabe, Y. Nakajima, A. Brandeker, et al. Simultaneous X-ray, radio, near-infrared, and optical monitoring of young stellar objects in the Coronet cluster. *Astronomy & Astrophysics*, 464(3):1003–1013, 2007.

E. Franciosini, I. Pillitteri, B. Stelzer, G. Micela, K.R. Briggs, L. Scelsi, A. Telleschi, M. Audard, F. Palla, and M. Güdel. Spectral properties of X-ray bright variable sources in the Taurus Molecular Cloud. *Astronomy & Astrophysics*, 468(2):485–499, 2007.

G. Fuller, J. Forbrich, J. Rathborne, S. Longmore, and S. Molinari. Star and stellar cluster formation: ALMA-SKA synergies. *Advancing Astrophysics with the Square Kilometre Array (AASKA14)*, art. 152, April 2015. URL `http://adsabs.harvard.edu/abs/2015aska.confE.152F`.

I. Furno, T. Intrator, E. Torbert, C. Carey, M.D. Cash, J.K. Campbell, W.J. Fienup, C.A. Werley, G.A. Wurden, and G. Fiksel. Reconnection scaling experiment: A new device for three-dimensional magnetic reconnection studies. *Review of scientific instruments*, 74(4):2324–2331, 2003.

R.S. Furuya, H. Shinnaga, K. Nakanishi, M. Momose, and M. Saito. A giant flare on a T-Tauri star observed at millimeter wavelengths. *Publications of the Astronomical Society of Japan*, 55(6):L83–L87, 2003.

M. Gagné, S.L. Skinner, and K.J. Daniel. Simultaneous Chandra and Very Large Array observations of young stars and protostars in ρ Ophiuchus cloud core A. *The Astrophysical Journal*, 613(1):393, 2004.

S. Galtier. *Introduction to modern magnetohydrodynamics*. Cambridge University Press, 2016.

H.A. Garcia and P.S. McIntosh. High-temperature flares observed in broadband soft X-rays. *Solar physics*, 141(1):109–126, 1992.

D.E. Gary and G.J. Hurford. Radio spectral diagnostics. In *Solar and space weather radiophysics*, pages 71–87. Springer, 2004.

W. Gekelman, R.L. Stenzel, and N. Wild. Magnetic field line reconnection experiments. *Physica Scripta*, 1982(T2B):277, 1982.

K.V. Getman, E.D. Feigelson, L. Townsley, P. Broos, G. Garmire, and M. Tsujimoto. Chandra study of the Cepheus B star-forming region: Stellar populations and the initial mass function. *The Astrophysical Journal Supplement Series*, 163(2):306, 2006.

K.V. Getman, E.D. Feigelson, G. Micela, M.M. Jardine, S.G. Gregory, and G.P.

Garmire. X-ray flares in Orion young stars. II. Flares, magnetospheres, and protoplanetary disks. *The Astrophysical Journal*, 688(1):437, 2008.

K.V. Getman, P.S. Broos, D.M. Salter, G.P. Garmire, and M.R. Hogerheijde. The young binary DQ Tau: a hunt for X-ray emission from colliding magnetospheres. *The Astrophysical Journal*, 730(1):6, 2011.

G. Giardino, F. Favata, B. Silva, G. Micela, F. Reale, and S. Sciortino. X-ray and optical bursts and flares in YSOs: results from a 5-day XMM-Newton monitoring campaign of L1551. *Astronomy & Astrophysics*, 453(1):241–252, 2006.

G. Giardino, F. Favata, G. Micela, S. Sciortino, and E. Winston. The onset of X-ray emission in young stellar objects - A Chandra observation of the Serpens star-forming region. *Astronomy & Astrophysics*, 463(1):275–288, 2007.

R.G. Giovanelli. A theory of chromospheric flares. *Nature*, 158(4003):81–82, 1946.

S.G. Gregory, M. Jardine, C.G. Gray, and J.F. Donati. The magnetic fields of forming solar-like stars. *Reports on Progress in Physics*, 73(12):126901, 2010.

S.G. Gregory, J-F. Donati, and G.A.J. Hussain. The multipolar magnetic fields of accreting pre-main-sequence stars: B at the inner disk, B along the accretion flow, and B at the accretion shock. *arXiv preprint arXiv:1609.00273*, 2016.

N. Grosso, T. Montmerle, E.D. Feigelson, and T.G. Forbes. Chandra observation of an unusually long and intense X-ray flare from a young solar-like star in M78. *Astronomy & Astrophysics*, 419(2):653–665, 2004.

N. Grosso, J. Bouvier, T. Montmerle, M. Fernández, K. Grankin, and M.R.Z Osorio. Observation of enhanced X-ray emission from the CTTS AA Tauri during one transit of an accretion funnel flow. *Astronomy & Astrophysics*, 475(2):607–617, 2007.

M. Güdel. Radio and X-ray emission from main-sequence K stars. *A&A*, 1992.

M. Güdel. Stellar radio astronomy: probing stellar atmospheres from protostars to giants. *Annual Review of Astronomy and Astrophysics*, 40(1):217–261, 2002.

M. Güdel and A.O. Benz. X-ray/microwave relation of different types of active stars. *The Astrophysical Journal*, 405:L63–L66, 1993.

M. Güdel, M. Audard, K. Briggs, F. Haberl, H. Magee, A. Maggio, R. Mewe, R. Pallavicini, and J. Pye. The XMM-Newton view of stellar coronae: X-ray spectroscopy of the corona of AB Doradus. *Astronomy & Astrophysics*, 365(1):L336–L343, 2001.

M. Güdel, K.R. Briggs, K. Arzner, M. Audard, J. Bouvier, E.D. Feigelson, E. Franciosini, A. Glauser, N. Grosso, G. Micela, et al. The XMM-Newton extended survey of the Taurus Molecular Cloud (XEST). *Astronomy & Astrophysics*, 468(2): 353–377, 2007.

L. Hartmann. Comparisons between the accretion flows of low-and intermediate-mass stars. *New Astronomy Reviews*, 43(1):1–29, 1999.

L. Hartmann, G. Herczeg, and N. Calvet. Accretion onto pre-main-sequence stars. *Annual Review of Astronomy and Astrophysics*, 54:135–180, 2016.

G. Huang, V. F. Melnikov, H. Ji, and Z. Ning. *Solar flare loops: observations and interpretations*. Springer, 2018.

Y. Huang, O. Morata, P. M. Koch, C. Kemper, Y-J. Hwang, C-C. Chiong, P. Ho, Y-H. Chu, C-D. Huang, C-T. Liu, et al. The Atacama Large Millimeter/sub-millimeter Array band-1 receiver. In *Modeling, Systems Engineering, and Project Management for Astronomy VI*, volume 9911, page 99111V. International Society for Optics and Photonics, 2016.

D.P. Huenemoerder, J.H. Kastner, P. Testa, N.S. Schulz, and D.A. Weintraub. Evidence for accretion in the high-resolution X-ray spectrum of the T-Tauri star system Hen 3-600. *The Astrophysical Journal*, 671(1):592, 2007.

G.A.J. Hussain, A. Collier Cameron, M.M. Jardine, N. Dunstone, J. Ramirez Velez, H.C. Stempels, J-F. Donati, M. Semel, G. Aulanier, T. Harries, et al. Surface magnetic fields on two accreting T-Tauri stars: CV Cha and CR Cha. *Monthly Notices of the Royal Astronomical Society*, 398(1):189–200, 2009.

K. Imanishi, K. Koyama, and Y. Tsuboi. Chandra observation of the ρ Ophiuchi cloud. *The Astrophysical Journal*, 557(2):747, 2001.

K. Imanishi, H. Nakajima, M. Tsujimoto, K. Koyama, and Y. Tsuboi. A systematic study of X-Ray flares from low-mass young stellar objects in the Ophiuchi star-forming region with Chandra. *Publications of the Astronomical Society of Japan*, 55(3):653–681, 2003.

J.R. Ipser and R.H. Price. Synchrotron radiation from spherically accreting black holes. *The Astrophysical Journal*, 255:654–673, 1982.

H. Isobe, K. Shibata, T. Yokoyama, and K. Imanishi. Hydrodynamic modeling of a flare loop connecting the accretion disk and central core of young stellar objects. *Publications of the Astronomical Society of Japan*, 55(5):967–980, 2003.

C.M. Johns-Krull. The magnetic fields of classical T-Tauri stars. *The Astrophysical Journal*, 664(2):975, 2007.

K.J. Johnston, R.A. Gaume, A.L. Fey, C. de Vegt, and M.J. Claussen. The variable radio source T-Tauri. *The Astronomical Journal*, 125(2):858, 2003.

C.P. Johnstone, M. Jardine, S.G. Gregory, J-F. Donati, and G. Hussain. Classical T-Tauri stars: magnetic fields, coronae and star-disc interactions. *Monthly Notices of the Royal Astronomical Society*, 437(4):3202–3220, 2013.

A.H. Joy. T-Tauri variable stars. *The Astrophysical Journal*, 102:168, 1945.

M. Karlickỳ, J. Kašparová, and R. Sych. Radio, EUV, and X-Ray observations during a filament rise in the 2011 June 7 solar flare. *The Astrophysical Journal*, 888(1):18, 2019.

T. Kawamichi and K. Shibata. A simulation of protostar flares and the expected X-ray spectrum. In *The Seventh Pacific Rim Conference on Stellar Astrophysics*, volume 362, page 304, 2007.

C.F. Kennel. Consequences of a magnetospheric plasma. *Reviews of Geophysics*, 7 (1-2):379–419, 1969.

K-L. Klein. Microwave radiation from a dense magneto-active plasma. *Astronomy and Astrophysics*, 183:341–350, 1987.

E.P. Kontar, J.C. Brown, A.G. Emslie, W. Hajdas, G.D. Holman, G.J. Hurford, J. Kašparova, P.C.V. Mallik, A.M. Massone, M.L. McConnell, et al. Deducing electron properties from hard X-ray observations. *Space science reviews*, 159(1-4):301, 2011.

E.P. Kontar, G.G. Motorina, N.L.S. Jeffrey, Y.T. Tsap, G.D. Fleishman, and A.V. Stepanov. Frequency rising sub-THz emission from solar flare ribbons. *Astronomy & Astrophysics*, 620:A95, 2018.

M. Kounkel, L. Hartmann, L. Loinard, A.J. Mioduszewski, S.A. Dzib, G.N. Ortiz-León, L.F. Rodríguez, G. Pech, J.L. Rivera, R.M. Torres, et al. The Gould's Belt

Very Large Array survey. III. The Orion region. *The Astrophysical Journal*, 790(1): 49, 2014.

M.A. Kuhn, K.V. Getman, E.D. Feigelson, B. Reipurth, S.A. Rodney, and G.P. Garmire. A Chandra observation of the obscured star forming complex W40. *The Astrophysical Journal*, 725(2):2485–2506, dec 2010. doi: 10.1088/0004-637x/725/2/2485.

A.K. Kulkarni and M.M. Romanova. Accretion to magnetized stars through the Rayleigh–Taylor instability: global 3D simulations. *Monthly Notices of the Royal Astronomical Society*, 386(2):673–687, 2008.

P. Kundurthy, M.R. Meyer, M. Robberto, S.V.W. Beckwith, and T. Herbst. Mid-infrared observations of T-Tauri stars: Probing the star-disk connection in rotational evolution. *The Astronomical Journal*, 132(6):2469, 2006.

A.A. Kuznetsov, G.M. Nita, and G.D. Fleishman. Three-dimensional simulations of gyrosynchrotron emission from mildly anisotropic nonuniform electron distributions in symmetric magnetic loops. *The Astrophysical Journal*, 742(2):87, 2011.

C.J. Lada. Star formation: from OB associations to protostars. In *Symposium-International astronomical union*, volume 115, pages 1–18. Cambridge University Press, 1987.

M. Long, M.M. Romanova, and R.V.E. Lovelace. Accretion to stars with non-dipole magnetic fields. *Monthly Notices of the Royal Astronomical Society*, 374(2):436–444, 2007.

M. Long, M.M. Romanova, and F.K. Lamb. Accretion onto stars with octupole magnetic fields: Matter flow, hot spots and phase shifts. *New Astronomy*, 17(2):232–245, 2012.

S. Mairs, B. Lalchand, G.C. Bower, J. Forbrich, G.S. Bell, G.J. Herczeg, D. Johnstone, W-P. Chen, J-E. Lee, and A. Hacar. The JCMT transient survey: An extraordinary submillimeter flare in the T-Tauri binary system JW 566. *The Astrophysical Journal*, 871(1):72, 2019.

K.G. McClements. Reconnection and fast particle production in tokamak and solar plasmas. *Advances in Space Research*, 63(4):1443–1452, 2019.

M. McKinnon and R. Selina. The next-generation very large array: Technical overview. In *American Astronomical Society Meeting Abstracts# 231*, volume 231, 2018.

D.B. Melrose. The emission mechanisms for solar radio bursts. *Space Science Reviews*, 26(1):3–38, 1980.

D.B. Melrose. Coherent emission mechanisms in astrophysical plasmas. *Reviews of Modern Plasma Physics*, 1(1):5, 2017.

K. Mooley, L. Hillenbrand, L. Rebull, D. Padgett, and G. Knapp. B and A type stars in the Taurus-Auriga star-forming region. *The Astrophysical Journal*, 771(2):110, 2013.

K. Namekata, T. Sakaue, K. Watanabe, A. Asai, and K. Shibata. Validation of a scaling law for the coronal magnetic field strength and loop length of solar and stellar flares. *Publications of the Astronomical Society of Japan*, 69(1), 2017.

W.M. Neupert. Comparison of solar X-ray line emission with microwave emission during flares. *The Astrophysical Journal*, 153:L59, 1968.

G.M. Nita, G.D. Fleishman, A.A. Kuznetsov, E.P. Kontar, and D.E. Gary. Three-dimensional radio and X-ray modeling and data analysis software: Revealing flare complexity. *The Astrophysical Journal*, 799(2):236, 2015.

M. Oka, J. Birn, M. Battaglia, C.C. Chaston, S.M. Hatch, G. Livadiotis, S. Imada, Y. Miyoshi, M. Kuhar, F. Effenberger, et al. Electron power-law spectra in solar and space plasmas. *Space Science Reviews*, 214(5):82, 2018.

D. O'Neal, E.D. Feigelson, R.D. Mathieu, and P.C. Myers. A radio survey of weak T-Tauri stars in Taurus-Auriga. *The Astronomical Journal*, 100:1610–1617, 1990.

S. Orlando, F. Reale, G. Peres, and A. Mignone. Mass accretion to young stars triggered by flaring activity in circumstellar discs. *Monthly Notices of the Royal Astronomical Society*, 415(4):3380–3392, 2011.

S. Orlando, R. Bonito, C. Argiroffi, F. Reale, G. Peres, M. Miceli, T. Matsakos, C. Stehlé, L. Ibgui, L. De Sa, et al. Radiative accretion shocks along nonuniform stellar magnetic fields in classical T-Tauri stars. *Astronomy & Astrophysics*, 559: A127, 2013.

G.N. Ortiz-León, L. Loinard, A.J. Mioduszewski, S.A. Dzib, L.F. Rodríguez, G. Pech, J.L. Rivera, R.M. Torres, A.F. Boden, L. Hartmann, et al. The Gould's Belt Very Large Array Survey. II. The Serpens Region. *The Astrophysical Journal*, 805(1):9, 2015.

C.M.J. Osborne and P.J.A. Simões. Thyr: a volumetric ray-marching tool for simulating microwave emission. *Monthly Notices of the Royal Astronomical Society*, 485 (3):3386–3397, 2019.

R.A. Osten and S.J. Wolk. Multiwavelength signatures of magnetic activity from young stellar objects in the LkHα 101 cluster. *The Astrophysical Journal*, 691(2): 1128, 2009.

R.A. Osten, A. Brown, T.R. Ayres, S.A. Drake, E. Franciosini, R. Pallavicini, G. Tagliaferri, R.T. Stewart, S.L. Skinner, and J.L. Linsky. A multiwavelength perspective of flares on HR 1099: 4 years of coordinated campaigns. *The Astrophysical Journal Supplement Series*, 153(1):317, 2004.

H. Ozawa, N. Grosso, and T. Montmerle. The X-ray emission from young stellar objects in the ρ Ophiuchi cloud core as seen by XMM-Newton. *Astronomy & Astrophysics*, 429(3):963–975, 2005.

E.N. Parker. Sweet's mechanism for merging magnetic fields in conducting fluids. *Journal of Geophysical Research*, 62(4):509–520, 1957.

G. Pech, L. Loinard, S.A. Dzib, A.J. Mioduszewski, L.F. Rodríguez, G.N. Ortiz-León, J.L. Rivera, R.M. Torres, A.F. Boden, L. Hartman, et al. The Gould's Belt Very Large Array Survey. V. The Perseus Region. *The Astrophysical Journal*, 818(2): 116, 2016.

V. Petrosian. Synchrotron emissivity from mildly relativistic particles. 1981.

H.E. Petschek. Magnetic field annihilation. *NASA Special Publication*, 50:425, 1964.

RB Phillips, CJ Lonsdale, and ED Feigelson. Milliarcsecond radio structure of weak-lined t tauri stars. *The Astrophysical Journal*, 382:261–269, 1991.

I. Pillitteri, S. Sciortino, E. Flaccomio, B. Stelzer, G. Micela, F. Damiani, L. Testi, T. Montmerle, N. Grosso, F. Favata, and G. Giardino. Results from DROXO. *Astronomy and Astrophysics*, 519:A34, sep 2010. doi: 10.1051/0004-6361/200911873.

E. Priest. *Magnetohydrodynamics of the Sun*. Cambridge University Press, 2014.

E. Priest and T. Forbes. Magnetic reconnection: MHD theory and applications, cambridge univ. *Prees, Cambridge*, 2000.

R. Ramaty. Gyrosynchrotron emission and absorption in a magnetoactive plasma. *The Astrophysical Journal*, 158:753, 1969.

R. Ramaty, R.A. Schwartz, S. Enome, and H. Nakajima. Gamma-ray and millimeter-wave emissions from the 1991 June X-class solar flares. *The Astrophysical Journal*, 436:941–949, 1994.

S.V. Ramírez, L. Rebull, J. Stauffer, S. Strom, L. Hillenbrand, T. Hearty, E.L. Kopan, S. Pravdo, R. Makidon, and B. Jones. Chandra X-Ray observations of young clusters. II. Orion flanking fields data. *The Astronomical Journal*, 128(2):787–804, aug 2004. doi: 10.1086/422349.

F. Reale, R. Betta, G. Peres, S. Serio, and J. McTiernan. Determination of the length of coronal loops from the decay of X-ray flares I. Solar flares observed with YOHKOH SXT. *Astronomy and Astrophysics*, 325:782–790, 1997.

P.H. Roberts. *An introduction to magnetohydrodynamics*, volume 6. Longmans London, 1967.

C.E. Robinson, J.E. Owen, C.C. Espaillat, and F.C. Adams. Time-dependent models of magnetospheric accretion onto young stars. *The Astrophysical Journal*, 838(2): 100, 2017.

M.M. Romanova, G.V. Ustyugova, A.V. Koldoba, and R.V.E. Lovelace. The propeller regime of disk accretion to a rapidly rotating magnetized star. *The Astrophysical Journal Letters*, 616(2):L151, 2004.

G.G. Sacco, C. Argiroffi, S. Orlando, A. Maggio, G. Peres, and F. Reale. X-ray emission from dense plasma in classical T-Tauri stars: hydrodynamic modeling of the accretion shock. *Astronomy & Astrophysics*, 491(2):L17–L20, 2008.

G.G. Sacco, S. Orlando, C. Argiroffi, A. Maggio, G. Peres, F. Reale, and R.L. Curran. On the observability of T-Tauri accretion shocks in the X-ray band. *Astronomy & Astrophysics*, 522:A55, 2010.

N.S. Schulz, D.P. Huenemoerder, M. Günther, P. Testa, and C.R. Canizares. X-Ray properties of low-mass pre-main sequence stars in the Orion Trapezium Cluster. *The Astrophysical Journal*, 810(1):55, 2015.

K. Shibata and T. Magara. Solar flares: magnetohydrodynamic processes. *Living Reviews in Solar Physics*, 8(1):6, 2011.

K. Shibata and T. Yokoyama. Origin of the universal correlation between the flare temperature and the emission measure for solar and stellar flares. *The Astrophysical Journal Letters*, 526(1):L49, 1999.

P.J.A Simões and J.E.R Costa. Solar bursts gyrosynchrotron emission from three-dimensional sources. *Astronomy & Astrophysics*, 453(2):729–736, 2006.

P.J.A. Simoes and J.E.R. Costa. Gyrosynchrotron emission from anisotropic pitch-angle distribution of electrons in 3-D solar flare sources. *Solar Physics*, 266(1): 109–121, 2010.

M. Simon. Time dependence of razin spectra in type IV solar radio bursts. *Astrophysical Letters*, 3:23, 1969.

S. Skinner, M. Gagne, and E. Belzer. A deep Chandra X-Ray observation of the embedded young cluster in NGC 2024. *The Astrophysical Journal*, 598(1):375–391, 2003. doi: 10.1086/378085.

S.L. Skinner. Circularly polarized radio emission from the T-Tauri star Hubble 4. *The Astrophysical Journal*, 408:660–667, 1993.

V.M. Souza, D. Koga, W. D. Gonzalez, and F.R. Cardoso. Observational aspects of magnetic reconnection at the Earth's magnetosphere. *Brazilian Journal of Physics*, 47(4):447–459, 2017.

J.H. Spencer and P.R. Schwartz. Radio emission from Pre-main stars. *The Astrophysical Journal*, 188:L105, 1974.

A.V. Stepanov and V.V. Zaitsev. The challenges of the models of solar flares. *Geomagnetism and Aeronomy*, 56(8):952–971, 2016.

P.A. Sweet. The neutral point theory of solar flares. In *Symposium-International Astronomical Union*, volume 6, pages 123–134. Cambridge University Press, 1958.

A. Telleschi, M. Güdel, K.R. Briggs, M. Audard, and F. Palla. X-ray emission from T-Tauri stars and the role of accretion: inferences from the XMM-Newton extended survey of the Taurus Molecular Cloud. *Astronomy & Astrophysics*, 468(2):425–442, 2007.

J.J. Tobin, L. Hartmann, H-F. Chiang, D.J. Wilner, L.W. Looney, L. Loinard, N. Calvet, and P. D'Alessio. A 0.2-solar-mass protostar with a Keplerian disk in the very young L1527 IRS system. *Nature*, 492(7427):83–85, 2012.

B.M. Tofflemire, R.D. Mathieu, D.R. Ardila, R.L. Akeson, D.R. Ciardi, C. Johns-Krull, G.J. Herczeg, and A. Quijano-Vodniza. Accretion and magnetic reconnection in the classical T-Tauri binary DQ Tau. *The Astrophysical Journal*, 835(1):8, 2017.

Y. Tsuboi, K. Koyama, H. Murakami, M. Hayashi, S. Skinner, and S. Ueno. ASCA detection of a superhot 100 million K X-ray flare on the weak-lined T-Tauri star V773 Tauri. *The Astrophysical Journal*, 503(2):894, 1998.

Y. Tsuboi, K. Yamazaki, Y. Sugawara, A. Kawagoe, S. Kaneto, R. Iizuka, T. Matsumura, S. Nakahira, M. Higa, M. Matsuoka, et al. Large X-ray flares on stars detected with MAXI/GSC: A universal correlation between the duration of a flare and its X-ray luminosity. *Publications of the Astronomical Society of Japan*, 68(5), 2016.

M. Tsujimoto, K. Koyama, Y. Tsuboi, M. Goto, and N. Kobayashi. X-ray properties of young stellar objects in OMC-2 and OMC-3 from the Chandra X-Ray observatory. *The Astrophysical Journal*, 566(2):974–981, feb 2002. doi: 10.1086/338110.

A. Uzawa, Y. Tsuboi, M. Morii, K. Yamazaki, N. Kawai, M. Matsuoka, S. Nakahira, M. Serino, T. Matsumura, T. Mihara, et al. A large X-ray flare from a single weak-lined T-Tauri star TWA-7 detected with MAXI GSC. *Publications of the Astronomical Society of Japan*, 63(sp3):S713–S716, 2011.

A.A. Vidotto, M. Opher, V. Jatenco-Pereira, and T.I. Gombosi. Simulations of winds of weak-lined T-Tauri stars. II. The effects of a tilted magnetosphere and planetary interactions. *The Astrophysical Journal*, 720(2):1262, 2010.

F.M. Walter. The naked T-Tauri stars: The low-mass pre-main sequence unveiled. *Publications of the Astronomical Society of the Pacific*, 99(611):31, 1987.

C.O.G. Waterfall, P.K. Browning, G.A. Fuller, and M. Gordovskyy. Modelling the radio and X-ray emission from T-Tauri flares. *Monthly Notices of the Royal Astronomical Society*, 483(1):917–930, 2019.

C.O.G. Waterfall, P.K. Browning, G.A. Fuller, M. Gordovskyy, S. Orlando, and F. Reale. Predicting the time variation of radio emission from mhd simulations of a flaring t-tauri star. *Monthly Notices of the Royal Astronomical Society*, 2020.

S.M. White, R. Pallavicini, and M.R. Kundu. Radio observations of weak-lined T-Tauri stars. *Memorie della Societa Astronomica Italiana*, 63:751–754, 1992.

J.P. Wild and E.R. Hill. Approximation of the general formulae for gyro and synchrotron radiation in a vacuum and isotropic plasma. *Australian Journal of Physics*, 24:43, 1971.

A. Wootten and A. R. Thompson. The Atacama Large Millimeter/submillimeter Array. *Proceedings of the IEEE*, 97(8):1463–1471, 2009.

Z. Wu, Y. Chen, H. Ning, X. Kong, and J. Lee. Gyrosynchrotron emission generated by nonthermal electrons with the energy spectra of a broken power law. *The Astrophysical Journal*, 871(1):22, 2019.

T. Yokoyama and K. Shibata. A two-dimensional magnetohydrodynamic simulation of chromospheric evaporation in a solar flare based on a magnetic reconnection model. *The Astrophysical Journal Letters*, 494(1):L113, 1998.

E.G. Zweibel and M. Yamada. Magnetic reconnection in astrophysical and laboratory plasmas. *Annual review of astronomy and astrophysics*, 47:291–332, 2009.

E.G. Zweibel and M. Yamada. Perspectives on magnetic reconnection. *Proceedings of the Royal Society A: Mathematical, Physical and Engineering Sciences*, 472(2196): 20160479, 2016.